2017

Altered Axon Initial Segment Structure and Function In Inflammatory Disease

Kareem C. Clark

ALTERED AXON INITIAL SEGMENT STRUCTURE AND FUNCTION IN INFLAMMATORY DISEASE

A dissertation submitted in partial fulfillment of the requirements for the degree of Doctor of Philosophy at Virginia Commonwealth University.

By

Kareem Clark
B.S. North Carolina State University, 2011

Director: Jeffrey L. Dupree, Ph.D.
Associate Professor
Department of Anatomy and Neurobiology

Virginia Commonwealth University
Richmond, Virginia

October 2017

ACKNOWLEDGEMENTS

I would like to thank my mentor Jeff Dupree who simultaneously encouraged my independence while providing invaluable guidance and support. He taught me to be fearless and go where the project takes you, even if it requires venturing into completely unfamiliar areas.

I would also like to thank the members of my committee for providing immense support and feedback along the way. Special thanks goes to Dr. Kimberle Jacobs for her incredibly valuable training and assistance with electrophysiology. Also to Dr. Unsong Oh who, in addition to contributing great ideas to the project, also spent a great deal of time in my training for EAE induction. To Dr. George DeVries for acting as a sounding board during every aspect of the project and ensuring that every manuscript I published was grammatically pristine. Also to Dr. Kurt Hauser, who has made himself and his lab available for valuable guidance and assistance with numerous aspects of the project, including calcium imaging and oxidative stress assays.

Additional thanks to the VCU Dept. of Anatomy and Neurobiology Microscopy Facility, including Dr. Scott Henderson and Fran White for their assistance with training, image collection, and data analysis.

Thank you to the members of the Dupree lab, former and current. I would especially like to express my gratitude to Savannah Benusa for commiserating during the lows, and celebrating during the highs of research. I hope that I have provided her with a fraction of the support she has given me.

Finally, I would like to thank my family for their unconditional love and support.

TABLE OF CONTENTS

Page

LIST OF FIGURES

Page

LIST OF TABLES

Page

LIST OF ABBREVIATIONS

A6	Annexin 6
α-Act	Alpha Actinin
AIS	Axon Initial Segment
ALS	Amyotrophic Lateral Sclerosis
AnkG	Ankyrin G
ANOVA	Analysis of Variance
AP	Action Potential
BBB	Blood Brain Barrier
Ca^{2+}	Calcium
CAM	Cell Adhesion Molecule
Caspr-2	Contactin Associated Protein-2
CIS	Clinically Isolated Syndrome
CNS	Central Nervous System
CO	Cisternal Organelle
CSF	Cerebrospinal Fluid
EBV	Epstein-Barr virus
GABA	Gamma-Aminobutyric Acid
HVA	High-Voltage-Activated
IFN	Interferon
IL	Interleukin
iNOS	Inducible Nitric Oxide Synthase
IP_3	Inositol 1,4,5-Trisphosphate
LVA	Low-Voltage-Activated
MBP	Myelin Basic Protein
mM	Millimolar
µM	Micromolar
MOG	Myelin oligodendrocyte glycoprotein
MRI	Magnetic Resonance Imaging
MS	Multiple Sclerosis
Na_v^+	Voltage-Gated Sodium
NF	Neurofascin
NOR	Node of Ranvier
NOX	Nicotinamide Adenine Dinucleotide Phosphate Oxidase
PLP	Proteolipid Protein
PPMS	Primary-Progressive Multiple Sclerosis
PRMS	Primary-Relapsing Multiple Sclerosis
RNS	Reactive Nitrogen Species
ROS	Reactive Oxygen Species
RRMS	Relapsing-Remitting Multiple Sclerosis
SERCA	Sarco-Endoplasmic Reticulum Ca^{2+}-ATPase
SPMS	Secondary Progressive Multiple Sclerosis
Synpo	Synaptopodin
Tag-1	Transient Axonal Glycoprotein-1
TBI	Traumatic Brain Injury
TGF-β	Transforming growth factor beta
TMEV	Theiler's Murine Encephalomyelitis Virus
VGCC	Voltage Gated Calcium Channels

ABSTRACT

ALTERED AXON INITIAL SEGMENT STRUCTURE AND FUNCTION IN INFLAMMATORY DISEASE

By Kareem Clark, B.S.

A dissertation submitted in partial fulfillment of the requirements for the degree of Doctor of Philosophy at Virginia Commonwealth University.

Virginia Commonwealth University, 2017

Director: Jeffrey L. Dupree, Ph.D.
Associate Professor
Department of Anatomy and Neurobiology

Axonal pathology is a key contributor to long-term disability in multiple sclerosis (MS), an inflammatory demyelinating disease of the central nervous system (CNS), but the mechanisms that underlie axonal insults remain unclear. While most axonal pathologies characterized in MS are a direct consequence of myelin loss, we propose that axonal pathologies also occur independent of demyelination. In support of this idea, we recently reported that mice that develop experimental autoimmune encephalomyelitis (EAE), a model commonly used to mimic the pathogenesis of MS, exhibit a structural and functional disruption of the axon initial segment (AIS), a subdomain of the axon that acts as the trigger-zone for action potential generation. Importantly, this disruption is independent of myelin loss. Although the mechanism responsible for AIS disruption remains unclear, we observed an attenuation of the AIS insult following treatment with a known scavenger of oxygen free radicals. To further investigate the role of oxidative stress in modulating AIS stability, we employed an *in vitro* model in which neurons were exposed to a spontaneous reactive oxygen and nitrogen species generator. Through this

approach, we demonstrated that oxidative stress is capable of AIS modulation acting through induction of cytosolic calcium (Ca^{2+}) influx from both extracellular and intracellular sources, resulting in calpain protease activation. Furthermore, because rises in intracellular Ca^{2+} are central to these and other mechanisms of AIS disruption, we next investigated the cisternal organelle (CO), an AIS-localized Ca^{2+}-regulating structure. Although this organelle could prove to be central to AIS modulation, very little is known about the mechanisms regulating its stability. Through this line of investigation, we provide the first evidence of pathological alteration to the CO in a disease state. This disruption precedes loss of AIS protein clustering and axo-axonic GABAergic input in both EAE and MS postmortem tissue. Overall, these studies reveal a primary axonal insult, independent of myelin loss, in a disease classically characterized as a white-matter pathology. Instead, this insult is most likely driven by oxidative stress through local Ca^{2+} dysregulation at the AIS, providing novel therapeutic targets for MS.

CHAPTER ONE

INTRODUCTION

1.1 The Central Nervous System

The central nervous system (CNS), which integrates information and coordinates activity throughout the body, consists of two major structures: the brain and spinal cord, as opposed to the peripheral nervous system which consists of nerves that travel outside of the skull or spinal column (de Lahunta et al., 2016). This system is composed of gray and white matter which contain neuronal cell bodies and processes respectively (de Lahunta et al., 2016). Entry of circulating blood flow components into the CNS is restricted by a highly selective blood brain barrier (BBB). Additionally, a unique set of cell types reside in the CNS, including neuronal and glial cells, which include astrocytes, microglia, and oligodendrocytes (Zuchero and Barres, 2015).

Astrocytes are one of three main types of glial cells present in the CNS (Oberheim et al., 2012). These star-shaped cells have perhaps the most diverse set of functions including guiding laminar organization, providing neuronal trophic support, modulating synaptic activity, and maintaining BBB integrity. These cells are also interconnected through gap-junctions that aid in the synchrony during reactivity (Orellana et al., 2013). Microglia, a separate glial cell type, are the resident innate immune cells of the CNS. While the periphery contains a host of lymphocyte and macrophage related cells, the inflammatory response in the CNS is largely mediated by microglia (Kabba et al., 2017). These cells survey the surrounding CNS environment ready to respond to potential insults (Kabba et al., 2017). As effectors of the inflammatory response, these cells can exhibit a

spectrum of reactivity profiles depending on the nature of the insult. Microglia are capable of displaying either pro-inflammatory or resolving phenotypes which mediate destructive or reparative processes respectively (Tang and Le, 2016).

A third type of glial cell, oligodendrocytes, are critical for efficient neuronal firing activity (Simons and Nave, 2015). These cells form the myelin sheaths, fatty membranes which wrap around and insulate the axon and allow for rapid propagation of an action potential (AP) (Simons and Nave, 2015). These myelin forming glial cells are responsible for the establishment and maintenance of several neuronal subdomains along the axon that are crucial for AP transmission (Chang and Rasband, 2013). Oligodendrocytes arise from progenitor cells which develop into non-myelin forming immature oligodendrocytes. These pro-oligodendrocytes then mature and express critical myelin components necessary for initiation of myelination (Barateiro et al., 2016). While myelin consists of ~70% lipids, proteins such as myelin basic protein (MBP), proteolipid protein (PLP), myelin oligodendrocyte glycoprotein (MOG), and myelin associated glycoprotein (MAG) are important for proper myelination (Jahn et al., 2009). As oligodendrocyte processes wrap around an axon, cytoplasm in the oligodendrocyte membranes is compressed towards the lateral edges of the myelin segments, resulting in regions of compacted and non-compacted myelin (Zuchero and Barres, 2015). While some axons are unmyelinated, AP conduction speed is significantly slower. Without myelin, axons typically have an AP conduction velocity of ~10 m/s, while compact myelinated axons can propagate at speeds around 100 m/s. (Salzer, 2003; Zalc, 2006).

While glial cells have important roles within the CNS, they serve primarily to support neurons, the functional units of the nervous system. Acting as the effectors of impulse

transmission, these cells control a vast array of physiological functions (Raichle, 2010). Neurons of the CNS can be subclassified into pyramidal cells or interneurons which exhibit excitatory or inhibitory neurotransmitter release respectively (Hu et al., 2014). Important for their firing function, neurons exhibit cellular polarity which involves the establishment of distinct cellular compartments such as the somatodendritic region, which receives input from other neurons, and the axonal compartment which transmits signals to other targets (Britt et al., 2016).

1.2 Axonal Domains

A myelinated axon of the CNS contains distinct specialized domains including; the internode, juxtaparanode, paranode, node of Ranvier, and axon initial segment (AIS), which are diagramed in Figure 1.1 (modified from Susuki et al., 2013). These domains have similarities and differences with regards to protein composition, function, and mechanisms of establishment and maintenance (Buttermore et al., 2013).

1.2.1 The Internode

Spanning a distance of about 99% of the myelinated segment length, the internode is the region of the myelinated axon where the myelin is most compact (Buttermore et al., 2013; Salzer, 2003; Thaxton and Bhat, 2009). This domain contains axoglial interactions mediated by cell adhesion molecules (CAMs) called nectin-like proteins, which form junctions between the internodal axonal membrane and the overlying myelin sheath. These nectin-like proteins are important for both the initiation of myelin wrapping, as well as the maintenance of these axoglial interactions following myelination (Park et al., 2008,

Spiegel et al., 2007). The cytoskeletal network in the internode consists of the scaffolding proteins βII- and αII-spectrin, protein 4.1B, and the adaptor protein ankyrin B which form a complex that interacts with actin to establish and maintain neuronal polarity (Buttermore et al., 2013; Galiano et al., 2012). While ion channels are not clustered at the internode, they are diffusely distributed along the length of this domain (Freeman et al., 2016). Despite the lack of ion channel clustering, the internode plays a critical role in AP propagation through the maintenance of close axonal-myelin association of the protein interactions described above (Buttermore et al., 2013; Maurel et al., 2007; Salzer, 2003; Thaxton and Bhat, 2009).

1.2.2 The Juxtaparanode

Flanking the internodes is an axonal domain that is crucial for repolarization following AP transmission known as the juxtaparanode. This domain contains a high density of delayed rectifier potassium channels which function to return the membrane potential to resting state following AP propagation and prevents its backpropagation (Buttermore et al., 2011; Rasband et al., 1998; Thaxton and Bhat, 2009). Similar to the internode, the juxtaparanode makes contact with the overlying myelin sheath via specific protein interactions. The protein complex, however, is distinct from that of the internodal axoglial interactions. Transmembrane cell adhesion molecule contactin associated protein-2 (caspr-2) binds the CAM known as transient axonal glycoprotein-1 (tag-1) on the axolemma (Gollan et al., 2003; Thaxton and Bhat, 2009; Zoupi et al., 2013). Axonal caspr-2 and tag-1 then form interactions with tag-1 expressed on the myelin membrane to form axoglial junctions (Traka et al., 2003; Zoupi et al., 2013). Similar to the internode, this

complex is linked to the cytoskeleton through the same scaffolding proteins αII- and βII-spectrin, protein 4.1B, and the adaptor ankyrin B. The caspr-2/tag-1 complex is also important for the clustering of the rectifier potassium channels, as a mutation in either of these proteins results in diffusion of these channel clusters (Poliak et al., 2003; Thaxton and Bhat, 2009; Zoupi et al., 2013).

1.2.3 The Paranode

Located immediately adjacent to the juxtaparanode is the paranodal axonal domain, which forms junctions with the lateral edges of myelin segments (Buttermore et al., 2013; Rosenbluth et al., 2013; Salzer, 2003; Thaxton and Bhat, 2009). The length of the paranode is highly conserved at ~3.5 µm (Shepherd et al., 2012). As myelin wraps around the axon, the cytoplasm contained in the oligodendrocyte process is forced to the edges, creating pockets of cytoplasm (non-compact myelin) in the glial membrane called “paranodal loops” (Buttermore et al., 2013; Snaidero et al., 2014). These loops make contact with the axonal membrane (axolemma) through protein interactions termed transverse bands or axoglial septate-like junctions which provide a barrier against lateral diffusion of the distinct axonal domains (Buttermore et al., 2011; Buttermore et al., 2013; Snaidero et al., 2014). The junctions between the axolemma and the paranodal myelin loops consist of 2 proteins on the axolemmal side: CAM caspr-1 which binds in *cis* with contactin (Buttermore et al., 2013) and a single transmembrane CAM neurofascin 155 (NF-155) on the glial side (Gollan et al., 2003). Additionally these axoglial interactions are stabilized by the spectrin, protein 4.1B, and ankyrin B actin scaffolding complex as in the internode and juxtaparanode (Faivre-Sarrailh and Devaux et al., 2013; Thaxton et al.,

2011). The establishment and maintenance of the paranode is dependent on these interactions with the myelin membrane through this complex (Pillai et al., 2009). The paranodal domain, while crucial for myelin contact, does not contain functional ion channel clusters in the axolemma (Buttermore et al., 2013). Despite this, the paranode nevertheless plays an important role in AP propagation serving as a "fence," demarcating nodal and juxtaparanodal ion channels and allowing for rapid saltatory conduction (Dupree et al., 1999; Rosenbluth et al., 2003; Thaxton and Bhat, 2009).

1.2.4 The Node of Ranvier

The nodes of Ranvier are myelin-bare regions of the axon spanning approximately 1-2 μm in length (Salzer, 1997). Saltatory conduction, the "jumping" of action potentials from node to node along the axon, is made possible by a high density clustering of voltage gated sodium channels at the node of Ranvier (Salzer, 2003; Arancibia‐Carcamo and Attwell, 2014). Without this clustering, AP conduction would be severely hindered. These sodium channels are anchored to the cytoskeleton through interaction with the nodal- and AIS-specific scaffolding protein ankyrin G (AnkG) (Buttermore et al., 2013; Thaxton and Bhat, 2009). AnkG associates with the spectrin-actin cytoskeleton through interactions with βIV-spectrin, which is also exclusively localized in the node and AIS (Berghs et al. 2000; Buttermore et al., 2013; Komada and Soriano, 2002). The node of Ranvier also contains extracellular matrix (ECM) molecules such as the proteoglycans; brevican (Bekku et al., 2009) and versican (Dours-Zimmermann et al., 2009), as well as specific CAMs such as neurofascin-186 (NF-186) and neural cell adhesion molecule (NrCAM) (Davis et al., 1996; Eshed-Eisenbach and Peles, 2013), which also interact with the

scaffolding protein AnkG (Lustig et al., 2001; Rasband, 2010). Establishment and maintenance of nodal protein clustering is dependent on both extrinsic glial cues and intrinsic neuronal cues through initial clustering of NF-186 driven by myelin contact followed by recruitment of the AnkG scaffolding protein which clusters other scaffolding proteins and voltage gated ion channels (Yang et al., 2007; Zonta et al., 2008).

1.2.5 The Axon Initial Segment

The AIS is the unmyelinated region of the axon, spanning about 35-45 μm distally from the soma, located between the axon hillock and the first myelin segment (Grubb and Burone, 2010; Rasband, 2010). The AIS provides two critical functions: serving as the trigger zone for AP initiation as well as establishing and maintaining neuronal polarity (Yosihmura and Rasband, 2014). Consistent with the AIS and the NOR both playing roles in AP transmission, their protein clusters are very similar in composition (Rasband, 2010). The AIS, like the node, contains a high density of voltage gated sodium channels which are ~40-50 times more densely clustered in the AIS compared to the somatodendritic domain (Rasband, 2010; Kole et al., 2008). Unlike the node, which assists in the propagation of action potentials, these AIS sodium channel clusters instead serve as the trigger zone for firing (Meeks et al., 2007). In addition to its role in AP initiation, modulation of the AP amplitude, duration, and frequency is made possible by a variety of voltage gated potassium channel subtypes (Kole et al., 2007; Sánchez-Ponce et al., 2012). The AIS also serves as a barrier between the somatodendritic and axonal compartments; thus maintaining neuronal polarity (Rasband, 2010). This AIS barrier, while not fully understood, is hypothesized to act as a sieve to filter out large cytoplasmic molecules

(Nakada et al., 2003; Rasband, 2010). Diffusion within the membrane is also restricted due to physical interactions with the AIS cytoskeletal and scaffolding proteins (El-Husseini et al., 2000; Rasband, 2010).

Establishing and maintaining the protein complexes that constitute the AIS is critical for both initiation and modulation of action potentials, as well as retaining neuronal polarity. Establishment and maintenance of this domain is under the sole control of cytoskeletal scaffolding protein AnkG, which is dubbed the “master organizer” of the AIS complex (Dzhashiashvili et al., 2007; Hedstrom, et al., 2007; Rasband, 2010). AnkG silencing and its removal from the mature AIS results in dismantling of the AIS, as detected through dispersion of sodium channels, βIV-spectrin, NF-186, and NrCAM immunolabeling (Hedstrom et al., 2008). AnkG is therefore, not only required for the initial recruitment and clustering of AIS proteins, but also for the long-term maintenance of this domain. The AIS, once established, is highly plastic, exhibiting alterations to ion channel localization and expression in response to neuronal activity. (Adachi et al., 2014; Grubb and Burrone 2010; Kaphzan et al., 2011; Kuba et al., 2012).

Although the node of Ranvier and the AIS contain very similar protein clusters, they are established and maintained through drastically different processes. In addition to the differences in roles that NF-186 and AnkG play in recruitment and stabilization of the two domains, as described above, perhaps the most extreme difference lies in the role of myelin contact. In fact, none of the nodal, paranodal, juxtaparanodal, and internodal domains can successfully form without glial contact (Dupree et al., 1999; Buttermore et al., 2013; Dzhashiashvili et al., 2007; Eshed-Eisenbach and Peles, 2013; Susuki et al., 2013; Thaxton and Bhat, 2009). The AIS, however, is formed intrinsically through AnkG

restriction to the proximal end of the developing axon, completely independent of myelination (Bennett and Baines, 2001; Galiano et al., 2012).

1.3 Axonal Domains in Injury and Disease

As described above, the nodal and initial segment domains are responsible for critical functions such as AP firing and neuronal polarity maintenance (Nelson et al., 2017). Because of these vital functions, pathological disruption of these domains yields severe downstream consequences responsible for a wide array of CNS insults (Nelson et al., 2017).

1.3.1 The Nodal Domains in Injury and Disease

As detailed above, the major regulator of the nodal axonal domain stability is myelin integrity. For this reason, nodal disruption is characteristic of all CNS insults with demyelination as a pathogenic feature. Our laboratory and others have demonstrated loss of nodal protein clustering as a downstream consequence of demyelination in mouse models of MS and postmortem MS tissue (Dupree et al., 2004; Coman et al., 2006; Howell et al., 2010; Pomicter et al., 2010; Zoupi et al., 2013). Following loss of myelin contact on the axon, voltage gated ion channels, as well as cytoskeletal scaffolding molecules, diffuse away from the domains at which they were clustered (Arancibia-Carcamo and Attwell, 2014). Interestingly, nodal clustering can be re-established upon remyelination. In the cuprizone demyelinating model of MS, mice that were withdrawn from the cuprizone treatment display endogenous remyelination which paralleled reestablishment of nodal ion channel and scaffolding protein clustering (Dupree et al., 2004). Similarly, analysis of

partially remyelinated lesions in MS postmortem tissue revealed similar restoration of nodal clustering (Coman et al., 2006). Other demyelinating disorders of the CNS that include nodal domain disruption include optic neuritis, phenylketonuria, Tay-Sachs, Gaucher disease, and other leukodystrophies (Mehndiratta and Gulati, 2014).

Interestingly, there is evidence of nodal domain dysfunction in CNS disorders that lack detectible myelin loss. For example, mutations in ion channels as well as cytoskeletal scaffolding proteins at the NOR, paranode and juxtaparanode are implicated in several psychiatric disorders including epilepsy, bipolar disorder and autism (Susuki, 2013). Additional myelin-independent mechanisms of nodal domain disruption, in the form of reduced ion channel expression and localization, occurs in disorders involving the peripheral nervous system, such as amyotrophic lateral sclerosis (ALS) (Shibuya et al., 2011). Traumatic brain injury, as induced through mild fluid percussion, can also result in intrinsic disruption of nodal domains through neuronal calpain activation and proteolytic cleavage of critical nodal scaffolding components (Reeves et al., 2010). Unlike the myelin-dependent nodal pathologies, restoration of nodal structure and function following insult has yet to be demonstrated.

1.3.2 The Axon Initial Segment in Injury and Disease

While nodal axonal domains are crucial for AP propagation, AIS function is perhaps more crucial to neuronal firing as the site of AP initiation (Adachi et al., 2014). Unlike the nodal axonal domains, the AIS does not require myelin for establishment of the domain (Nelson et al., 2017). The role of myelination in maintenance of AIS integrity, however, has only very recently been investigated by our lab (see Chapter 2; Clark et al., 2016)

and others (Hamada and Kole, 2015). Other CNS insults, however, are known to induce structural and functional alterations to this domain. AIS disruption is prominent, and thought to be a causative factor, in several animal models of epilepsy (Marco et al., 1997, Wimmer et al., 2010; Harty et al., 2013; Liu et al., 2017). These findings are consistent with the role of the AIS as a modulator of neuronal firing (Kole et al., 2008). Additionally, traumatic brain injury (TBI), as modeled by blast wave exposure and mild central fluid percussion, induces reductions in AIS length, which correlate to functional changes in AP generation (Baalman et al., 2013; Greer et al., 2013; Vascak et al., 2017). Disrupted AISs are also observed in close proximity to Amyloid-β plaques in models of Alzheimer's disease (León-Espinosa et al., 2012; Marin et al., 2016). These changes in models of Alzheimer's disease are believed to result from decreased AnkG expression by increased levels of specific microRNAs (Sun et al., 2014). These structural changes correlated to impairment of the selectivity function of the AIS allowing macromolecules such as pathogenic forms of Tau into the somatodendritic compartment (Li, et al., 2011; Zempel et al., 2017). AIS structure is also a downstream consequence of ischemic injury as induced through middle cerebral artery occlusion, focal cortical, and focal white matter stroke (Schafer et al., 2009; Hinman et al., 2013). Similarly, excitotoxicity to high levels of purinergic and glutamate signaling also result in alterations to the AIS complex (Del Puerto et al., 2015; Benned-Jensen et al., 2016) As detailed below, AIS dismantlement under ischemic and excitotoxic conditions involves activation of a calcium activated protease revealing an important role for calcium regulation at the AIS in the maintenance of domain stability.

1.4 The Role of Calcium at the AIS

As described above, all established mechanisms of AIS alterations under CNS insults involve Ca^{2+} dysregulation and activation of downstream Ca^{2+}-dependent enzymatic processes. Understanding mechanisms of Ca^{2+} entry and storage is, therefore, vital to addressing these pathologies in an array of CNS conditions.

1.4.1 Extracellular Ca^{2+} Entry

Influx of extracellular Ca^{2+} at the AIS is achieved through a variety of membrane channels that involve both voltage as well as ligand-gated entry (Rao et al., 2007; Simms et al., 2014). Voltage-gated Ca^{2+} channels (VGCCs), which remain closed at resting membrane potential, require a depolarizing shift in order for Ca^{2+} influx to occur (Simms et al., 2014). These channels respond to membrane depolarization through a conformational change of the channel subunits, which allows pore formation and entry of Ca^{2+} down its concentration gradient (Catterall et al., 2011). Multiple subfamilies of VGCCs are classified according to a variety of properties including; strength of voltage-dependence, conductance of ion flow, and sensitivity to pharmacological antagonists (Catterall et al., 2011). These VGCC subfamilies include Ca_v1, Ca_v2, and Ca_v3, which are further classified into channel subtypes correlating with the type of Ca^{2+} current they conduct. Additionally, each VGCC subfamily is also described based on the degree of changes to membrane potential required for activation: either low-voltage activated (LVA) or high-voltage activated (HVA). These subfamilies include L-type, N-type, P/Q-type, T-type and R-type currents (Catterall et al., 2011; Simms et al., 2014).

T-type VGCCs, belonging to the Ca_v3 subfamily, are classified separately from all other subfamilies as LVA, since they open in response to small depolarizing currents (Cain et al., 2013). Three subtypes of T-type VGCCs are identified each with a unique pore forming subunit (Cain et al., 2013). These include $Ca_v3.1$, $Ca_v3.2$, and $Ca_v3.3$ (Cain et al., 2013). While T-type channels are the only LVA type of VGCCs described, they are not the only type classified differently from the HVA channels. R-type channels ($Ca_v2.3$), despite belonging to the Ca_v2 subfamily of VGCCs, share activation and inactivation properties with both HVA and LVA channels, lending them to an intermediate-voltage activated classification (Guéguinou et al., 2014). Both T- and R-type VGCCs are present at the AIS of hippocampal neurons, neocortical pyramidal cells, cerebellar Purkinje cells, as well as cartwheel interneurons of the dorsal cochlear nucleus (Bender and Trussell, 2009, Bender et al., 2010, Grubb and Burrone, 2010). AIS expression of these channels, however, seems to vary among cell type as T-type channels are excluded from the AIS-like region of retinal bipolar cells, and are instead localized exclusively to the somatodendritic compartment. While T- and R-type VGCCs are expressed in a variety of neuronal cell types axonally and/or somatodendritically (Puthussery et al., 2013), their localization at the AIS in other CNS regions remains to be investigated.

The Ca_v2 subfamilies of VGCCS contain P/Q-type and N-type VGCCs are both HVA channels further characterized as $Ca_v2.1$ and $Ca_v2.2$, respectively (Nimmrich and Gross, 2012; Adams et al., 2013). While N-type channels were named for their ubiquitous expression in the “nervous” system, P/Q-type VGCCs were originally identified in cerebellar Purkinje cells but later found to be expressed in a variety of other CNS regions (Gazulla and Tintore, 2007). Among several neuronal functions, these channel subtypes

are important for vesicle release of specific neurotransmitters at synaptic terminals (Molderings et al., 2000; Nimmrich and Gross, 2012). They are also localized at the AIS where their proposed function is in the modulation of AP wave form and spike timing (Yu et al., 2010).

Another type of HVA channels, L-type VGCCs, belong to the Ca_V1 subfamily (Furukawa, 2013). These subtypes are named for their “long-lasting” duration of activation, and are extensively characterized in cardiomyocytes (Eisner et al., 2014). Neuronal L-type VGCCs, however, are expressed and involved in a variety of neuronal functions such as regulating synaptic transmission and plasticity at the somatodendritic compartment. Interestingly, while L-type VGCCs are heavily involved in modulating AIS plasticity and injury in a variety of CNS insults as described below, they are absent at the AIS plasma membrane (Griggs et al., 2017; Jamann et al., 2017). These are not the only non-AIS localized Ca^{2+} channels that influence domain stability. Purinergic (P2X7) and glutamate (NMDA) receptors, which are non-selectively permeable to cations including Ca^{2+}, also reside in the somatodendritic compartment where they are thought to influence AIS Ca^{2+} levels through changes in membrane potential and subsequent activation of AIS-localized VGCCs (Del Puerto et al., 2015; Benned-Jensen et al., 2016).

1.4.2 Intracellular Ca^{2+} Stores: The Cisternal Organelle

While cell surfaced localized channels are important for extracellular Ca^{2+} entry, local storage at the AIS is also critical for buffering cytoplasmic Ca^{2+} levels (Benedeczky et al., 1994). The AIS contains a unique Ca^{2+} storing structure known as the cisternal organelle (CO), which is a specialized form of smooth endoplasmic reticulum (Bas Orth

et al., 2007). Insight into the function of the CO is largely gained from the nature of the proteins expressed at this structure. The CO contains annexin 6 (A6), sarco-endoplasmic reticulum Ca^{2+}-ATPase (SERCA), and Inositol 1,4,5-trisphosphate (IP3) receptor type 1 (IP3R1); all suggesting a role for the CO in the sequestration and release of Ca^{2+} at the AIS (Benedeczky et al., 1994; Sánchez-Ponce et al., 2011). The CO maintains its stability through interactions with the actin cytoskeleton via synaptopodin and α-actinin, which are actin-associated proteins crucial for CO establishment and maintenance (Bas Orth et al., 2007; Sánchez-Ponce et al., 2011; Sánchez-Ponce et al., 2012). The AIS and CO seem to be reciprocally dependent for stability, as loss of AIS clustering disrupts CO integrity, and proper CO localization drives AIS plasticity during development (Sánchez-Ponce et al., 2011; Schlüter et al., 2017). Overall, while the CO appears to be important for local Ca^{2+} regulation at the AIS, alterations to CO integrity under pathological conditions have yet to be demonstrated.

1.4.3 The Role of Ca^{2+} in AIS Plasticity and Injury

The AIS, while a highly stable complex, undergoes homeostatic alterations in length and positioning along the axon as a response to changes in neuronal activity (Jamann et al., 2017). For example, overstimulation of hippocampal neurons results in relocation of the AIS complex in an anterograde direction along the axon (Grubb and Burrone, 2010). Additionally, several studies have demonstrated AIS length changes in response to neuronal activity (Jamann et al., 2017). Input deprivation results in lengthened AISs while increased stimulation induces shortening of the complex (Evans et al., 2015). All reported mechanisms of activity-dependent AIS plasticity are also dependent on Ca^{2+}.

More specifically, this involves Ca^{2+} flow specifically through L-type VGCCs and subsequent activation of calcineurin, a Ca^{2+}-dependent phosphatase that destabilizes interactions between AIS proteins such as AnkG and voltage gated ion channels (Evans et al., 2013). Overall, these Ca^{2+} dependent AIS alterations are thought to serve as a mechanism for fine tuning neuronal excitability in response to synaptic input (Jamann et al., 2017).

In addition to neuronal activity, changes to AIS protein clustering can also be induced through pathological insult as described above (Buffington and Rasband, 2011). The mechanisms of AIS dismantlement under ischemic and excitotoxic conditions, like that induced through homeostatic plasticity, is driven by Ca^{2+} influx (Stoler et al., 2016). Instead of calcineurin, these mechanisms of AIS injury involve proteolytic cleavage of critical AIS proteins including AnkG, βIV spectrin and voltage gated sodium channels by calpain, a Ca^{2+} activated cysteine protease (Schafer et al., 2009; Del Puerto et al., 2015; Benned-Jensen et al., 2016). Unlike calcineurin-mediated homeostatic AIS plasticity, calpain-dependent proteolysis of the AIS is thus far reported to be irreversible (Schafer et al., 2009). It remains unclear how Ca^{2+} influx selectively triggers calcineurin- versus calpain-driven AIS modulation.

1.5 Multiple Sclerosis: Definition and Epidemiology

1.5.1 Definition and Diagnosis

Multiple Sclerosis (MS) is an immune-mediated disease of the CNS in which myelin, the protective insulating sheath surrounding neuronal fibers is targeted for degeneration (Hemmer et al., 2015). Patients typically present with an initial episode of neurological

symptoms lasting at least 24 hours, known as a clinically isolated syndrome (CIS). While not all cases of CIS lead to a diagnosis of MS, about ~80% of these cases manifest into the disease within several years following the initial event (Brownlee and Miller, 2014). Following a CIS, MS can present as one of three types of disease courses: relapsing-remitting (RRMS), secondary-progressive (SPMS), or primary-progressive (PPMS). With 85% of MS patients initially diagnosed with RRMS, this is the most common form of the disease (Gallo et al., 2015). The RRMS disease course consists of periods of worsening neurologic symptoms, or “relapses,” interspersed between periods of symptom alleviation, or “remissions” (Gallo et al., 2015). Most patients initially diagnosed with RRMS will eventually develop SPMS, in which there is a steady progression of neurological deficits over time (Lassmann et al., 2012). A third form of MS, known as PPMS, presents with worsening clinical symptoms from the start, lacking the periods of remission characteristic of RRMS or the early stages of SPMS (Rice et al., 2013). During sudden relapses, PPMS can be also subclassified as “active”, a disease course formally referred to as progressive-relapsing MS (PRMS) (Ontaneda and Fox, 2015).

No matter the disease course, all diagnoses of MS must meet a specific set of clinical criteria (Katz Sand, 2015). Neurological function can be assessed clinically through several types of evoked potential testing (Kraft, 2013). Recording electrodes placed on the scalp record brain activity following presentation of visual or somatosensory stimulations which should yield impaired nerve conduction in MS patients (Kraft, 2013). While these tests can identify general neurological deficits, further criteria are necessary to rule out a diagnosis of a variety of other CNS diseases (Katz Sand, 2015). A diagnosis of MS must also present with regions of CNS myelin loss, termed lesions or plaques, as

visualized through Magnetic Resonance Imaging (MRI). Furthermore, a patient diagnosed with MS must demonstrate “dissemination of lesions in both space and time” according to the McDonald diagnostic criteria for MS (Milo and Miller, 2014). Additionally, patients diagnosed with MS also frequently present with oligoclonal bands, which are immunoglobulins present in the cerebrospinal fluid (CSF). These immunoglobulins, while originally thought to represent autoantibodies against certain CNS components, appear to present only as a secondary consequence of the disease, but remain valuable biomarkers nonetheless (Milo and Miller, 2014).

1.5.2 Epidemiology

MS is estimated to affect 2.3 million individuals worldwide, with about 300,000 of those cases found in the United States (Schiess and Calabresi, 2016). Most patients are diagnosed between the ages of 20 and 50 (~85% of cases), with pediatric and geriatric cases of MS representing about 3-10% and 1-10% of diagnoses, respectively (Buhse et al., 2015; Cappa et al., 2017; Tenembaum, 2017). Diagnosing MS in children, however, is confounded by transient demyelinating events that may occur early in life, as well as the difficulty in identifying lesion progression through both space and time as described above (Kamate et al., 2010; Tenembaum, 2017). As with most autoimmune diseases (Fairweather et al., 2008), there is also an unequal predominance of MS based on sex, with an approximate 3:1 female to male prevalence of the disease (Bove and Chitnis, 2013) potentially a consequence of differential effects that sex hormones have on immune system function (Golden and Voskuhl, 2016).

1.5.3 Risk Factors

While the specific causes of MS are unclear, several risk factors, both environmental and genetic, are believed to be associated with the disease (Belbasis et al., 2015; Didonna et al., 2015). Interestingly, disease prevalence is higher among individuals residing in temperate climates such as those found in Canada, the northern United States, New Zealand, southeastern Australia and Europe. Low rates of incidence are observed among inhabitants of tropical climates, indicating an environmental component may contribute to MS development (Marrie, 2004). One hypothesis for this phenomenon is that living farther away from the equator, where exposure to sunlight is reduced, results in lower vitamin D production, a well-documented risk factor for MS (Lucas et al., 2015). There is strong evidence for a correlation between vitamin D levels and MS prevalence with levels typically lower in MS patients experiencing more severe disabilities (Simpson et al., 2017). Supporting this correlation, clinical trials have demonstrated that supplementing with vitamin D yields favorable immunomodulatory effects including suppressed lymphocyte reactivity and pro-inflammatory cytokine production (Røsjø E et al., 2015; Sotirchos et al., 2016; Muris et al., 2016B). No clinical trials to date, however, have successfully demonstrated a significant reduction in the frequency and severity of MS symptoms following vitamin D supplementation (Muris et al., 2016A).

Another heavily investigated environmental risk factor associated with MS development is exposure to the Epstein-Barr virus (EBV) (Wingerchuk, 2011). EBV correlates with a large number of MS cases with an increased incidence risk estimated around four-fold (Sundström et al., 2008; Wingerchuk, 2011; Burnard et al., 2017). Studies have found evidence of EBV infection in the serum and CNS of MS patients; including

increased antibody titers to the virus and virally infected T- and B-lymphocytes (Ascherio and Munger, 2007; Serafini et al., 2007; Farrell et al., 2009). Additionally, patients display an impaired EBV-specific lymphocytic response, suggesting that the MS immune system is inadequately equipped to control the virus, unlike that of healthy individuals (Jilek et al., 2012; Laurencea and Benito-León, 2017). Despite this support for a link between EBV and MS development, mounting counter-evidence casts doubt on this hypothesis. Clinical trials have found no association between increased EBV antibody levels and the risk of developing MS following a CIS; a finding contradictory to its proposed role as a risk factor (Munger et al., 2015).

While MS is not considered a hereditary disease, familial and ethnic relationships have been identified (Hollenbach and Oksenberg, 2015). Existing evidence supports the involvement of a genetic component in the development of MS potentially acting to create a pre-disposition that would result in enhanced susceptibility to other disease triggers such as those described above. Supporting this idea, risk gene CYP24A1, which encodes an enzyme involved in vitamin D degradation, was found to be overexpressed in MS (Shahijanian et al., 2013). This may explain the extensive vitamin D deficiencies associated with severe neurological deficits in MS (Simpson et al., 2017). A variant of a critical allele of the HLA-DRB1 gene, which encodes a type of MHC class II cell surface receptor, has also been demonstrated in MS patients (Alcina et al., 2012). This receptor is crucial for proper recognition of the EBV by T-lymphocytes providing a possible explanation for the increased risk of EBV infection in MS patients (Kumar et al., 2013).

1.6 Multiple Sclerosis: Murine Models

While multiple sclerosis is strictly a human disease, key pathological features such as inflammation, demyelination, remyelination, and neuronal insults can be closely recapitulated in murine models (Kipp et al., 2017). The most commonly utilized mouse models of MS include toxin-induced demyelinating models, viral-induced demyelinating models, and experimental autoimmune/allergic encephalomyelitis (EAE) (Kipp et al., 2017).

1.6.1 Toxin-Induced Demyelinating Models

Because demyelination is a hallmark pathological feature of MS (Filippi et al., 2016), recapitulating this in mouse models is essential for uncovering the mechanisms underlying white matter injury and repair. This is effectively achieved through the use of toxin-induced demyelinating models such as the cuprizone and lysolecithin models. The cuprizone toxin, which is regularly administered through chow, yields detectible myelin loss around 1-2 weeks on cuprizone treatment with peak demyelination by 5-6 weeks of exposure (Denic et al., 2011). CNS targets of cuprizone-induced demyelination include white matter tracts such as the corpus callosum, striatum, and anterior commissure, but also grey matter areas such as the cerebral cortex, hippocampus and cerebellum (Herder et al., 2011). Lysolecithin, which is administered through focal stereotactic injection into specific CNS regions of interest, induces demyelination much sooner, with myelin loss appearing hours after injection (Torre-Fuentes et al., 2017). Unlike cuprizone, lysolecithin-induced demyelinating insults are limited to the site of injection which commonly include the spinal cord or corpus callosum (Torre-Fuentes et al., 2017). While both toxins yield

substantial myelin loss, the mechanisms underlying these white matter insults remain unclear.

Cuprizone, a copper chelating agent, results in the death of oligodendrocytes presumably through impairment of mitochondrial enzymes responsible for cellular respiration (Torre-Fuentes et al., 2017). In contrast to cuprizone, lysolecithin, is thought to stimulate demyelination through disruption of myelin membranes rather than induction of oligodendrocyte death. (Höflich et al., 2016). In addition to providing a means of examining the downstream consequences of myelin loss, the toxin-induced models also allow for the investigation of remyelination mechanisms as both models display endogenous myelin repair following removal of the toxins (Baker and Amor, 2015). These demyelinating models, however, lack peripheral immune system involvement, a major component of MS pathogenesis, which involves autoimmune lymphocyte reactivity and CNS infiltration (Filippi et al., 2016). While this may be viewed as a pitfall of the models in their deviation from MS pathogenesis, it can also effectively be exploited to uncover mechanisms of demyelination and remyelination in a more pure environment. Despite the lack of peripheral inflammatory involvement, the inflammatory environment of the CNS is altered in both models. This includes increased reactivity and recruitment of microglia, the resident innate immune cells of the CNS, to lesion sites where they seem to promote myelin debris clearance and remyelination (Rawji and Yong, 2013). Overall, the toxin-induced models are commonly used to investigate mechanisms of demyelination and remyelination, such as those present in MS, but fail to recapitulate the peripheral inflammatory component of the autoimmune disease.

1.6.2 Viral-Induced Demyelinating Models

As described above, development of MS is linked to certain viral infections (Mecha et al., 2013). To examine the viral contribution to MS pathogenesis, viruses such as Murine Hepatitis virus, Semliki Forest virus, and Theiler's murine encephalomyelitis virus (TMEV) are employed. TMEV, the most commonly studied demyelination-inducing virus, is a mouse pathogen capable of infecting neuronal and glial cells resulting in the activation and recruitment of peripheral lymphocytes into the CNS (DePaula-Silva et al., 2017). Intracerebral injection of TMEV leads to the induction of a late-onset demyelinating disease with motor deficits and myelin loss not evident until 4-5 weeks post injection (McCarthy et al., 2012). As with the toxin-induced models, the mechanisms that trigger demyelination remain unknown with possibilities including demyelination as a secondary consequence to axonal damage, direct viral effects on oligodendrocytes, or macrophage mediated phagocytosis (Mecha et al., 2013). Unlike the cuprizone model, the majority of the demyelinating lesions are restricted to the spinal cord despite initial intracerebral infection. The chronic inflammatory environment, however, is present in a variety of CNS regions and closely mimics that of MS (Olson, 2014). A major advantage of the viral-induced demyelinating models is that, much like MS, the disease persists for the entire lifespan of the animals making it most useful for studying effective therapies for the chronic progressive forms of MS (DePaula-Silva et al., 2017). Because of this, effectively studying mechanisms of remyelination is challenging since white matter recovery is limited in the viral-induced models of MS (Oleszak et al., 2004).

1.6.3 Experimental Autoimmune Encephalomyelitis

EAE is the most commonly utilized mouse model of MS, and arguably the most successful in our understanding of disease pathogenesis since at least three of the approved therapies were developed solely through the use of this model (Denic et al., 2011). EAE is induced through subcutaneous injection of myelin proteins accompanied by pertussis toxin and an adjuvant to ignite an inflammatory response (Beeton et al., 2007). Immunized myelin proteins in this model include myelin oligodendrocyte glycoprotein (MOG), myelin basic protein (MBP), or proteolipid protein (PLP) (Badawi and Siahaan, 2013). Interestingly, induction of EAE with each of these proteins results in distinct disease courses with MOG- and MBP-induced EAE displaying a course closer to primary progressive MS with PLP more closely recapitulating the relapsing-remitting form (Badawi and Siahaan, 2013).

Within 1-2 weeks following induction, EAE mice display motor deficits that can present as mild or severe (Beeton et al., 2007). Similar to the viral-induced models, demyelination is limited to the spinal cord, but lymphocyte infiltration and microglial reactivity is prevalent throughout the CNS (Fletcher et al., 2010; Luo et al., 2017). With extensive peripheral and central inflammatory involvement, EAE is arguably the most successful at recapitulating the inflammatory environment associated with MS (Kipp et al., 2017). Furthermore, pathogenesis of this model, much like MS, is T-cell driven, as transfer of EAE-activated T-cells into Naïve mice results in adoptive progression of the disease (Rangachari and Kuchroo, 2013). The central role of the autoimmune component in EAE distinguishes this model from the toxic models of demyelinating disease which utilize more artificial triggers to recapitulate MS symptoms (Denic et al., 2011). Although EAE is

the most widely utilized murine model of MS, it is not without its pitfalls. While lymphocytic CNS infiltration is successfully replicated in EAE, the prominent T-cell subtype contributing to disease progression of this model is CD4+, with CD8+ T-cells known to play the predominant role in MS pathogenesis (Babbe et al., 2000; Kipp et al., 2017). Despite leading to the development of several currently prescribed MS drugs, EAE also has an incredibly high rate of failure for potential therapies, which showed promise in the model but proved ineffective in clinical trials (Sriram and Steiner, 2005). Overall, these models, along with their advantages and disadvantages, provide close recapitulation of a variety of pathogenic components associated with MS.

1.7 Multiple Sclerosis: The Inflammatory Environment

1.7.1 Peripheral Inflammation

While MS is considered an autoimmune disease of the CNS, the inflammatory response in MS is initiated in the periphery and thought to drive the early phase of disease (Hemmer et al., 2015). Effectors of the inflammatory response associated with MS pathogenesis include antigen presenting cells (APCs), T-cells, and B-cells. While T-cells are the primary peripheral immune cell type driving MS pathogenesis, their activity is dependent on APCs (Sie and Korn, 2017). Peripheral APCs, including macrophages, monocytes and dendritic cells, are involved in activating T-cells in the periphery through phagocytosis and presentation of myelin antigens on MHC class II receptors along with costimulatory molecules (Chastain et al., 2011). This process is necessary for development and pathogenesis of both the TMEV and EAE models of MS (Greter et al., 2005; Chastain et al., 2012). Ultimately, this method of T-cell activation results in

maturation into specific T-cell subsets depending on the costimulatory signals presented alongside the antigen (Breed et al., 2017).

T-cells, which play a major role in the adaptive immune response, are $CD3^+$ lymphocytes that mature in the thymus to yield one of three subsets: CD4 expressing helper T-cells (Th), CD8 expressing cytotoxic T-cells, and the more enigmatic $CD4^-/CD8^-$ gamma delta T-cells (Germain, 2002; Wiest, 2016). Helper T-cells, upon activation by APCs, further mature into effector subsets including Th1, Th2, Th17 and regulatory T-cells (Tregs) which are classified based on cytokine profiles. Th1 cells, which mount responses against bacterial infections under non-autoimmune conditions, release pro-inflammatory cytokines such as IFN-gamma (IFN-γ), Interleukin (IL)-2, and tumor necrosis factor beta (TNF-β) (Zhu et al., 2010). In contrast, Th2 cells, which normally protect against parasitic infection, release several immunosuppressive cytokines including IL-10 and IL-4 (Allen and Sutherland, 2014). The Th1 to Th2 balance appears critical for MS pathogenesis, as alleviation of disease symptoms is achieved by shifting the balance towards the resolving Th2 population (Oreja-Guevara et al., 2012; Aharoni, 2014). Th17 cells, named for their effector cytokine IL-17, are a distinct pro-inflammatory subset of helper T-cells that play a large role in pathogen clearance at mucosal membranes but are heavily implicated in a variety of autoimmune disorders upon dysregulation (Tabarkiewicz et al., 2015). While these autoimmune functions have proven effective for tumor regression, this T-cell subset plays a detrimental role in MS pathogenesis (Brucklacher-Waldert et al., 2009; Bailey et al., 2014). Autoreactive Th17 cells in MS permit CNS lymphocytic infiltration through breakdown of BBB tight junctions, and promotion of lymphocyte adhesion to the vascular endothelium (Kebir et al., 2007;

Brucklacher-Waldert et al., 2009). While still ongoing, clinical trials targeting the Th17 population in MS have shown promise (Dos Passos et al., 2016). Whereas Th1 and Th17 subsets are considered to exhibit pro-inflammatory effector functions, Tregs function to suppress these subsets and promote resolution of the inflammatory response; producing a variety of anti-inflammatory cytokines such as Transforming growth factor beta (TGF-β), IL-35, and IL-10 (Duffy et al., 2017). Because modulating the proper T-cell subset balance has proven essential for successful disease alleviation in models and clinical trials, these cells are of interest for MS therapeutic strategies (Danikowski et al., 2017). Interestingly, Tregs are significantly downregulated in MS with those present exhibiting dysfunctional receptor expression and cytokine release (Danikowski et al., 2017). Most current MS therapies do not target the Treg population but on-going clinical trials are aiming to achieve this (Danikowski et al., 2017). Additionally, while much less is known about gamma delta T-cells, they are capable of suppressing the Treg population, thus exacerbating the autoimmune response. Consistent with a downregulated Treg population, the gamma delta T-cell population is significantly increased in MS lesions (Paul et al., 2015). Finally, $CD8^+$ T-cells, which normally possess anti-tumor and anti-viral functions, are the predominant T-cell subtype found in MS plaques (Sinha et al., 2015). The role for these cytotoxic T-cells, however, is controversial with conflicting evidence supporting both a pathogenic, as well as an immune regulatory role in MS (Salou et al., 2015). $CD8^+$ T-cells appear detrimental to MS pathogenesis as they secrete factors involved in BBB disruption, and are sufficient to adoptively transfer EAE, which presents as a more severe form than that of the donor animal (Salou et al., 2015). Supporting a regulatory role, $CD8^+$ T-cells, are important for EAE recovery and display higher activity

levels during phases of remissions rather than relapses in MS (Denic et al., 2013; Sinha et al., 2015).

In addition to T-cells, B-cells are also critical for adaptive immunity with antibody production being the most notable function during the inflammatory response (Hoffman et al., 2016). B-cells are responsible for the production of CSF oligoclonal immunoglobulins, one of the hallmarks of MS clinical diagnosis (Bankoti et al., 2014). These cells produce autoantibodies against myelin and axonal specific proteins within CNS plaques, and direct the T-cell population toward pro-inflammatory effector functions (Rawes et al., 1997; DeVries, 2004; Wootla et al., 2011). Further supporting a pathogenic role for B-cells in MS, depletion of B-cells in clinical trials resulted in significant improvement of MS disability (Cree et al., 2005; Hauser et al., 2008). Overall, these lymphocytes and macrophages, while activated peripherally, infiltrate the CNS where they ultimately contribute to plaque formation and disease progression (Larochelle et al., 2011).

1.7.2 Central Inflammation

The CNS, once thought to be immune privileged, is now known to undergo immune surveillance by lymphocytes residing in the meninges (Louveau et al., 2015). Despite this connection to the peripheral immune system, Microglia serve as the major regulators of the CNS inflammatory response (Fernandes et al., 2014). Interestingly, microglia in MS adopt a biphasic response, serving as either pro-inflammatory or resolving, depending on their location within the diseased CNS (Luo et al., 2017).

Microglia in EAE and the TMEV-induced models display a pro-inflammatory phenotype, classically referred to as M1, which contributes to a destructive environment such as that found in actively demyelinating MS lesions (Gao and Tsirka, 2011). These microglia release a litany of pro-inflammatory cytokines such as IFN-γ, TNF-α, IL-6, IL-12, and IL-23 and overexpress enzymes that contribute to oxidative stress such as inducible nitric oxide synthase (iNOS) and nicotinamide adenine dinucleotide phosphate oxidase (NOX) (Rawji and Yong, 2013). These cytotoxic cytokines and free radical generating enzymes contribute to extensive damage to surrounding neurons and glial cells (Yamasaki et al., 2014). In addition to direct effects on neurons and oligodendrocytes, these pro-inflammatory microglia also act to re-stimulate T-cells that were activated in the periphery through presentation of new myelin antigens and costimulatory molecules (Croxford et al., 2002).

In contrast, microglia in toxin-induced demyelinating models such as cuprizone display an immunosuppressive phenotype, classically labeled as M2, which contributes to the reparative environment found in remyelinating, or “shadow”, plaques (Clemente et al., 2013). These microglia release resolving and neurotrophic factors such as IL-4, IL-10, and TGF-β (Tang and Le, 2016). Additionally, these microglia promote remyelination of demyelinated axons both through the clearance of myelin debris, and the secretion of factors necessary for recruitment and maturation of oligodendrocyte progenitors (Miron et al., 2013).

Interestingly, microglia are not the only antigen presenting cells in the CNS. Astrocytes, while not traditionally considered immune cells, perform immunomodulatory functions (Claycomb et al., 2013). In animal models of MS for example, astrocytes

enhance proliferation rate and activation of myelin-specific T-cells by phagocytosis and presentation of myelin antigens (Nair et al., 2008). Additionally, they indirectly promote myelin damage and T-cell activation through the recruitment of other APCs, such as dendritic cells, to sites of damaged myelin (Claycomb et al., 2013).

Overall, modulation of the inflammatory response in MS is crucial, and a common target of all currently approved therapies (Dargahi et al., 2017). The lack of a cure, however, suggests the necessity for a solution more intricate than dampening the systemic inflammatory response. This is highlighted by several failed clinical trials which aimed to suppress pro-inflammatory cytokines previously implicated in disease pathogenesis in animal models (Denic et al., 2011), but either failed to alleviate or worsened MS deficits (Anon, 1999; Panitch et al., 1987; Segal et al., 2008; Longbrake and Racke, 2009).

In order to investigate the contribution of central inflammation in the models used in this study, we treated mice with an anti-inflammatory drug termed 3,4-dihy dihydroxybenzohydroxamic acid, *Didox* (Molecules for Health Inc., Richmond, VA). Didox was originally purposed as a tumor suppressive drug due to its function as a potent ribonucleotide reductase inhibitor (Inayat et al., 2010; Matsebatlela et al., 2015; Shah et al., 2015). This drug, however, has also proven effective in suppressing central inflammation through inhibition of the peripheral T-cell response, free radical scavenging, and reduction of the pro-inflammatory NFkB pathway (Matsebatlela et al., 2015). Due to these immunosuppressive properties, Didox will be utilized in these studies to investigate the contribution of the inflammatory environment on our pathologies of interest.

1.8 Chapter Summary

Ultimately, while our lab has previously demonstrated disruption of nodal domains under the pathological conditions associated with MS, stability of the compositionally similar AIS under these conditions has not been investigated. In the subsequent chapters we explore this unaddressed potential neuropathology utilizing a variety of approaches including MS mouse models, primary neuronal cultures, and postmortem human tissue. In Chapter 2 we exploit two separate mouse models of MS, the cuprizone and EAE models, to investigate AIS stability under distinct hallmark conditions of MS pathogenesis (Dargahi et al., 2017), demyelination and inflammation, respectively. In an attempt to address AIS insults in a wide variety of CNS pathologies, Chapter 3 includes a study utilizing a primary neuronal *in* vitro system of oxidative stress to investigate potential mechanisms of reactive oxygen and nitrogen species (ROS/RNS)-induced AIS modulation. Finally, in Chapter 4 we examine the cisternal organelle, the enigmatic structure responsible for local Ca^{2+} regulation at the AIS. This includes investigation of the mechanisms regulating its stability as well as the consequences of its disruption in MS and its inflammatory model.

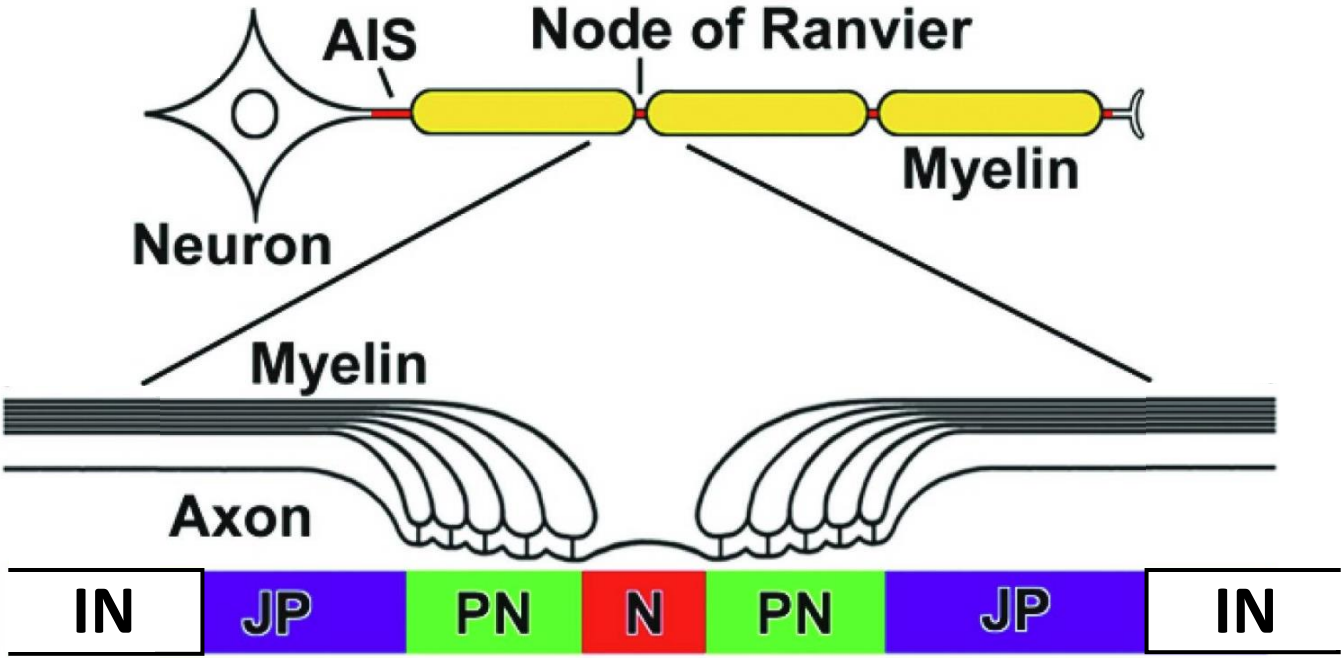

Modified from: Susuki et al., 2013

Figure 1.1. Schematic of Axonal Domains. A myelinated axon exhibits five domains critical for action potential initiation and propagation. The axon initial segment (AIS) is the proximal unmyelinated portion of the axon. The node of Ranvier (N) is the unmyelinated

gap between the myelin segments. The node is flanked by the paranode (PN), the region where the lateral edges of the myelin segments contact the axon. The juxtaparanode (JP) is located adjacent to the paranodal domains, while the internode (IN) is the axonal region underlying the majority of the compacted myelin segments.

CHAPTER TWO

COMPROMISED AXON INITIAL SEGMENT INTEGRITY IN EAE IS PRECEDED BY MICROGLIAL REACTIVITY AND CONTACT

Clark et al., 2016. *Glia*

2.1 Abstract

Axonal pathology is a key contributor to long-term disability in multiple sclerosis (MS), an inflammatory demyelinating disease of the central nervous system (CNS), but the mechanisms that underlie axonal pathology in MS remain elusive. Evidence suggests that axonal pathology is a direct consequence of demyelination, as we and others have shown that the node of Ranvier disassembles following loss of myelin. In contrast to the node of

Ranvier, we now show that the axon initial segment (AIS), the axonal domain responsible for action potential initiation, remains intact following cuprizone-induced cortical demyelination. Instead, we find that the AIS is disrupted in the neocortex of mice that develop experimental autoimmune encephalomyelitis (EAE) independent of local demyelination. EAE-induced mice demonstrate profound compromise of AIS integrity with a progressive disruption that corresponds to EAE clinical disease severity and duration, in addition to cortical microglial reactivity. Furthermore, treatment with the drug didox results in attenuation of AIS pathology concomitantly with microglial reversion to a less reactive state. Together, our findings suggest that inflammation, but not demyelination, disrupts AIS integrity and that therapeutic intervention may protect and reverse this pathology.

2.2 Introduction

Multiple Sclerosis (MS) is an immune-mediated inflammatory disease of the central nervous system (CNS) characterized by lymphocytic infiltration (Greer, 2013) and focal demyelination (Popescu et al., 2013). In addition to myelin loss, axonal pathology is prevalent and postulated to be responsible for irreversible clinical disability (Trapp et al., 1998). Although present at all stages of MS (Criste et al., 2014), axonal pathology is generally considered a consequence of demyelination (Black et al., 2007; Waxman, 2008). Consistent with this view, deterioration of the node of Ranvier (NOR), the specialized axonal domain required for action potential propagation (Susuki and Rasband, 2008), is a consequence of myelin loss in MS (Coman et al., 2006;

Desmazieres et al., 2012; Howell et al., 2010) and mouse models of CNS demyelination (Dupree et al., 2004) and inflammation (Zoupi et al., 2013).

Here, we examined the effect that demyelination has on another specialized axonal domain- the axon initial segment (AIS), which clusters many of the same proteins as the NOR (Buffington and Rasband, 2011). The AIS is located distal to the soma, contains a high density of ion channels including voltage-gated sodium (Na_v^+) channels (Kole et al., 2008) and is responsible for action potential initiation and modulation (Buffington and Rasband, 2011). Mice incapable of clustering AIS proteins develop ataxia and fail to initiate action potentials (Zhou et al., 1998). The Na_v^+ channels clustered at the AIS are linked to the spectrin-actin cytoskeleton through interactions with the scaffolding protein ankyrin-G (AnkG) (Buffington and Rasband, 2011). AnkG is considered the master organizer of the AIS, as it is required for the establishment and maintenance of AIS protein clusters and neuronal polarity (Hedstrom et al., 2008; Jenkins and Bennett, 2001). While the establishment of the AIS is well defined (Galiano et al., 2012), the mechanisms that regulate AIS stability remain poorly understood. AIS protein clustering is compromised in a variety of neuropathological models including stroke (Schafer et al., 2009; Hinman et al., 2013) and traumatic brain injury (Baalman et al., 2013; Greer et al., 2013) while protein clustering is preserved following demyelination (Hamada and Kole, 2015). To our knowledge, however, this is the first study to investigate AIS stability in an immune-mediated CNS model of inflammation.

Our findings, consistent work of Hamada and Kole (2015), show that local demyelination is not sufficient to trigger disruption of AIS protein clusters, indicating that the mechanisms that maintain the node/paranode are distinct from those that maintain

the AIS. In contrast, we provide the first evidence that AIS clustering is lost in an inflammatory model of MS. AIS disruption is preceded by microglial reactivity and correlates with increased microglia/AIS contact and expression of pro-inflammatory factors. Moreover, we report that pharmacological intervention can prevent and reverse these microglial changes and lead to the protection of AIS integrity.

2.3 Materials and Methods

Animals

Five and 11 weeks old c57bl/6 mice were purchased from Jackson Laboratories (Bar Harbor, ME) and maintained in the Virginia Commonwealth University Division of Animal Resources (VCU DAR) or the McGuire Veterans Affairs Medical Center (VAMC) vivariums, respectively, which are both AAALAC accredited facilities. Treatments were initiated after the mice acclimated for one week resulting in treatment initiation at six and 12 weeks of age. Food and water were provided *ad libitum*. In addition, 12 weeks old Thy1-YFP-H mice [B6Cg-TgN (Thy1-YFP-H)2Jrs, stock number 003782 obtained from the Jackson Laboratories] were obtained from an established colony maintained in the VCU DAR. All procedures were conducted in accordance with the methods outlined in approved VCU and McGuire VAMC IACUC protocols.

The Cuprizone Model

To induce cortical demyelination, ground chow (5001 Rodent Diet; PMI Nutrition International, LLC, Brentwood, MO) was mixed with cuprizone (Bis(cyclohexanone) oxaldihydrazone; Sigma-Aldrich, St. Louis, MO; 0.2% w/w) as previously described

(Dupree et al., 2004). Briefly, six weeks old mice were maintained on a ground chow diet without (0%; n=7) or with (0.2% w/w) cuprizone for 1 (n=6), 3 (n=6) or 5 (n=6) weeks. These durations were chosen based on previous studies that reported initial signs of cortical demyelination occur following 3.5 weeks and maximum demyelination occurs following 5 weeks of cuprizone exposure (Fjaer et al., 2013). An additional group was maintained on cuprizone for 5 weeks followed by 3 weeks of normal (non-cuprizone; n=6) chow, allowing remyelination. Table 2.1 outline treatment duration and the number of mice per treatment group.

The Chronic EAE Model

To evaluate AIS integrity in an inflammatory environment, we induced the chronic model of experimental autoimmune encephalomyelitis (EAE) as previously described (DeVries et al., 2012; Secor McVoy et al., 2015; Dupree et al., 2015). Briefly, 12 weeks old c57bl/6 mice or Thy1-YFP-H mice were injected subcutaneously over each shoulder with 50 μL of a solution containing 3 mg/mL myelin oligodendrocyte glycoprotein peptide 35–55 ($MOG_{35–55}$, MEVGWYRSPFSRVVHLYRNGK) (AnaSpec, Inc., Fremont, CA) emulsified with complete Freund's adjuvant containing 2 mg/mL of heat-killed *M. tuberculosis* (Invitrogen Life Technologies, Grand Island, NY). Mice were also injected intraperitoneal (i.p.) on the same day with 300 ng Pertussis toxin (PT) (List Biological Labs, Campbell, California) in 200 μL phosphate buffered saline (PBS) with a booster PT injection 48 hours later. Clinical motor symptoms were scored daily and recorded as follows: 0= no signs, 1.0= limp tail, 2.0= loss of righting reflex, 3.0= paralysis of single hind limb and 4.0= paralysis of both hind limbs.

Mice achieved peak clinical symptoms at ~15 days post injection (Fig. 2.1A). Immunohistochemical analysis was conducted at two time points along the EAE disease course; an early inflammatory time point (3 days post peak clinical symptoms; ~18 days post induction) and a late inflammatory time point (9 days post peak clinical symptoms; ~24 days post induction) as indicated in Figure 2.1A. As illustrated, not all mice achieved the more severe clinical scores (Fig. 2.1A). We have exploited this variation in model progression and grouped the mice into 2 categories based on clinical scores which provided a clinical score-to-structural disruption analysis. Within each time point, mice were categorized as either EAE 1&2 (Early n=4; Late n=3) or EAE 3&4 (Early n=4; Late n=7) based on daily scoring. Only animals that maintained consistent scores for the period of 3 or 9 days post peak score were used in the study. Table 2.2 displays the clinical scores and the number of mice used in each group.

Didox Administration

Didox (N-3,4-tridhydroxy-benzamide), a ribonucleotide reductase inhibitor supplied by Molecules for Health, Inc., (Richmond, VA), is a multifunctional compound that inhibits DNA replication and T-cell proliferation, reduces oxidative injury and attenuates microglia/macrophage production of inflammatory factors (Bhave et al., 2013; Inayat et al., 2010; Matsebatlela et al., 2015; Turchan et al., 2003). Based on prior optimization studies to determine drug dose, frequency, and route of administration (DeVries et al., 2012, Elford et al., 2013), 200 µl of carboxymethylcellulose containing 550 mg/kg of didox was administered via oral gavage to a separate cohort of mice (n=4) at the Early time point. Vehicle control mice (n=4), also at the Early EAE time point, were administered 200

µl of carboxymethylcellulose solution by oral gavage. The vehicle solution contained 0.5% (w/v) carboxymethylcellulose, 0.9% (w/v) sodium chloride, 0.4% (w/v) polysorbate 30, and 0.9% (w/v) benzyl alcohol in deionized water. Administration of didox or vehicle was continued daily for 6 days (Fig. 2.1B).

Antibodies

Axon initial segments (AISs) were visualized using mouse monoclonal antibodies directed against ankyrin-G (AnkG) (NeuroMab, Davis, CA; N106/36, 1:200) and the Na_v^+ channel isoform 1.6 ($Na_v1.6$) (NeuroMab; K87A/10, 1:100) Microglia were labeled with a rabbit polyclonal antibody directed against the ionized calcium binding adaptor molecule-1 (IBA-1) (Wako Chemicals, Richmond, VA; 1:1000). An antibody directed against myelin basic protein (MBP) (Covance, Chantilly, VA, 1:1000) was used to assess myelin integrity in the EAE-induced and cuprizone treated mice. Neurons were identified using the NeuN antibody (Millipore; Billerica, MA; 1:1000). To distinguish nodes of Ranvier from potentially fragmented AISs, an antibody directed against Caspr (anti-guinea pig; generous gift from Dr. Manzoor Bhat, University of Texas San Antonio) was used to label paranodes. To assess inflammatory molecular profiles of reactive microglia, antibodies directed against tumor necrosis factor alpha (TNFα) (abcam; Cambridge, MA, 1:200), inducible nitric oxide synthase (iNOS) (BD Biosciences; San Jose, CA, 1:200), and macrophage colony stimulating factor (M-CSF) (Santa Cruz Biotechnology; Dallas, TX, 1:200) were used. All secondary antibodies were obtained from Invitrogen Life Technologies (Grand Island, NY; Alexa^{TM} Fluor) and used at a dilution of 1:500.

Tissue Preparation

Mice were deeply anesthetized using 0.016 mL/gm body weight of a 2.5% solution of avertin (2, 2, 2 tribromoethanol) (Sigma-Aldrich; St. Louis, MO) in 0.9% sodium chloride (Sigma-Aldrich, St. Louis, MO) and transcardially perfused with 4% paraformaldehyde (Ted Pella, Redding, CA) (Dupree et al., 1999; Shepherd et al., 2012). Following perfusion the cortex was cryopreserved in 0.1 M PBS containing 30% sucrose for 48 hours, frozen in Optimal Cutting Temperature compound, and serially sectioned at 40 µm in a coronal orientation using a Leica CM 1850 cryostat. The cortical region spanning 1.1 mm anterior to bregma to 2.5 mm posterior to bregma was serially sectioned. Fifteen sets of six sections were collected and placed on ProbeOn Plus slides (Fisher Scientific, Loughborough, UK) and stored at -80°C. Additionally, a single mouse brain was sectioned transversely to assess microglia/AIS interactions from a different orientation.

Immunohistochemistry

Slides were immunolabeled with the appropriate primary and secondary antibodies as described (Dupree et al., 1999; Shepherd et al., 2012; Pomicter et al., 2010) with the modification that 0.5% Triton X-100 was used for AnkG labeling and 1% Triton X-100 was used for MBP labeling. Nuclear stain BisBenzimide (Sigma-Aldrich, St. Louis, MO, 1:1000) was used to identify cortical layers. Slides were mounted with Vectashield™ (Vector Laboratories, Burlingame, CA); and imaged using confocal microscopy.

Confocal Microscopy/Quantitation

Image Collection

All images were collected using a Zeiss LSM 710 confocal laser scanning microscope (Carl Zeiss Microscopy, LLC, Thornwood, NY) housed in the VCU Department of Anatomy and Neurobiology Microscopy Facility. Confocal z-stacks, each spanning an optical distance of 25μm, using a pin hole of 1 Airy disc unit and Nyquist sampling were collected from neocortical layer V for each of the six sections per mouse resulting in 12 images per animal for AIS quantitation and 24 images per animal for microglial morphological scoring. Images were taken with a 40X oil-immersion objective with a numerical aperture of 1.3; optical slice thickness was 0.49 μm, using a scan average of 2. X, Y and Z image dimensions were 212.43 μm x 212.43 μm x 25.00 μm, respectively. The gain and offset values were kept constant for all images. Spectral unmixing was employed to remove auto-fluorescence that resulted from lipofuscin and interfered with AIS quantitation. All quantitative analyses of AISs were limited to the AnkG-labeled slides since labeling intensity and consistency were superior with the AnkG antibody as compared to the $Na_v1.6$ antibody. Although not quantified, $Na_v1.6$ labeled sections were used to confirm, qualitatively, the changes in AIS integrity.

AIS Quantitation

AIS length measurements and counts were performed using ImageJ analysis software by manually tracing initial segments from maximum intensity projection images resulting in the analysis of >1000 AISs per Naïve mouse. To eliminate AISs that extended beyond

the boundaries of the captured field of view (FOV), which would result in an artificial shortening of the segment, AISs touching any of the six edges of the collected z-stack were excluded from analysis. To compare the number of AISs, the data are presented as percent of Naïve (% Naïve ± SEM). To compare AIS length, the average length of the AISs in micrometers is presented as mean ± SEM. We also determined AIS length as a percent of AIS length from Naïve mice and these data are presented as % Naïve ± SEM. After determining normal distribution of the data sets using normal quantile (Q-Q) plots, one-way ANOVAs with Tukey's Honest Significant Difference (HSD) post hoc tests were performed for both mean AIS number and length comparisons. All graphing and statistical analyses were performed using GraphPad Prism version 6.03 for Windows (GraphPad Software, San Diego, CA).

Neuronal Number Quantitation

To compare neuron number, neuronal nuclei were immunolabeled with the NeuN antibody (Mullen et al., 1992) and NeuN+ cells were counted in three Naïve mice and three EAE 3&4 mice at the Late time point. Double immunolabeling with AnkG was also performed to determine the percent of NeuN+ cells with and without an associated AIS. Three confocal images per mouse were collected using a 20X objective with a numerical aperture of 1.4 and a pinhole of 1 Airy disc unit, resulting in ~900 neurons analyzed per Naïve mouse. A two-tailed T-test with Welch's correction was performed on the average number of NeuN+ cells using GraphPad Prism version 6.03 for Windows.

Quantitation of Microglial Morphology

Microglial morphology was quantified using a modification of a method previously published (Hutson et al., 2011; Taetzsch et al., 2015). Briefly, microglia, as identified by IBA-1 immunolabeling in confocal Z-stacks, were scored with values ranging from “0” to “3” based on cell morphology wherein a stage “0” represents a ramified, surveying microglia, and a stage “3” represents an amoeboid form, consistent with reactivity. Microglia exhibiting each morphological stage are presented in Supplementary Figure S2.1. Categorizing characteristics included cell body size as well as process thickness, length and branching complexity as described (Hutson et al., 2011; Taetzsch et al., 2015); quantification was conducted blindly and independently by two individuals resulting in scoring of approximately 250 cells per mouse. Results of microglial phenotype quantitation varied by <10% per mouse between the two blinded evaluators. The findings from the two blinded evaluators were averaged, and the data presented as morphological stage distribution graphs as a percent of the total microglia present. For statistical analysis, two-way ANOVAs with Tukey’s HSD post hoc tests were performed using GraphPad Prism software version 6.03 for Windows.

Quantitation of Microglial-AIS Interactions

Contact between microglia and AISs was quantified using Volocity™ 3D Image Analysis Software version 6.3 allowing each confocal z-stack to be observed in three dimensions. The number of microglia, AISs, and contact points in each double immunolabeled z-stack was counted manually. Contact points along the six edges of the z-stacks were excluded from analysis. Data are presented as the number of contact

points per FOV as a percent of Naïve. One way ANOVAs with Tukey's HSD post hoc tests were performed using GraphPad Prism version 6.03 for Windows.

The z-stacks used for the quantitation of microglia and AIS contact were also used for production of isosurfaced images. These images were generated as a 3D-reconfiguration of the optical slices to facilitate visual assessment.

Isolation of Mouse Cortical Microglia

Isolation of adult cortical microglia was performed as described (Taetzsch et al., 2015). Briefly, Naïve, cuprizone treated (3 wk), and EAE induced (Early 1&2) mice were perfused with 50mL of ice-cold PBS. After removal of the meninges, cerebral cortices of three mice were pooled per sample (3 mice = 1 n) and suspended in Hank's balanced salt saline solution (HBSS) without $CaCl_2$ and $MgCl_2$ (Corning, Corning, NY). A single-cell suspension was prepared using the Miltenyi Neural Tissue Dissociation Kit (Miltenyi Biotec, San Diego, CA). Myelin depletion was performed by suspension in 30% isotonic Percoll™ (GE Healthcare Life Sciences, Pittsburgh, PA) followed by a spin at 700xg (4^{o}C). Isolation of microglia was performed using CD11b microbead labeling (Miltenyi, San Diego, CA) followed by passage of the cells through MACS LS columns and magnetic separator (Miltenyi, San Diego, CA).

Quantitative Reverse Transcriptase Polymerase Chain Reaction

Total RNA was extracted from CD11b+ isolated cells using a Qiagen RNeasy mini kit (Qiagen, Germantown, MD). Contaminating DNA was eliminated through treatment with Ambion DNase I (Invitrogen Life Technologies, Grand Island, NY). iScript Reverse Transcription Supermix (BioRad, Hercules, CA) was used to create cDNA from the isolated RNA (0.3 µg/sample). Quantitative RT-PCR was performed with a CFX96 (BioRad, Hercules, CA) RT-PCR detection system using 1 µL of cDNA, SsoFast Evagreen Supermix (BioRad), and forward and reverse primers (500 nM). Cycling parameters were one cycle at 95°C (5 min), 40 cycles of 95°C (5 sec) and 56°C (5 sec) followed by a melt curve measurement consisting of 5 sec 0.5°C incremental increases from 65°C to 95°C. The fold changes in expression of the genes M-CSF (forward: 5'-CGAGACCCTCAGACATTGGA -3'; reverse: 5'- TGGTGAGGGGTCATAGAATCC -3'), iNOS (forward: 5'-TCCAGAATCCCTGGACAAGCTGC-3'; reverse: 5'-TGCAAGTGAAATCCGATGTGGCCT-3'), and TNFα (forward: 5'-GCCCACGTCGTAGCAAACCACC-3; reverse: 5'-CCCATCGGCTGGCACCACTA-3') in CD11b+ cells were calculated using the formula $RQ = 2^{-\Delta\Delta Ct}$, using Cyclophilin A (forward: 5'- CTAGAGGGCATGGATGTGGT -3'; reverse: 5'-TGACATCCTTCAGTGGCTTG -3') as an endogenous reference gene. For statistical analysis, two-way ANOVAs with Tukey's HSD post hoc tests were performed using GraphPad Prism software for Windows (v6.03).

2.4 Results

Axon initial segments are not disrupted following cuprizone-induced demyelination

Our laboratories (Dupree et al., 2004; Coman et al., 2006) and others (Howell et al., 2010; Zoupi et al., 2013) have shown that demyelination results in the loss of NOR protein clustering. Here, we investigated the effect that demyelination has on another axonal domain -- the AIS. Consistent with previous studies (Skripuletz et al., 2008) and as shown in Figure 2.2, mice maintained on a normal diet (Fig. 2.2A) or a cuprizone diet for 1 week (Fig. 2.2B) revealed robust MBP labeling in cortical grey matter, while extensive reduction was observed following 3 (Fig. 2.2C) and 5 (Fig. 2.2D) weeks of cuprizone exposure (Fig. 2.2D). Mice that were maintained for 5 weeks on cuprizone followed by 3 weeks of normal chow revealed increased MBP labeling consistent with remyelination (Fig. 2.2E).

To assess AIS number and length in the control, 1, 3 and 5 weeks cuprizone treated and recovered (5+3 weeks) mice, AISs were immunolabeled for AnkG (Fig. 2.2F-J) and $Na_v1.6$ (not shown). Consistent with the findings of Hamada and Kole (2015), who showed that AnkG, $Na_v1.6$ and βIV spectrin maintained AIS clustering following cuprizone treatment, no significant difference was observed among any of the groups as compared to the Naïve with regard to either AIS number (Fig. 2.2K; Table 2.1) or length (Fig. 2.2L; Table 2.1), indicating that unlike the NOR, AIS maintenance is independent of myelination.

Axon initial segments are shortened following Early EAE

Although cuprizone treatment provides an excellent model to study demyelination and subsequent remyelination, the inflammatory aspects of MS are better studied by exploiting the EAE model. Following EAE induction, we analyzed AIS number and length

in cortical layer V of EAE mice at the Early disease stage (3 days post peak; Fig. 2.1A). For comparison, EAE mice were grouped according to clinical disease severity as mild (scores 1&2 or EAE 1&2) or severe (scores 3&4 or EAE 3&4). No change in AIS number was observed among either of the Early groups (Fig. 2.3A-C, G; Table 2.2) and no difference in the mean AIS length was observed between Naïve (19.9 ± 0.3μm; Table 2.2) and Early EAE 1&2 (17 ± 1.6 μm; Table 2.2) animals. In contrast, the Early EAE 3&4 mice showed significantly shorter mean AIS lengths (13.4 ± 0.4μm; Table 2.2) as compared to both the Naïve and the Early EAE 1&2 groups (compare Fig. 2.3C against Fig. 2.3A, B; Fig. 2.3H). As shown in Figure 2.3, AIS labeling was frequently discontinuous in the Early EAE 3&4 mice suggesting that AIS clustering was modestly compromised at this stage of disease.

Axon initial segments are lost during Late EAE

Our findings from the Early EAE mice indicate that AISs are structurally vulnerable (i.e. AIS shortening); however, recent studies have shown that the AIS is a highly dynamic structure with regard to length (Evans et al., 2013; Grubb and Burrone, 2010). Therefore, to determine whether the changes in length observed in the EAE mice during the Early stages of disease were maintained, we assessed AIS morphology in the EAE mice at 9 days post peak clinical score (Late EAE).

In contrast to the mice at the Early EAE stage, EAE-induced mice at the Late stage presented significantly fewer AISs in both the EAE 1&2 (Fig. 2.3E) and the EAE 3&4 group (Fig. 2.3F) compared to the Naïve (Fig. 2.3D). As shown in Figure 2.3G and Table 2.2, approximately 60% of the AISs were lost in the Late EAE 1&2 group while nearly 75% of the AISs were lost in the Late EAE 3&4 mice, with a statistically significant difference between the latter two groups.

For the above data, AIS counts from all sections spanning the entire anterior to posterior axis of the brains were combined. To determine whether AIS stability was different along the anterior-posterior axis, counts were compared between comparable regions with regard to their location. Consistent with the compiled findings, AISs were equally susceptible to disruption at each bregma location along the anterior-posterior axis (Supplementary Figure S2.2).

With the loss of AISs, AnkG-labeled puncta were more readily observed. To determine whether these puncta were remnants of disrupted AISs or possibly nodes of Ranvier, we double labeled EAE brain sections for AnkG and the paranodal protein Caspr (Bhat et al., 2001; Peles and Salzer, 2000). As shown in Figure 2.3F inset, these AnkG-positive puncta were flanked by Caspr labeling indicating that these structures were preserved nodes of Ranvier.

As with the Early group, we also measured AIS lengths in the Late group (Fig. 2.3H). The average AIS length for the Late EAE 1&2 mice was 12.0 ± 0.3 µm (Table 2.2), which was significantly shorter than that of the Early group with similar clinical scores (17.0 ±1.6 µm for Early EAE 1&2). The average AIS length for the EAE 3&4 mice in the Late group was 16.0 ± 0.6 µm, which was significantly shorter than that of the Naïve (19.9 ± 0.3 µm).

Although the AISs from the Late EAE 3&4 mice were significantly shorter than those of the Naïve group, the mean AIS length of the Late EAE 3&4 mice was significantly longer than that of the Early EAE 3&4 mice (compare 13.4 ± 0.4 μm for Early versus 16.0 ± 0.6 μm; p=0.0071). At first glance these findings appear to suggest that the Early stage of the disease resulted in greater AIS disruption, with regard to length; however, the average length for the Late mice reflects AISs that remained intact. As shown in Figure 2.3, about 75% of the AISs were lost in the Late EAE 3&4 group. These findings suggest that the AISs of cortical neurons have differential vulnerabilities and that the AISs that were not lost were less susceptible to shortening.

AIS loss is not due to demyelination, neuronal death, or axonal transection

Our findings demonstrated that AIS integrity of cortical layer V neurons was significantly compromised in EAE. To determine whether AIS disruption was a primary insult and not a result of upstream neuropathology, we assessed the neuronal population as well as myelin and axonal integrity. While EAE is primarily an inflammatory model, demyelination is consistently reported in the spinal cord (Dupree et al., 2015), cerebellum (Noor et al., 2015), parahippocampus (Sun et al., 2015), corpus callosum and cortical regions (Mangiardi et al., 2011). However, unlike the cuprizone model (Fig. 2.2) cortical demyelination is less prominent. In order to assess the extent of demyelination in our mice, we performed MBP immunolabeling on both Early and Late EAE animals and observed no reduction in intensity (Fig. 2.4A-C). The absence of cortical myelin loss was also confirmed by western blot analyses for the myelin proteins cyclic nucleotide phosphodiesterase and MBP (Supplementary Figure S2.3).

Studies have reported a reduced number of cortical layer V neurons in EAE (Burns et al., 2014; Spence et al., 2014). In order to determine if the AIS disruption observed in this study was a consequence of neuronal loss, we performed counts based on NeuN labeling (Fig. 2.4D, E). Counts revealed no difference in the neuronal populations (Fig. 2.4F; Late EAE 3&4 was 104% of the Naïve). In addition to total neuronal counts, we also quantified the number of NeuN-positive cells with or without an associated AIS. 96.2% ± 0.4% of neurons counted in the Naïve had an associated AIS which was reduced to 27.7% ± 3.7% of neurons in the Late EAE 3&4 mice, consistent with the findings reported in Figure 2.3G. Lastly, we induced EAE in Thy1-YFP mice to assess axonal transection and degeneration. Neither pathology was observed even in neurons with deteriorated AISs at a Late EAE 3&4 stage (Fig. 2.4G, H). Together these findings suggest that AIS loss is not due to demyelination, neuronal death or axonal transection.

Microglia exhibit reactive morphology during both Early and Late EAE

Baalman et al. (2015) recently reported that AISs within the cortex are contacted by microglia. Presently, the role that these cells play in AIS structure/function is not known but may involve AIS structural modulation. Therefore, we focused our attention on the role that microglia, the resident innate immune cells of the CNS, play in changes in AIS organization.

In the spinal cord of EAE-induced mice, reactive microglia clear myelin debris (Lewis et al., 2014). In the cortex of EAE-induced mice where demyelination is limited, the role

of reactive microglia is not as well characterized. It should be noted that while microglia were identified as IBA-1 positive cells, peripheral monocyte-derived macrophages, which infiltrate the CNS in EAE, are IBA-1 positive also. However, based on their distinct morphology, as previously described (Yamasaki et al., 2014), we will refer to IBA-1 positive cells as “microglia.”

As shown in Figure 2.5A and 2.5D, surveying (non-reactive) microglia, identified by the presence of long, thin, highly branched processes and small cell bodies, were prevalent throughout cortical layer V of Naïve mice. Following EAE induction, however, the percent of microglia that exhibited a reactive phenotype, as revealed by thicker and shorter branches and large cell bodies, was significantly increased in both the Early (Fig. 2.5B, C, G, H) and Late (Fig. 2.5E, F, I, J) stages regardless of disease severity, as shown by the shift towards more reactive morphologies. Importantly, microglial reactivity was observed in the Early EAE 1&2 mice indicating that microglial reactivity preceded AIS disruption.

Microglia are reactive in cuprizone treated mice

Because microglial reactivity paralleled AIS disruption in the EAE model, we investigated the state of microglial reactivity in the cuprizone model in which AIS integrity was not altered. The cuprizone model is generally described as a model of demyelination, without inflammation, at least with regard to T-cell infiltration due to an intact blood-brain-barrier (McMahon et al., 2002). However, reactive microglia play a critical role in both MS and the cuprizone model acting as phagocytes to clear myelin debris (Gudi et al., 2014).

In our cuprizone treated mice, we found that microglia exhibited morphologies consistent with reactivity only during periods of active demyelination—3 and 5 weeks of cuprizone treatment (Fig. 2.6C, D, G, H). Following 1 week of cuprizone treatment, a time point when demyelination was not observed (Fig. 2.2B), microglia displayed ramified morphologies (Fig. 6B, 6F) resembling the microglia in the untreated mice (Fig. 2.6A, F). Following termination of cuprizone exposure (5+3 wks Cup), the microglia returned to their ramified morphology during a period of repair (Fig. 2.6E, I).

Microglial-AIS interactions increase with disease progression in both the cuprizone and EAE models

The presence of reactive microglia, not only in EAE but also in cuprizone mice, negated our hypothesis that the presence of reactive microglia alone is sufficient to cause AIS disruption. Since a recent paper reported that a subset of microglia contact the AIS (Baalman et al., 2015), consistent with these cells playing a role in AIS plasticity, we quantified microglia/AIS contact in the two models proposing that a difference in the frequency of interaction between the AIS and the microglia would shed light on the role that these cells play in the observed AIS breakdown (EAE) and preservation (cuprizone).

For this analysis we utilized Volocity™ to quantify microglial/AIS contact while preserving 3-dimensional relationships since the use of collapsed projection images can provide misleading associations. In both the cuprizone (Fig. 2.7B, H) and the EAE (Fig. 2.7C, I) models, our quantitative analyses revealed a significant increase in the number of microglial/AIS contact points per FOV as compared to Naïve mice (Fig. 2.7A) and this

increase paralleled and preceded both myelin loss (cuprizone; 1 wk - 122.9 ± 4.3%; 3 wk – 145.3 ± 5.9%; 5 wk – 216.4 ± 8.5%; 5+3 wk – 179.7 ± 6.3%; all values are expressed as percent of Naïve) and AIS breakdown (EAE; Early 1&2 – 153.8 ± 22.5%; Early 3&4 – 185.0 ± 5.9%; Late 1&2 – 205.6 ± 33.9%; Late 3&4 – 169.4 ± 31.2%; all values are expressed as percent of Naïve) (Fig. 2.7H, I). Interestingly, the types of contact were highly varied with some of the microglia extending processes that ran along the AIS (Fig. 2.7D, F) while other processes completely ensheathed the AIS (Fig. 2.7E).

Reactive microglia in cuprizone-treated and EAE-induced mice exhibit different molecular profiles

Based on the above findings, there is a significant increase in the percent of AISs that are contacted by microglia in both the cuprizone and EAE models as compared to control but no difference in the extent of contact was noted between the models. Therefore, increased microglial contact is not sufficient to explain the difference in AIS integrity observed in the EAE and cuprizone models. We further proposed that the reactive microglia in these two models exhibit different molecular profiles resulting in functional diversity. To test this hypothesis, we double immunolabeled brain sections from cuprizone-treated and EAE-induced mice with IBA-1 and tumor necrosis factor alpha (TNFα), inducible nitric oxide synthase (iNOS), or macrophage colony stimulating factor (M-CSF) at the earliest time points when microglial morphology was altered and prior to pathology (3 wk cuprizone, Fig. 2.6; Early 1&2 EAE, Fig. 2.5). TNFα and iNOS are pro-inflammatory factors produced by reactive microglia (Block et al., 2007; Haji et al., 2012; Miron et al., 2013); M-CSF regulates microglial proliferation and survival (Elmore et al.,

2014). As shown in Figure 2.8, microglia from Naïve mice exhibit minimal labeling for these three markers (Fig. 2.8A, E, I), consistent with the surveying state of microglia in Naïve mice. In contrast, cuprizone treated mice (Fig. 2.8B, F, J) exhibited minimal labeling for TNFα and iNOS (comparable to Naïve) but elevated labeling for M-CSF. Interestingly, microglia in EAE induced mice (Fig. 2.8C, G, K) presented elevated labeling for TNFα, and iNOS while M-CSF labeling was comparable to Naïve. These results were confirmed using quantitative RT-PCR of cortical microglia isolated from Naïve, cuprizone (3 wk) and EAE mice (Early 1&2) (Fig. 2.8D, H, L). Therefore, consistent with previous work (reviewed by Rawji and Yong, 2013), we propose that the reactive microglia found in each model are phenotypically distinct, and play functionally distinct roles.

EAE-induced AIS disruption is attenuated with anti-inflammatory treatment

Since AIS disruption was preceded by microglial reactivity (Fig. 2.5), we proposed that reactive microglia may be involved. To test this hypothesis, we administered an anti-inflammatory drug to the EAE 3&4 mice at the Early time point, predicting that the inhibition of microglial reactivity would result in sparing of the AIS. For this approach we used didox, a drug that readily crosses the blood brain barrier (Fiqul et al., 2003), scavenges free radicals (Mayhew et al., 2002), down regulates NFκB activity (Inayat et al., 2002) and inhibits microglial reactivity and the production of pro-inflammatory factors that are produced by macrophages/microglia (Matsebatlela et al., 2015). Treatment with this drug resulted in an attenuation of the EAE clinical scores (Fig. 2.1B).

In addition to the attenuation of clinical scores and consistent with our hypothesis, didox treatment also resulted in a significant reduction in microglial reactivity based on morphological analysis (Fig. 2.9A-D) and microglia/AIS contact (Figure 2.9E-H). Although reversion back to a surveying phenotype was not complete in the didox treated animals (Fig. 2.9C, C', D), microglia/AIS contact reverted to near Naïve levels (Fig. 2.9G, H). Therefore, our findings indicate that didox inhibited progressive AIS deterioration and reversed AIS pathology with regard to length, and almost completely attenuated the reactive microglial morphology. Furthermore, didox treatment attenuated the elevated microglial expression of TNFα (Supplementary Fig. S2.4A-D), and iNOS (Fig. 2.9I-L) consistent with a return to a surveying phenotype.

Moreover, Early EAE 3&4 mice treated with didox (Fig. 2.10C) displayed, at the Late stage, AISs with lengths that were indistinguishable from Naïve (compare 19.5 ± 0.9 µm for didox; 19.9 ± 0.3 µm for Naïve; Fig. 2.10A; Table 2.2) indicating that didox treatment reversed AIS pathology observed in the Early EAE 3&4 group. Didox treated mice also exhibited significantly longer AISs than the vehicle control (16.8 ± 1.2 µm; Fig. 2.10B, 2.10E; Table 2.2) and EAE 3&4 Early and Late mice (13.4 ± 0.4 µm, and 16.0± 0.6, respectively; Table 2.2). In addition, the loss of AISs was significantly attenuated with a preservation of 68.4% ± 5.5% of the AISs following didox treatment compared to the preservation of only 27.7% ± 0.5% in the vehicle control group and only 28.5 ± 0.5% in the Late EAE 3&4 (Figs. 2.10D, Table 2.2).

2.5 Discussion

In contrast to the NOR, here we show that protein clustering in the AIS is not lost following demyelination but is disrupted following inflammation. Initially, AIS length is reduced followed by a significant loss in AIS number in later disease stages. Although the mechanism of disruption is unknown, microglial reactivity and increased microglial/AIS contact preceded AIS pathology. Additionally, treatment with didox, a drug known to reduce macrophage/microglia inflammation (Matsebatlela et al., 2015), resulted in suppression of microglial reactivity, reversal of AIS shortening and prevention of AIS breakdown. Finally, we provide evidence that the roles that microglia play in demyelinating and inflammatory disease are dependent on their expression profiles.

AIS integrity is not compromised by demyelination

Axonal function requires maintenance of the NORs and the AISs (Buttermore et al., 2013). The maintenance of these domains, however, differs with respect to myelin dependency as we (Dupree et al., 1999; 2004) and others (Bhat et al., 2001; Ishibashi et al., 2002; Pillai et al., 2009; Rasband et al., 1999; Rosenbluth et al., 2003; Suzuki et al., 2004) have shown that myelin contact is critical for NOR maintenance. For example, cuprizone-induced demyelination resulted in complete loss of nodal and paranodal clustered proteins (Dupree et al., 2004). In contrast, we now show that AIS maintenance is not dependent on myelin as cortical demyelination did not alter AIS number or length consistent with work by Hamada and Kole (2015). Therefore, while the NOR and AIS maintain clusters of similar proteins (Buffington and Rasband, 2011), the mechanisms responsible for domain maintenance are distinct.

AIS integrity is compromised following EAE disease induction

Although we are the first to report AIS disruption in EAE, we are not the first to report AIS vulnerability following disease or injury. Schafer et al. (2009) reported a significant loss of cortical and striatal AISs following ischemia in vivo, and showed that AIS deterioration resulted from calpain activity. Although calpain inhibitors prevented AIS deterioration, reversal of the pathology was not achieved. Similarly, Hinman et al. (2013) reported AIS shortening following ischemia and showed sprouting of immature AISs suggesting the potential for AIS replacement but not repair.

Following traumatic brain injury (TBI), AISs were significantly shortened consistent with altered neuronal excitability (Baalman et al., 2013) and developed amyloid precursor protein-containing axonal swellings (Greer et al., 2012; 2013). Although the mechanisms responsible for AIS disruption following TBI are unclear, cytoskeletal disruption has been observed (Buki and Povlishock, 2006; Povlishock et al., 1999). Similar to the findings of Schafer et al. (2009), spectrin and AnkG are degraded following TBI (Buki et al., 1999; Reeves et al., 2010), which is accompanied by calpain activation suggesting that related mechanisms underly AIS breakdown in distinct models.

Is the axon a primary target of pathology in MS?

Demyelination is a hallmark feature of MS (Lassmann, 1999), but axonal insults are also prevalent in this disease (Kornek and Lassmann, 1999). The formation of axonal swellings, reduced levels of Na^+/K^+ ATPase, synaptic damage, axon transection, and disruption of nodal domains are among the known axonal pathologies associated with MS and its models (Black et al., 2007; Dutta et al., 2011; Howell et al., 2010; Peterson et

al., 2001; Pomicter et al., 2010). These axonal pathologies, which contribute to disability progression (Dutta and Trapp, 2011), are postulated as consequential to demyelination; however, the axon may also be a primary target (Calabrese et al., 2015). For instance, MS plaque load does not correlate with axonal loss (DeLuca et al., 2006); analysis of post-mortem MS tissue reveals axonal swellings and end bulbs located in normal appearing white matter (Kutzelnigg et al., 2005; Nikić et al., 2011) and axonal number is reduced in regions lacking demyelination in MS and EAE (Bjartmar et al., 2001; Recks et al., 2013). Similarly, our findings suggest that axonal pathology results from a demyelination-independent mechanism further suggesting that the axon may be a primary target in inflammatory disease.

Are microglia responsible for inflammation-dependent AIS disruption?

Microglia are reactive in MS and play a role in the progression of the disease (Rawji and Yong, 2013). EAE progression closely correlates with microglial reactivity and inhibition of these inflammatory cells attenuates disease course (Bhasin et al., 2007; Heppner et al., 2005). Triggers for microglial reactivity in MS include oligodendrocyte stress and demyelination (Hendrickx et al., 2014; Huizinga et al., 2012; Lassmann et al., 2001); however, microglial reactivity also occurs in the absence of demyelination (Marik et al., 2007) and, consistent with our findings, these cells may directly target axons in MS and its animal models (Nikić et al., 2011; Rawji and Yong, 2013).

Baalman et al. (2015) recently established a relationship between microglia and the AIS by reporting that a subpopulation of microglia contact the AIS during development and maintain this contact throughout adulthood suggesting a role in AIS organization.

Interestingly, following TBI reactive microglia lost AIS contact. Our results further confirm the existence of microglia/AIS contacts in the Naïve cortex but demonstrate that these contacts are increased in a pathological environment-- either inflammatory (EAE) or demyelinating (cuprizone model). Our results also highlight a differential response to TBI and EAE induction concerning AIS stability. Indeed, Baalman et al. (2013) reported that following blast injury, the AIS is only modestly, yet significantly, shortened whereas in EAE our results show a dramatic early shortening followed by AIS loss, the latter being preceded by an increase in microglia/AIS contact.

In EAE, reactive microglia release pro-inflammatory factors including reactive oxygen species (ROS) (Guemez-Gamboa et al., 2011), and TNFα (Haji et al., 2012). Each of these factors is capable of increasing intraneuronal calcium levels by triggering calcium channel currents specifically through L-type calcium channels (Furukawa and Mattson, 1998; Das et al., 2011; Guemez-Gamboa et al., 2011; Sama and Norris, 2013; Vogel et al., 2015). Thus, both TNFα and ROS have the potential to contribute to AIS modulation, since L-type calcium channels are crucial for plasticity at the AIS (Grubb and Burrone, 2010). Moreover, neurons in EAE-induced mice exhibit elevated calcium levels with a corresponding increase in calpain activity and axonal cytoskeletal pathology that is ameliorated by calpain inhibition (Guyton et al., 2005, 2009). Calpain inhibitors also reduce symptomatic severity in EAE mice (Das et al., 2013) potentially through anti-inflammatory and neuroprotective mechanisms (Trager et al., 2014). This scenario of AIS disruption is consistent with our data suggesting that pro-inflammatory microglia can trigger a cascade that drives this disruption.

Is microglial function dependent on their inflammatory profile?

Although an easy culprit for AIS disruption, reactive microglia were also abundant in the cuprizone model where AISs were not compromised. However, reactive microglia in the EAE and cuprizone models presented with different inflammatory profiles providing a viable explanation for distinct functions (Hanisch and Kettenmann, 2007). Consistent with AIS disruption, numerous studies have implicated iNOS and TNFα as mediators of neurodegeneration (Block et al., 2007; Glass et al., 2010). In contrast, an up-regulation of M-CSF, a growth factor involved in proliferation and survival of microglia and macrophages (Stanley et al., 1997), promotes remyelination in demyelinating mouse models through the recruitment of microglia to lesioned sites, followed by oligodendrocyte progenitor differentiation (Döring et al., 2015). While these distinct expression profiles are consistent with microglia playing different roles in these models, it is important to point out that TNFα and iNOS also have neuroprotective roles (Arnett et al., 2001; 2002; Liu et al., 1998) and that anti-inflammatory cytokines may also have differential expression patterns in these models (Janssens et al., 2015) indicating the complex nature of these cells.

Is AIS disruption reversible?

In the ischemic injury model (Schafer et al., 2009), calpain inhibitors preserved AIS integrity; however, AIS repair was not observed suggesting an irreversible pathology (Schafer et al., 2009). Here, AIS length was restored following didox treatment. AISs alter their length during development (Gutzmann et al., 2014) and in response to changes in presynaptic input (Kuba et al., 2010) indicating that the AIS is a dynamic domain.

However, the present study is the first to report a therapeutic attenuation of AIS pathology. It remains to be determined if the more severe consequences, such as complete loss of AIS protein clustering, as observed in Late EAE, can be reversed.

In summary, we report that AIS integrity was preserved in the demyelinated cortex, but significant disruption was observed in the non-demyelinated cortex of EAE-induced mice suggesting that the AIS is a potential primary axonal target during inflammation. Morphological analyses at two distinct time points along the disease course indicates AIS shortening is an early event that is followed by loss of AIS protein clustering. Importantly, AIS pathology, potentially mediated by reactive microglia, appears both preventable and reversible through therapeutic intervention. Taken together, our results open new perspectives into the understanding of disability progression in inflammatory demyelinating disease such as MS, with potential innovative therapeutic avenues.

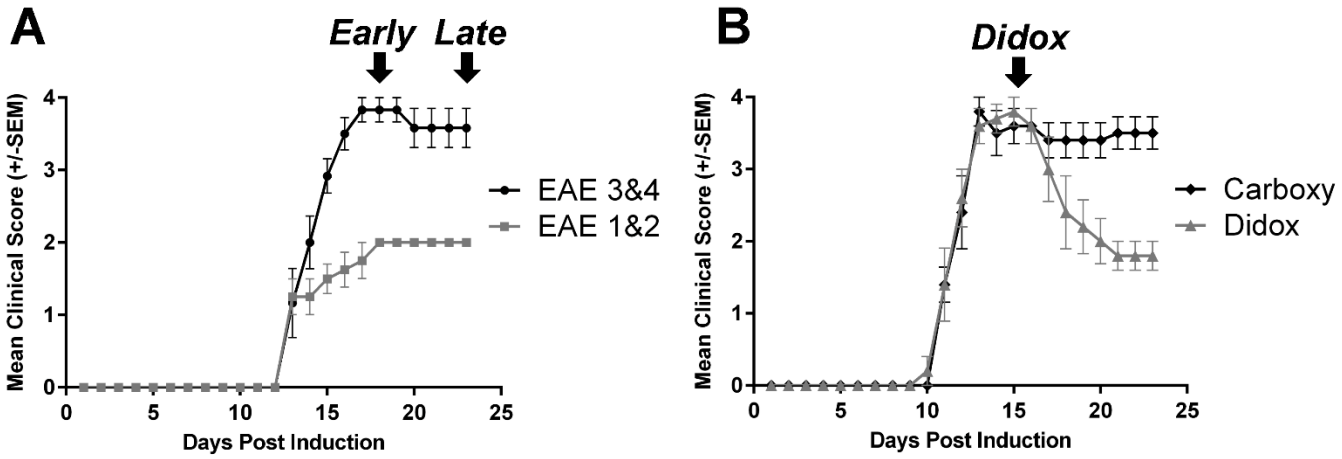
A
Early
Late
Mean Clinical Score (+/-SEM)
Days Post Induction
EAE 3&4
EAE 1&2
B
Didox
Mean Clinical Score (+/-SEM)
Days Post Induction
Carboxy
Didox

Figure 2.1. Clinical Progression of EAE model. Mean clinical scores of the EAE mice used in this study are graphed showing the consistent progression of the disease of each clinical score group (EAE 1&2 and EAE 3&4) as well as the time points at which these groups were analyzed (Early and Late; arrows) (A). Treatment with the anti-inflammatory didox at the Early time point resulted in reduced EAE clinical scores, while treatment with the vehicle carboxymethylcellulose had no effect on EAE progression (B).

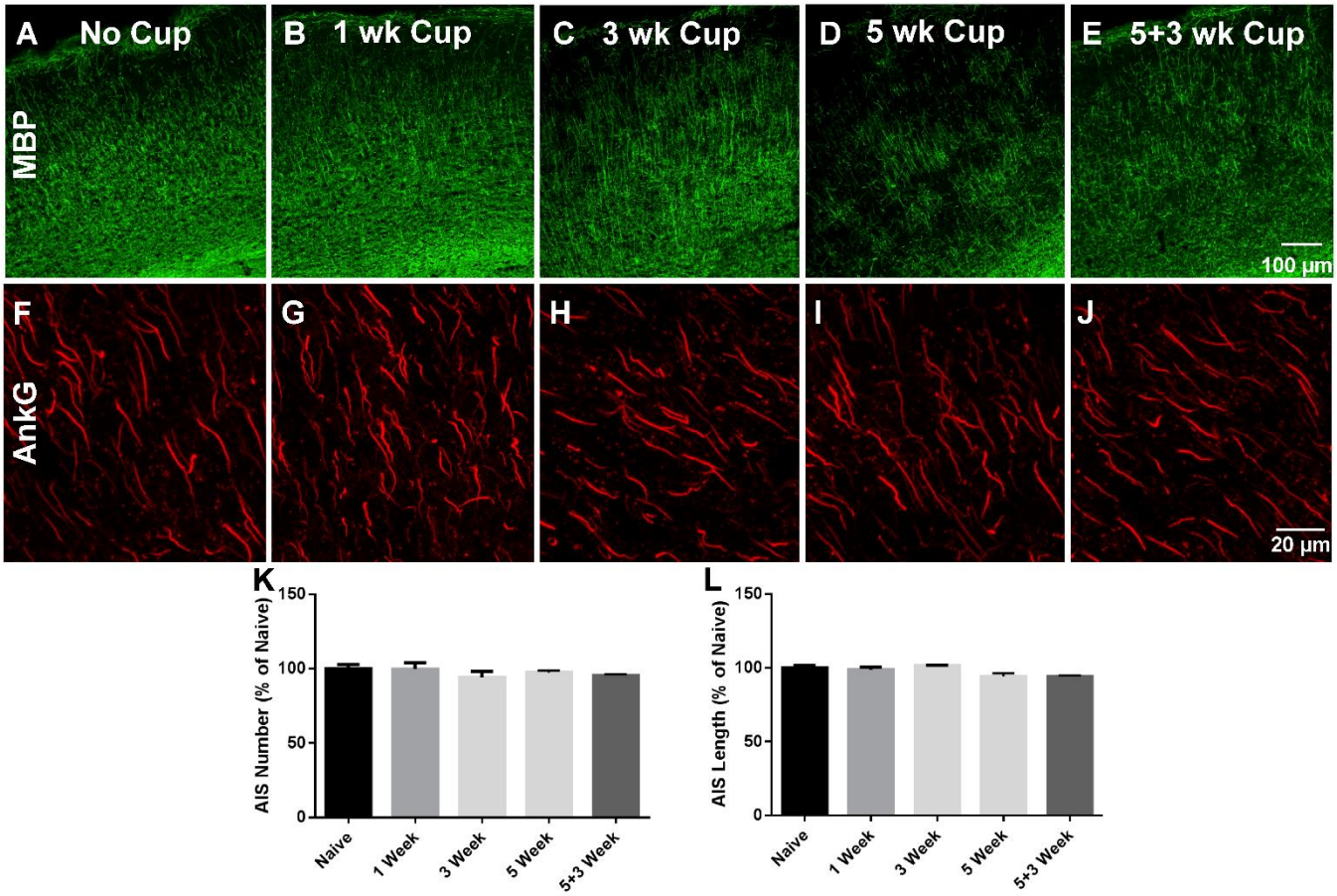
A No Cup
B 1 wk Cup
C 3 wk Cup
D 5 wk Cup
E 5+3 wk Cup
MBP
100 µm
F
G
H
I
J
AnkG
20 µm
K
AIS Number (% of Naive)
150
100
50
0
Naive
1 Week
3 Week
5 Week
5+3 Week
L
AIS Length (% of Naive)
150
100
50
0
Naive
1 Week
3 Week
5 Week
5+3 Week

Figure 2.2. AISs are not disrupted following cuprizone-induced demyelination. Cortical demyelination was assessed by immunolabeling for MBP (A–E). No myelin loss was detected following 1 week of cuprizone treatment (B). Note a slight reduction in MBP labeling following 3 weeks of cuprizone exposure (compare A and C) with a continued decrease in labeling by 5 weeks of treatment (D). Following an additional 3 weeks without cuprizone, MBP labeling increased consistent with remyelination (E). Ankyrin-G labeling of cortical layer V axon initial segments (AIS) revealed no difference among mice that were maintained on ground chow without cuprizone (F) and mice maintained on cuprizone for 1 week (G), 3 weeks (H), 5 weeks (I), or 5 weeks with an additional 3 weeks of recovery (J). Quantitative analysis confirmed that neither AIS number (K) nor AIS length (L) was altered following cortical demyelination at any exposure time point or as compared to untreated (Naïve) mice.

Table 2.1: AIS Number and Length Measurements from Mice Treated with and without Cuprizone

Treatment group	AIS number (% Naive ± SEM)	AIS length (% Naive ± SEM)	AIS length (Avg. ± SEM; μm)	*n*
No Cup.	100.0 ± 7.2	100.0 ± 4.5	19.9 ± 0.9	7
1 wk Cup.	99.7 ± 7.4	98.8 ± 2.7	19.7 ± 0.5	6
3 wk Cup.	94.1 ± 7.1	101.4 ± 0.8	20.2 ± 0.2	6
5 wk Cup.	97.4 ± 2.4	94.2 ± 3.9	18.3 ± 0.8	6
5 + 3 wk Cup.	95.5 ± 1.3	94.1 ± 1.5	18.8 ± 0.3	6

No significant difference was detected with regard to the percent of AIS number, percent of AIS length or actual length among any of the treatment groups or the control group.

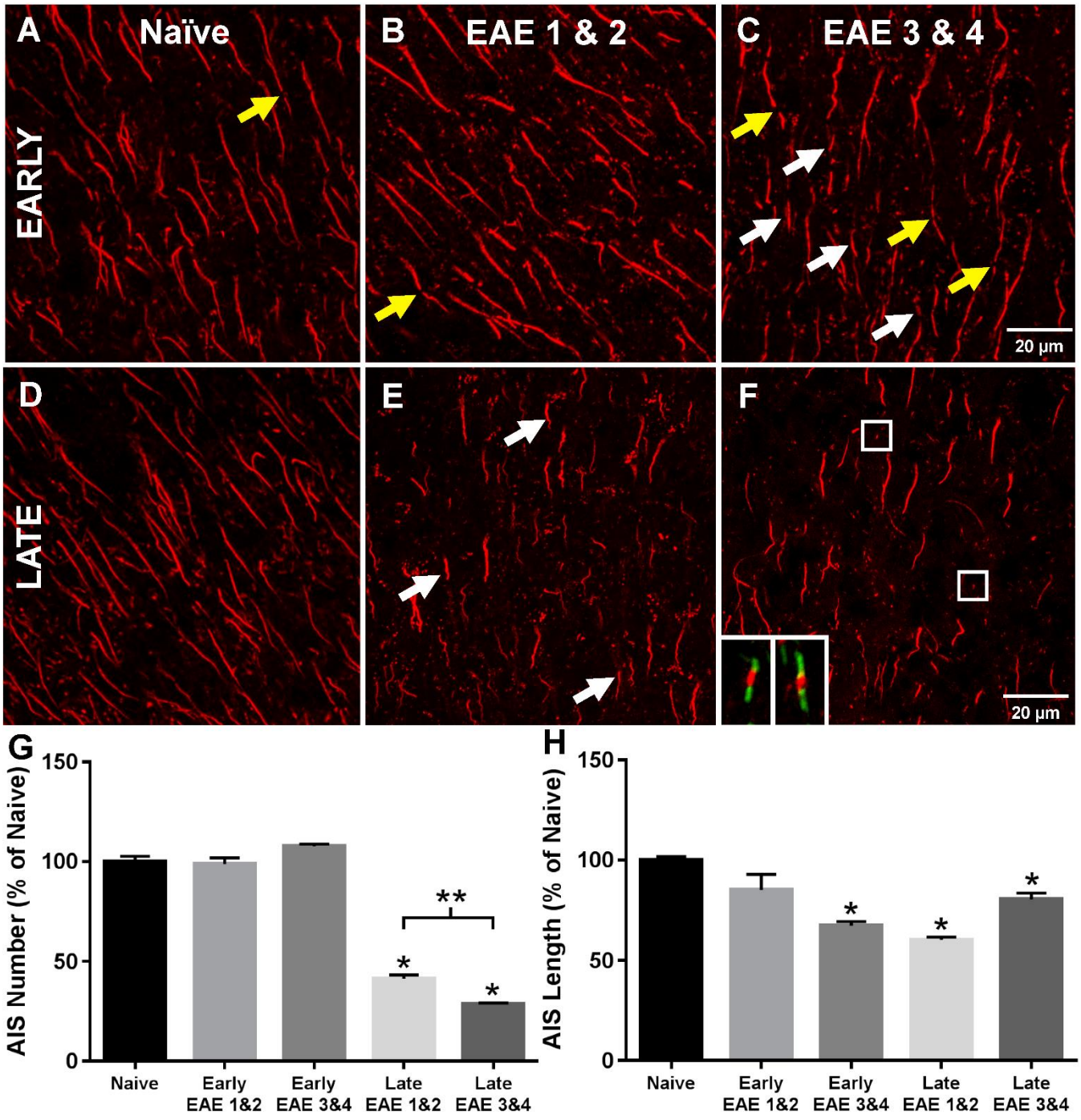
A
Naïve
B
EAE 1 & 2
C
EAE 3 & 4
EARLY
20 µm
D
E
F
LATE
20 µm
G
AIS Number (% of Naive)
150
100
50
0
**
*
*
Naive
Early EAE 1&2
Early EAE 3&4
Late EAE 1&2
Late EAE 3&4
H
AIS Length (% of Naive)
150
100
50
0
*
*
*
Naive
Early EAE 1&2
Early EAE 3&4
Late EAE 1&2
Late EAE 3&4

Figure 2.3. AIS length is reduced in early stages of EAE while the number of AISs is decreased in the late stages of disease. In Early disease stage (3 days post peak clinical symptoms), AISs in cortical layer V neurons of Naïve (A) and EAE 1&2 (B) mice were abundant, presented with uniform length and rarely revealed discontinuous labeling indicative of fragmentation (yellow arrows). In contrast, AISs of layer V cortical neurons in Early EAE 3&4 mice (C) were frequently reduced in length (white arrows) and fragmented (yellow arrows). Quantitative analysis confirmed the immunohistochemical observations. No difference in AIS number was observed among the Early EAE groups (G). Although no difference in AIS length was observed between Naïve and Early EAE 1&2 mice (H), a significant shortening was observed with the Early EAE 3&4 mice compared to Naïve animals (H). In contrast, the Late EAE 1&2 mice (E,G) exhibited a significantly reduced number of AISs with a continued progression in AIS loss observed in the Late EAE 3&4 mice (F,G). While there was a significant decrease in AIS length for the Late EAE 1&2 mice, a significant but less dramatic shortening was observed for the Late EAE 3&4 mice as compared to the Naïve animals (H). Note that with the loss of AISs (Panel F), punctate AnkG labeling was observed. Double labeling for AnkG and the paranodal marker Caspr (see F inset; AnkG – red; Caspr – green) revealed that these puncta were nodes of Ranvier that were not disrupted following EAE induction. (Asterisks with no associated bracket represent a significant difference from the Naïve group; *P = 0.0001, ** P = 0.008).

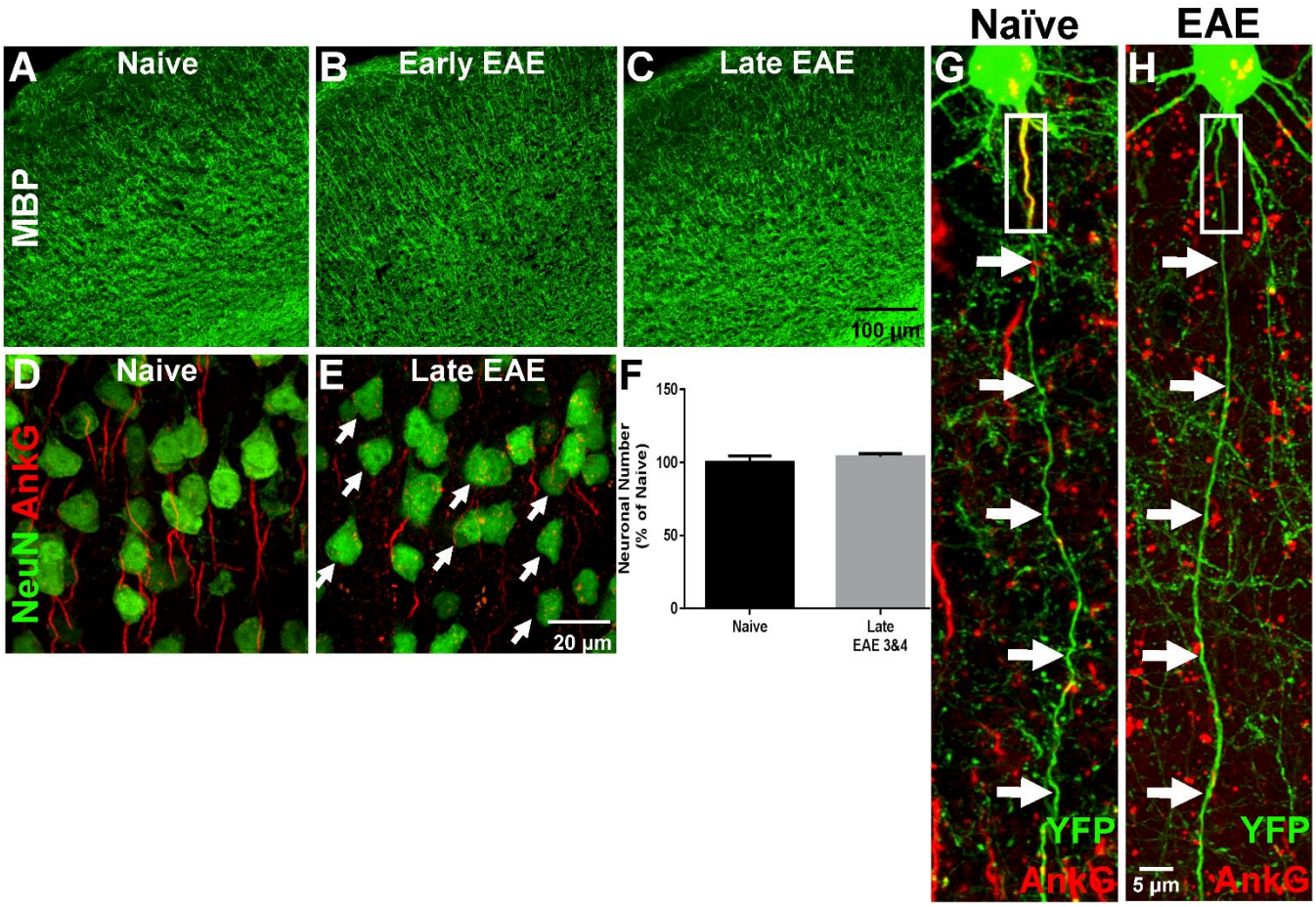
A
Naive
MBP
B
Early EAE
C
Late EAE
100 µm
D
Naive
NeuN AnkG
E
Late EAE
20 µm
F
Neuronal Number
(% of Naive)
150
100
50
0
Naive
Late
EAE 3&4
Naïve
EAE
G
H
YFP
AnkG
5 µm

Figure 2.4. Disrupted AISs in EAE are not the consequence of demyelination, neuronal death or axonal transection. Based on immunohistochemical labeling for MBP, no difference in cortical myelin was observed among Naïve (A), Early EAE 3&4 mice (B) or Late EAE 3&4 mice (C). The density of neuronal cell bodies, as determined by NeuN immunolabeling (D–F) also remained constant, indicating AIS loss is not a result of cell death. Note the presence of numerous NeuN/AnkG double positive cells in Panel D while most NeuN positive cells in Panel E lack AnkG labeling (white arrowheads) Immunolabeling of AnkG (red) in Thy1-YFP (green) mice induced with EAE (Late 3&4) revealed intact axons following disruption of the AIS protein clustering (H; white rectangle) while Naïve Thy1-YFP mice revealed robust AnkG labeling in the AIS (G; white rectangle).

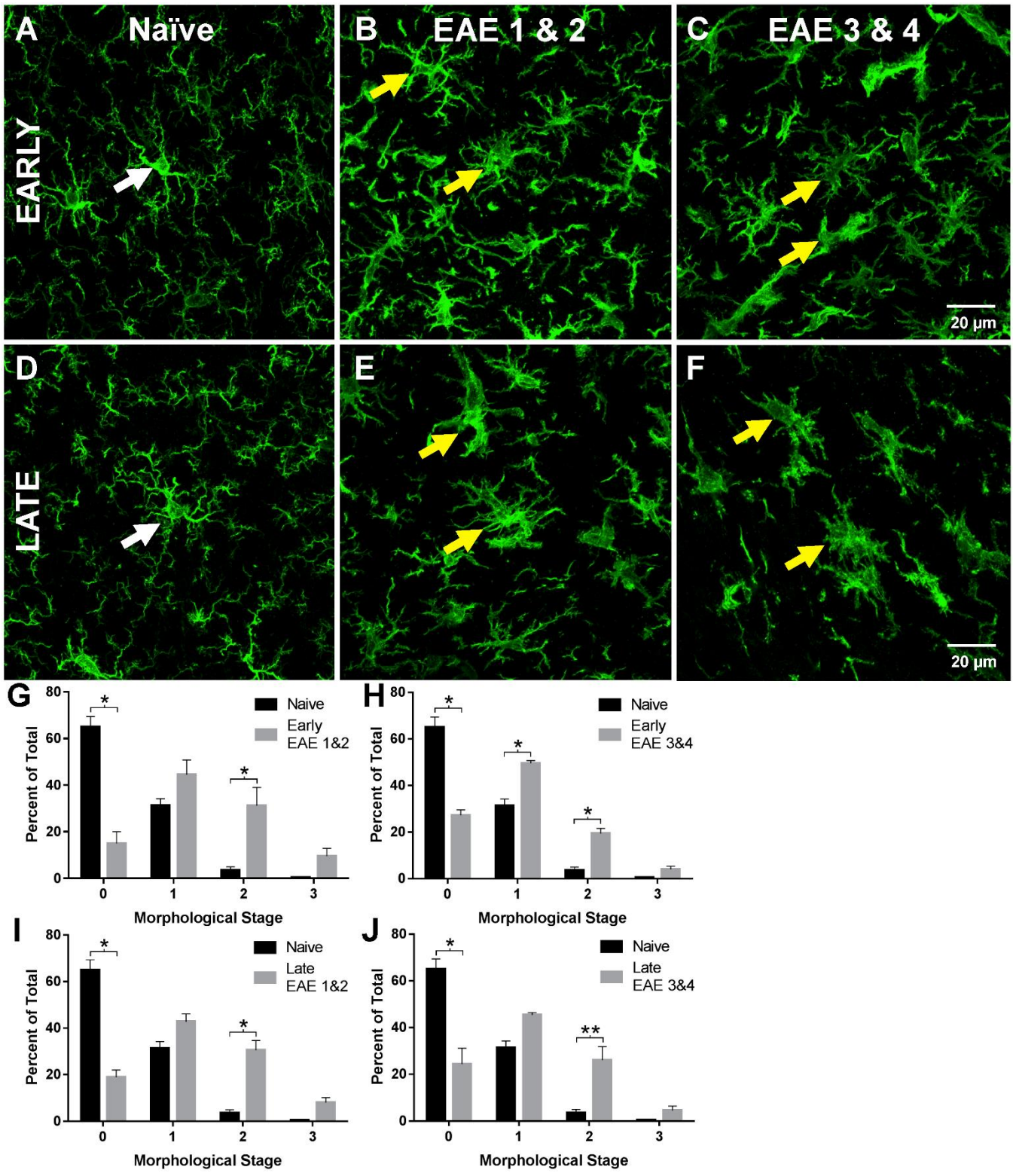
A
Naïve
B
EAE 1 & 2
C
EAE 3 & 4
EARLY
20 µm
D
E
F
LATE
20 µm
G
Naive
Early
EAE 1&2
Percent of Total
Morphological Stage
H
Naive
Early
EAE 3&4
Percent of Total
Morphological Stage
I
Naive
Late
EAE 1&2
Percent of Total
Morphological Stage
J
Naive
Late
EAE 3&4
Percent of Total
Morphological Stage

Figure 2.5. Microglia exhibit a reactive morphology at Early and Late stages of EAE. Microglia in Naïve mice (A,D) exhibited small cell bodies with long, thin and highly branched processes indicative of a surveying phenotype (white arrows). In contrast, microglia from Early and Late EAE 1&2 (B,E) and EAE 3&4 (C,F) mice displayed enlarged cell bodies with short, thick processes with reduced branching consistent with cells in a state of reactivity (yellow arrows). Distribution graphs of microglial morphological stages provide quantitative evidence confirming this significant shift from the Naïve (G-J). (*P = 0.0001, ** P = 0.003).

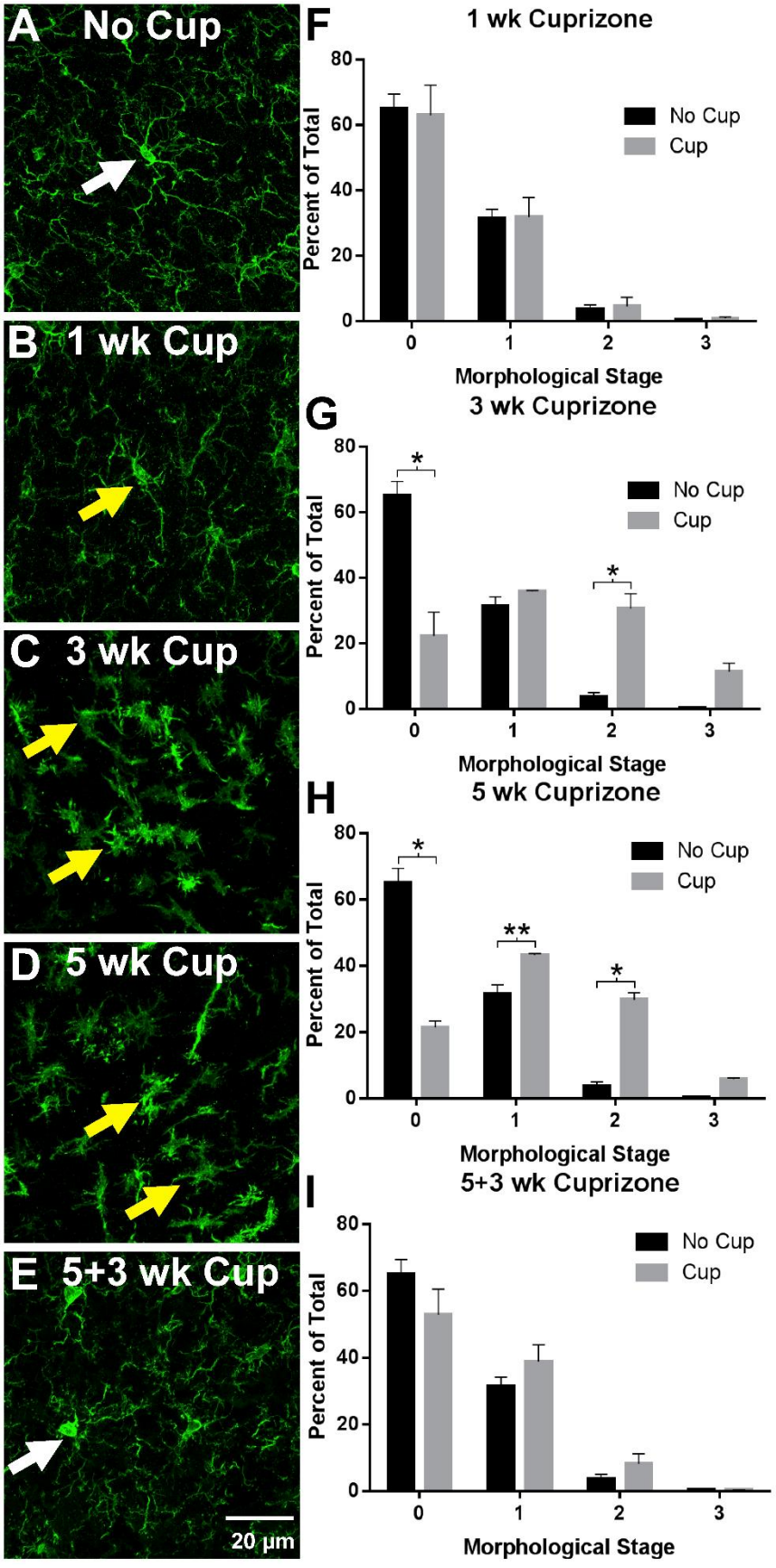
A No Cup
B 1 wk Cup
C 3 wk Cup
D 5 wk Cup
E 5+3 wk Cup
20 µm
F
1 wk Cuprizone
Percent of Total
No Cup
Cup
Morphological Stage
G
3 wk Cuprizone
H
5 wk Cuprizone
I
5+3 wk Cuprizone

Figure 2.6. Microglia exhibit a reactive morphology during periods of demyelination in the cuprizone model. Based on immunohistochemical labeling for IBA-1, mice maintained on normal chow (no cuprizone) exhibited ramified microglia (A), indicative of a surveying role. Scoring of microglial morphology indicated that the cells remained ramified following 1 week of cuprizone treatment (B,F). Following 3 (C,G) and 5 (D,H) weeks of treatment, microglia exhibited an amoeboid morphology consistent with reactivity. Removal of cuprizone from the diet resulted in a shift in the presented morphologies consistent with untreated mice (E,I). (*P = 0.0001, ** P = 0.006).

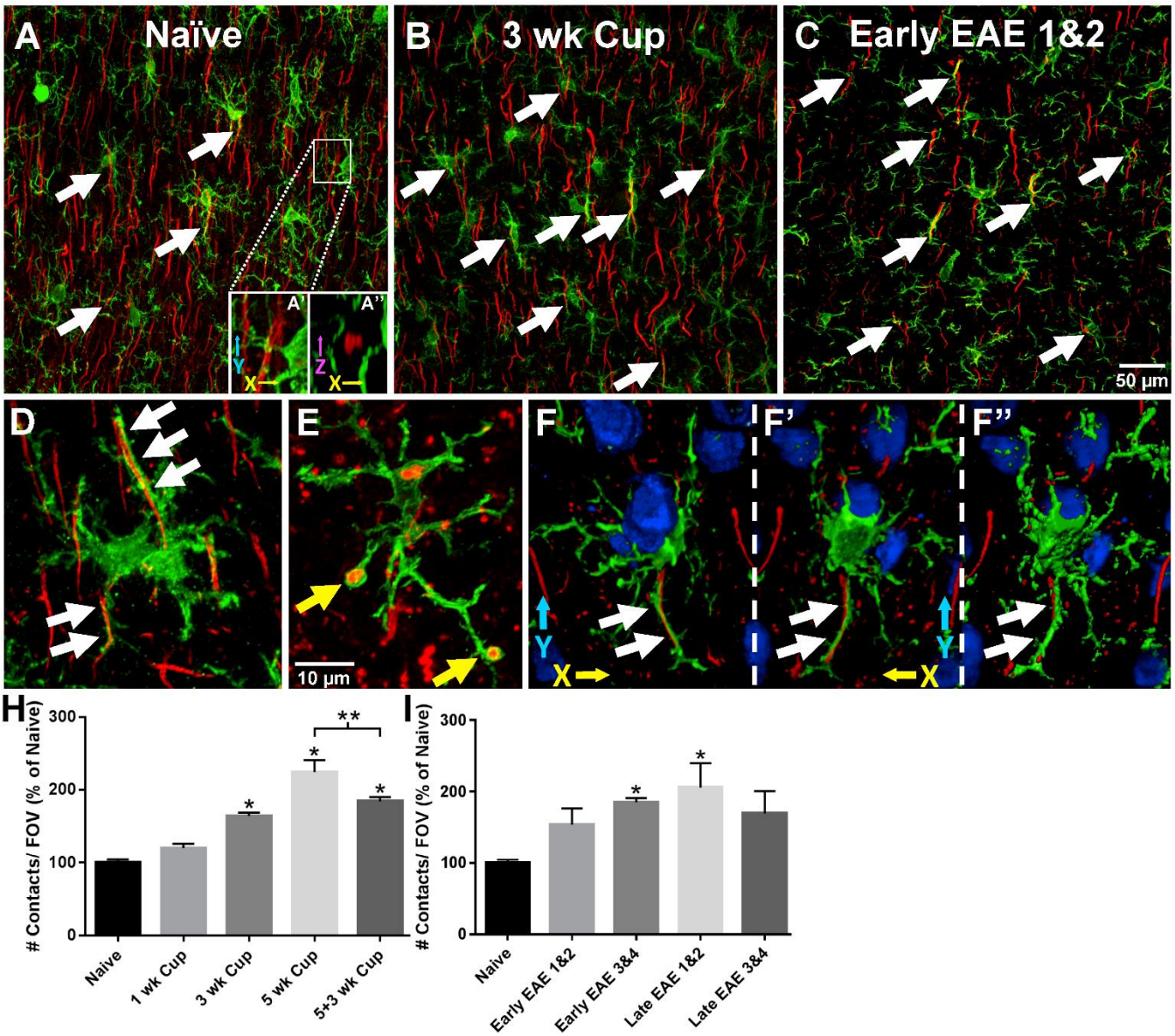
A
Naïve
A'
A''
Y
X
Z
X
B
3 wk Cup
C
Early EAE 1&2
50 µm
D
E
10 µm
F
F'
F''
Y
X
Y
X
H
Contacts/ FOV (% of Naive)
300
200
100
0
*
*
*
**
Naive
1 wk Cup
3 wk Cup
5 wk Cup
5+3 wk Cup
I
Contacts/ FOV (% of Naive)
300
200
100
0
*
*
Naive
Early EAE 1&2
Early EAE 3&4
Late EAE 1&2
Late EAE 3&4

Figure 2.7 Microglia exhibit increased contact with the AIS in Cuprizone treated and EAE induced mice. Double immunolabeling of IBA-1 and AnkG revealed an increase in the percent of AISs contacted by microglia in both the cuprizone (B) and EAE (C) models temporally corresponding with microglial reactivity (H,I). Confocal z-stacks were analyzed in 3D to rule out apparent contact points in 2D as demonstrated by the inset AIS (A′) which was rotated 90° along the X-axis, revealing no microglial contact (A″). Examples of microglial-AIS interactions are depicted with reactive microglia making contact onto one (F) or more AISs (D, E). Processes frequently aligned along the AIS (white arrows, D,F). Transverse sections of the cortex revealed microglial processes wrapping completely around AISs cut in cross section (E, yellow arrows). The number of contact points per FOV as a percent of the Naïve was significantly increased following 3 and 5 weeks of cuprizone treatment, with a slight, but significant, decrease in contact following 3 weeks of recovery (no cuprizone) (H). Similarly, microglial-AIS interactions were increased along with EAE progression (I). Panels F and F′ present the same microglia but display anterior (F) and posterior (F′) views. The image in Panel F″ was generated with the software Volocity™ from the z-stack of images used to compile the images in F and F′. The Volocity™ generated image provides shadowing to display the image with 3 dimensions providing a better depiction of the microglia and neuron interaction. (Asterisks with no associated bracket represent a significant difference from the Naïve group; * P = 0.0001, ** P = 0.01).

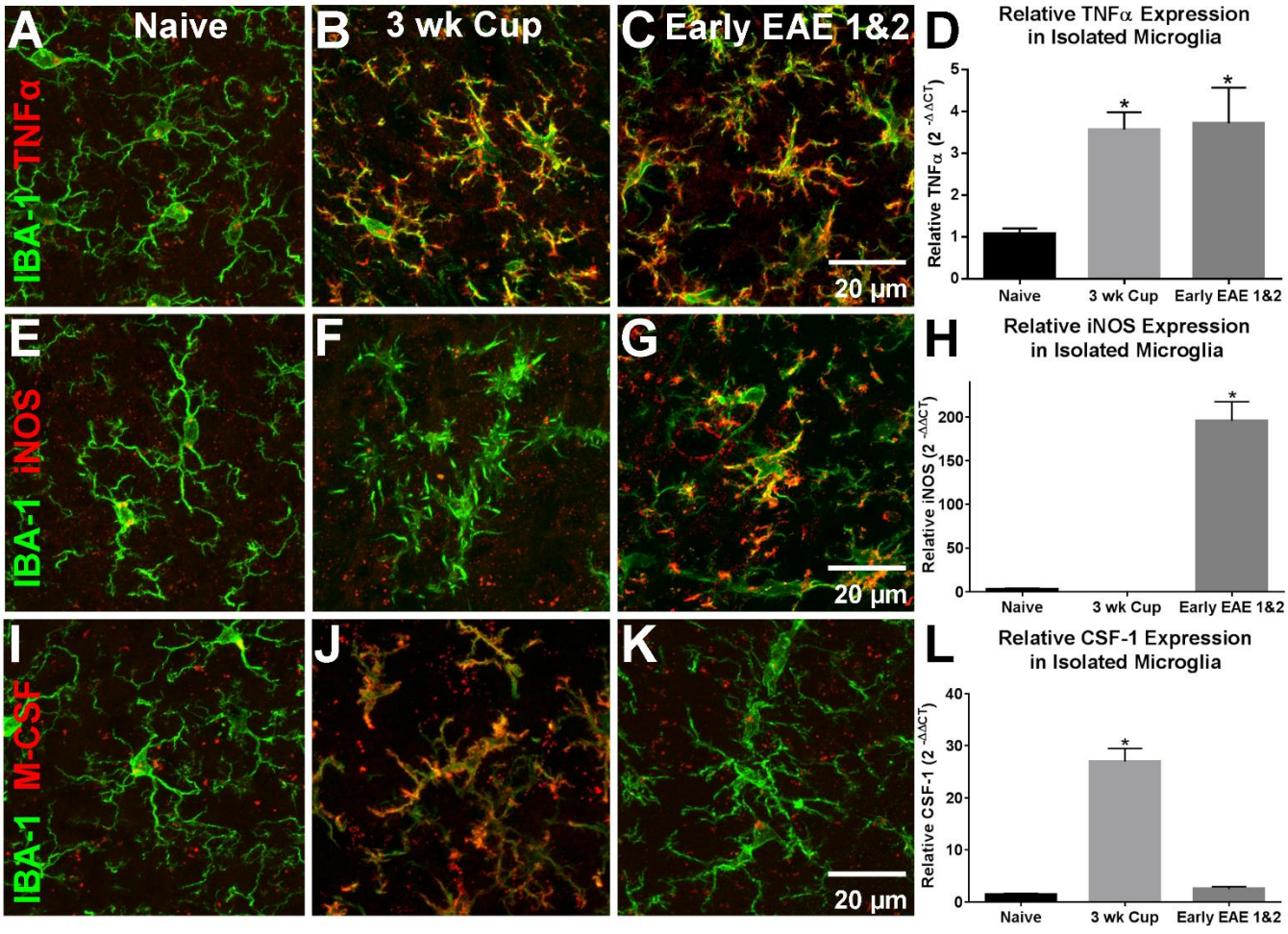
A
Naive
B
3 wk Cup
C Early EAE 1&2
IBA-1 TNFα
20 μm
D
Relative TNFα Expression
in Isolated Microglia
Relative TNFα (2 -ΔΔCT)
Naive
3 wk Cup
Early EAE 1&2
E
F
G
IBA-1 iNOS
20 μm
H
Relative iNOS Expression
in Isolated Microglia
Relative iNOS (2 -ΔΔCT)
Naive
3 wk Cup
Early EAE 1&2
I
J
K
IBA-1 M-CSF
20 μm
L
Relative CSF-1 Expression
in Isolated Microglia
Relative CSF-1 (2 -ΔΔCT)
Naive
3 wk Cup
Early EAE 1&2

Figure 2.8. Microglia present distinct phenotypes in Cuprizone vs. EAE. Double immunolabeling at the onset of microglial reactivity (3 weeks for cuprizone and Early 1&2 for EAE), for IBA-1 (green) in combination with either TNFα (A-C; red), iNOS (E-G; red), or M-CSF (I-K; red) indicated distinct phenotypes of the reactive microglia between the two models. Labeling intensities for TNFα were elevated in the microglia from both models (B,C). Labeling intensities for iNOS were elevated, as compared to Naïve, only in the microglia of the EAE mice (G), while M-CSF labeling intensities were elevated only in the microglia of the cuprizone treated mice (J). Immunohistochemistry results were confirmed by qRT-PCR of cortical microglia isolated from Naïve, cuprizone and EAE mice (D, H, L) (Asterisks represent a significant difference from the Naïve group; * $P = 0.0001$).

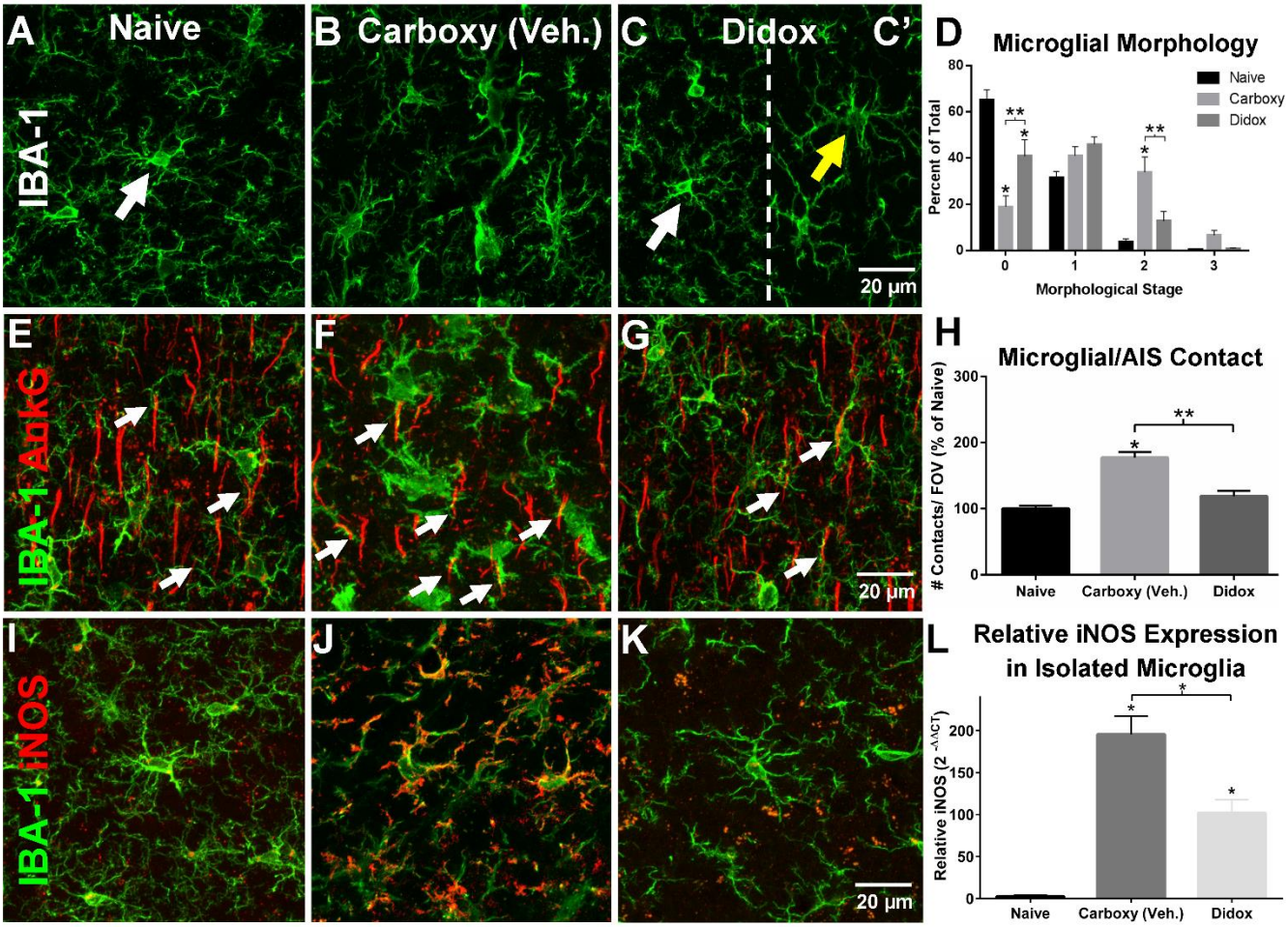
A
Naive
IBA-1
B Carboxy (Veh.)
C
Didox
C'
20 µm
D
Microglial Morphology
Naive
Carboxy
Didox
Percent of Total
Morphological Stage
E
IBA-1 AnkG
F
G
20 µm
H
Microglial/AIS Contact
Contacts/ FOV (% of Naive)
Naive
Carboxy (Veh.)
Didox
I
IBA-1 iNOS
J
K
20 µm
L
Relative iNOS Expression in Isolated Microglia
Relative iNOS (2^-ΔΔCT)
Naive
Carboxy (Veh.)
Didox

Figure 2.9 Didox treatment attenuates microglial reactivity and AIS-contact. Microglia in the Naïve mice (A,D) were not reactive based on their morphology (white arrows) while the microglia in the vehicle-treated animals were reactive as evidenced by large cell bodies and thick processes with limited branching (B,D). Although didox treatment attenuated microglial reactivity (white arrows) (C,D), treatment did not result in a complete reversion as reactive microglia (yellow arrow) were also detected in the didox treated animals (C′,D). In addition to reactivity, didox treatment also attenuated the increased microglial-AIS contact (G,H) while carboxymethylcellulose vehicle treatment maintained the enhanced number of contact points (F,H) as compared to the Naïve (E,H). Importantly, didox administration to EAE mice attenuated the elevated labeling intensities of iNOS (K) consistent with didox attenuation of microglial reactivity. iNOS immunolabeling (J) and mRNA expression (L) in the vehicle treated group remained increased compared to the Naïve group (I,L) (Asterisks with no associated bracket represent a significant difference from the Naïve group; * P =0.0001, ** P =0.02, *** P =0.002).

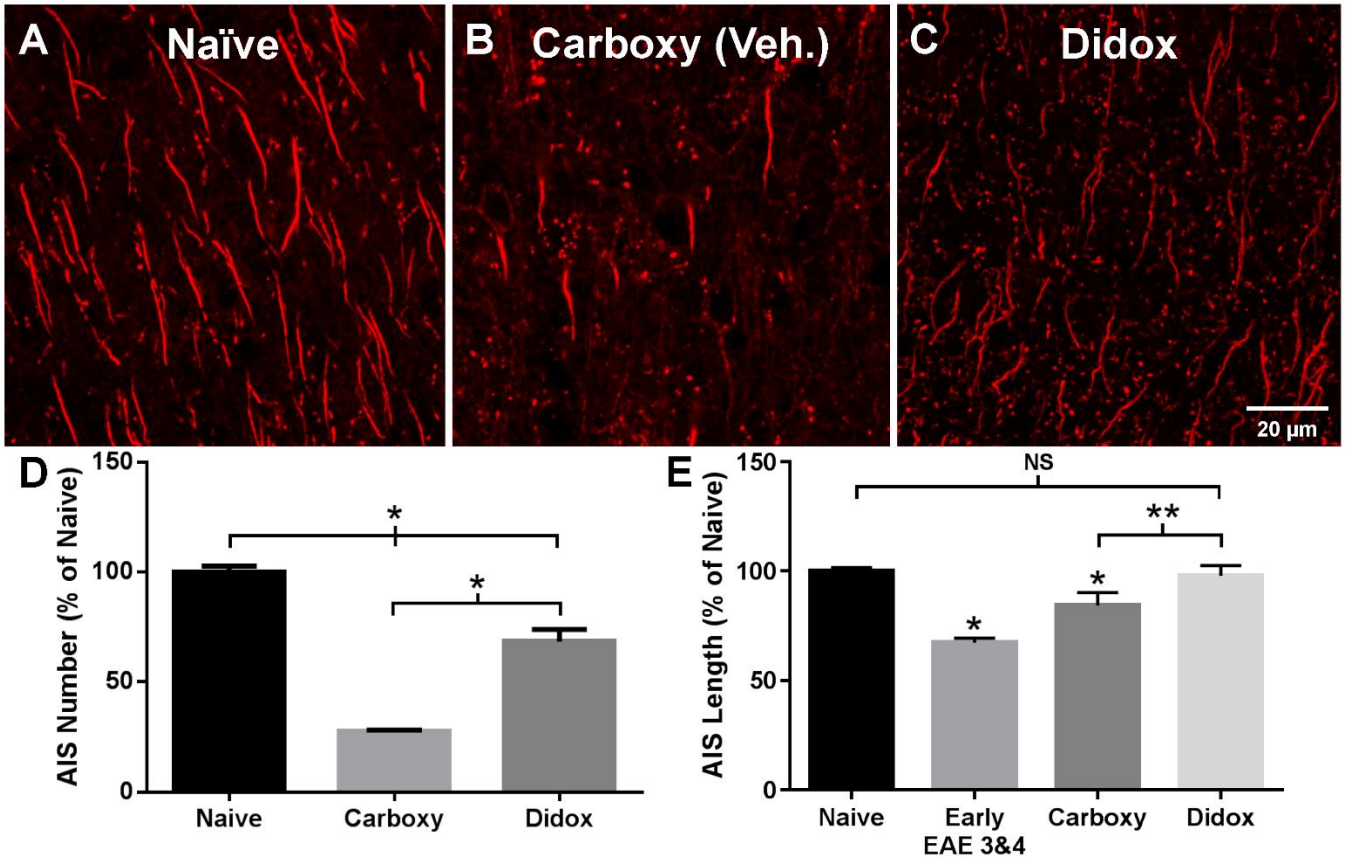
A
Naïve
B
Carboxy (Veh.)
C
Didox
20 µm
D
AIS Number (% of Naive)
150
100
50
0
*
*
Naive
Carboxy
Didox
E
AIS Length (% of Naive)
150
100
50
0
NS
**
*
*
Naive
Early EAE 3&4
Carboxy
Didox

Figure 2.10 Didox treatment attenuates AIS disruption. Naïve mice exhibited numerous AISs (A). Initiating didox treatment at the Early stage of disease in EAE 3&4 mice resulted in inhibition of AIS loss (C,D). In contrast to the didox treated mice, animals maintained on the vehicle, carboxymethylcellulose, displayed continued AIS degeneration (B,D,E). In addition to AIS preservation, Early EAE 3&4 mice treated with didox revealed a reversal of AIS shortening by the Late EAE stage. These are the first data to indicate a therapeutic reversal of AIS pathology.

Table 2.2: AIS Number and Length from EAE-Induced and Naïve Mice

Animal Group	Early inflammation (EAE) (3 Days post peak)				Late inflammation (EAE) (9 Days post peak)			
	AIS Number (% Naive ± SEM)	AIS Length (% Naive ± SEM)	AIS Length (Avg. ± SEM; μm)	*n*	AIS Number (% Naïve ± SEM)	AIS Length (% Naive ± SEM)	AIS Length (Avg. ± SEM; μm)	*n*
Naïve	100.0 ± 2.7	100.0 ± 1.7	19.9 ± 0.3	7	100.0 ± 2.7	100.0 ± 1.7	19.9 ± 0.3	7
EAE 1&2	98.8 ± 3.1	85.2 ± 7.8	17.0 ± 1.6	4	40.9* ± 1.9	60.3* ± 1.5	12.0 ± 0.3	3
EAE 3&4	107.6 ± 1.2	67.3* ± 2.1	13.4* ± 0.4	4	28.5* ± 0.7	80.5* ± 3.2	16.0* ± 0.6	7
Carboxy Veh.	-	-	-	-	27.7* ± 0.5	84.3* ± 5.9	16.8* ± 1.2	4
Didox	-	-	-	-	68.4** ± 5.5	98.0*** ± 4.6	19.5*** ± 0.9	4

Single asterisks indicate a significant difference from the Naïve mice (*$P = 0.03$). Double asterisks indicate significantly more AISs than the vehicle control (Carboxy Veh.) but significantly less than the Naïve mice (**$P = 0.0001$). Triple asterisks indicate a significant difference compared to the vehicle-treated mice but not the Naïve mice (***$P = 0.02$).

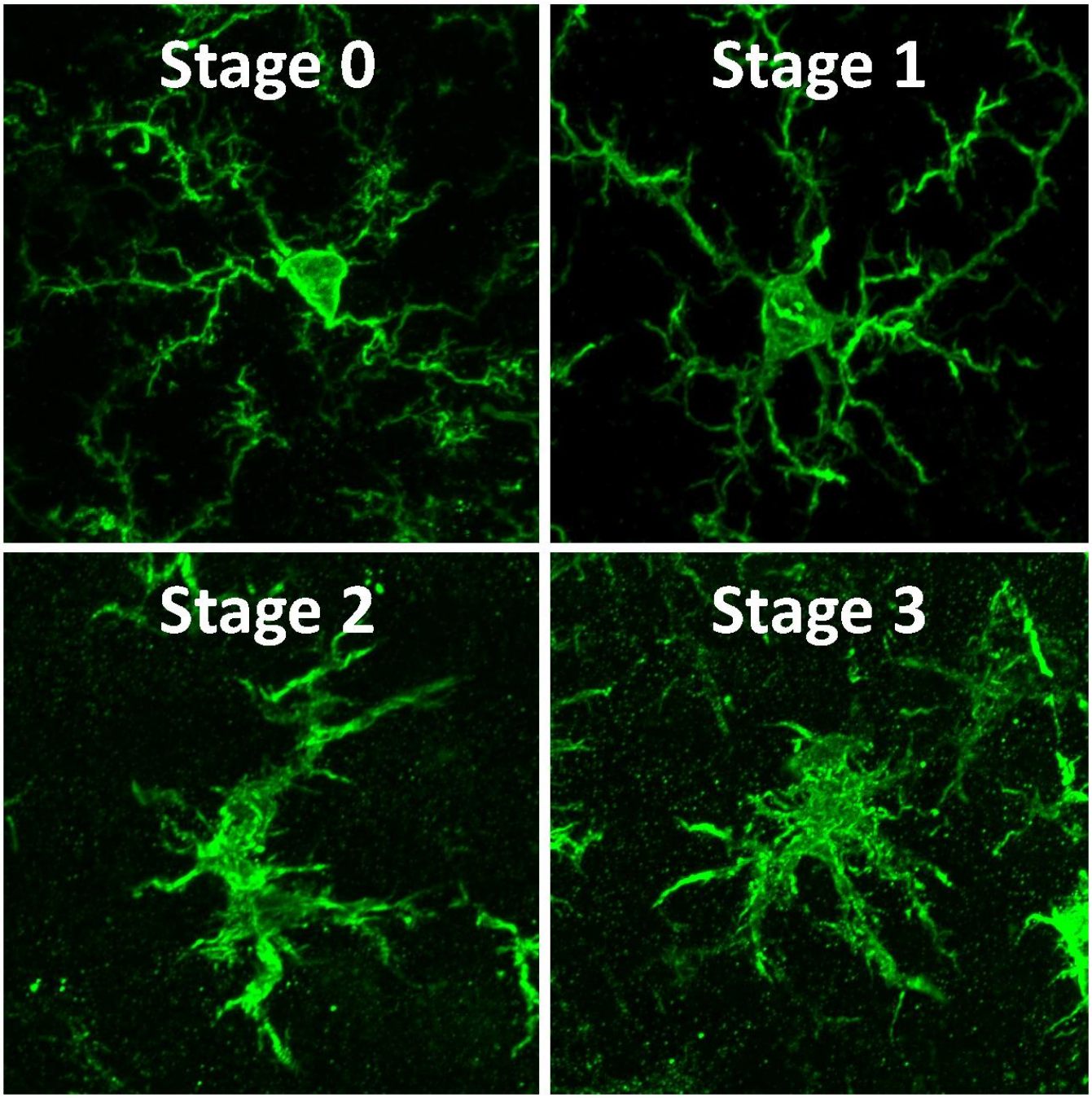
Stage 0
Stage 1
Stage 2
Stage 3

Figure S2.1. Microglia present distinct morphologies consistent with state of reactivity. Microglia present unique morphology representing specific stages of reactivity as visualized through IBA-1 immunolabeling (B). Surveying microglia are scored as a Stage 0. Increasing cell body size, shorter and thicker processes and fewer processes are indicative of higher stage scores and are equated to cells with a higher level of reactivity.

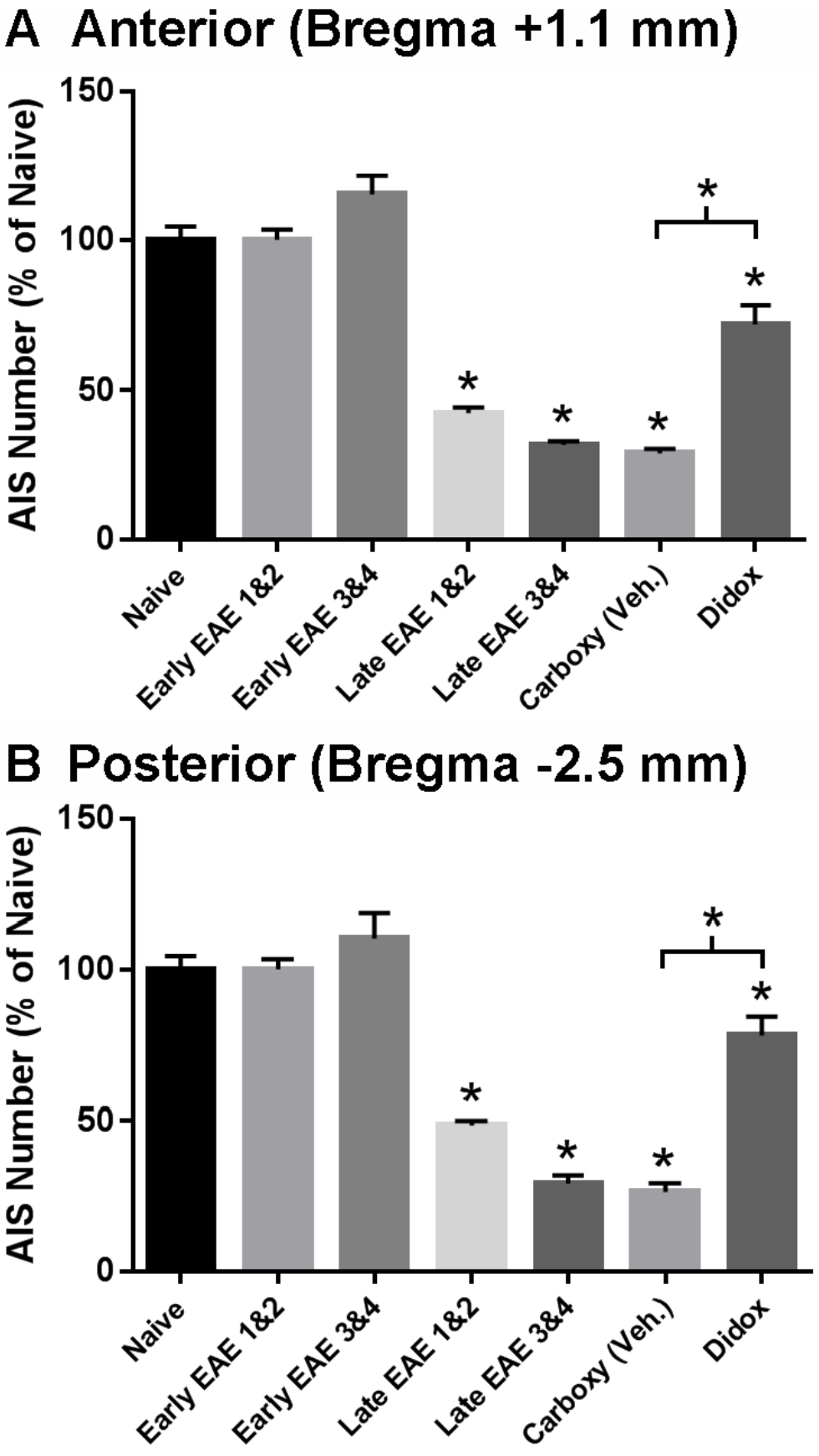
A Anterior (Bregma +1.1 mm)
AIS Number (% of Naive)
150
100
50
0
*
*
*
*
*
Naive
Early EAE 1&2
Early EAE 3&4
Late EAE 1&2
Late EAE 3&4
Carboxy (Veh.)
Didox
B Posterior (Bregma -2.5 mm)
AIS Number (% of Naive)
150
100
50
0
*
*
*
*
*
Naive
Early EAE 1&2
Early EAE 3&4
Late EAE 1&2
Late EAE 3&4
Carboxy (Veh.)
Didox

Figure S2.2. AISs are consistently disrupted throughout the anterior/posterior axis following EAE induction. Comparison of the number of AISs among all treatment groups at each position along the anterior/posterior axis revealed no difference in AIS susceptibility to disruption. Although all 6 locations were separately compared, only the results of those quantitative comparisons for the most anterior (bregma +1.1 mm) and posterior (bregma -2.5 mm) positions are shown. Note the findings for each distinct anterior/posterior location precisely mirror the compiled data (Figure 2.3).

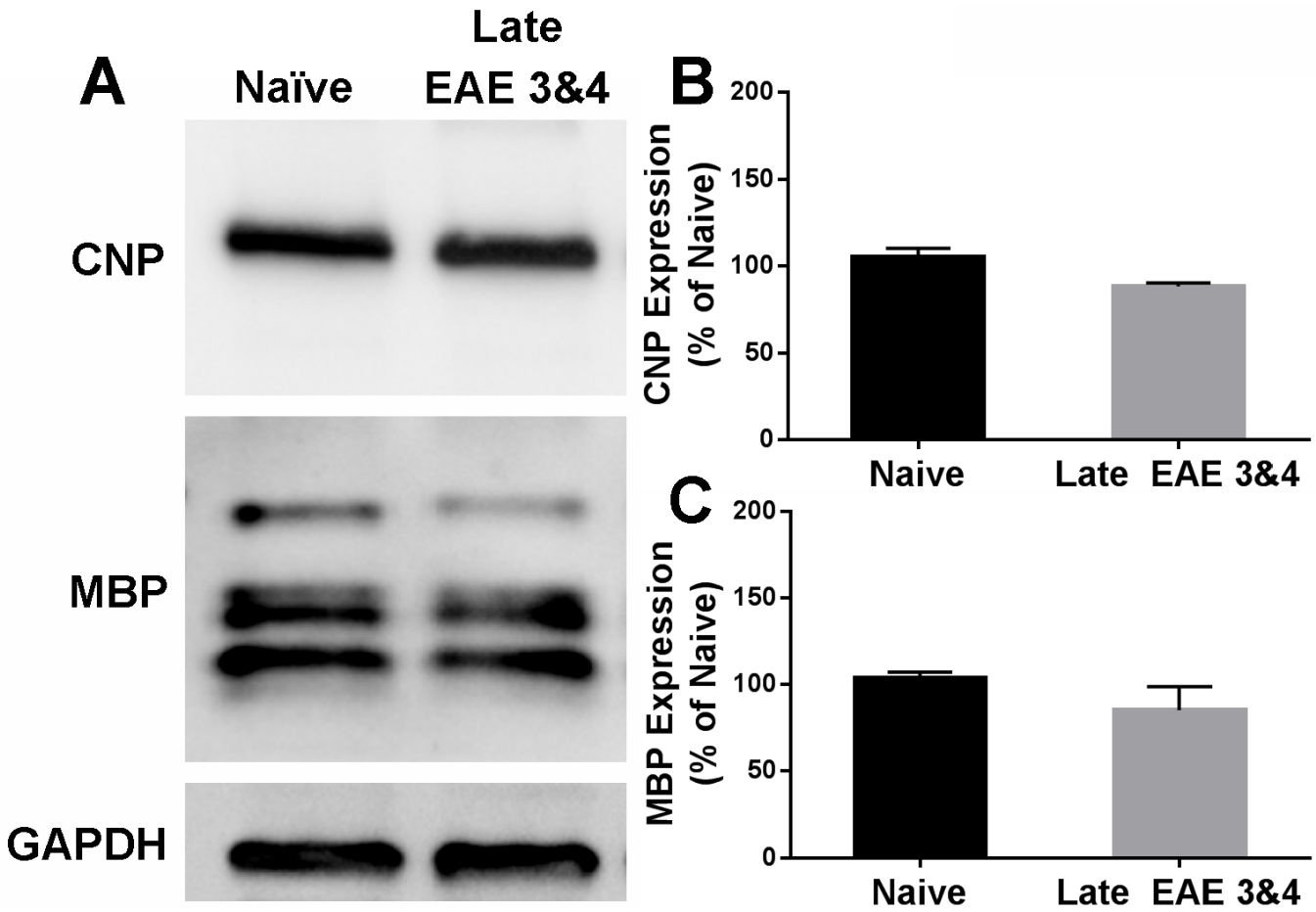
A
Naïve
Late
EAE 3&4
CNP
MBP
GAPDH
B
CNP Expression
(% of Naive)
200
150
100
50
0
Naive
Late EAE 3&4
C
MBP Expression
(% of Naive)
200
150
100
50
0
Naive
Late EAE 3&4

Figure S2.3 Western blot analysis revealed no cortical demyelination in EAE mice. Western blot analyses of isolated cortices from Naïve and Late EAE 3&4 mice revealed no difference in the levels of the myelin proteins CNP (A) and MBP (C). Quantitative densitometry confirmed the absence of myelin protein loss.

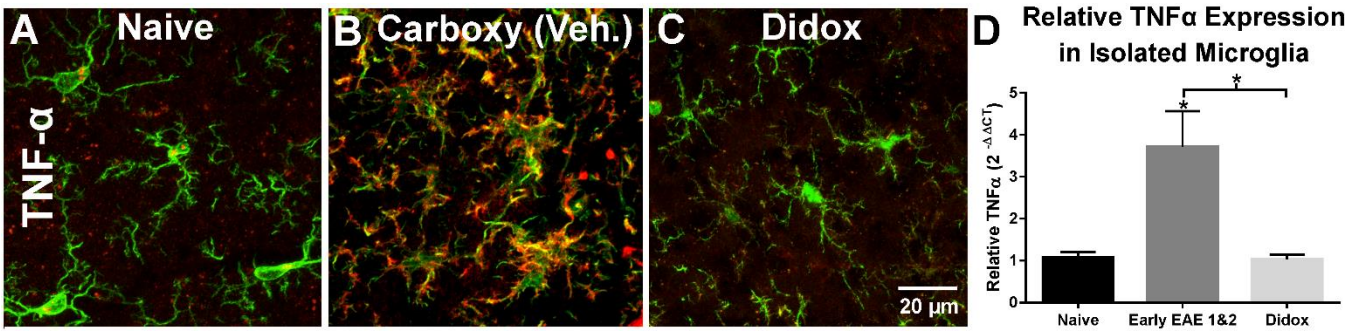
A
Naive
TNF-α
B Carboxy (Veh.)
C
Didox
20 µm
D
Relative TNFα Expression
in Isolated Microglia
Relative TNFα (2 -ΔΔCT)
0
1
2
3
4
5
*
*
Naive
Early EAE 1&2
Didox

Figure S2.4 Didox treatment attenuates TNFα expression in EAE induced mice. Immunolabeling (A-C) and RNA expression (D) for TNFα indicated low levels of cytokine expression in the Naïve and EAE induced mice treated with didox while EAE induced mice that received only the vehicle carboxymethylcellulose maintained high levels of both the protein and RNA.

CHAPTER THREE

OXIDATIVE STRESS INDUCES DISRUPTION OF THE AXON INITIAL SEGMENT

Clark et al., *ASN Neuro* (In Revision)

3.1 Abstract

The axon initial segment (AIS), the domain responsible for action potential initiation and maintenance of neuronal polarity, is targeted for disruption in a variety of central nervous system (CNS) pathological insults. Previous work in our laboratory implicates oxidative stress as a potential mediator of structural AIS alterations in two separate mouse models of CNS inflammation, as these effects were attenuated following reactive oxygen species scavenging and NADPH oxidase 2 ablation. While these studies suggest a role for oxidative stress in modulation of the AIS, the direct effects of reactive oxygen and nitrogen species (ROS/RNS) on the stability of this domain remain unclear. Here we demonstrate that oxidative stress, as induced through treatment with 3-morpholinosydnonimine (SIN-1), a spontaneous ROS/RNS generator, drives a reversible loss of AIS protein clustering in primary cortical neurons *in vitro*. Pharmacological inhibition of both voltage dependent and intracellular calcium (Ca^{2+}) channels suggests that this mechanism of AIS disruption involves Ca^{2+} entry specifically through L-type voltage dependent Ca^{2+} channels and its release from IP_3-gated intracellular stores. Furthermore, ROS/RNS-induced AIS disruption is dependent upon activation of calpain, a Ca^{2+}-activated protease previously shown to drive AIS modulation. Overall, we

demonstrate for the first time that oxidative stress, as induced through exogenously applied ROS/RNS, is capable of driving structural alterations in the AIS complex.

3.2 Introduction

The axon initial segment (AIS) is a specialized region of the axon located at the junction between the somatodendritic and distal axonal domains that is essential for both action potential generation, and the maintenance of neuronal polarity (Hedstrom et al., 2008; Buffington and Rasband, 2011). This complex consists of cytoskeletal scaffolding proteins ankyrin-G (AnkG) and βIV-spectrin, which cluster the high density of voltage-gated ion channels required for action potential initiation and modulation (Jenkins and Bennett, 2001). The AIS is a highly dynamic and plastic structure regulated by changes in neuronal activity (Yamada and Kuba, 2016), but its integrity is compromised consequential of a variety of pathological central nervous system (CNS) insults. These include models of epilepsy (Wimmer et al., 2010; Harty et al., 2013), ischemic injury (Schafer et al., 2009; Hinman et al., 2013), traumatic brain injury (Baalman et al., 2013; Greer et al., 2013; Vascak et al., 2017), Alzheimer's disease (León-Espinosa et al., 2012; Sun et al., 2014; Marin et al., 2016; Zempel et al., 2017), and multiple sclerosis (Hamada and Kole, 2015; Clark et al., 2016). While the AIS is frequently and extensively targeted for disruption in CNS pathology, the mechanisms underlying altered stability of this domain have not been fully elucidated.

Our laboratory has previously demonstrated that AIS integrity is targeted for disruption in inflammatory environments. For example, induction of experimental autoimmune

encephalomyelitis (EAE), a model commonly used to mimic the inflammatory component of MS (Kipp et al., 2017), resulted in severe disruption of the AIS domain, which was preceded by and correlated with microglial reactivity and increased contact (Clark et al., 2016). Similarly, peripheral injection of lipopolysaccharide (LPS), a classic model of systemic inflammation, was sufficient to drive the loss of AIS protein clustering, which was reversed following resolution of the inflammatory response (Benusa et al., 2017). In both of these inflammatory models, treatment with Didox, a novel scavenger of reactive oxygen and nitrogen species (ROS/RNS) (Mayhew et al., 2002; Turchan et al., 2003; Matsebatlela et al., 2015), prevented and reversed the AIS pathology (Clark et al., 2016; Benusa et al., 2017). Additionally, LPS injection in mice deficient in the major ROS producing enzyme NADPH oxidase 2 (Pollock et al., 1995) resulted in the complete preservation of the AIS (Benusa et al., 2017). Together, these data highlight a potential role for ROS and RNS in the alteration of AIS protein clustering; however, direct evidence that ROS/RNS are capable of driving AIS disruption is lacking. Here, to address this void in our understanding, we investigate the effect of exogenously applied ROS/RNS on AIS stability in primary cortical neurons *in vitro*, utilizing the spontaneous ROS/RNS generator SIN-1 (Singh et al., 1999).

Our findings demonstrate that oxidative stress, induced through exogenous application of ROS/RNS, is sufficient to drive structural disruption of the AIS protein complex. Pharmacological inhibition of voltage-dependent calcium channels (VDCCs), intracellular calcium (Ca^{2+}) stores, and enzymatic activity suggests this mechanism of ROS/RNS-induced AIS disruption to involve cytosolic Ca^{2+} entry extracellularly through

L-type VDCCs, and intracellularly from IP_3-gated store release, as well as calpain protease activation.

3.3 Materials and Methods

Animals

Timed pregnant embryonic day 14 (E14) c57bl/6 mice were purchased from Charles River (Wilmington, MA) and maintained in the Virginia Commonwealth University Division of Animal Resources (VCU DAR) or the McGuire Veterans Affairs Medical Center (VAMC) vivariums, respectively, which are both AAALAC accredited facilities. Timed pregnant mice were maintained in the facilities until pups were removed on embryonic day 15. Animals were maintained on an alternating 12 hour light and dark cycle and food and water were provided ad libitum. All procedures were conducted in accordance with the methods outlined in approved VCU and McGuire VAMC IACUC protocols.

Primary Neuronal Cultures

Primary cortical neuron cultures were prepared from cerebral cortices of E15 mouse pups. Timed pregnant females were anesthetized with isoflurane and sacrificed by decapitation. Pups were removed and decapitated to allow for removal of the brains. Following removal of the meninges, cortices were incubated on ice in Accutase® Cell Detachment Solution (Innovative Cell Technologies, San Diego, CA) and dissociated step-wise using 1000 µL and 200 µL-sized pipette tips. Cells were counted and diluted in

plating medium consisting of Neurobasal® medium (Thermo Fisher Scientific, Waltham, MA; Formulation detailed in Supplementary Table S3.1) supplemented with glutamate (25 µM, Sigma-Aldrich, St. Louis, MO), glutamine (0.5 mM, Thermo Fisher Scientific, Waltham, MA), Antibiotic-Antimycotic (Thermo Fisher Scientific, Waltham, MA), and B-27® supplement (Thermo Fisher Scientific, Waltham, MA). Cells were then plated at a density of 3000 cells/cm^2 on poly-d-lysine (1 mg/mL; Sigma-Aldrich, St. Louis, MO) coated glass coverslips (12 mm) in 24-well plates. Following cell attachment, wells were filled with the medium described above, in which the B-27® supplement was replaced with B-27® supplement minus antioxidants (Thermo Fisher Scientific, Waltham, MA). All experiments were performed starting at 12 days *in vitro* (DIV).

SIN-1 and Pharmacological Treatments

12 DIV neurons were treated with spontaneous ROS/RNS generator SIN-1 (3-Morpholinosydnonimine hydrochloride, Sigma-Aldrich, St. Louis, MO) diluted in the maintenance media described above at concentrations ranging from 0.1-100 µM and analyzed 3, 6, 12, 24, or 72 hours post-treatment. All pharmacological reagents were added simultaneously with SIN-1 and included EGTA (0.001-2 mM), $NiCl_2$ (0.1-50 µM), (S)-(−)-Bay K8644 (0.00001-50 µM), MK-801 (0.001-50 µM), 2-APB (0.1-50 µM) and FK-506 (0.001-50 µM) obtained from Sigma-Aldrich (St. Louis, MO) as well as ω-Conotoxin MVIIC (0.001-50 µM), nifedipine (0.001-50 µM), ryanodine (0.001-50 µM) and MDL 28170 (0.001-50 µM) obtained from Tocris Bioscience (Avonmouth, Bristol, England). Stock dilutions of all pharmacological reagents were prepared in DMSO (Thermo Fisher Scientific, Waltham, MA) with subsequent dilutions performed in culture medium, except

for EGTA, $NiCl_2$ and ω-Conotoxin MVIIC in which all dilutions were performed in culture medium. While a larger concentration range of pharmacological inhibitors and activators was tested, only non-cytotoxic concentrations are reported. All SIN-1 and pharmacological treatments were performed in three separate cell culture preparations (n=3). Within each preparation, three technical replicates at the 24 hour time point were performed.

Measurement of Calpain Activity

Calpain activity was quantified using a fluorometric assay kit (Biovision, Milpitas, CA) according to the manufacturer's instructions. Briefly, neurons were treated with the extraction buffer provided by the manufacturer to extract cytosolic proteins while preventing the auto-activation of calpain during the extraction procedure. The neuronal supernatant was then incubated with a calpain substrate (Ac-LLY-AFC) which fluoresces at 505 nm upon cleavage. Fluorescence intensities at each SIN-1 concentration were measured on a spectrophotometric microplate reader and compared against an untreated sample at each time point. Six coverslips of neurons were pooled at each time point and SIN-1 concentration. Data from these measurements are presented as relative fluorescence units (RFU) as a percent increase over untreated samples. A total of three separate culture preparations (n=3), each run in three technical replicates, were compared at each measurement. Statistical comparisons were made by repeated measures one-way ANOVA with a Dunnett’s multiple comparisons post-hoc test. All graphing and statistical analyses were performed using GraphPad Prism version 6.03 for Windows (GraphPad Software, San Diego, CA).

Immunofluorescence

Cells were immunolabeled with the appropriate primary and secondary antibodies (see below) as described previously (Shepherd et al., 2012; Clark et al., 2016; Benusa et al., 2017) with the modification that cells were fixed with 4% paraformaldehyde (Ted Pella, Redding, CA) for 5 minutes and permeabilized with -20^{o}C methanol (Fisher Scientific, Waltham, MA). Slides were mounted with Vectashield™ mounting medium with DAPI (Vector Laboratories, Burlingame, CA); and imaged using confocal microscopy.

Antibodies

Axon initial segments were visualized using mouse monoclonal antibodies directed against ankyrin-G (AnkG) (NeuroMab, Davis, CA; N106/36, 1:200) or βIV-spectrin (a generous gift from Dr. Matthew Rasband, Baylor College of Medicine; 1:500). Neurons were identified using an antibody directed against NeuN (Millipore; Billerica, MA; 1:1000). All secondary antibodies for immunofluorescence were purchased from Invitrogen Life Technologies (Grand Island, NY; Alexa^{TM} Fluor) and used at a dilution of 1:500.

Confocal Microscopy/Quantitation

Image Collection

All images were collected using a Zeiss LSM 710 confocal laser scanning microscope (Carl Zeiss Microscopy, LLC, Thornwood, NY) housed in the VCU Department of Anatomy and Neurobiology Microscopy Facility. Confocal z-stacks, each spanning an

optical distance of 10 μm, using a pin hole of 1 Airy disc unit and Nyquist sampling were collected from three technical replicate coverslips (12 mm) per treatment and time point resulting in 12 images per experimental group for AIS quantitation (~ 600 neurons per treatment group). All comparisons were made using three independent culture preparations (n=3). Images were taken with a 20X objective with a numerical aperture of 1.4; optical slice thickness was 0.49 µm, using a scan average of 2. X, Y and Z image dimensions were 212.43 µm x 212.43 µm x 10.00 µm, respectively. The gain and offset values were kept constant for all images.

AIS Quantitation

AIS stability was determined using ImageJ analysis software by manually counting initial segments from maximum intensity projection images resulting in the analysis of >600 AISs per experimental treatment and time point. The number of neurons in a FOV was also determined in the same images used for AIS analysis by counting NeuN-positive cells. Data are presented as the percent of NeuN-positive cells with an associated AIS as a percent of the control. One-way ANOVAs with Tukey's Honest Significant Difference (HSD) post hoc tests were performed for these comparisons. All graphing and statistical analyses were performed using GraphPad Prism version 6.03 for Windows (GraphPad Software, San Diego, CA).

Cell Viability Quantitation

The extent of neuronal survival following SIN-1 treatment was determined using a propidium iodide (PI) exclusion assay to identify non-viable cells. Prior to paraformaldehyde fixation, cells were treated with a 0.01 mg/mL propidium iodide (Molecular Probes, Eugene, OR) solution for 10 minutes. Cells were then fixed and immunolabeled for NeuN as described above. The number of PI-positive and NeuN-positive cells was manually counted from maximum intensity projection images using ImageJ analysis software. Data are presented as the percent of NeuN-positive cells negative for PI as a percent of the control (% neuronal survival). One-way ANOVAs with Tukey's Honest Significant Difference (HSD) post hoc tests were performed for these comparisons. All graphing and statistical analyses were performed using GraphPad Prism version 6.03 for Windows (GraphPad Software, San Diego, CA).

Measurement of ROS Production

Quantification of neuronal ROS production induced by SIN-1 treatment was performed using the CellROX® Green Reagent kit (Thermo Fisher Scientific, Walthanm, MA) according to the manufacturer's instructions. Briefly, 12 DIV primary cortical neurons grown on coverslips were treated with SIN-1 at concentrations ranging from 0.1-100 μM and analyzed 3, 6, 12, 24, or 72 hours post treatment. Cells were incubated for 30 minutes at 37ºC with CellROX® Reagent at a concentration of 5 μM. Coverslips were rinsed with PBS and mounted on slides with Vectashield™ hard set mounting medium with DAPI (Vector Laboratories, Burlingame, CA); and imaged using confocal microscopy as described above. The CellROX® green fluorescence intensity was measured from maximum intensity projection images using ImageJ analysis software. Data from these

measurements are presented as the percent fluorescence increase over the untreated at each SIN-1 treatment concentration and time point. Data from these measurements are presented as relative fluorescence units (RFU) as a percent increase over untreated samples. A total of three separate culture preparations (n=3) were compared at each measurement. Statistical comparisons were made by repeated measures one-way ANOVA with a Dunnett's multiple comparisons post-hoc test. All graphing and statistical analyses were performed using GraphPad Prism version 6.03 for Windows (GraphPad Software, San Diego, CA).

3.4 Results

ROS/RNS generator, SIN-1, induces primary neuronal oxidative stress *in vitro*

In order to directly test the effect of ROS/RNS on AIS stability, we treated primary cortical neurons *in vitro* with the NO and superoxide donor SIN-1 (Singh et al., 1999; Trackey et al., 2001; Rocchitta et al., 2005; Zhaowei et al., 2014). Optimal SIN-1 treatment conditions were first determined using a combination of cell death analysis, and a ROS production assay to identify SIN-1 concentrations that generated ROS/RNS without inducing cortical neuron death. Our first step was to administer the SIN-1 reagent, ranging in concentrations from 0.1 µM to 100 µM consistent with previous studies (Trackey et al., 2001; Rocchitta et al., 2005; Zhaowei et al., 2014), to determine the maximum SIN-1 concentration that could be tolerated by the cultured cells. Neuronal survival was assessed by the propidium iodide exclusion assay 24 hours post-treatment, a time point consistent with previous SIN-1 cytotoxicity studies (Trackey et al., 2001). As shown in

Figure 3.1 A-F and M, significant cell death was observed at the highest concentrations (50 µM and 100 µM) while no cell loss occurred at the concentrations of 25 µM and below. Specifically, the percent of NeuN positive cells that were also propidium iodide negative (defined as % neuronal survival) 24 hours after the addition of SIN-1 was 90.7% ± 6.6% (0.1 µM), 84.0% ± 5.9% (1 µM), 91.6% ± 4.9% (10 µM) and 89.0% ± 9.5% (25 µM). Significant neuronal loss, however, was detected at SIN-1 concentrations of both 50 µM (54.4% ± 12.5%, $p=0.0004$; Fig. 3.1M) and 100 µM (4.1% ± 0.42%, $p<0.0001$; Fig. 3.1F, M). Therefore, these findings indicated that 25 µM was an appropriate concentration for SIN-1 treatment to ensure that cell death was not induced.

Our initial studies to identify optimal SIN-1 concentrations were conducted at the 24 hour time point based on previous work (Trackey et al., 2001). However, to better understand the profile of ROS/RNS production in our culture system, we employed the CellROX® Green assay, a fluorogenic cell-permeable probe which fluoresces upon oxidation by ROS (Isaev et al., 2016; Liu et al., 2014), to quantify levels of neuronal ROS over time. No significant increase in neuronal ROS levels was detected 3 (Fig. 3.1H, N) and 6 hours (Fig. 3.1I, N) post SIN-1 treatment, at a concentration of 25 µM (the highest non-cytotoxic concentration), as compared to the untreated cultures (Fig. 3.1G, N). However, by 12 hours (Fig. 3.1J, N) post SIN-1 addition, ROS levels were significantly increased with the levels highest at 24 hours (Fig. 3.1K, N) post SIN-1 treatment. By 72 hours (Fig. 3.1L, N) post SIN-1 addition, ROS production returned to baseline levels indicating a resolution of the oxidative insult. With an established time course of SIN-1 induced oxidative stress through the CellROX® assay, we next asked whether AIS integrity was compromised as a result of this insult.

Exogenously applied ROS/RNS induce AIS disruption *in vitro*

In order to assess the effects of exogenously applied ROS/RNS on AIS stability, primary cortical neurons were treated with SIN-1 at all of the non-cytotoxic concentrations tested above (0.1-25 µM) and subsequently double immunolabeled for AnkG and NeuN at 3, 6, 12, and 24 hours post-treatment. Data are presented as the percent of neurons (defined as NeuN+ cells) with an associated AIS (defined as AnkG+). Representative images for only the 25 µM SIN-1 treatments are shown for each time point (Fig. 3.2B-F). No significant alteration in AIS integrity was observed at any of the tested SIN-1 concentrations (0.1-25 µM) 3 hours (Fig. 3.2B, G), 6 hours (Fig. 3.2C, H), or 12 hours (Fig. 3.2D, I) post-treatment as compared to the non-treated cultures (Fig. 3.2A). Similarly, at 24 hours (Fig. 3.2J), neither 0.1 µM nor 1 µM of SIN-1 was sufficient to induce disruption of the AIS. However, AIS loss was observed 24 hours after SIN-1 addition at concentrations of 10 µM (Fig. 3.2J; $p=0.034$) and 25 µM (Fig. 3.2E, J; $p=0.003$) with a significant reduction in the percent of neurons with an associated AIS of 29.0% ± 5.2% and 43.2% ± 3.7% respectively. Results from AnkG quantitation were confirmed by immunolabeling for βIV-spectrin, another AIS protein crucial for domain stability (data not shown).

Since the CellROX® assay indicated a return to baseline levels of ROS/RNS by 72 hours, we next analyzed AIS integrity at this late time point to determine whether the ROS/RNS-induced AIS disruption is reversible. Interestingly, recovery was observed 72 hours following SIN-1 treatment at both the 10 µM (Fig. 3.2K) and 25 µM (Fig. 3.2F, K) concentrations. To ensure that the recovery in the percentage of AIS+ cells was not due

to a loss of neurons that lacked positively labeled AISs, the relative number of NeuN+ cells was compared between the treated and non-treated groups. No significant difference was observed between groups (data not shown) indicating that NeuN+ cells that lost their AISs did not die, but recovered from the SIN-1 treatment and restored their AIS. This recovery at 72 hours post-treatment corresponds to a return to baseline of neuronal ROS levels as shown in Figure 3.1L & N. Overall, these data provide a time-course for ROS/RNS-induced AIS disruption in our *in vitro* system, allowing for subsequent pharmacological manipulations to elucidate the underlying mechanism. All further experiments were performed 24 hours following treatment of 25 µM SIN-1, the time point of peak AIS loss, and the highest non-cytotoxic concentration of SIN-1, respectively.

ROS/RNS-induced AIS disruption requires extracellular Ca^{2+}

Calcium (Ca^{2+}) is central to most previously identified mechanisms of AIS modulation, during both activity-dependent plasticity (Yamada and Kuba, 2016), as well as pathological insult (Stoler and Fleidervish, 2016). In order to determine if ROS/RNS-induced AIS disruption involves extracellular Ca^{2+} entry, neurons were pre-treated with the non-membrane permeable Ca^{2+}-chelating agent EGTA, prior to SIN-1 addition. EGTA pre-treatment at concentrations of 0.001 mM and 0.01 mM were not sufficient to prevent the AIS disruption previously observed (Fig. 3.3D), and SIN-1 treated cells exposed to these concentrations were indistinguishable from those without EGTA (Fig. 3.3B, D). EGTA concentrations of 1 mM (Fig. 3.3D) and 2 mM (Fig. 3.3C, D), however, were capable of attenuating the AIS disruption, resulting in the preservation of 81.9% ± 0.8%

(p=0.0004) and 94.9% ± 0.7% (p<0.0001) of neurons with an associated AIS, respectively, as compared to the 62.3% ± 1.6% percent observed with SIN-1 treatment alone. Similar to other previously established models of AIS plasticity and injury (Schafer et al., 2009; Stoler and Fleidervish, 2016; Yamada and Kuba, 2016), these data demonstrate that extracellular Ca^{2+} is central to AIS disruption; however, we implicate ROS/RNS as upstream activators of this degenerative pathway.

L-type voltage-dependent calcium channels are required for ROS/RNS-induced AIS disruption

While the importance of extracellular Ca^{2+} entry was demonstrated with EGTA, the site of Ca^{2+} entry into the cell during ROS/RNS-induced AIS modulation remains unclear. To address this, we pre-treated neurons with a series of inhibitors to the known types of voltage-dependent calcium channels prior to SIN-1 treatment (Catterall, 2011). Inhibition of T and R-type VDCCs by $NiCl_2$ (Evans et al., 2013; Bhattacharjee et al., 1997) revealed no significant attenuation of SIN-1 induced AIS disruption at the range of concentrations tested (0.1-50 µM; Fig. 3.4C, G). Similarly, no AIS protection was observed following application of the P, Q and N-type VDCC inhibitor ω-Conotoxin MVIIC (0.0001-1 µM; Fig. 3.4D, H). Concentrations of these inhibitors higher than those presented resulted in significant neuronal death (data not shown). Additionally, specific inhibition of L-type VDCCs with nifedipine (Nguemo et al., 2013) at concentrations of 0.001-0.1 µM was not sufficient to protect AIS integrity. However, attenuation of SIN-1 induced AIS disruption was observed following pre-treatment with the L-type specific VDCC inhibitor at concentrations of 1 µM and 10 µM (Fig. 3.4E, I) resulting in the preservation of 88.3% ±

3.66% (p=0.0147) and 92.1% ± 4.3% (p=0.0055) of AISs respectively, as compared to the 60.2% ± 3.9% percent observed with SIN-1 treatment alone.

We then asked whether Ca^{2+} flow through L-type VDCCs in the absence of SIN-1 was sufficient to drive disruption of the AIS. To address this, a selective irreversible activator of L-type channels, (S)-(-)-Bay K 8644 (Ravens and Schöpper, 1990; Fusi et al., 2017), was used at concentrations ranging from 0.00001–1 µM with AIS assessment performed 24 hours post-treatment. This treatment resulted in a significant reduction in the percent of neurons with an associated AIS at concentrations of 0.1 µM and 1 µM by 22.6% ± 3.9% (p=0.0002) and 32.5% ± 3.9% (p<0.0001) respectively (Fig. 3.4F, J). Importantly, these concentrations of (S)-(-)-Bay K 8644 did not result in neuronal death as determined by the propidium iodide exclusion assay described above (data not shown). Overall, these data suggest that ROS/RNS-mediated disruption of the AIS involves extracellular Ca^{2+} flow specifically through L-type VDCCs, and that activation of these channels, independently of SIN-1, is sufficient to drive similar AIS alterations.

ROS/RNS-mediated AIS modulation involves IP_3-gated Ca^{2+} stores

Because AIS stability is heavily dependent on the level of intracellular of Ca^{2+} (Stoler and Fleidervish, 2016; Yamada and Kuba, 2016) and on the function of VDCCs for ROS/RNS-mediated AIS disruption, we next asked if release from intracellular stores is involved in this SIN-1 induced insult. Prior to SIN-1 addition, neurons were pre-treated with inhibitors to both ryanodine and inositol 1,4,5-trisphosphate (IP_3) receptors, the two major mediators of Ca^{2+} release from intracellular stores (Marks, 1997; Evans et al., 2013). Inhibition of ryanodine receptors with ryanodine at concentrations of 0.001-10 µM

did not result in protection of the AIS from SIN-1 induced disruption (Fig. 3.5C, E). Concentrations greater than 10 µM resulted in significant neuronal death (data not shown). Conversely, pre-treatment with IP_3 receptor inhibitor 2-Aminoethoxydiphenyl borate (2-APB) was capable of significantly preserving AIS integrity in a dose dependent manner at concentrations of 10 µM and 20 µM, resulting in the preservation of 80.4% ± 7.3% (p=0.0290) and 95.1% ± 2.7% (p=0.0002) of neurons with an intact AIS respectively (Fig. 3.5D, F). Interestingly, low concentrations of 2-APB (<10 µM) result in the release of Ca^{2+} from IP_3-gated intracellular stores (DeHaven et al., 2008), a possible explanation for the exacerbated effect of SIN-1 on the AIS at the 0.1 µM concentration (Fig. 3.5F; p=0.0010). Taken together, these data highlight an important role for Ca^{2+} release from IP_3, but not ryanodine-sensitive intracellular stores in ROS/RNS-induced AIS disruption.

Calpain, but not calcineurin activity, is involved in ROS/RNS-induced AIS disruption

While Ca^{2+} from both extracellular and intracellular sources appears to play a critical role in ROS/RNS-mediated AIS disruption, the downstream mediator of this AIS modulation remains unknown. Previously described mechanisms of AIS plasticity and injury have implicated two Ca^{2+}-activated enzymes as critical regulators of AIS stability (Evans et al., 2013; Schafer et al., 2009). These include calcineurin, a Ca^{2+}-activated phosphatase responsible for disassembly of the AIS protein complex in models of activity-dependent plasticity (Evans et al., 2013), as well as calpain, a Ca^{2+}-activated protease whose substrates include critical structural and functional AIS proteins (Schafer et al., 2009). In order to assess the contribution of each potential AIS modulator in ROS/RNS-

induced AIS disruption, pharmacological inhibitors of each were employed prior to SIN-1 addition. Inhibition of calcineurin with FK-506 (Evans et al., 2013) in the presence of SIN-1 was insufficient to prevent AIS disruption at all concentrations tested (0.001-10 μM) (Fig. 3.6C, E). Concentrations greater than 10 μM resulted in significant neuronal death (data not shown).

Treatment with the well-established calpain inhibitor MDL 28170 (Schafer et al., 2009; Donkor, 2015), however, prevented AIS loss in a dose-dependent manner, at concentrations of 1 μM and 10 μM, yielding preservation of 83.3% ± 0.6% ($p<0.0001$) and 96.8% ± 0.8% ($p<0.0001$) of AISs respectively (Fig. 3.6D, F). A fluorescent activity assay was used to determine the time-course of calpain activity, at the time points tested in Figure 3.2, in order to correlate with SIN-1 induced AIS loss and recovery. While elevated calpain activity was observed at 12 hours post SIN-1 treatment (69.4% ± 4.8% increase over untreated; $p=0.0036$; Fig. 3.6G), peak activity was observed at 24 hours (255.5% ± 14.9% increase over untreated; $p<0.0001$; Fig. 3.6G); the time point at which AIS loss is greatest (Fig. 3.2E, J). Interestingly, by 72 hours post SIN-1 treatment, calpain activity returned to baseline levels (34% ± 9.9% increase over untreated; Fig. 3.6G), corresponding to the point at which neuronal ROS levels have returned to baseline (Fig. 3.1L, N) and AIS recovery is achieved (Fig. 3.2F, K). Overall, these data implicate a role for calpain, but not calcineurin, as an effector of AIS disruption downstream of oxidative stress.

3.5 Discussion

Previous work from our lab implicated oxidative stress as a mediator of AIS disruption, since free radical scavenger treatment was sufficient to protect and recover the domain in an inflammatory mouse model of MS (Clark et al., 2016). Additionally, ablation of NOX2, a major source of ROS/RNS production in the CNS, was sufficient to preserve AIS integrity in an LPS model of systemic inflammation (Benusa et al., 2017). While these studies suggested a role for oxidative stress in AIS modulation, the direct effects of reactive oxygen and nitrogen species on AIS stability remained unclear. The present study demonstrates for the first time that oxidative stress, induced through exogenous ROS/RNS application, drives structural alterations of the AIS. Additionally, pharmacological inhibition of both voltage-dependent and intracellular Ca^{2+} channels suggests that Ca^{2+} entry through L-type VDCCs and its release from IP_3-gated stores is involved in ROS/RNS-mediated AIS modulation. Furthermore, this AIS insult is dependent upon calpain, but not calcineurin, activity.

The Role of ROS/RNS in Axonal Pathology

The data presented in this study highlight a role for ROS/RNS in disruption of the AIS protein complex, but other axonal targets of oxidative stress have been described. These include the F-actin cytoskeleton (Hung et al., 2011; Sakai et al., 2012), axonal growth cones (Munnamalai and Suter, 2009; Munnamalai et al., 2014), and microtubule-associated stabilizers and motors (Stroissnigg et al., 2007; Carletti et al., 2011; Redondo et al., 2015). Reactive oxygen and nitrogen species have also been associated with the pathogenesis of many CNS insults including axonal loss in peripheral nerve and spinal cord injury (Kuo et al., 2017; Maggio et al., 2017), hyperphosphorylation of tau in

Alzheimer's disease (Sepulveda-Diaz et al., 2015), loss of cortical connections following ischemia (Rosenzweig and Carmichael, 2013), and demyelination and axonal degeneration in MS (Forte et al., 2007; Qi et al., 2007).

Because oxidative stress is a key contributor to many CNS pathologies (Lewén et al., 2000; Smith et al., 2013; Méndez-Armenta et al., 2014; Islam, 2017), it is likely that this mechanism of ROS/RNS-induced AIS modulation may underlie many models of CNS injury. Our laboratory has recently identified AIS disruption in both an inflammatory model of multiple sclerosis (Clark et al., 2016), as well as a model of systemic inflammation (Benusa et al., 2017), which was prevented and/or reversed upon free-radical scavenger treatment. Additionally, other labs have reported alterations in AIS stability in models of epilepsy (Wimmer et al., 2010; Harty et al., 2013), ischemic injury (Schafer et al., 2009; Hinman et al., 2013), traumatic brain injury (Baalman et al., 2013; Greer et al., 2013; Vascak et al., 2017), and Alzheimer's disease (León-Espinosa et al., 2012; Sun et al., 2014; Marin et al., 2016; Zempel et al., 2017), which have all been shown to be associated with CNS oxidative stress through ROS/RNS dysregulation (Lewén et al., 2000; Smith et al., 2013; Méndez-Armenta et al., 2014; Islam, 2017).

ROS/RNS and Ca^{2+} Entry

Our data suggest that ROS/RNS-mediated AIS disruption involves extracellular Ca^{2+} entry through L-type VDCCs, as well as intracellular release from IP_3-gated stores. While

the mechanistic link between ROS/RNS application and cytosolic Ca^{2+} levels is not well defined in our system, previous studies examining this link may provide insight. Similar to the present study, SIN-1 treatment is known to induce Ca^{2+} entry through L-type channels in CA1 pyramidal neurons, cardiomyocytes, and striatal neurons (Pan et al., 2004; Rocchitta et al., 2005; Zhaowei et al., 2014). Peroxynitrite treatment of cerebral cortical neurons, the cell type used in the present study, also resulted in increased Ca^{2+} entry through L-type VDCCs (Ohkuma et al., 2001). However, the effects of SIN-1 have been shown to vary in other cell types, as treatment resulted in decreased Ca^{2+} flow through L-type VDCCs in cerebellar granule cells and vestibular hair cells (Gutiérrez-Martín et al., 2005; Almanza et al., 2007; Tiago, et al., 2011). While the mechanism of ROS/RNS modulation of L-type VDCCs remains unclear for most cell types described, S-glutathionylation of the L-type VDCCs has been shown to be involved in increased Ca^{2+} flow through these channels in cardiomyocytes (Tang et al., 2011; Johnstone and Hool, 2014). It remains to be determined if this, or other modifications, could underlie SIN-1-induced Ca^{2+} influx through L-type VDCCs in our primary cortical neuron system.

In addition to L-type VDCCs, we demonstrate the involvement of IP_3-gated intracellular Ca^{2+} stores on ROS/RNS-induced AIS disruption. Similar to the present study, previous work has shown SIN-1 and its ROS/RNS products to induce release of Ca^{2+} specifically through IP_3-gated stores in neuroblastoma SH-SY5Y cells and cardiomyocytes (Saeki et al., 2000; De Simoni et al., 2013). It has been reported, however, that SIN-1 derived ROS/RNS can induce intracellular Ca^{2+} release non-specifically in renal epithelial cells and ventral horn spinal cord neurons (Ohashi et al., 2016; Munoz et al., 2017) or specifically through ryanodine-sensitive stores in smooth and skeletal muscle cells (Pan

et al., 2004; Yamada et al., 2015). Given the cell-type specific effects of ROS/RNS on both voltage-dependent and intracellular Ca^{2+} channel function reported in the literature, the mechanistic action of SIN-1 on L-type VDCCs and IP_3-gated intracellular stores in our system remains to be determined.

How does Calpain Modulate the AIS?

In the present study, we have identified ROS/RNS-induced AIS disruption to be dependent upon calpain activation. Similarly, calpain activity is shown to drive AIS alterations in other model systems including ischemic injury (Schafer et al., 2009), glutamate excitotoxicity (Benned-Jensen et al., 2016), and P2X7 purinergic activation (Del Puerto et al., 2015). Schafer et al. (2009) demonstrated that proteolytic degradation of essential AIS proteins, such as ankyrinG, βIV spectrin, and voltage-gated Na^+ channels, was the mechanism underlying calpain-mediated AIS modulation following ischemic injury. Benned-Jensen et al. (2016) and Del Puerto et al. (2015) did not analyze the extent of proteolysis, but speculated that a mechanism similar to that reported by Schafer et al. (2009) was most likely involved in their models of AIS injury. It is likely that calpain-mediated proteolysis of the AIS complex underlies the alterations observed following the ROS/RNS-induced insult presented in this study, as this mechanism is well characterized by Schafer et al. (2009).

In summary, for the first time, we demonstrate that oxidative stress, stimulated directly through exogenously applied ROS/RNS, is capable of reversible structural modulation of the AIS. This mechanism involves activity of L-type VDCCs, as well as intracellular IP_3-

gated stores. Additionally, calpain, but not calcineurin, activity is involved in this ROS/RNS-induced disruption. These findings provide new insights into the mechanisms underlying altered AIS stability in a variety of CNS pathologies.

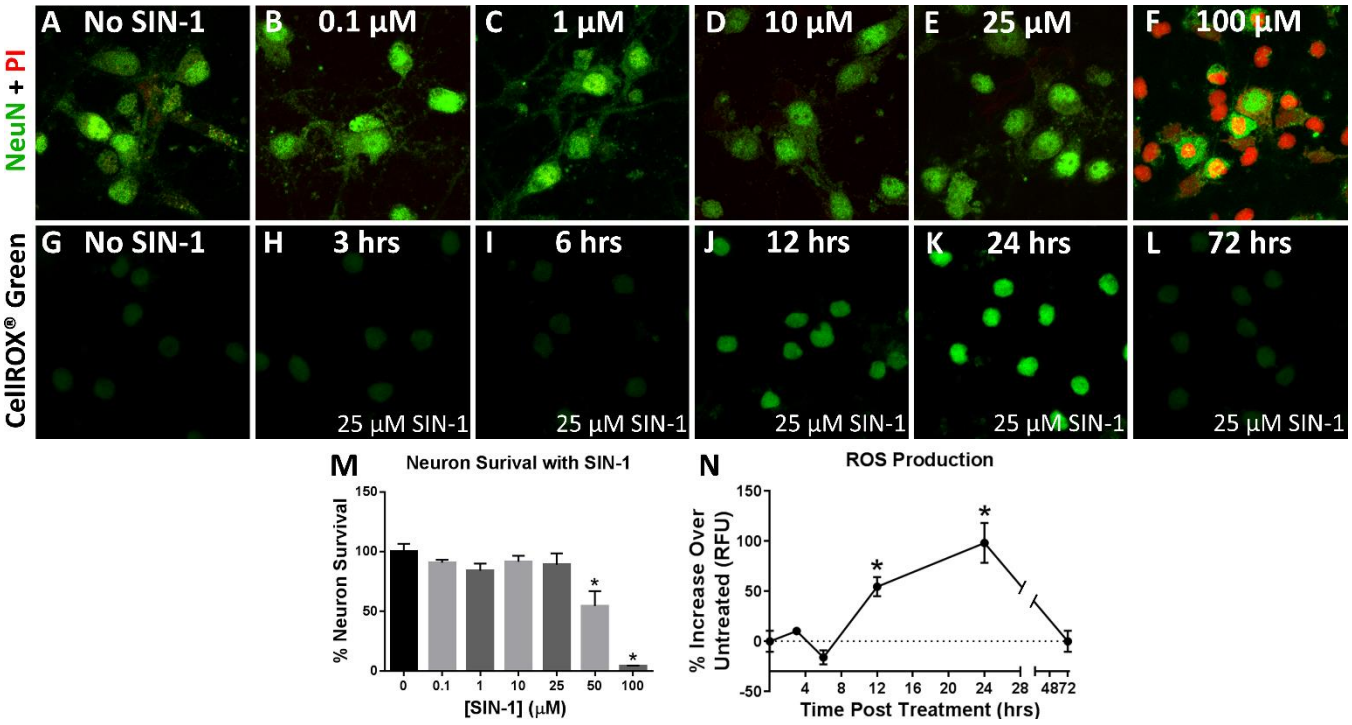
NeuN + PI
A No SIN-1
B 0.1 µM
C 1 µM
D 10 µM
E 25 µM
F 100 µM
CellROX® Green
G No SIN-1
H 3 hrs
I 6 hrs
J 12 hrs
K 24 hrs
L 72 hrs
25 µM SIN-1
M
Neuron Surival with SIN-1
% Neuron Survival
[SIN-1] (µM)
N
ROS Production
% Increase Over Untreated (RFU)
Time Post Treatment (hrs)

Figure 3.1. ROS/RNS generator, SIN-1, induces oxidative stress *in vitro*. Cortical neurons (NeuN+ cells, green) treated with (B-F) and without (A) SIN-1 at increasing concentrations reveal no propidium iodide (PI) staining at concentrations of 25 μM and below (B-E) 24 hours post treatment; however, robust staining was present at concentrations of 50 μM (not shown) and 100 μM (F). Quantitation of percent neuronal survival, determined as the percentage of NeuN+ cells that were also PI- (as a percent of the untreated cells), revealed significant cell death at SIN-1 concentrations of 50 μM and 100 μM (M). The CellROX® Green assay for detection of ROS production by the cortical neurons revealed baseline levels of ROS at ≤6 hours post SIN-1 treatment (G-I, N) with significantly elevated levels at 12 hours (J, N), peak levels at 24 hours (K, N) and a return to baseline by 72 hours (L, N). Asterisks represent a significant difference from the SIN-1 untreated group (*$p < 0.05$).

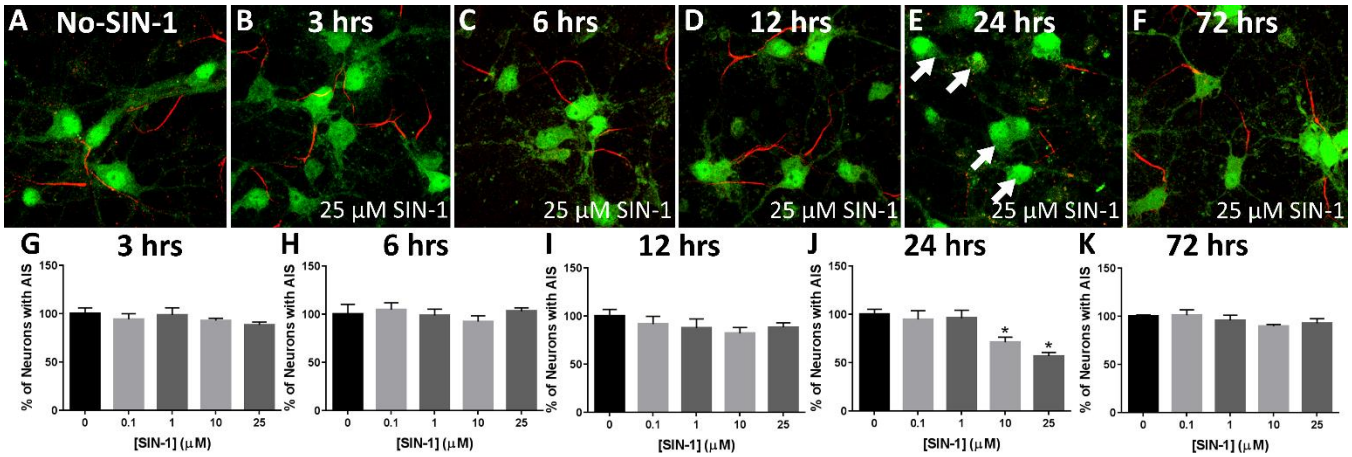
A No-SIN-1
B 3 hrs
25 µM SIN-1
C 6 hrs
25 µM SIN-1
D 12 hrs
25 µM SIN-1
E 24 hrs
25 µM SIN-1
F 72 hrs
25 µM SIN-1
G 3 hrs
H 6 hrs
I 12 hrs
J 24 hrs
K 72 hrs
% of Neurons with AIS
0
50
100
150
0
0.1
1
10
25
[SIN-1] (µM)
*

Figure 3.2. Exogenous ROS/RNS drive disruption of the AIS *in vitro*. Axon initial segments of cultured cortical neurons maintain their integrity with no SIN-1 treatment (A) or 3 (B,G), 6 (C,H), or 12 (D,I) hours following exposure to 25 μM SIN-1, a concentration that did not induce cell death. However, at this same concentration, a significant dose-dependent reduction in the number of cortical neurons (NeuN+, green) that presented ankyrin-G (red) positive AISs was observed 24 hours after SIN-1 exposure (white arrows; E,J). By 72 hours post SIN-1 exposure, AIS integrity was restored (F,K) demonstrating the reversibility of AIS disruption and further indicating that AIS loss was not a consequence of cell death. Asterisks represent a significant difference from the SIN-1 untreated group (*$p < 0.05$).

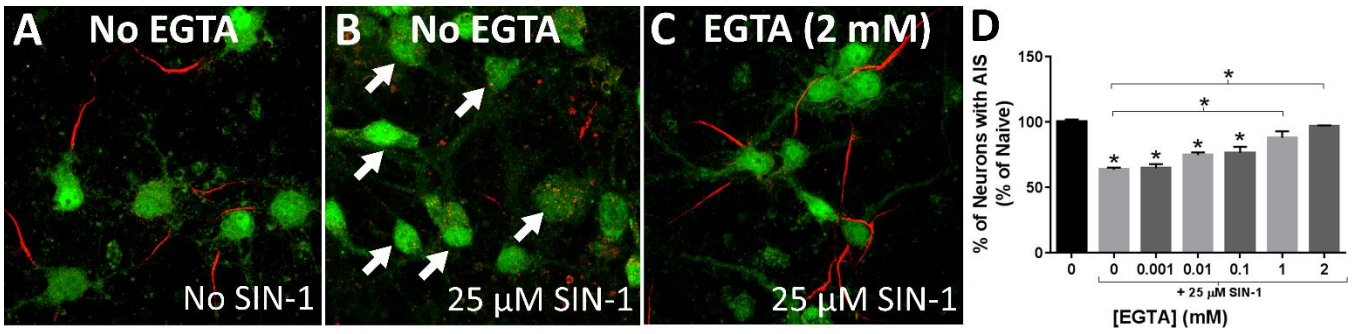
A
No EGTA
No SIN-1
B
No EGTA
25 µM SIN-1
C
EGTA (2 mM)
25 µM SIN-1
D
% of Neurons with AIS
(% of Naive)
150
100
50
0
0
0
0.001
0.01
0.1
1
2
+ 25 µM SIN-1
[EGTA] (mM)

Figure 3.3. ROS/RNS-induced AIS disruption is attenuated following chelation of extracellular Ca^{2+}. The loss of AIS labeling (white arrows) following exposure to 25 μM SIN-1 (B) was inhibited by the addition of EGTA (C) to the medium prior to SIN-1 treatment. The extent of AIS maintenance was directly dependent on the dose of EGTA (D). An asterisk with an associated bracket indicates significant differences between treated groups; asterisks without an associated bracket represent a significant difference from the SIN-1 untreated group (A, $*p < 0.05$). (NeuN, green; AnkG, red)

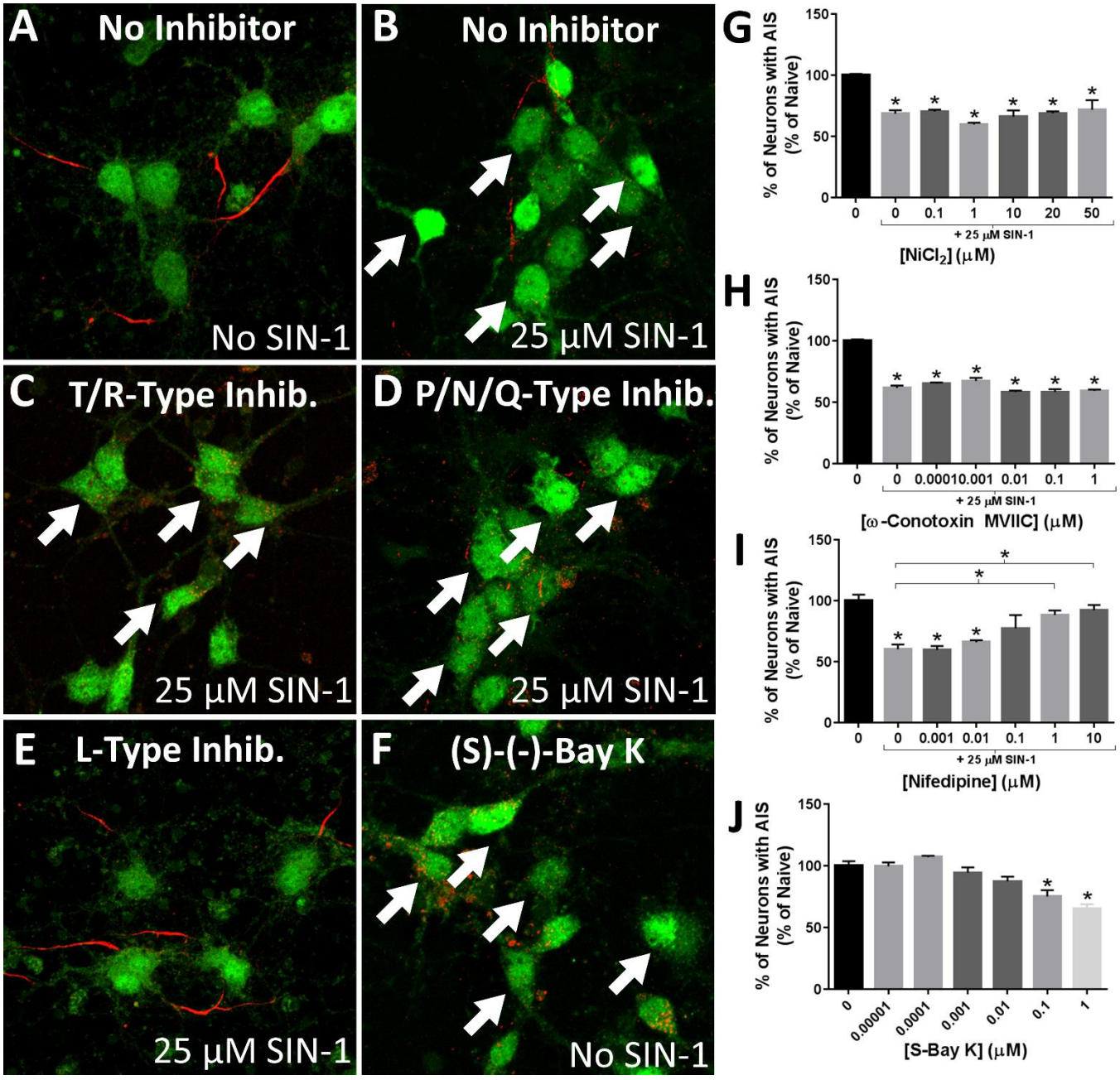
A No Inhibitor
No SIN-1
B No Inhibitor
25 µM SIN-1
C T/R-Type Inhib.
25 µM SIN-1
D P/N/Q-Type Inhib.
25 µM SIN-1
E L-Type Inhib.
25 µM SIN-1
F (S)-(-)-Bay K
No SIN-1
G
% of Neurons with AIS (% of Naive)
150
100
50
0
0 0 0.1 1 10 20 50
+ 25 µM SIN-1
[NiCl2] (µM)
H
% of Neurons with AIS (% of Naive)
150
100
50
0
0 0 0.0001 0.001 0.01 0.1 1
+ 25 µM SIN-1
[ω-Conotoxin MVIIC] (µM)
I
% of Neurons with AIS (% of Naive)
150
100
50
0
0 0 0.001 0.01 0.1 1 10
+ 25 µM SIN-1
[Nifedipine] (µM)
J
% of Neurons with AIS (% of Naive)
150
100
50
0
0 0.00001 0.0001 0.001 0.01 0.1 1
[S-Bay K] (µM)

Figure 3.4. L-type voltage dependent calcium channels are required for ROS/RNS-induced AIS disruption. Similar to SIN-1 treated neurons without inhibitor pre-treatment (B), neurons (NeuN+, green) treated with inhibitors directed against T/R- (C,G) or P/N/Q-type (D,H) calcium channels prior to SIN-1 exposure presented with significant loss (white arrows) in AIS labeling (AnkG, red). In contrast, cultured cortical neurons treated with an L-type calcium channel inhibitor (E,I) resulted in a significant preservation of the AISs. Further demonstrating a role for L-type calcium channels in mediating AIS alterations, cortical neurons treated with (S)-(-)-Bay K 8644 also resulted in a significant disruption of the AISs (F,J). Asterisks without an associated bracket represent a significant difference from the SIN-1 untreated group (A, $*p < 0.05$).

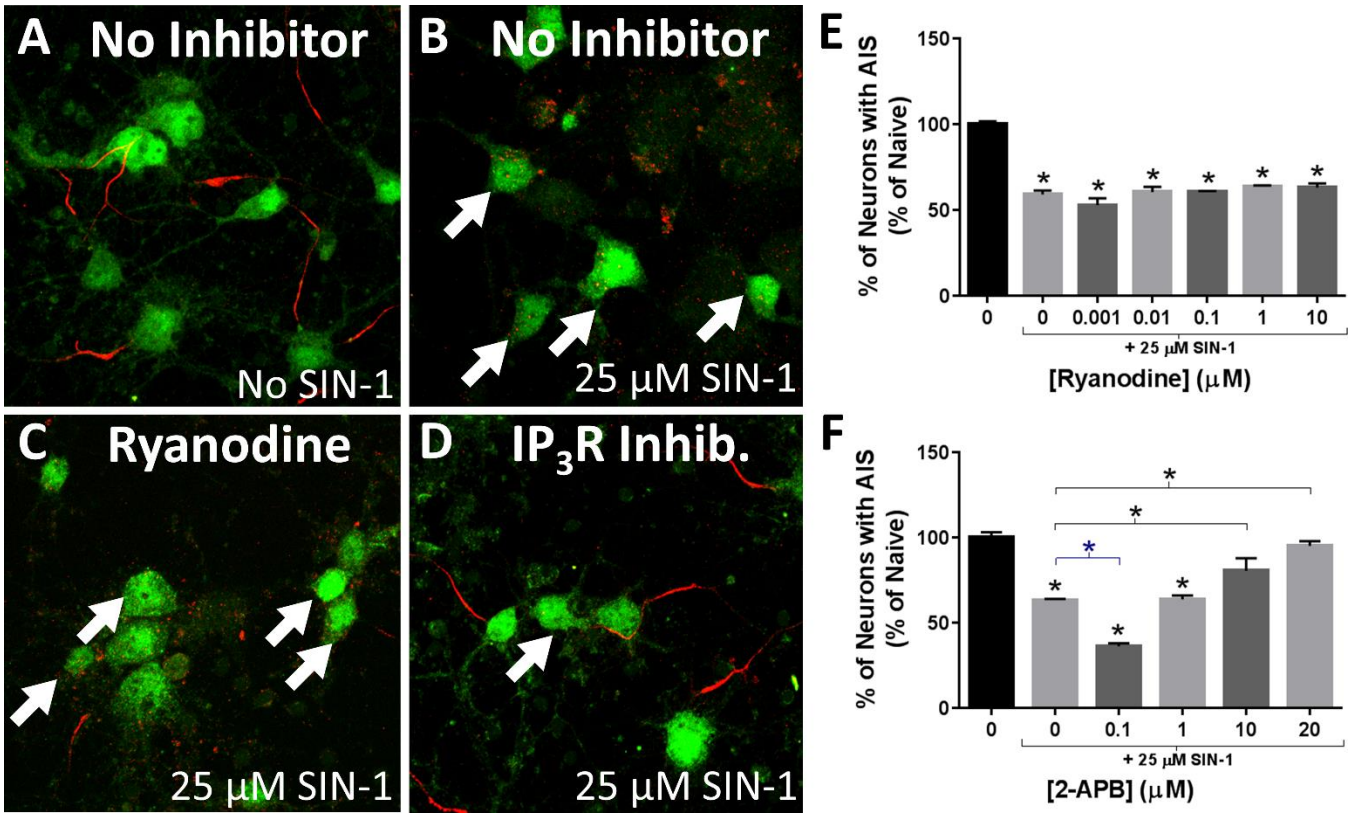
A No Inhibitor
No SIN-1
B No Inhibitor
25 µM SIN-1
C Ryanodine
25 µM SIN-1
D IP3R Inhib.
25 µM SIN-1
E
% of Neurons with AIS (% of Naive)
150
100
50
0
0 0 0.001 0.01 0.1 1 10
+ 25 µM SIN-1
[Ryanodine] (µM)
F
% of Neurons with AIS (% of Naive)
150
100
50
0
0 0 0.1 1 10 20
+ 25 µM SIN-1
[2-APB] (µM)

Figure 3.5. IP_3-gated Ca^{2+} stores are required for ROS/RNS-induced AIS disruption. AIS labeling (AnkG, red) was lost (white arrows) following exposure of cortical neurons (NeuN+, green) to 25 μM SIN-1 (B). This disruption was prevented by pre-treatment with an IP_3-receptor inhibitor (D,F) but not an inhibitor to ryanodine receptors (C,E). Asterisks without an associated bracket represent a significant difference from the SIN-1 untreated group (A, $*p < 0.05$).

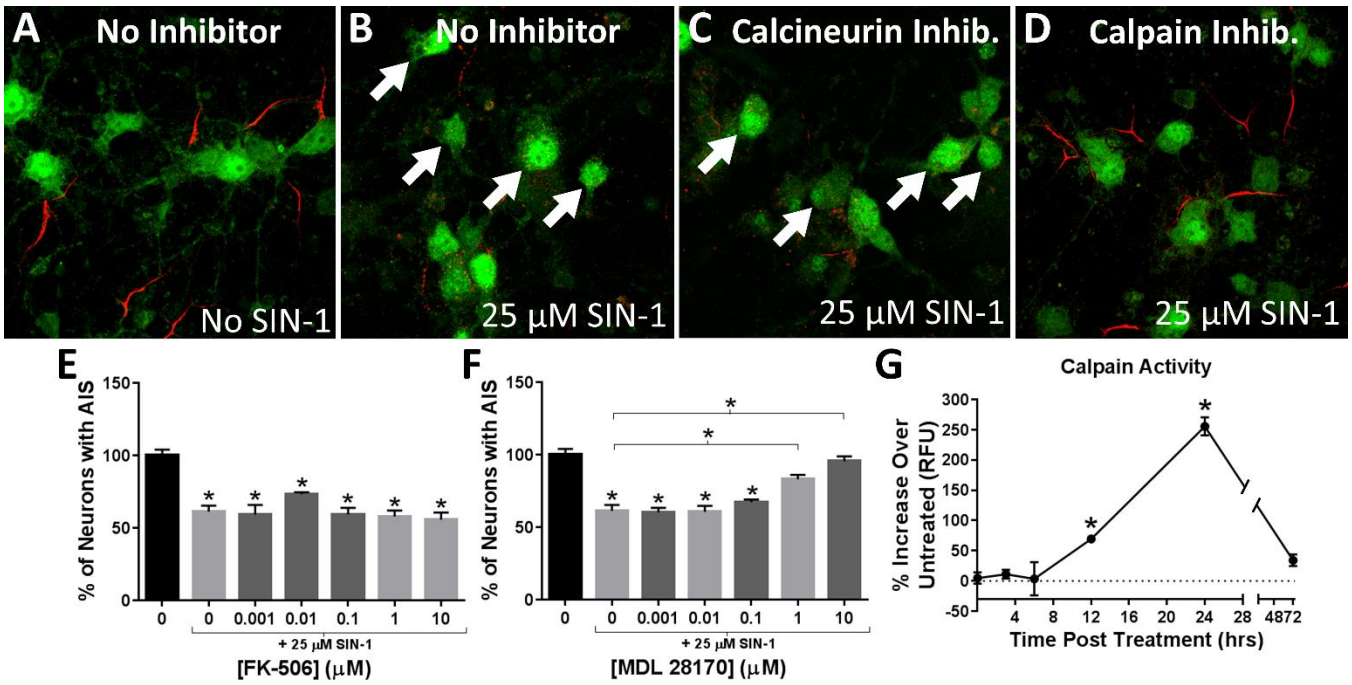
A
No Inhibitor
No SIN-1
B
No Inhibitor
25 µM SIN-1
C
Calcineurin Inhib.
25 µM SIN-1
D
Calpain Inhib.
25 µM SIN-1
E
% of Neurons with AIS
150
100
50
0
0
0
0.001
0.01
0.1
1
10
+ 25 µM SIN-1
[FK-506] (µM)
F
% of Neurons with AIS
150
100
50
0
0
0
0.001
0.01
0.1
1
10
+ 25 µM SIN-1
[MDL 28170] (µM)
G
Calpain Activity
% Increase Over Untreated (RFU)
300
250
200
150
100
50
0
-50
4
8
12
16
20
24
28
4872
Time Post Treatment (hrs)

Figure 3.6. ROS/RNS-induced AIS disruption is mediated by calpain but not calcineurin activity. Cultured cortical neurons (NeuN+, green) treated with an inhibitor directed against calcineurin (C,E) prior to SIN-1 exposure presented with a significant loss (white arrows) of AIS labeling (AnkG, red) similar to the SIN-1 treated neurons without inhibitor pre-treatment (B). In contrast, neurons treated with a calpain inhibitor displayed a significant preservation of AISs (D,F). A calpain protease activity assay revealed significantly elevated activity at 12 hours, peak activity at 24 hours and a return to baseline by 72 hours post SIN-1 treatment (25 μM) which is represented as the percent increase over untreated neurons (G). Asterisks without an associated bracket represent a significant difference from the SIN-1 untreated group (A, $*p < 0.05$).

Supplementary Table S3.1. Neurobasal™ Medium Formulation

Components	Molecular Weight (kDa)	Concentration (mg/L)
Amino Acids		
Glycine	75.0	30.0
L-Alanine	89.0	2.0
L-Arginine hydrochloride	211.0	84.0
L-Asparagine-H_2O	150.0	0.83
L-Cysteine	121.0	31.5
L-Histidine hydrochloride-H_2O	210.0	42.0
L-Isoleucine	131.0	105.0
L-Leucine	131.0	105.0
L-Lysine hydrochloride	183.0	146.0
L-Methionine	149.0	30.0
L-Phenylalanine	165.0	66.0
L-Proline	115.0	7.76
L-Serine	105.0	42.0
L-Threonine	119.0	95.0
L-Tryptophan	204.0	16.0
L-Tyrosine	181.0	72.0
L-Valine	117.0	94.0
Vitamins		
Choline Chloride	140.0	4.0
D-Calcium Pantothenate	477.0	4.0
Folic Acid	441.0	4.0
Niacinamide	122.0	4.0
Pyridoxal Hydrochloride	204.0	4.0
Riboflavin	376.0	0.4
Thiamine Hydrochloride	337.0	4.0
Vitamin B12	1355.0	0.0068
i-Inositol	180.0	7.2
Inorganic Salts		
Calcium Chloride (anhydrous)	111.0	200.0
Ferric Nitrate	404.0	0.1
Magnesium Chloride (anhydrous)	95.0	77.3
Potassium Chloride	75.0	400.0
Sodium Bicarbonate	84.0	2200.0
Sodium Chloride	58.0	3000.0
Sodium Phosphate Monobasic	138.0	125.0
Zinc Sulfate	288.0	0.194
Other Components		
D-Glucose (Dextrose)	180.0	4500.0
HEPES	238.0	2600.0
Phenol Red	376.4	8.1
Sodium Pyruvate	110.0	25.0

CHAPTER FOUR

DISRUPTION OF THE CISTERNAL ORGANELLE IN EAE AND MULTIPLE SCLEROSIS

Clark et al., *Cerebral Cortex* (Submitted)

4.1 Abstract

The axon initial segment (AIS), the neuronal subcompartment responsible for action potential generation, is altered through activity-dependent plasticity and pathological insult. While there may be many triggers for AIS modulation, all described mechanisms converge on calcium (Ca^{2+}) dysregulation which activates enzymes leading to AIS destabilization and neuronal dysfunction. Understanding the mechanisms that regulate Ca^{2+} levels at the AIS is therefore critical for addressing AIS alterations that underlie many CNS insults. Here, we investigate the cisternal organelle (CO), a poorly understood structure located specifically at the AIS and reported to buffer Ca^{2+} at this domain. Our findings of CO disruption in postmortem multiple sclerosis (MS) tissue are the first to show pathologically-induced CO alteration. Further characterization in a mouse model of MS (experimental autoimmune encephalomyelitis) suggests F-actin depolymerization and axo-axonic GABAergic synapse loss is a trigger and consequence of CO disruption, respectively. Importantly, we also demonstrate that F-actin depolymerization, synaptic loss, and CO instability are reversible upon treatment with didox, a potent free radical scavenger. Overall, these findings identify a novel neuronal insult which may provide insight into new therapeutic targets for MS and other CNS pathologies.

4.2 Introduction

The axon initial segment (AIS) is a specialized axonal subdomain responsible for both action potential initiation, and maintenance of neuronal polarity (Kole et al., 2008; Rasband, 2010). Consistent with its role as the trigger zone for neuronal firing, voltage gated ion channels are clustered at the AIS by the cytoskeletal scaffolding protein ankyrinG (AnkG) (Nelson and Jenkins, 2017). Structural and functional stability of this domain is heavily dependent on the master regulatory protein AnkG, as its loss at the AIS results in complete disassembly of the complex (Hedstrom et al., 2008). Our lab (Clark et al., 2016, Benusa et al., 2017, Clark et al., in press), and others (Buffington and Rasband, 2011; Yamada and Kuba, 2016) have demonstrated alterations to the AIS as a result of either activity-dependent plasticity or pathological insult. While the initial triggers of AIS modulation may differ, local calcium (Ca^{2+}) dysregulation at this axonal complex is central to all established mechanisms of AIS plasticity and injury (Buffington and Rasband, 2011; Yamada and Kuba, 2016). To elucidate the mechanisms underlying plasticity- and pathologically-induced Ca^{2+} changes at the AIS, we investigated the cisternal organelle (CO), an enigmatic structure localized specifically at the AIS reported to play a role in local cytosolic Ca^{2+} regulation (Benedeczky et al., 1994; Sánchez-Ponce et al., 2011).

The CO is a specialized form of smooth endoplasmic reticulum, arranged similarly as stacks of electron-dense membranous cisternae (Benedeczky et al., 1994; Bas Orth et al., 2007). This structure lies in close apposition to the axolemma while also associating with the submembranous cytoskeleton at the AIS (Sánchez-Ponce et al., 2012). Surprisingly, the functional role of the CO has not been fully elucidated. In fact, most insight into the function of this structure is derived from the nature of the expressed

proteins such as annexin 6 (A6), sarco-endoplasmic reticulum Ca^{2+}-ATPase (SERCA), and Inositol 1,4,5-trisphosphate (IP_3) receptor type 1 (IP_3R1). The functional nature of these proteins suggests a role for the CO in the sequestration and release of Ca^{2+} at the AIS (Benedeczky et al., 1994; Sánchez-Ponce et al., 2011). Recently, a role for the CO in AIS maturation and plasticity during development was demonstrated in the visual cortex (Schlüter et al., 2017). Additional insight into the functional role of the CO is gleaned from existing knowledge about a distinct, but structurally analogous organelle found in dendritic spines, termed the spine apparatus (Segal et al., 2010). Unlike the CO, the functional role of the spine apparatus as a regulator of local Ca^{2+} levels at the dendritic spine has been extensively characterized (Segal et al., 2010). Despite the elusive functional role of the CO, evidence for the mechanisms involved in its establishment and maintenance is provided by *in vitro* and *in vivo* studies (Bas Orth et al., 2007; Sánchez-Ponce et al., 2011; Schlüter et al., 2017). Stability of this organelle is dependent on both AnkG localization and clustering of filamentous actin (F-actin), as both AnkG silencing and actin depolymerization results in the loss of this structure at the AIS (Sánchez-Ponce et al., 2011). In addition to these extrinsic AIS components, CO integrity is also regulated intrinsically by synaptopodin (Synpo), an actin-binding protein critical for stabilizing the CO with the F-actin cytoskeleton (Kremerskothen et al., 2004; Sánchez-Ponce et al., 2011), as Synpo-deficient mice fail to establish COs (Bas Orth et al., 2007).

While the mechanisms that establish and maintain the CO are becoming clear, the structural and functional vulnerability of this organelle under any pathological condition has yet to be demonstrated. Presently, the only study to investigate CO integrity under

pathological conditions found the CO to remain structurally intact in a model of Alzheimer's disease (León-Espinosa et al., 2012).

Interestingly, we have recently reported that Ca^{2+} regulation is altered at the AIS following inflammatory insults that mimic those present in multiple sclerosis (MS) (Clark et al., 2017), a disease classically characterized by demyelination but known to exhibit extensive axonal pathology (Trapp et al., 1998; Criste et al., 2014). Based on our previous findings, we investigated CO stability in MS and experimental autoimmune encephalomyelitis (EAE), an animal model of MS, and found that CO integrity is compromised in both the human disease and the animal model. Our findings provide the first evidence that the CO is vulnerable to pathologically-induced disruption. Additionally, we provide evidence of a potential upstream trigger, and downstream consequence of CO instability in the form of F-actin depolymerization and GABAergic axo-axonic synapse loss, respectively. Importantly, we show that the CO disruption is reversible following free radical scavenger treatment suggesting that this newly described form of neuronal injury is potentially amenable to clinical manipulation for novel therapeutic approaches to combat MS.

4.3 Materials and Methods

Animals

11 week old female C57BL/6J mice were purchased from Jackson Laboratories (Bar Harbor, ME) and maintained in the McGuire Veterans Affairs Medical Center (VAMC) vivarium, an AAALAC accredited facility. The EAE model was induced following

one week of acclimation post-arrival resulting in induction at 12 weeks of age. Food and water were provided *ad libitum*. All procedures were conducted in accordance with the methods outlined in the approved McGuire VAMC IACUC protocols.

The EAE Model and Didox Administration

Induction of EAE was performed in 12 week old female C57BL/6J mice as previously described (Clark et al., 2016). Briefly, subcutaneous injection of 100 µL of myelin oligodendrocyte glycoprotein peptide 35-55 (3 mg/mL; AnaSpec, Fremont, CA) was emulsified in complete Freund's adjuvant (Thermo Fisher Scientific, Waltham, MA) containing heat-killed *M. tuberculosis* (2 mg/mL, Invitrogen Life Technologies, Waltham, MA). Intraperitoneal (IP) injection with PBS-diluted pertussis toxin (0.25 µg/µL, List Biological Labs, Campbell, California) was performed on the same day, followed by a booster injection 48 hours later. Clinical motor symptoms were scored daily and recorded as follows: 1.0 = limp tail, 2.0 = loss of righting reflex, 3.0 = paralysis of single hind limb and 4.0 = paralysis of both hind limbs consistent with previous reports (Dupree et al., 2015; Clark et al., 2016). For analysis, EAE mice were grouped into two clinical score groups: those presenting with mild scores (1&2) and severe scores (3&4) as previously described (Clark et al., 2016). Additionally, these two groups were assessed at two different time points along the EAE disease course: an early inflammatory time point (3 days after peak clinical score presentation) and a late inflammatory time point (9 days after peak clinical score presentation). This resulted in EAE groups termed: Early EAE 1&2, Early EAE 3&4, Late EAE 1&2 and Late EAE 3&4 (Clark et al., 2016). Only animals

that maintained consistent scores (whether 1&2 or 3&4) for the duration of their designated EAE duration were included in the study.

As previously described (Clark et al., 2016), EAE mice presenting with severe clinical scores (3&4) were treated with didox, a ribonucleotide reductase inhibitor (Bhave et al., 2013) which has been shown to dampen the inflammatory response (Matsebatlela et al., 2015; Clark et al., 2016; Caslin et al., 2017) and act as a potent free radical scavenger (Szekeres et al., 1997). Didox was supplied by Molecules for Health, Inc. (Richmond, VA) and administered via IP injection based on prior studies optimizing the treatment parameters (DeVries et al., 2012, Clark et al., 2016). Didox was dissolved at a concentration of 250 mg/kg in a solution containing: 0.5% (w/v) carboxymethylcellulose (Sigma-Aldrich Corp., St. Louis, MO), 0.9% (w/v) sodium chloride (Sigma-Aldrich Corp., St. Louis, MO), 0.4% (w/v) polysorbate 80 (Sigma-Aldrich Corp., St. Louis, MO), and 0.9% (w/v) benzyl alcohol (Sigma-Aldrich Corp., St. Louis, MO) in deionized water. Didox treatment was initiated in the Early EAE 3&4 mice and continued once daily for 6 days. For analysis, these mice were compared against similarly EAE staged animals treated daily with vehicle solution for the same duration (termed Carboxy Veh. group).

Mouse Tissue Preparation

Mouse tissue preparation was performed as previously described (Clark et al., 2016). Briefly, mice were transcardially perfused with 4% paraformaldehyde (Ted Pella, Inc., Redding, CA) and brains cryopreserved in 30% sucrose solution (in PBS), frozen in Tissue TEK Optimal Cutting Temperature compound at -80^{o}C, and serially sectioned

coronally at 40 µm thickness. Fifteen slides of six sections spanning the region 1.1 mm anterior to bregma to 2.5 mm posterior to bregma were collected as described previously (Clark et al., 2016).

Human Tissue

All human tissue used in this study, including postmortem samples from non-demented control or MS individuals, was obtained from the Netherlands Brain Bank (Amsterdam, Netherlands). Tissue characterization and donor history data are detailed in Supplementary Table S4.1.

Antibodies and Immunohistochemistry

A complete list of the primary antibodies used in this study is provided in Supplementary Table S4.2. All secondary antibodies were obtained from Invitrogen Life Technologies (Waltham, MA) (1:500, Alexa^{TM} Fluor). Human and mouse tissue was immunolabeled with the appropriate primary and secondary antibodies as described previously (Clark et al., 2016; Benusa et al., 2017), and imaged using confocal microscopy.

Image Collection and Quantitation

Confocal z-stacks spanning an optical distance of 20 µm were collected using a Zeiss LSM 710 confocal laser scanning microscope (Carl Zeiss Microscopy, Jena, Germany)

housed in the VCU Department of Anatomy and Neurobiology Microscopy Facility. Imaging parameters described previously (Clark et al., 2016) were used for all immunofluorescent analyses in the present study. Twelve fields of view were collected for both mouse and human tissue samples, yielding >1000 or >500 AISs per animal or donor, respectively. Neocortical layer V, the region previously revealed to exhibit severe AIS disruption following EAE induction (Clark et al., 2016), was the area of focus for analysis. A minimum of four mice (n=4) were used per treatment group, while the number of human tissue samples analyzed was five and 18 for non-demented controls (n=5) and MS (n=18), respectively (Supplementary Table S4.1).

Z-stack image files were analyzed using Volocity™ 3D Image Analysis Software version 6.3 (PerkinElmer, Waltham, MA). For CO, F-actin, and GABAergic axo-axonic synaptic analyses, automated measurements in the 3D z-stack allowed for specific selection and measurements of the CO through colocalization with AnkG (Supplementary Fig. S4.1). Automated exclusion of CO markers (Synpo, αAct, annexin 6, SERCA, IP_3R1), F-actin (phalloidin) and GABAergic axo-axonic synaptic components (VGAT, gephyrin) not colocalized with AnkG was performed in order to restrict analysis to the AIS (Supplementary Fig. S4.1). COs were analyzed based on the 1. percent of AISs with COs, 2. number of COs as a function of AIS length (per 10 µm) and 3. combined CO length as a function of AIS length (per 10 µm). Similar automated 3D measurements were used for the analyses of F-actin and GABAergic synaptic labeling. Data from these analyses are presented as the percent of AISs with F-actin or GABAergic synaptic clustering, as well as the number of these clusters as a function of AIS length (per 10 µm). Representative images shown for individual AISs are presented as isosurface images (generated in

Volocity™ 3D Image Analysis Software) with the raw images provided in Supplementary Figures S4.3, S4.4 and S4.5. One way ANOVAs with Tukey's HSD post hoc tests were performed for all analyses using GraphPad Prism version 6.03 (GraphPad Software, Inc., La Jolla, CA).

In order to determine the extent of parvalbumin $(PV)^+$ and total neuronal cell death, tissue was immunolabeled for PV and NeuN in combination with TUNEL labeling (Roche *In Situ* Cell Death Detection Kit, Fluorescein, Sigma-Aldrich Corp., St. Louis, MO). Images were collected as described above and qualitatively assessed for the presence of neuronal death at all EAE disease stages and time points used in this study (Supplementary Fig. S4.2). Additionally, TUNEL labeling was utilized in the postmortem human tissue to restrict CO and GABAergic synapse analysis to tissue sections containing only non-apoptotic neurons (Supplementary Fig. S4.2).

4.4 Results

The cisternal organelle is disrupted in an inflammatory model of MS

Our lab has previously reported disruption of the AIS in EAE (Clark et al., 2016), a murine model commonly used to recapitulate the inflammatory environment associated with MS (Kipp et al., 2017). Follow-up *in vitro* studies identified dysregulation of Ca^{2+} as a potential driver of the observed AIS pathology (Clark et al., in press) consistent with all previously reported mechanisms underlying AIS modulation (Leterrier et al., 2016; Jamann et al., 2017). Since we and others have implicated Ca^{2+} as a regulator of AIS stability, we investigated the integrity of the CO, a Ca^{2+}-storing organelle localized

specifically in the AIS which regulates local cytosolic Ca^{2+} levels (Benedeczky et al., 1994; Sánchez-Ponce et al., 2011). Based on our previous findings suggesting Ca^{2+} dysregulation at the AIS in EAE (Clark et al., 2016), CO integrity was first assessed in this model at all previously established time points and disease stages (Clark et al., 2016).

In the Early EAE 1&2 disease group, no difference in the percent of AISs containing COs (identified as synaptopodin, or "Synpo"$^{+}$ puncta), number of COs per 10 µm of AIS or total combined length of COs per 10 µm was observed as compared with Naïve mice (Fig. 4.1A&B, 4.1K&M). However, in the Early EAE 3&4 disease group (Fig. 4.1C), the percent of AISs with Synpo^{+} puncta was significantly reduced (Fig. 4.1K) as was the number of puncta (Fig. 4.1M) and the combined length of puncta per 10 µm of AISs (data not shown). By Late EAE, in both the 1&2 (Fig. 4.1D) and 3&4 (Fig. 4.1E) groups, Synpo labeling exhibited a continued and/or progressed reduction with regard to all three quantified parameters indicating that CO disruption parallels disease development (Fig. 4.1K&M).

To further analyze CO integrity, we next conducted immunolabeling of α-actinin (α-Act), a separate actin-binding protein important for CO stabilization (Sánchez-Ponce et al., 2012). Similar to the Synpo findings, co-immunolabeling for α-Act and AnkG revealed no significant changes in CO integrity in the Early EAE 1&2 clinical group (Figs. 4.1G, L, N) as compared to the Naïve (Figs. 4.1F, L, N). In contrast with the results of the Synpo analysis, the Early EAE 3&4 mice did not show a significant reduction in the percent of AISs containing α-Act^{+} puncta (Figs. 4.1H, L). However, CO stability was still impaired in this disease group as the number and total combined length of αAct-immunoreactive (IR) puncta per 10 µm of AnkG labeling were significantly reduced (Figs. 4.1H, N). Also,

consistent with the Synpo analysis, both clinical score groups at the late time point presented with a significant reduction in the percent of AISs containing αAct-IR puncta (Figs. 4.1I, J, L) as well as the number and combined length of puncta per 10 µm of AIS (Figs. 4.1I, J, N). Overall, we have identified disruption of the CO following EAE induction and confirmed this disruption separately through immunohistochemical analysis of two proteins critical for organelle structural stability.

Calcium-regulating proteins at the cisternal organelle are also lost in EAE

In order to further characterize the EAE-induced pathological alteration of the CO, we next investigated the CO-specific expression of several Ca^{2+}-associated proteins which are critical for its proposed function as a regulator of cytosolic Ca^{2+} at the AIS (Sánchez-Ponce et al., 2011).

Consistent with the CO analysis performed through Synpo and α-Act immunolabeling and based on the same parameters of analysis, no change in the expression of Ca^{2+}-associated proteins (annexin 6, SERCA and IP_3R1) on the COs of Early EAE 1&2 mice was observed as compared to the Naïve group (Figs. 4.2P-X). Also consistent with Synpo and α-Act analysis, mice in the Early EAE 3&4, Late EAE 1&2, and Late EAE 3&4 groups exhibited significant reduction in the percent of AISs containing annexin 6^+, $SERCA^+$, and $IP3R1^+$ COs (Figs. 4.2P-R). Similarly, these groups exhibited significant reductions in the number of Ca^{2+}-associated $protein^+$ COs per 10 µm of AIS (Figs. 4.2S-U), as well as in the percent of COs positive for these Ca^{2+}-associated proteins (Figs. 4.2V-X). Overall, in addition to the EAE-induced structural changes in CO integrity (Fig. 4.1), these data also

suggest an impaired function as these Ca^{2+}-associated proteins are vital for the proposed role of the CO as a Ca^{2+}-regulating structure (Sánchez-Ponce et al., 2011).

Loss of F-actin clustering precedes cisternal organelle disruption in EAE

We have demonstrated significant CO disruption following EAE induction and next asked what pathological mechanism could trigger this insult. While very little is known about the mechanisms that regulate CO integrity, AnkG and F-actin are both known to stabilize this organelle (Sánchez-Ponce et al., 2011). Because we are investigating CO stability in the AnkG-intact population of AISs, we focused our analysis instead on the integrity of the F-actin clusters at the AIS. To determine if altered F-actin stability could act as an upstream trigger of CO disruption, we quantified F-actin puncta associated with the AIS, as visualized through fluorescently conjugated Phalloidin staining, at all previously described EAE clinical score groups and time points.

Interestingly, a significant reduction in the percent of AISs with F-actin puncta, the number of F-actin puncta per 10 μm of AnkG labeling, and the combined length of these puncta per 10 μm of AnkG labeling (data not shown) was detected in all EAE clinical score groups and time points (Figs. 4.3A-E, K&L). In order to temporally correlate this loss of F-actin clustering with CO integrity at the AIS, double immunolabeling for Synpo and AnkG in combination with Phalloidin staining was performed within the same tissue sections. While an approximate one-to-one ratio of the number of F-actin puncta to CO ($Synpo^{+}$) puncta within the AIS was maintained in the Naïve mice (Figs. 4.3F, M), this ratio dropped significantly in the Early EAE 1&2 mice (Figs. 4.3G, M) in which the F-actin clustering was

lost (Fig. 4.3L) but no change in CO stability was detected (Fig. 4.1). This F-actin to CO ratio, however, was not significantly different between the Naïve group and mice belonging to the Early EAE 3&4, Late EAE 1&2, and Late EAE 3&4 disease groups (Figs. 4.3H-J, M) since these mice also exhibit CO disruption (Fig. 4.1) in addition to F-actin loss. Taken together, these data demonstrate that loss of F-actin clustering precedes CO disruption along the EAE disease course consistent with F-actin destabilization acting as a trigger for this pathological CO insult.

GABAergic axo-axonic synapse loss follows cisternal organelle disruption in EAE

As our findings implicate F-actin destabilization as a potential upstream trigger of CO disruption in EAE, we next wanted to identify downstream consequences of this insult. Although not associated with disease, previous studies have suggested that the CO provides functional support for inhibitory GABAergic synaptic input on the AIS (Benedeczky et al., 1994; Jedlicka et al., 2009; King et al., 2014). This is evidenced by strong colocalization between the CO and GABAergic synaptic boutons along the AIS (King et al., 2014), as well as a functionally impaired inhibitory network in Synpo-deficient mice which fail to establish COs (Jedlicka et al., 2009). In light of these findings, we next investigated the structural stability of the GABAergic synaptic terminals on AISs of cortical pyramidal neurons of the EAE mice which displayed compromised CO stability. The morphological integrity of GABAergic synaptic input at the AIS made by chandelier cells, a subset of GABAergic cortical interneurons (King et al., 2014; Wang et al., 2016), was determined through co-immunolabeling of AnkG and either vesicular GABA transporters (VGAT) or gephyrin to visualize the pre- and postsynaptic compartments, respectively.

No change in either the percent of AISs with VGAT$^+$ puncta or the number of presynaptic puncta per 10 µm of AIS was detected at the early time point in either clinical score group (Figs. 4.4U&V). In contrast to the early EAE groups, a significant reduction in the percent of AISs containing VGAT$^+$ puncta, as well as in the number of these boutons per 10 µm of AIS was observed in the Late EAE 1&2 and Late EAE 3&4 groups (Figs. 4.4U&V). These data demonstrate a loss of the presynaptic component of the GABAergic synaptic complex at the AIS in EAE.

To determine if the postsynaptic component of the GABAergic synaptic complex was also disrupted, immunolabeling for gephyrin, a postsynaptically localized scaffolding protein critical for the establishment and maintenance of these axo-axonic synapses (Choii and Ko, 2015), was performed on all EAE disease groups. Consistent with the VGAT analysis, no significant differences were observed in the percent of AISs containing gephyrin$^+$ postsynaptic puncta nor the number of these puncta per 10 µm of AnkG immunolabeling between the Naïve and Early EAE 1&2 disease groups (Figs. 4.4X&Y). Also consistent with the VGAT analysis, significant loss in the percent of AISs containing gephyrin$^+$ synapses and the number of synaptic puncta as a function of AIS length (per 10 µm) was observed in both the Late EAE 1&2 and Late EAE 3&4 disease groups (Figs. 4.4X&Y). Surprisingly, a significant reduction in these parameters was also detected in the Early EAE 3&4 group (Figs. 4.4X&Y), which displayed intact VGAT$^+$ presynaptic terminals (Figs. 4.4U&V).

As shown in Figure 4.4, we then correlated the disruption of the GABAergic synaptic complex with the CO integrity within each AIS. Triple immunolabeling for VGAT, Synpo, and AnkG revealed the ratio of CO to VGAT$^+$ puncta number to be maintained at a two-

to-one ratio in the Naïve and Early EAE 1&2 groups (Fig. 4.4W). This ratio is significantly reduced only in the Early EAE 3&4 disease group (Fig. 4.4H&W), a point at which VGAT immunolabeling is reduced (Fig. 4.4U&V) but CO number is maintained (Fig. 4.1). In contrast, the ratio of CO to $VGAT^+$ puncta number was not significantly different from Naïve in both clinical score groups at the late time point (Figs. 4.4W) since CO number is also reduced at this disease stage (Fig. 4.1). Additionally, triple immunolabeling for gephyrin, Synpo, and AnkG and subsequent determination of the CO to $gephyrin^+$ postsynaptic puncta ratio revealed similar trends to that of the VGAT-CO correlative analysis (Fig. 4.4Z). Overall, these data suggest that instability of the GABAergic synaptic complexes at the AIS is a downstream consequence of CO disruption in EAE.

Cisternal organelle disruption in EAE is reversible following anti-inflammatory treatment

In the present study, we have provided the first evidence for pathological alterations to the CO. While we now know that the CO is vulnerable to disruption, we asked whether these pathological changes are reversible. Our lab has previously demonstrated, not only an alleviation of disease clinical scores, but also an attenuation of AIS pathology in EAE through treatment with a novel anti-inflammatory and free radical scavenger known as didox (Clark et al., 2016). To investigate whether the loss of the CO in EAE is also recoverable, we began treatment in the Early EAE 3&4 mice, a time point and disease stage at which significant CO loss is observed (Fig. 4.1). Following didox treatment, we first assessed CO integrity through immunolabeling for the two actin-associated markers utilized in Figure 4.1: Synpo (Fig. 4.5A-E) and α-Act (data not shown), both of which are

important for CO stability (Sánchez-Ponce et al., 2012). CO loss was indeed reversible, with the percent of AISs containing Synpo^{+} or α-Act^{+} organelles indistinguishable from Naïve, and significantly increased compared to the vehicle treated mice (Figs. 4.5A-D). Similarly, the number of Synpo- or α-Act-IR puncta was also reduced in the vehicle treated mice but significantly attenuated in the didox treated group (Figs. 4.5A-C, E). CO number, however, did not completely return to baseline when compared to the Naïve mice (Figs. 4.5A, C, E).

We next investigated whether the CO integrity was also reversible based on immunolabeling of the functional Ca^{2+}-regulating proteins assessed previously (Fig. 4.2). Triple immunolabeling with AnkG (βIV-spectrin in the case of the SERCA analysis), Synpo, and either annexin 6 (data not shown), IP_3R1, or SERCA revealed a decrease in the percent of AISs containing COs positive puncta for these markers and a significant recovery following didox treatment (Figs. 4.5F-I, K-N). Didox treated mice, however, did display mixed results when assessing the percent of COs positive for each of the three Ca^{2+}-associated proteins. Only the IP_3R1 but not annexin 6 (data not shown) or SERCA (Figs. 4.5K-M, 5O) analysis revealed a significant return to Naïve levels for this measurement. SERCA labeling, however, reminiscent of the IP_3R1 analysis, displayed significant recovery when compared to vehicle treated mice (Figs. 4.5K-M, O). Taken together, these findings reveal at least a partial, but potentially incomplete, recovery of CO proteins important for Ca^{2+} regulation at the AIS.

Finally, we investigated the reversibility of the F-actin and GABAergic synaptic complex loss at the AIS, a potential trigger (Fig. 4.3) and consequence (Fig. 4.4) of this pathological CO insult, respectively. As expected, phalloidin staining revealed significant

F-actin loss in the vehicle treated mice (Figs. 4.5P-T). Interestingly, this loss was also reversible with didox treatment (Figs. 4.5P-T). Immunolabeling for both the presynaptic (VGAT) and postsynaptic (gephyrin, data not shown) GABAergic complex components revealed a similar attenuation following didox treatment as compared to the loss observed in vehicle treated EAE mice (Figs. 4.5U-Y). Overall, these findings demonstrate that loss of CO integrity and GABAergic synaptic complexes at the AIS are reversible insults in EAE.

The cisternal organelle and GABAergic axo-axonic synapses are lost in multiple sclerosis

The findings in the EAE model suggest that CO and axo-axonic synaptic loss at the AIS may represent previously unidentified insults associated with MS pathogenesis. In an effort to investigate the relevancy of these observations to the human disease, postmortem MS tissue was analyzed for each of these potential neuronal pathologies. As shown in Figure 4.6, double immunolabeling for AnkG and Synpo was performed to quantify the percent of AISs containing COs, the number of COs as a function of AIS length (number of COs per 10 µm of AIS) and the combined CO length as a function of AIS length (combined CO length per 10 µm of AIS). While no change in the percent of AISs containing the CO was detected between MS and control tissue (data not shown), significant reductions in CO number and total CO length per 10 µm of AnkG immunolabeling, as compared to the non-demented control tissue, were observed (Fig 4.6). These findings are the first to demonstrate CO pathology in any human disease.

As demonstrated in Figure 4.4, loss of the CO in EAE was observed preceding that of GABAergic axo-axonic boutons at the AIS. To investigate this relationship in the postmortem MS tissue, immunolabeling for VGAT was used to identify the axo-axonic GABAergic presynaptic terminals formed by chandelier cells (King et al., 2014; Wang et al., 2016). Similar to the findings of CO stability, a significant reduction in the number of $VGAT^+$ synaptic terminals was also observed in postmortem MS tissue (Fig. 4.6). AISs in MS tissue presented with significantly fewer GABAergic boutons per 10 µm of AnkG immunolabeling, as compared to non-demented control tissue. Overall, these findings reveal a loss of both the CO and GABAergic axo-axonic synapses at the AIS, two previously unidentified neuronal insults associated with MS pathogenesis.

4.5 Discussion

In the present study, we have identified the first pathological alterations to the CO, an organelle critical for the regulation of Ca^{2+} levels at the AIS (Benedeczky et al., 1994; Sánchez-Ponce et al., 2011). Additionally, the loss of this structure, as well as the GABAergic synaptic complexes on the AIS, represent previously unidentified neuronal insults associated with MS pathogenesis (Fig. 4.6). Investigating CO integrity in the inflammatory EAE model provided a more complete characterization of this novel pathology. Loss of F-actin clustering at the AIS presents before detectable changes to CO stability during EAE progression (Fig. 4.7B). In contrast, loss of the axo-axonic GABAergic synaptic complexes appear to occur downstream of the CO insult along the disease course (Fig. 4.7D). Importantly, the morphological alterations to the GABAergic synaptic terminals are consistent with the functional impairment of the GABAergic

inhibitory network previously reported in the Synpo deficient mice (Jedlicka, et al., 2009). Finally, structural disruption of the CO as well as its potential downstream pathology are reversible upon anti-inflammatory and free radical scavenger treatment (Figs. 4.5, 4.7) suggesting that these novel MS pathologies are clinically subject to therapeutic modification.

How does cisternal organelle integrity affect AIS stability?

While our lab has previously identified extensive AIS disruption in EAE (Clark et al., 2016), here we demonstrate loss of the CO in the population of AISs that remain morphologically intact ($AnkG^{+}$). It remains unclear how CO and AIS loss may correlate mechanistically, but previous work *in vitro* and *in vivo* provides some insight. AIS stability is required for both the establishment and maintenance of the CO (Sánchez-Ponce et al., 2011). Not only does AIS maturation precede that of the CO, but AnkG silencing in cultured hippocampal neurons results in complete destabilization of this organelle (Sánchez-Ponce et al., 2011). While these findings provide strong evidence for the dependence of the CO on AIS stability, the reciprocal relationship is not as clearly defined. Initial findings from Synpo deficient mice, in which the CO is not established, revealed no consequence on structural or functional integrity of the AIS with respect to AnkG localization and action potential generation (Bas Orth et al., 2007). The authors, however, acknowledged the possibility that the CO could play a role at the AIS distinct from the basic electrophysiological parameters tested (Bas Orth et al., 2007). A recent study suggested a role for the CO in modulating developmental plasticity of the AIS. Schlüter et al. (2017) demonstrated altered AIS length in the visual cortex of mice lacking the CO

following dark rearing. In addition to its role in AIS development, the CO may also play a role in maintaining GABAergic axo-axonic synaptic complexes based on immunocytochemistry colocalization (Benedeczky et al., 1994; King et al., 2014). Consistent with this possibility, electrophysiological studies in the Synpo deficient mice, which lack the CO and spine apparatus, revealed an impaired local inhibitory network (Jedlicka et al., 2009). Therefore, the apparent downstream consequence of CO loss, as observed in both previous (Jedlicka et al., 2009; King et al., 2014) and our present studies, is impaired structural and functional AIS stability, since the AIS is a highly plastic structure heavily regulated by neuronal activity (Yamada and Kuba, 2016; Jamann et al., 2017).

In addition to activity-dependent AIS alterations as a potential consequence of CO disruption, it is also likely that dysregulation of cytosolic Ca^{2+} at the AIS could lead to proteolytic modulation of this domain. Previous studies demonstrated cleavage of critical AIS components including AnkG, βIV-spectrin, and voltage-dependent sodium channels by calpain, a Ca^{2+}-activated protease (Schafer et al., 2009). Calpain activation is central to a wide array of pathological AIS insults including those induced by ischemia (Schafer et al., 2009; Hinman et al., 2013), purinergic receptor activation (Del Puerto et al., 2015), glutamate excitotoxicity (Benned-Jensen et al., 2016), LPS-mediated inflammation (Benusa et al., 2016), and oxidative stress (Clark et al., in press). Because regulation of local Ca^{2+} is crucial for AIS stability, it is possible that alterations to the CO could underlie many of these previously identified AIS pathologies.

Is F-actin destabilization mediated by the inflammatory environment?

Here we show loss of F-actin clustering at the AIS of EAE-induced mice which precedes CO disruption (Fig. 4.3). This finding is consistent with other studies in which F-actin is revealed to stabilize and maintain CO integrity at the AIS (Sánchez-Ponce et al., 2011). Although loss of F-actin could be mechanistically upstream of CO disruption in EAE, the trigger for F-actin destabilization in this model remains unclear. It is likely that the inflammatory environment of EAE is responsible for the alterations of F-actin, as actin dynamics are modulated by a variety of inflammatory components (Cross and Woodroofe, 1999; Delbro et al., 2009; Munnamalai and Suter, 2009; Tong et al., 2012; Munnamalai et al., 2014). Previous studies demonstrated loss of F-actin clustering in a variety of cell types as a result of an LPS-induced inflammatory insult and more specifically by cytokines such as IL-1β (Cross and Woodroofe, 1999; Delbro et al., 2009; Tong et al., 2012). Additionally, it is possible that oxidative stress plays a role in the F-actin alterations observed in this study, since clustering was recovered following free radical scavenger treatment (Fig. 4.5). Supporting this idea, reactive oxygen species (ROS) disassemble the F-actin cytoskeleton at the neuronal growth cone during normal neurite outgrowth (Munnamalai and Suter, 2009; Munnamalai et al., 2014). These changes are believed to be due to ROS-mediated activation of various kinases that regulate actin remodeling (Munnamalai and Suter, 2009). While these mechanisms are important for neural development, they may become pathological when overstimulated, as F-actin destabilization mediated through oxidative stress has been attributed to the pathogenesis of other neurodegenerative diseases such as Alzheimer's disease (Bamburg and

Bernstein, 2016). The specific trigger of F-actin destabilization in the EAE model requires further investigation.

Impairment of the GABAergic network in multiple sclerosis

In the present study, we have identified loss of the CO and GABAergic synaptic complexes localized at the AIS (Figs. 4.4, 4.6), two previously undescribed axonal insults in MS pathogenesis. These findings are consistent with the hypothesized role for the CO in maintaining these axo-axonic inputs at the AIS (Benedeczky et al., 1994; Jedlicka et al., 2009; King et al., 2014), and provide a possible explanation for the impaired GABAergic network reported in MS and its animal models (Dutta et al., 2006; Rossi et al., 2011; Falco et al., 2014; Mosayebi et al., 2016). Western blot, as well as immunohistological analysis on postmortem MS and EAE cortical tissue, previously revealed decreased overall expression of pre- and postsynaptic components of the GABAergic complex (Dutta et al., 2006; Falco et al., 2014). These morphological findings are consistent with functional studies performed in the EAE model demonstrating loss of the hippocampal paired-pulse inhibitory effect (Mosayebi et al., 2016), as well as impaired striatal GABAergic transmission (Rossi et al., 2011). Though the triggers of structural and functional impairment of the inhibitory network in EAE are not clearly defined, loss of PV^+ interneurons may contribute (Falco et al., 2014). In the present study, we reveal structural changes to the GABAergic axo-axonic synapses in the absence of PV^+ interneuron cell death (Supplementary Fig. 4.2), at a much earlier disease stage than those examined in previous studies (Falco et al., 2014). This suggests that these effects are not, at least initially, consequences of neuron cell death. In addition to the animal studies suggesting

a functionally impaired GABAergic network, Arpin et al. (2017) used magnetoencephalography (MEG) to record neural responses following paired-pulse stimulations showing similar functional abnormalities in MS patients consistent with a loss of GABAergic synaptic complexes.

Overall, we provide the first evidence of CO disruption under pathological conditions, an insult that would have profound effects on local Ca^{2+} regulation at the AIS. Additionally, we report the disruption of the CO as well as the axo-axonic GABAergic synaptic terminals at the AIS in postmortem MS tissue. Characterization of CO insult in EAE revealed this disruption to be preceded by loss of F-actin clustering at the AIS and followed by structural impairment of the GABAergic network, which is consistent with previous studies that reported compromised CO integrity and a disrupted CNS inhibitory network (Jedlicka et al., 2009; Sánchez-Ponce et al., 2011; King et al., 2014). Importantly, these changes are reversible upon free radical scavenger treatment in EAE, indicating that these neuronal MS deficits are potentially amendable to therapeutic approaches.

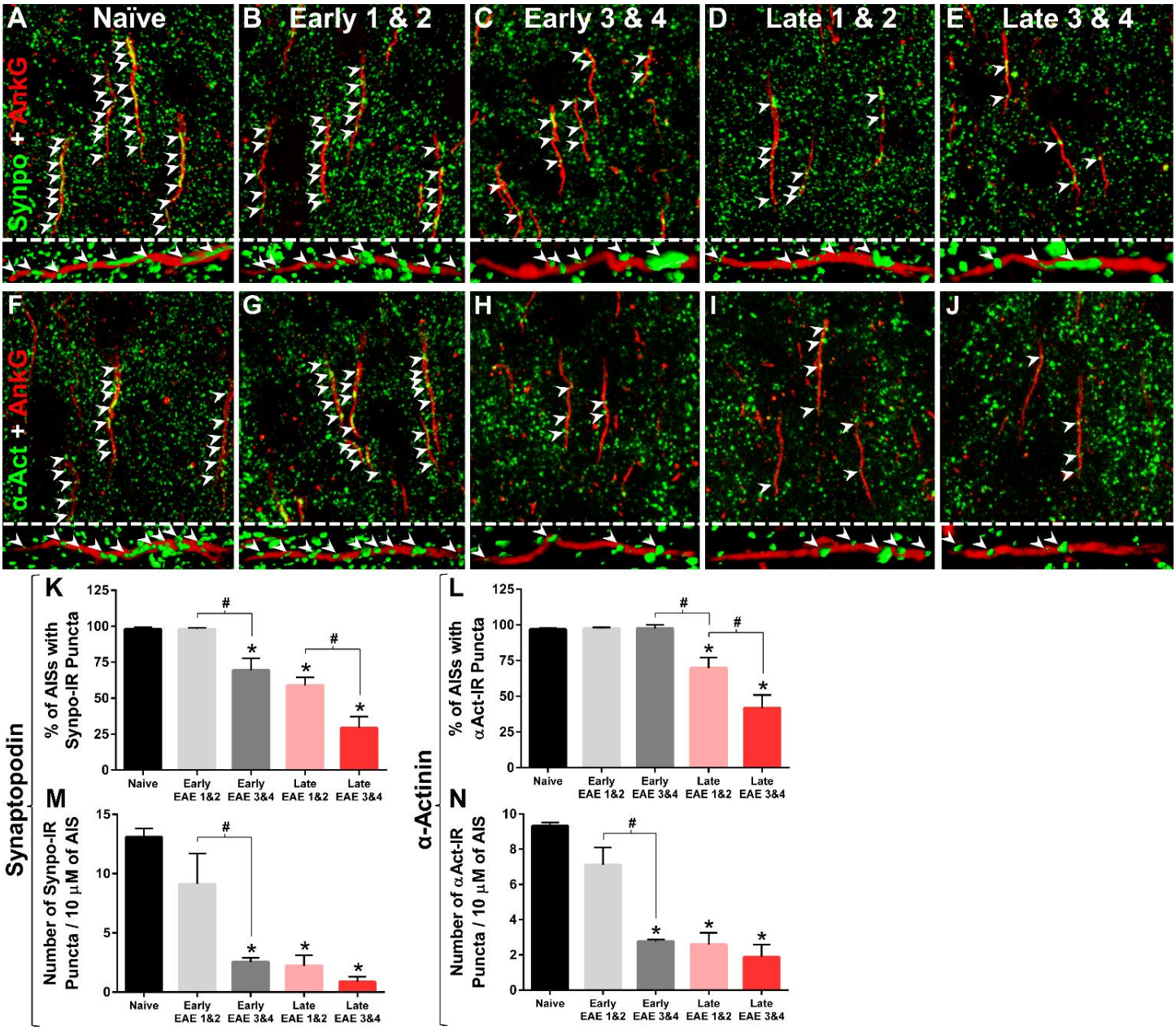
A Naïve
B Early 1 & 2
C Early 3 & 4
D Late 1 & 2
E Late 3 & 4
Synpo + AnkG
F
G
H
I
J
α-Act + AnkG
Synaptopodin
K
% of AISs with Synpo-IR Puncta
M
Number of Synpo-IR Puncta / 10 μM of AIS
α-Actinin
L
% of AISs with αAct-IR Puncta
N
Number of αAct-IR Puncta / 10 μM of AIS
Naive
Early EAE 1&2
Early EAE 3&4
Late EAE 1&2
Late EAE 3&4

Figure 4.1. The cisternal organelle is disrupted in early and late EAE. Representative immunolabeling for the CO using antibodies directed against two structural CO proteins (Synpo (A-E) and α-Act (F-J), green; white arrows) in Early EAE 1&2 mice (B,G) reveals no change in either the percent of AISs containing these structures (K,M), or the number of these organelles per 10 µm of AnkG labeling (L,N) as compared to the Naïve group (A,F). Significant reductions in both of these values were detected in mice belonging to the Early EAE 3&4 (C,H), Late EAE 1&2 (D,I), and Late EAE 3&4 (E,J) groups. Isosurface insets of individual AISs are shown below the low magnification representative images. Asterisks without an associated bracket represent a significant difference from the Naïve group (*$p < 0.05$).

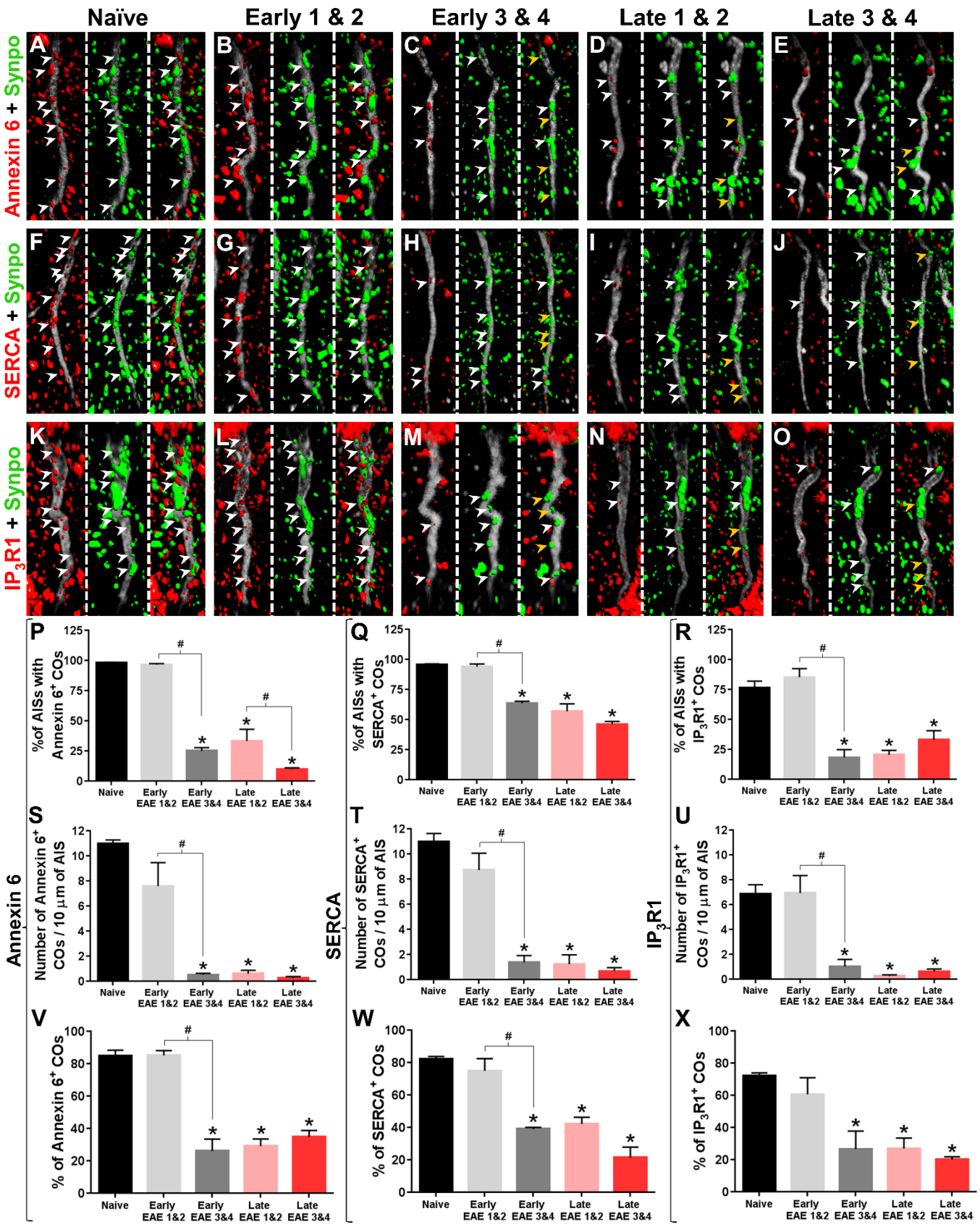
Naïve
Early 1 & 2
Early 3 & 4
Late 1 & 2
Late 3 & 4
Annexin 6 + Sympo
SERCA + Sympo
IP3R1 + Sympo
A
B
C
D
E
F
G
H
I
J
K
L
M
N
O
Annexin 6
SERCA
IP3R1
P
Q
R
S
T
U
V
W
X
%of AISs with Annexin 6+ COs
%of AISs with SERCA+ COs
% of AISs with IP3R1+ COs
Number of Annexin 6+ COs / 10 µm of AIS
Number of SERCA+ COs / 10 µm of AIS
Number of IP3R1+ COs / 10 µm of AIS
% of Annexin 6+ COs
% of SERCA+ COs
% of IP3R1+ COs
Naive
Early EAE 1&2
Early EAE 3&4
Late EAE 1&2
Late EAE 3&4

Figure 4.2. Calcium-regulating proteins at the cisternal organelle are compromised following EAE induction. Representative isosurface AISs immunolabeled with AnkG (grey), Synpo (green; white arrows), and either Annexin 6 (A-E), SERCA (F-J), or IP_3R1 (K-O) (red; white arrows) demonstrate no change in the expression of these Ca^{2+}-associated proteins on the CO in Naïve (A,F,K) and Early EAE 1&2 mice (B,G,L). Loss of each of these proteins on the CO is present in the Early EAE 3&4 (C,H,M), Late EAE 1&2 (D,I,N), and Late EAE 3&4 (E,J,O) groups. Yellow arrows denote COs that are negative for Annexin 6 (C-E), SERCA (H-J), or IP_3R1 (M-O) on the composite images. Data are presented as the percent of AISs containing COs positive for each of these Ca^{2+}-associated markers (P-R), the number of theses COs per 10 µm of AnkG labeling (S-U), and the percent of COs positive for each Ca^{2+}-associated protein (V-X). Asterisks without an associated bracket represent a significant difference from the Naïve group ($*p < 0.05$).

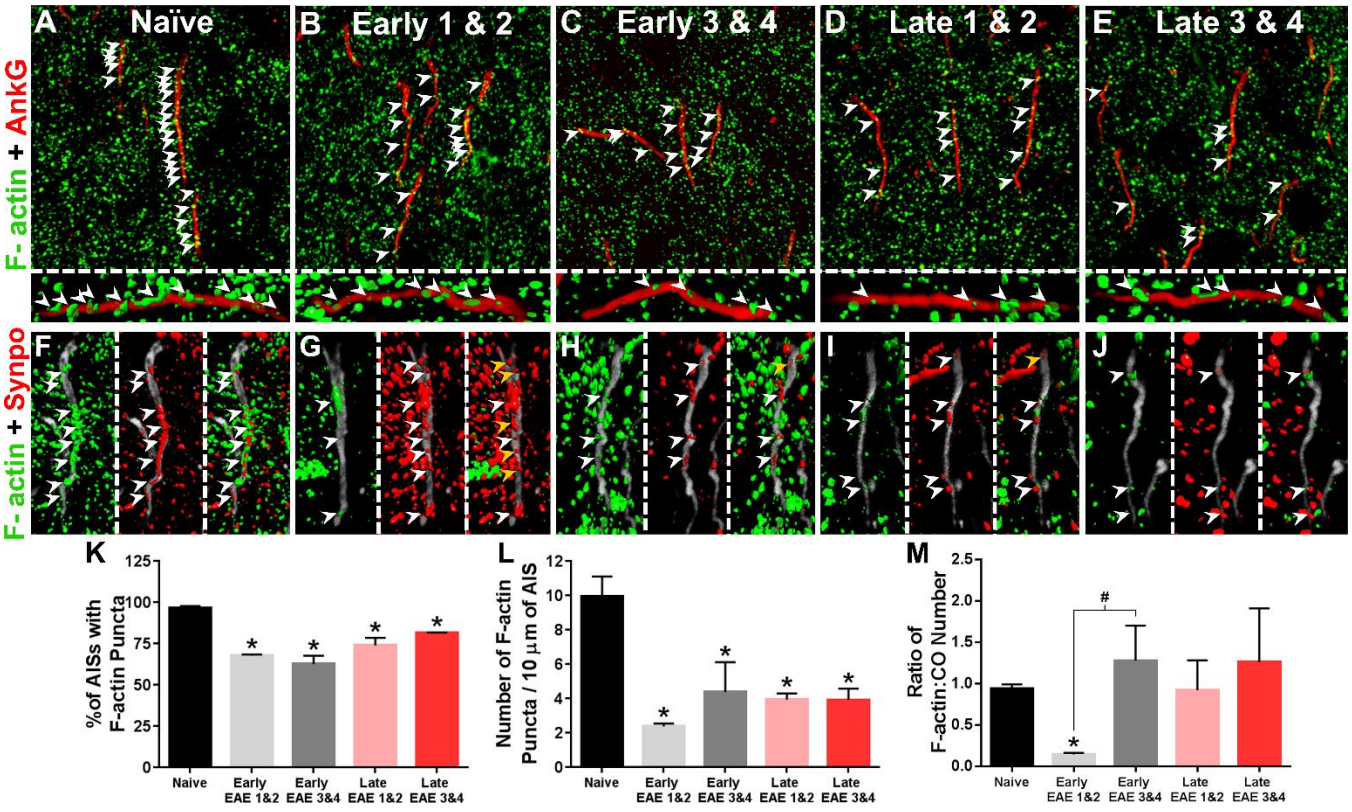
A Naïve
B Early 1 & 2
C Early 3 & 4
D Late 1 & 2
E Late 3 & 4
F- actin + AnkG
F- actin + Sympo
F
G
H
I
J
K
%of AISs with F-actin Puncta
L
Number of F-actin Puncta / 10 µm of AIS
M
Ratio of F-actin:CO Number
Naive
Early EAE 1&2
Early EAE 3&4
Late EAE 1&2
Late EAE 3&4

Figure 4.3. Loss of F-actin clustering at the AIS precedes cisternal organelle disruption. Staining of F-actin with phalloidin (green; A-E) in representative images collected from Naïve mice (A) display numerous AIS-localized (AnkG, red; A-E) clusters (white arrows). Significant reduction in F-actin clustering at the AIS is first observed at Early EAE 1&2 (B), which persists at the Late EAE time point for both clinical score groups (D,E). Data for this analysis are presented as the percent of AISs containing F-actin puncta (K), as well as the number of these puncta as a function of AIS length (per 10 µm; L). Isosurface insets of individual AISs are shown below the low magnification representative images (A-E). Staining of F-actin (green; white arrows) with simultaneous double immunolabeling for Synpo (CO, red; white arrows) and AnkG (AIS, grey) allow for correlation between F-actin and CO loss (F-J). The ratio of F-actin to CO number at the AIS is only significantly reduced in the Early EAE 1&2 group (H), the clinical stage where F-actin loss precedes CO disruption. The F-actin/CO ratio returns to baseline level in the Early EAE 3&4 (H), Late EAE 1&2 (I), and Late EAE 3&4 (J) groups as subsequent CO loss is also observed. Yellow arrows (most prevalent in G merged) denote COs not colocalized with F-actin. Representative AISs are depicted as isosurface images (F-J). Asterisks without an associated bracket represent a significant difference from the Naïve group (*$p < 0.05$).

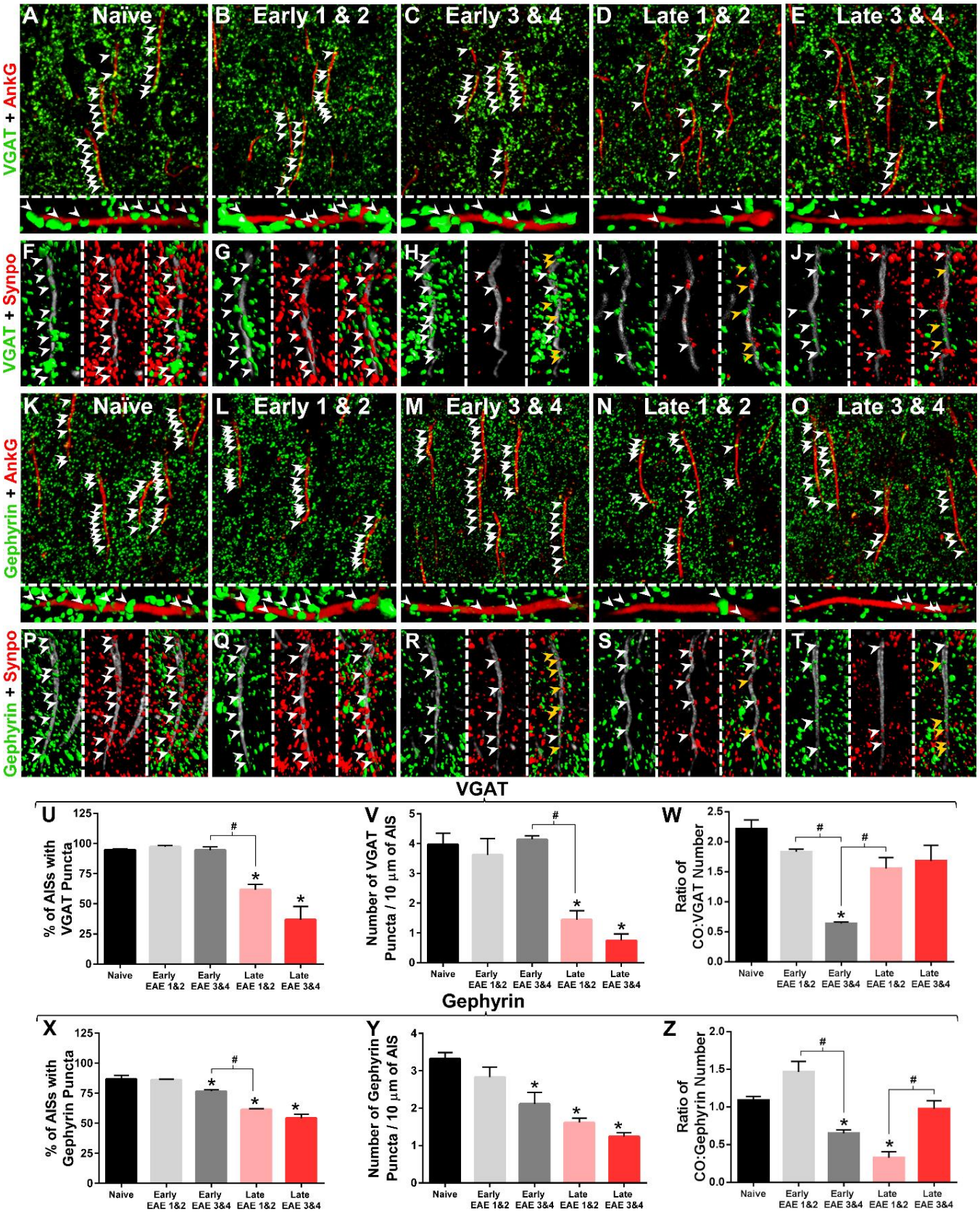
A Naïve
B Early 1 & 2
C Early 3 & 4
D Late 1 & 2
E Late 3 & 4
VGAT + AnkG
F
G
H
I
J
VGAT + Synpo
K Naïve
L Early 1 & 2
M Early 3 & 4
N Late 1 & 2
O Late 3 & 4
Gephyrin + AnkG
P
Q
R
S
T
Gephyrin + Synpo
VGAT
U
% of AISs with VGAT Puncta
V
Number of VGAT Puncta / 10 µm of AIS
W
Ratio of CO:VGAT Number
Gephyrin
X
% of AISs with Gephyrin Puncta
Y
Number of Gephyrin Puncta / 10 µm of AIS
Z
Ratio of CO:Gephyrin Number
Naive
Early EAE 1&2
Early EAE 3&4
Late EAE 1&2
Late EAE 3&4

Figure 4.4. Axo-axonic GABAergic synaptic complexes are lost following cisternal organelle disruption. Immunolabeling of GABAergic presynaptic (VGAT, green; A-J) axo-axonic terminals in representative images collected from Naïve (A,F), Early EAE 1&2 (B,G), and Early EAE 3&4 (C,H) mice display numerous AIS-localized (AnkG, red; A-E) GABAergic terminals (white arrows). Significant loss of these presynaptic axo-axonic synapses is observed, however, at the Late EAE time point of both clinical score groups (D,E). Similarly, postsynaptic (gephyrin, green; white arrows; K-T) GABAergic terminal labeling reveals no change in AIS localization (AnkG, red; P-T) in Early EAE 1&2 (L) mice as compared to the Naïve (K). This postsynaptic component of the GABAergic complex is, however, significantly disrupted in the Early EAE 3&4 (M), Late EAE 1&2 (N), and Late EAE 3&4 (O) groups. Isosurface insets of individual AISs are shown below the low magnification representative images (A-E). Data from these analyses are presented as the percent of AISs with either $VGAT^+$ (U) or $gephyrin^+$ (X) puncta, and the number of these GABAergic synaptic components (VGAT, V; gephyrin, Y) per 10 µm of AnkG labeling. Furthermore, the ratio of CO to pre- (VGAT; F-J, W) or postsynaptic number (gephyrin; P-T, Z) at the AIS (AnkG, grey) demonstrates a significant reduction beginning in the Early EAE 3&4 group, as CO disruption is observed to precede GABAergic axo-axonic synaptic loss at this point (yellow arrows). Representative AISs are depicted as isosurface images (A-E; P-T). Asterisks without an associated bracket represent a significant difference from the Naïve group ($*p < 0.05$).

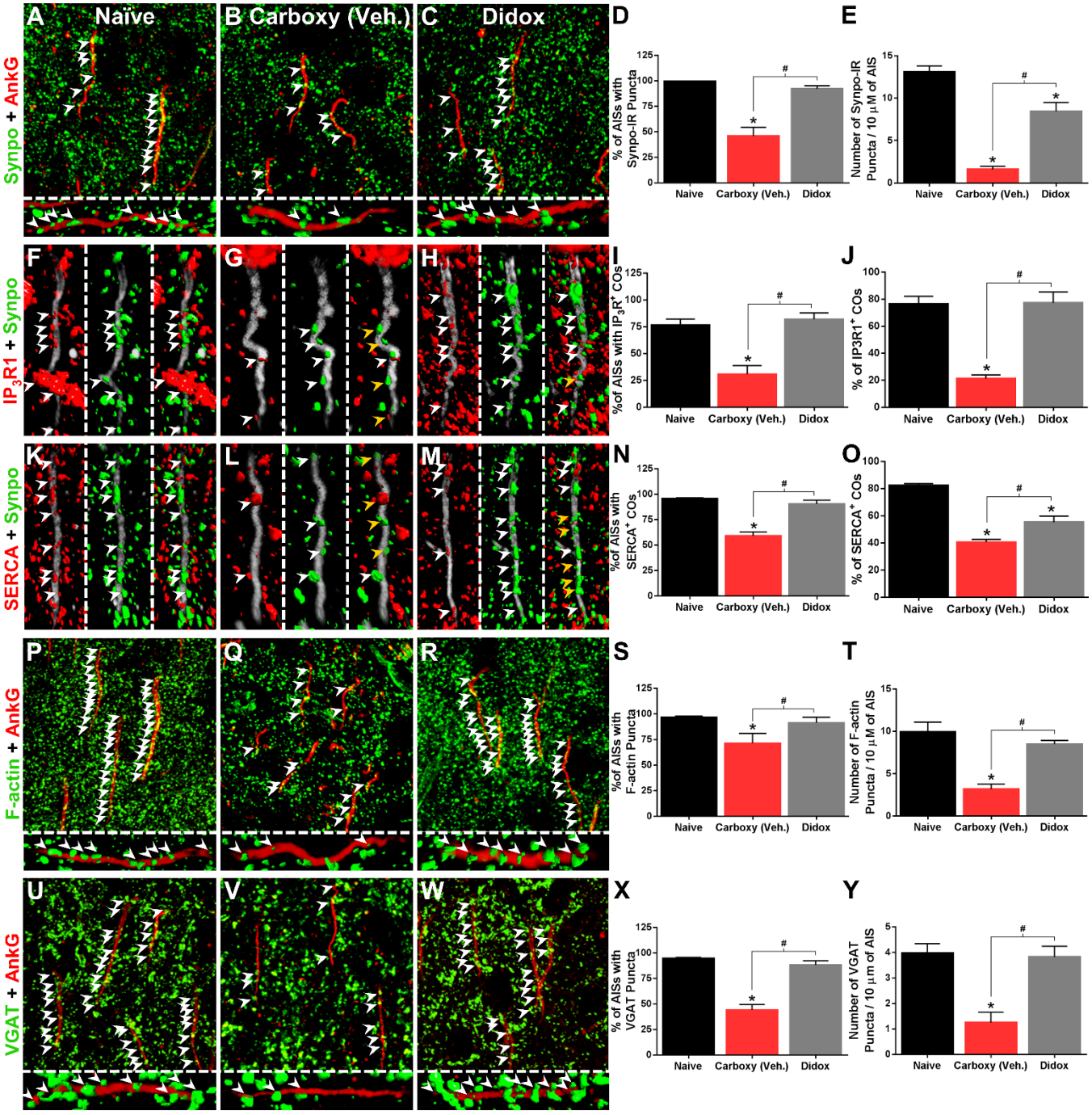
A Naïve
B Carboxy (Veh.)
C Didox
Sympo + AnkG
D
% of AISs with Sympo-IR Puncta
Naive
Carboxy (Veh.)
Didox
E
Number of Sympo-IR Puncta / 10 μM of AIS
F
G
H
IP3R1 + Sympo
I
%of AISs with IP3R+ COs
J
% of IP3R1+ COs
K
L
M
SERCA + Sympo
N
%of AISs with SERCA+ COs
O
% of SERCA+ COs
P
Q
R
F-actin + AnkG
S
%of AISs with F-actin Puncta
T
Number of F-actin Puncta / 10 μM of AIS
U
V
W
VGAT + AnkG
X
% of AISs with VGAT Puncta
Y
Number of VGAT Puncta / 10 μm of AIS

Figure 4.5. Cisternal organelle and axo-axonic GABAergic loss is reversible following free radical scavenger treatment. Immunolabeling for the CO (Synpo, green; A-C) in didox treated mice (C) reveals significant recovery in both the percent of AISs (AnkG, red; A-C) containing the CO (D), and the number of these structures per 10 µm of AnkG labeling (E) as compared to the Naïve (A) and vehicle treated (B) groups. Isosurface insets of individual AISs are shown below the low magnification representative images (A-C). Representative isosurface AISs immunolabeled with AnkG (grey; F-H), Synpo (green; F-H), and either IP_3R1 or SERCA (red; F-H) demonstrate recovery of CO-expression of these Ca^{2+}-associated proteins in didox treated mice (H,M) as compared to the Naïve (F,K) and vehicle treated (G,L) groups. Data from these analyses are presented as the percent of AISs containing either IP_3R1 or $SERCA^+$ COs (I,N) and the percent of COs that are positive for these markers (J,O). Yellow arrows denote COs without colocalization of either Ca^{2+}-associated proteins IP_3R1 (F-H) or SERCA (K-M). Finally, both F-actin clustering (phalloidin, green; P-R) and GABAergic axo-axonic synaptic puncta (VGAT, green; U-W) recovered following didox treatment (R,W) with respect to both the percent of AISs (red, P-W) positive for each of these markers (S,X), and the number of these puncta as a function of AIS length (T,Y), as compared to the Naïve (P,U) and vehicle treated (Q,V) groups. Isosurface insets of individual AISs are shown below the low magnification representative images (P-R; U-W). Asterisks without an associated bracket represent a significant difference from the Naïve group ($*p < 0.05$).

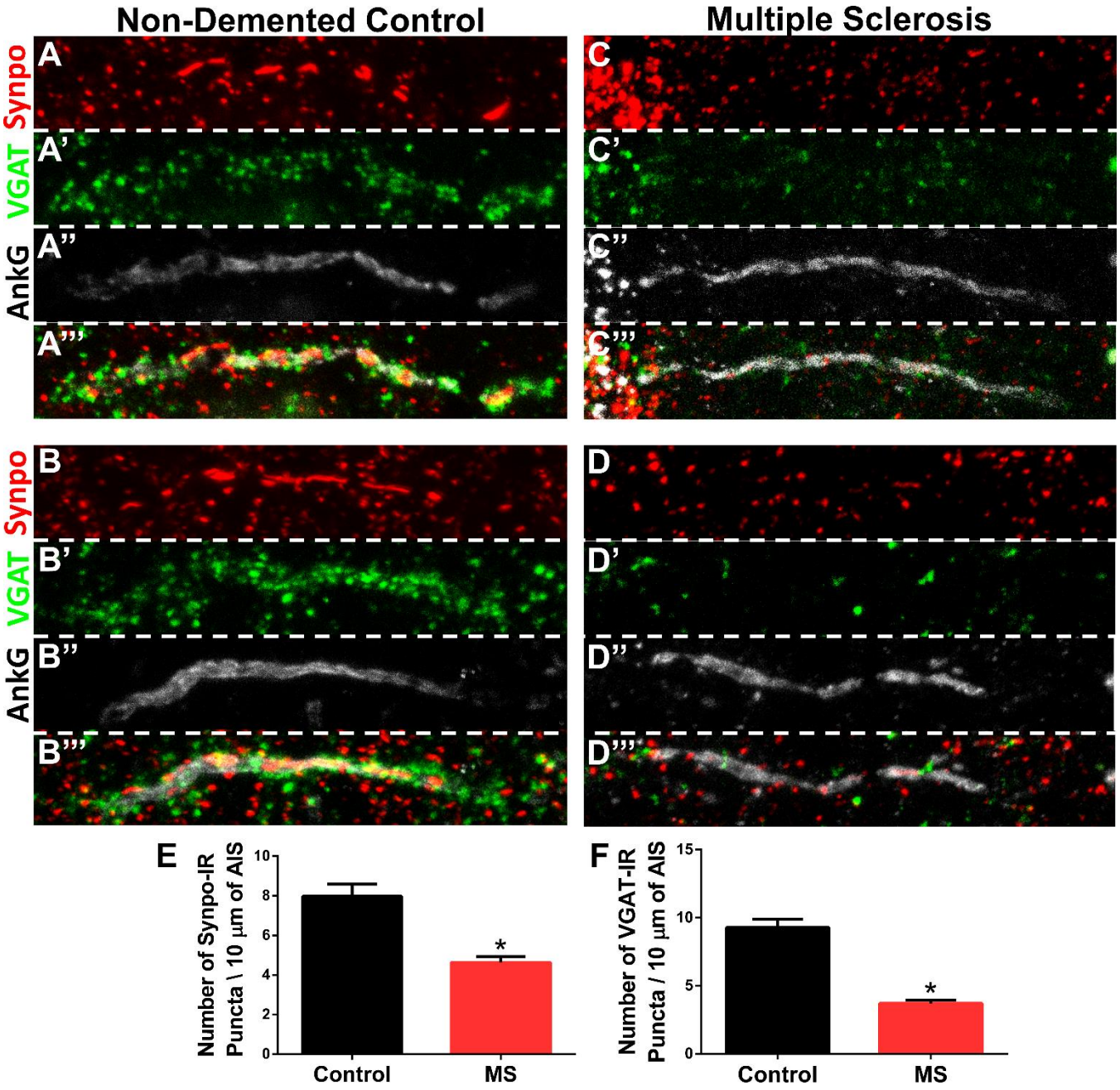
Non-Demented Control
Multiple Sclerosis
Synpo
VGAT
AnkG
A
A'
A''
A'''
C
C'
C''
C'''
B
B'
B''
B'''
D
D'
D''
D'''
E
Number of Synpo-IR Puncta \ 10 μm of AIS
10
8
6
4
2
0
*
Control
MS
F
Number of VGAT-IR Puncta / 10 μm of AIS
15
10
5
0
*
Control
MS

Figure 4.6. The cisternal organelle and axo-axonic GABAergic synaptic terminals on the AIS are lost in postmortem MS tissue. Representative AISs ($AnkG^+$, grey) immunolabeled in non-demented control (A,B) and multiple sclerosis (MS) (C,D) tissue reveal significant fewer $Synpo^+$ COs (red) and $VGAT^+$ GABAergic synaptic terminals (green) in disease. Quantitation of the number of these $Synpo^+$ (E) and $VGAT^+$ (F) structures, as a function of AIS length (per 10 µm), revealed significant reductions in MS tissue. Asterisks represent a significant difference from the control group ($^*p < 0.05$).

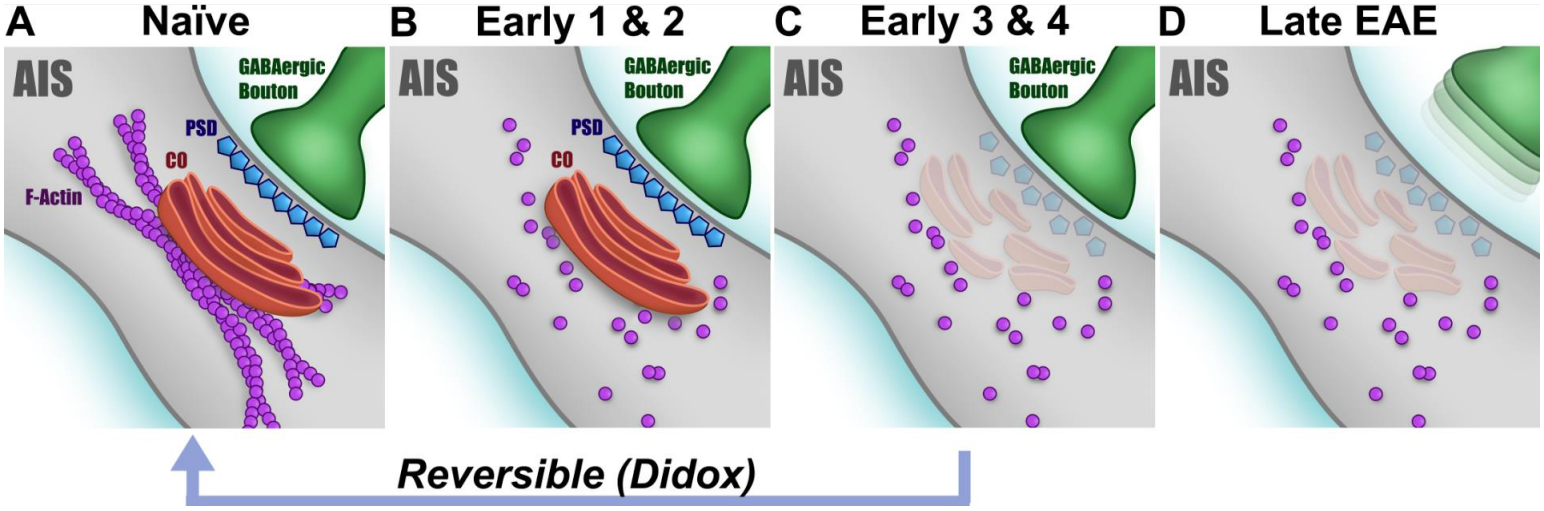
A
Naïve
AIS
GABAergic Bouton
PSD
CO
F-Actin
B
Early 1 & 2
AIS
GABAergic Bouton
PSD
CO
C
Early 3 & 4
AIS
GABAergic Bouton
D
Late EAE
AIS
Reversible (Didox)

Figure 4.7. Summary of findings for F-actin, cisternal organelle, and GABAergic synaptic disruption along EAE disease progression. Naïve mice present with intact filamentous actin (F-actin), cisternal organelle (CO), and an axo-axonic synaptic complex (composed of post synaptic density (PSD) and GABAergic Bouton) at the AIS. Destabilization of F-actin clustering is first observed in the early stages of the disease (Early EAE 1&2 (B)) preceding CO and axo-axonic GABAergic complex disruption. As the disease progresses, initial signs of CO loss are detected (Early EAE 3&4 mice (C)) preceding loss of axo-axonic GABAergic presynaptic clustering (VGAT), but coincident with reduced postsynaptic density (PSD) clustering at the AIS. In the later and more severe stages of disease (Late EAE (D)), loss of F-actin, COs, and axo-axonic GABAergic terminals is prevalent. Encouragingly, F-actin depolymerization, CO disruption, and loss of the GABAergic axo-axonic complex may be reversible (blue arrow); however, the therapeutic window for recovery has not been determined.

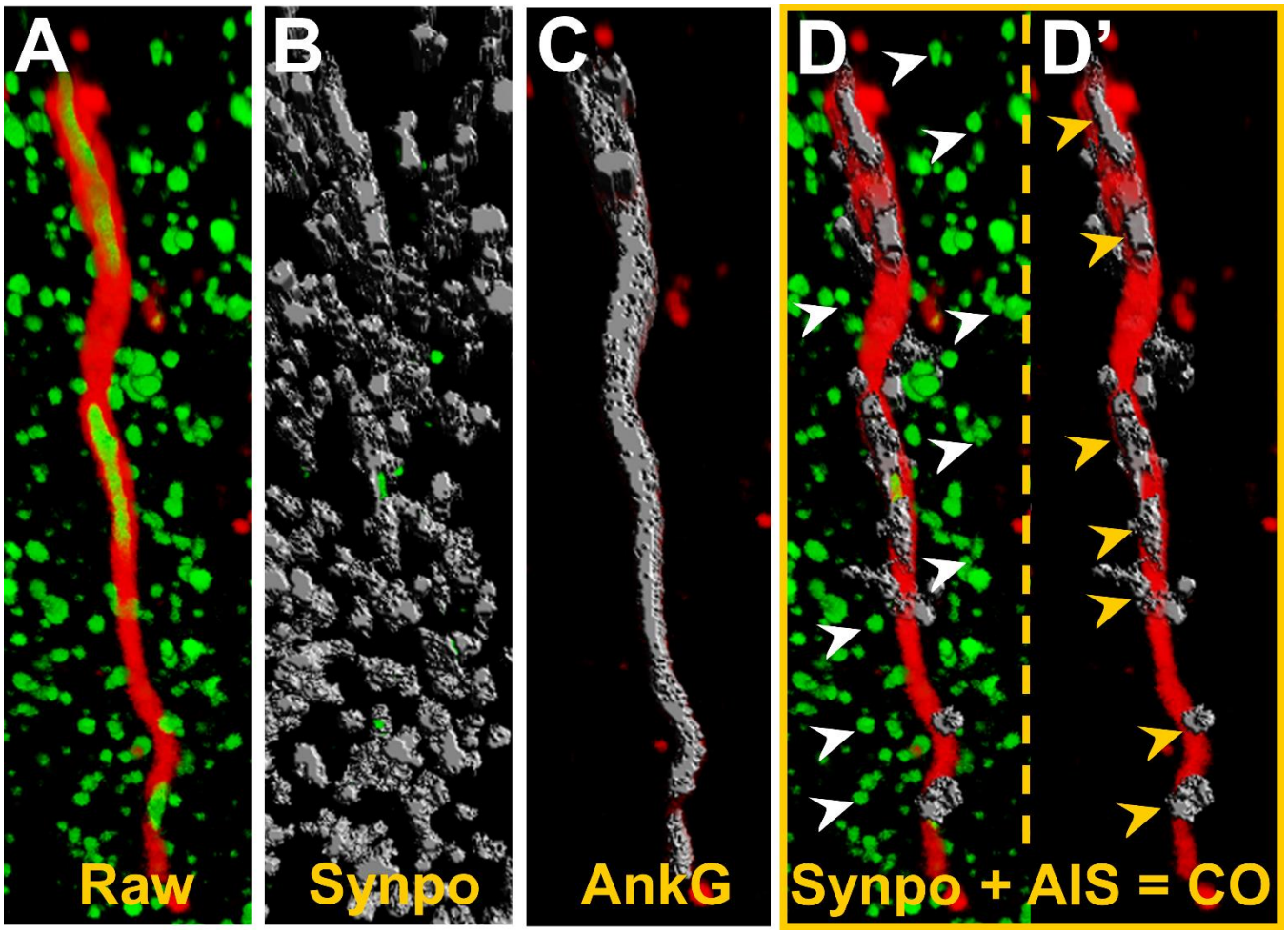
A
B
C
D
D'
Raw
Synpo
AnkG
Synpo + AIS = CO

Supplementary Figure S4.1. Methodology of 3D automated image analysis. A representative raw image with immunolabeling for synaptopodin (Synpo;green) and the AIS (AnkG, red) shows Synpo$^+$ puncta localized both at the AIS (termed the cisternal organelle), and outside the AIS (located on dendritic spines – termed the spine apparatus) (A). To focus our analysis specifically on the COs, Volocity™ 3D Image Analysis Software was used to select only those Synpo$^+$ puncta colocalized with AnkG (D', yellow arrows) in an automated fashion. This is performed through initial selection of total Synpo$^+$ (B) and AnkG$^+$ (C) positive objects, followed by exclusion of those Synpo$^+$ objects not colocalized with AnkG$^+$ structures (D, white arrows). Although Synpo is depicted as an example in this figure, all CO, F-actin, and GABAergic synapse analyses were performed using this quantifying approach.

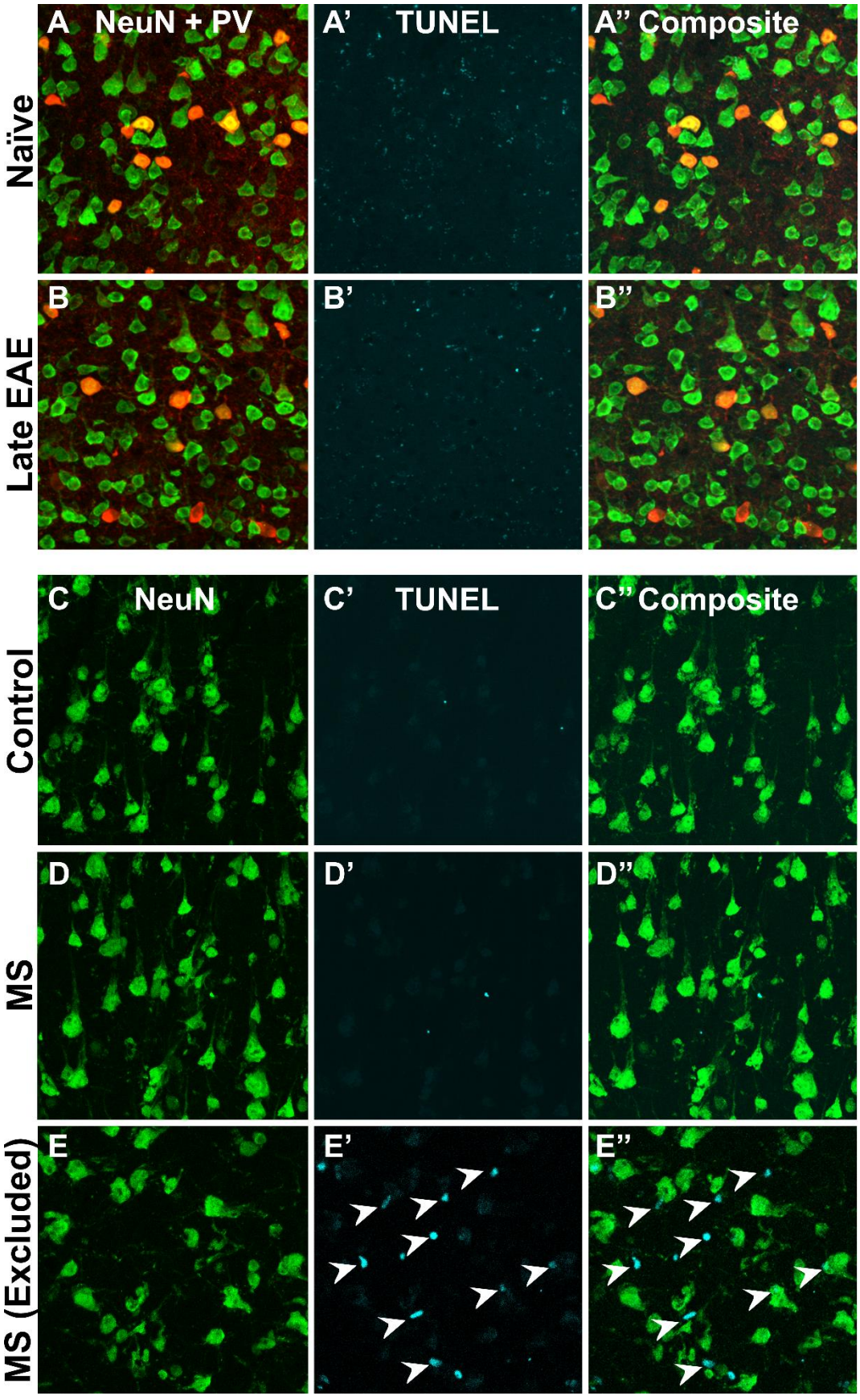
A NeuN + PV
A' TUNEL
A" Composite
Naïve
B
B'
B"
Late EAE
C NeuN
C' TUNEL
C" Composite
Control
D
D'
D"
MS
E
E'
E"
MS (Excluded)

Supplementary Figure S4.2. Neuronal loss was not detected in EAE or analyzed postmortem human MS tissue. Representative images of triple labelling for NeuN (green; total neurons), Parvalbumin (red; interneurons) and TUNEL (cyan) qualitatively show no apoptotic neurons in Naïve (A) or Late EAE mice (B). In contrast, some of the post mortem human Control (not shown) and MS (E; white arrows) samples revealed NeuN (green) and TUNEL (cyan) labelling indicative of apoptosis. These samples were excluded from analyses. All analyses were restricted to postmortem control (C) and MS tissue (D) that did not contain apoptotic neurons.

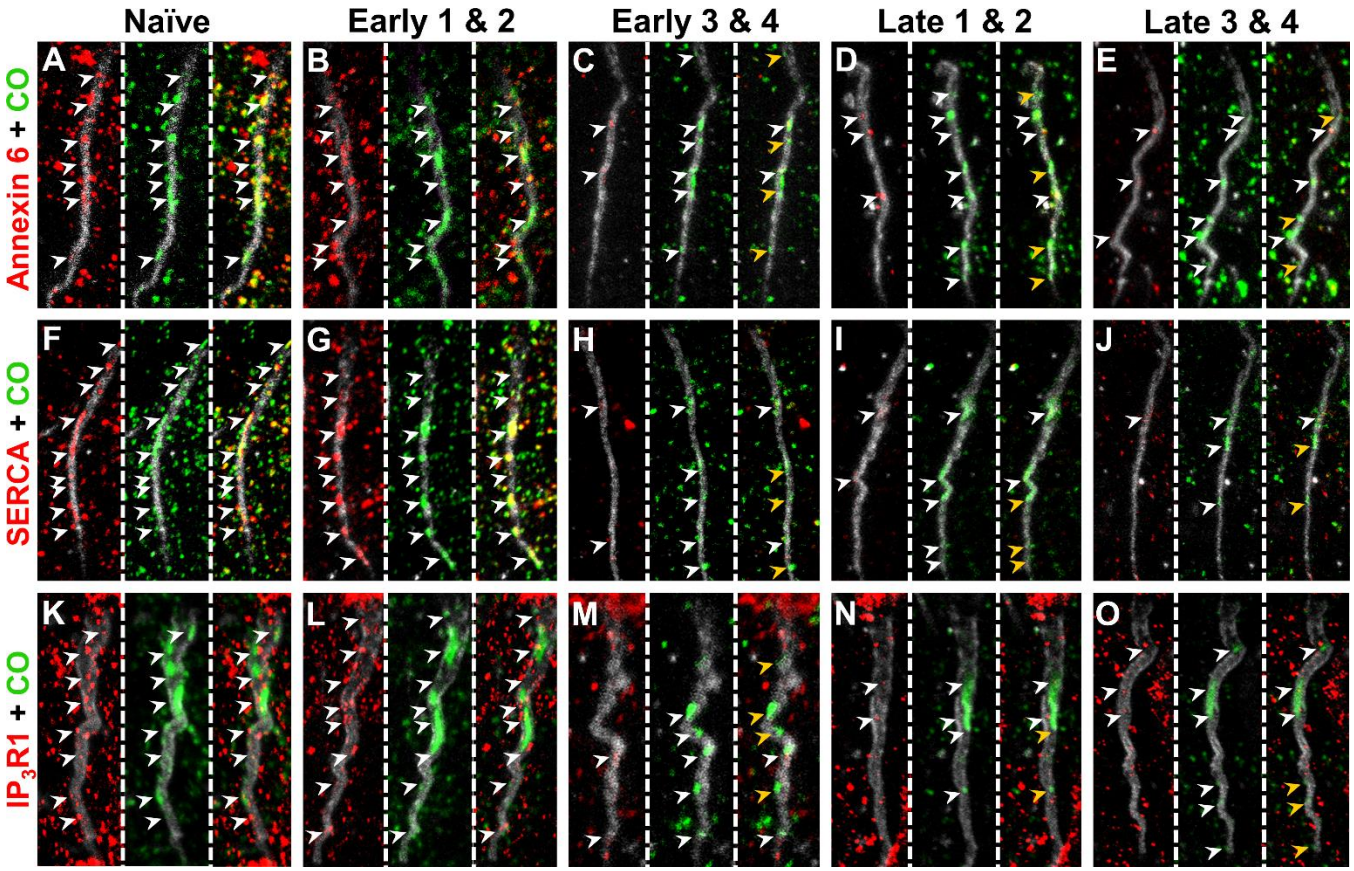
Naïve
Early 1 & 2
Early 3 & 4
Late 1 & 2
Late 3 & 4
Annexin 6 + CO
SERCA + CO
IP3R1 + CO
A
B
C
D
E
F
G
H
I
J
K
L
M
N
O

Supplementary Figure S4.3. Non-isosurface images from Figure 4.2. Non-isosurface raw images of triple labelled synpo, AnkG and either annexin 6, SERCA, or IP_3R1 from Figure 4.2.

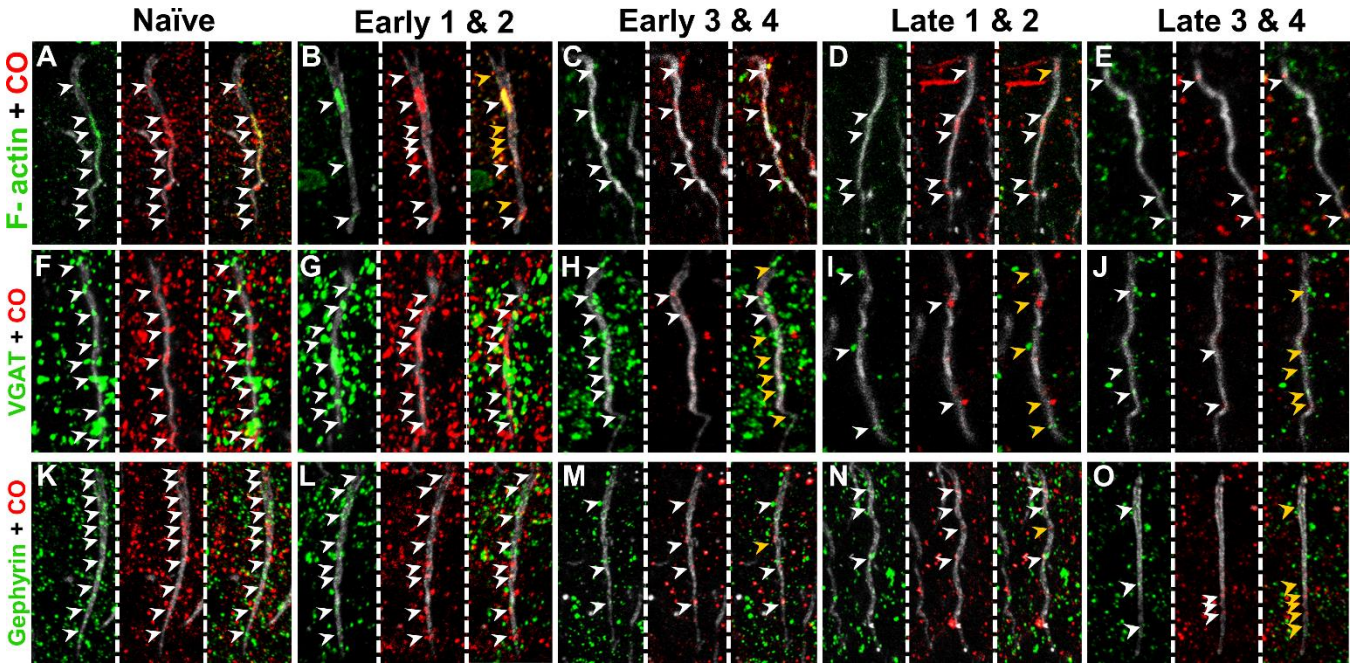
Naïve
Early 1 & 2
Early 3 & 4
Late 1 & 2
Late 3 & 4
F- actin + CO
VGAT + CO
Gephyrin + CO
A
B
C
D
E
F
G
H
I
J
K
L
M
N
O

Supplementary Figure S4.4. Non-isosurface images from Figures 4.3 and 4.4. Non-isosurface raw images of triple labelled synpo, AnkG and either phalloidin (F-actin), VGAT, or gephyrin from Figures 4.3 and 4.4.

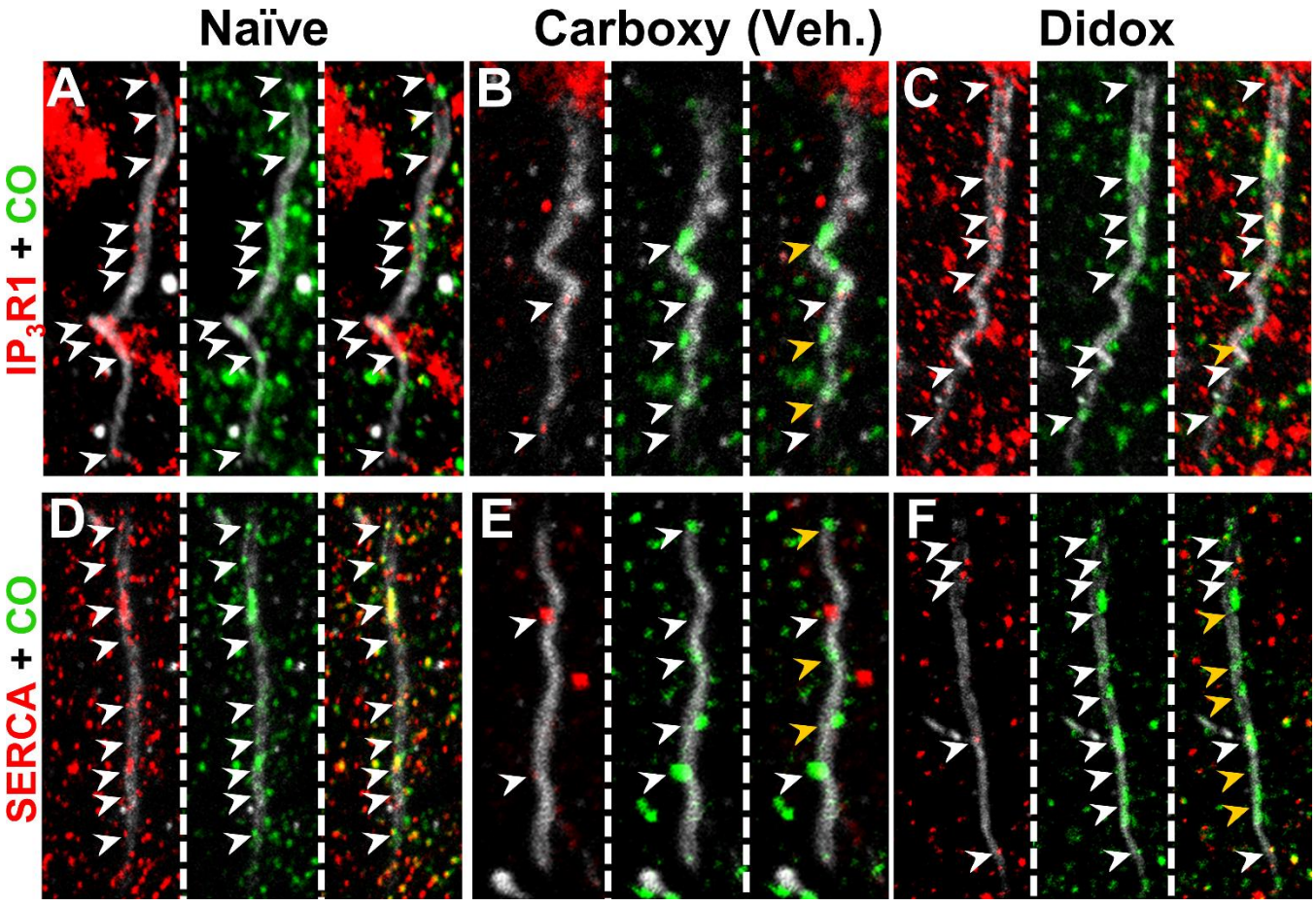
Naïve
Carboxy (Veh.)
Didox
A
B
C
D
E
F
IP3R1 + CO
SERCA + CO

Supplementary Figure S4.5. Non-isosurface images from Figure 4.5. Non-isosurface raw images of triple labelled synpo, AnkG and either SERCA, or IP_3R1 from Figure 4.5.

Supplementary Table S4.1. Summary of donor history and tissue characterization

Tissue ID	Sex	Age (years)	Diagnosis	MS Duration (years)	Postmortem Delay (hrs:min)	Brain Region
S11/044	M	51	Non-Demented Control	NA	7:45	Medial Temporal Gyrus
S95/056	F	86	Non-Demented Control	NA	13:30	Inferior Temporal Gyrus
S96/057	M	73	Non-Demented Control	NA	6:00	Superior Temporal Gyrus
S96/238	F	87	Non-Demented Control	NA	8:00	Inferior Temporal Gyrus
S96/251	M	84	Non-Demented Control	NA	9:00	Inferior Temporal Gyrus
S09/054	F	68	Multiple Sclerosis	4	8:25	Medial Temporal Gyrus
S10/085	F	57	Multiple Sclerosis	27	8:40	Medial Temporal Gyrus
S10/273	M	56	Multiple Sclerosis	14	9:50	Medial Temporal Gyrus
S11/048	M	53	Multiple Sclerosis	24	10:00	Medial Temporal Gyrus
S08/240	F	40	Multiple Sclerosis	6	8:55	Medial Temporal Gyrus
S08/302	F	77	Multiple Sclerosis	24	10:00	Medial Temporal Gyrus
S10/334	F	60	Multiple Sclerosis	7	10:40	Medial Temporal Gyrus
S11/080	F	56	Multiple Sclerosis	32	8:25	Medial Temporal Gyrus
S04/114	F	56	Multiple Sclerosis	20	6:35	Medial Temporal Gyrus
S96/102	F	74	Multiple Sclerosis	24	5:30	Inferior Temporal Gyrus
S96/115	F	57	Multiple Sclerosis	19	5:45	Inferior Temporal Gyrus
S07/127	F	48	Multiple Sclerosis	23	11:40	Medial Temporal Gyrus
S08/047	M	49	Multiple Sclerosis	25	8:00	Medial Temporal Gyrus
S09/251	M	75	Multiple Sclerosis	39	7:45	Medial Temporal Gyrus
S09/317	F	59	Multiple Sclerosis	24	4:45	Medial Temporal Gyrus
S10/052	M	44	Multiple Sclerosis	22	10:15	Medial Temporal Gyrus
S12/056	M	78	Multiple Sclerosis	33	8:45	Medial Temporal Gyrus
S96/232	F	40	Multiple Sclerosis	4	7:00	Medial Temporal Gyrus

Supplementary Table S4.2. Summary of markers used

Marker	Target Structure	Species/Isotype	Dilution	Manufacturer
Ankyrin-G (AnkG)	Axon Initial Segment	Mouse/IgG_{2a}	1:500	NeuroMab
βIV-Spectrin	Axon Initial Segment	Rabbit/IgG	1:500	Gift from Dr. Matthew Rasband
Synaptopodin (Synpo)	Cisternal Organelle	Mouse/IgG_1	1:100	OriGene
α-Actinin (α-Act)	Cisternal Organelle	Mouse/IgG_1	1:500	Thermo Fisher Scientific
Annexin 6 (A6)	Cisternal Organelle	Rabbit/IgG	1:500	Thermo Fisher Scientific
Sarco-endoplasmic reticulum Ca^{2+}-ATPase (SERCA)	Cisternal Organelle	Mouse/IgG_{2a}	1:250	Abcam
Inositol 1,4,5-trisphosphate receptor type 1 (IP_3R1)	Cisternal Organelle	Rabbit/IgG	1:250	Thermo Fisher Scientific
Vesicular GABA Transporter (VGAT)	Presynaptic GABAergic Synapses	Rabbit/IgG	1:500	Synaptic Systems
Gephyrin	Postsynaptic GABAergic Synapses	Mouse/IgG_{2b}	1:500	NeuroMab
Parvalbumin	PV^+ Neocortical Interneurons	Mouse/IgG_1	1:1000	MP Biomedicals
NeuN	Neuronal Nuclei	Rabbit/IgG	1:1000	Abcam
Phalloidin	Filamentous actin (F-actin)	NA	1:100	Thermo Fisher Scientific

CHAPTER FIVE

DISCUSSION

5.1 Synopsis

The focus of these studies was to better understand the stability and vulnerability of the axon initial segment in MS. While nodal disruption in MS was well characterized (Dupree et al., 2004; Coman et al., 2006; Howell et al., 2010; Pomicter et al., 2010; Zoupi et al., 2013), much less was known about the AIS, a compositionally similar axonal domain critical for neuronal function (Buttermore et al., 2013). To more effectively investigate the extent of AIS stability under hallmark conditions of MS pathogenesis, animal models of the disease were utilized and presented in Chapter 2. AIS integrity was assessed in both the cuprizone and EAE murine models, which are commonly used to recapitulate the demyelinating and inflammatory aspects of the disease, respectively (Kipp et al., 2017). Unlike the nodal domains, no changes in AIS stability were observed in the demyelinating cuprizone model. Extensive loss of AIS protein clustering was detected, however, following EAE induction. This disruption closely correlated with the inflammatory environment specifically with increased microglial reactivity and AIS contact (Figure 5.1). Treatment with a novel anti-inflammatory drug dampened the microglial response, attenuated AIS loss and restored AIS structure. This study revealed, for the first time, that the AIS, unlike the node of Ranvier, does not require myelin contact to maintain its integrity. This finding provides valuable insight into the pathogenesis of MS, as most neuronal insults in the disease are demonstrated to be consequential to myelin damage rather than primary pathogenic events. Furthermore, AIS alterations were found

to be driven by the local inflammatory environment suggesting that this mechanism of neuronal injury may not be restricted to MS pathogenesis.

While the study presented in Chapter 2 implicated the inflammatory environment in driving alterations at the AIS, the underlying mechanism remained unclear. The strongest insight was that oxidative stress was a key contributor as treatment with a free radical scavenger was capable of attenuating this insult. In order to investigate this further, we established an in vitro model that allowed us to more easily manipulate this AIS injury mechanism. In Chapter 3, AIS integrity was assessed in an in vitro primary cortical neuron system of oxidative stress induced through the application of SIN-1. The addition of this spontaneous ROS/RNS generator resulted in the loss of AIS stability, which was reversed upon resolution of the oxidative insult. ROS/RNS-induced AIS loss involves increased cytosolic Ca^{2+} entry specifically through L-type voltage-dependent Ca^{2+} channels and from IP_3-gated intracellular stores (Figure 5.1). These AIS alterations are also dependent upon activation of calpain, a Ca^{2+}-activated protease whose substrates include critical AIS components (Schafer et al., 2009) (Figure 5.1). Overall, we uncovered a mechanism of AIS injury driven by oxidative stress, a finding that could have implications for a variety of CNS pathologies.

Our lab and others have demonstrated that elevated levels of intracellular Ca^{2+} drive the pathologic mechanisms responsible for AIS disruption associated with ischemia, traumatic brain injury, Alzheimer's disease, epilepsy, and MS (Schafer et al., 2009; Baalman et al., 2013; Greer et al., 2013; Harty et al., 2013; Hinman et al., 2013; Hamada and Kole, 2015; Clark et al., 2016; Vascak et al., 2017). Therefore, elucidating the mechanisms that regulate local Ca^{2+} levels at the AIS is therefore vital to addressing the

AIS alterations associated with these pathologies. This led us to investigate the cisternal organelle (CO), an AIS-specific Ca^{2+}-storing organelle thought to regulate local cytosolic Ca^{2+} levels. Although this organelle may be central to AIS modulation, very little is known about the mechanisms regulating its stability and no pathological alterations have ever been described. To determine if CO integrity is altered coincident with AIS disruption, we performed morphological assessments in the EAE model in which severe AIS loss was previously observed. As presented in Chapter 4, extensive CO loss was detected and found to precede the AIS alterations in EAE (Figure 5.1). These changes were preceded by destabilization of F-actin at the AIS signifying a potential upstream trigger of CO instability under inflammatory conditions (Figure 5.1). Additionally, loss of GABAergic synapses at the AIS followed CO disruption consistent with the CO playing a critical role in stabilizing AIS axo-axonic synapses (Figure 5.1). Finally, CO disruption and loss of inhibitory synaptic complexes at the AIS were also detected in postmortem MS tissue. This study provided the first evidence of a pathologically-induced insult to the CO. Collectively, these studies provide crucial insight into the pathogenesis of not only MS, but an array of CNS insults in which axonal Ca^{2+} regulation is impaired.

5.2 The AIS and CO: Inflammatory Mediated Modulation

Findings from EAE and the *in vitro* system of oxidative stress implicate the inflammatory environment in modulation of AIS and CO stability. As described in the Introduction, the MS inflammatory environment involves immune mediators including peripheral lymphocytes and resident CNS microglia with the peripheral lymphocytes believed to prime and drive the microglial response (Larochelle et al., 2011). For this

reason, the present studies have largely focused on the contribution of microglia, rather than peripheral lymphocytes to AIS and CO instability under these inflammatory conditions. As described above, microglia have biphasic roles in MS pathogenesis exhibiting reactivity states that are either pro-inflammatory or resolving depending on the stage of CNS damage (Luo et al., 2017). Fortunately for the characterization of MS driven AIS insult, these phenomena are recapitulated separately in the cuprizone and EAE models in which microglia exhibit reparative or destructive reactivity profiles respectively (Gao and Tsirka, 2011; Clemente et al., 2013). While microglia make close associations with the AIS in the non-inflamed state (Baalman et al., 2015), increased AIS-contacts were made by microglia displaying both types of reactivity profiles in the two models as presented in Chapter 2. The increased AIS associations by pro-inflammatory microglia in EAE, however, likely have destructive rather than protective consequences for the AIS providing a possible explanation for the differential outcomes on AIS stability seen between the cuprizone and EAE models.

While microglia appear to be the modulators of AIS and CO disruption in EAE, oxidative stress is the likely downstream contributor to AIS and CO instability, as free radical scavenger treatment prevented and/or reversed these insults. As presented in Chapter 3, further characterization in an *in vitro* model of oxidative stress revealed that exogenously applied ROS/RNS was sufficient to induce changes to the AIS complex. This is likely contributing to the AIS disruption observed in EAE since microglia produce ROS/RNS (Guemez-Gamboa et al., 2011) in close proximity to the AIS. Due to the lability of ROS/RNS (Forkink et al., 2010), the most destructive effects would likely be observed in microglial-contacted rather than uncontacted AISs. While AIS disruption, as detected

through AnkG and βIV spectrin localization, closely correlated to microglial reactivity and contact in EAE, the present studies did not make this correlation for the CO. As presented in Chapter 4, CO disruption was first detected at the Early disease stage in mice exhibiting severe clinical scores (3 & 4), a time point and disease stage following detectable microglial reactivity and contact with the AIS (Chapter 2). Therefore, it is possible that microglia also drive CO disruption in EAE. Additionally, using the same free radical scavenger treatment paradigm as in Chapter 2, CO loss was attenuated much like that of disrupted AnkG localization. This implies that CO disruption can occur through ROS/RNS-induced insult as well. As discussed in Chapter 3, previous studies demonstrated oxidative stress-induced alterations to F-actin polymerization (Munnamalai et al., 2014), a component of the AIS cytoskeleton that is essential for proper CO maintenance (Sánchez-Ponce et al., 2011). Therefore, to further understand the mechanisms underlying these insults it would be important to investigate F-actin and CO stability following exogenous ROS/RNS treatment with SIN-1 *in vitro* and correlate the timing of this potential disruption to AnkG loss.

5.3 The AIS and CO: Calpain Mediated Modulation

As described in the Introduction, calpain protease activation underlies AIS disruption in a variety of CNS insults (Buffington and Rasband, 2011), including the ROS/RNS-induced insult presented in Chapter 3. Additional work in our lab revealed attenuation of LPS-induced AIS disruption following *in vivo* administration of a calpain inhibitor (Benusa et al., 2017) further implicating this protease in AIS modulation under inflammatory conditions. Previous studies have implicated calpain in MS pathogenesis with a proposed

role in myelin proteolytic breakdown (Rosenberger, 2014). Here, we propose an additional role for calpain under the inflammatory conditions associated with MS in targeting the AIS complex for disruption. Interestingly, calpain inhibition in the EAE model results in alleviation of clinical scores (Rosenberger, 2014); AIS stability, however, remains to be assessed.

In addition to AIS protein clustering, the relationship between CO stability and calpain activity remains elusive, but interesting. While no study has investigated this relationship specifically, calpain activation may occur both upstream and downstream of CO disruption under inflammatory conditions. For example, drebrin, an actin binding and F-actin stabilizing protein, is a known target of calpain mediated proteolysis, resulting in F-actin depolymerization (Chimura et al., 2015). This supports a role for calpain upstream of CO disruption since depolymerization of F-actin results in loss of CO stability (Sánchez-Ponce et al., 2011). In contrast, because calpain activation requires large Ca^{2+} influx, it is also likely that protease activation would be a downstream consequence of CO loss, since this organelle is responsible for regulation of cytosolic Ca^{2+} levels (Benedeczky et al., 1994; Sánchez-Ponce et al., 2011). Supporting this possibility, Chapter 3 demonstrates the involvement of IP_3-gated intracellular Ca^{2+} stores in ROS/RNS-induced AIS disruption. We propose that the receptors contributing to Ca^{2+} release at the AIS following this insult were those present on the CO which releases Ca^{2+} in an IP_3-gated manner (Benedeczky et al., 1994; Sánchez-Ponce et al., 2011). Because calpain requires micromolar to millimolar levels of Ca^{2+} for activation, cell death cascades could be activated if threshold levels are achieved cell-wide (Baudry and Bi, 2016). Perhaps the CO, instead, allows for local Ca^{2+} release at these levels specifically at the AIS to restrict

calpain activation to this axonal compartment. Further investigation in the SIN-1 *in vitro* model is required to elucidate the relationship between the CO and calpain during ROS/RNS-induced AIS disruption.

5.4 **Implications for MS Pathogenesis and Treatment**

Here, we describe two previously unidentified neuronal insults in MS: disruption of the CO and loss of axo-axonic GABAergic synaptic complexes at the AIS (Chapter 4). We propose that these pathologies have detrimental effects on neuronal function since Ca^{2+} dysregulation at the AIS leads to a dysfunctional trigger zone and loss of neuronal polarity (Buffington and Rasband, 2011). Additionally, loss of GABAergic input at the AIS could also impair neuronal firing capabilities (Jamann et al., 2017) and contribute to the impaired GABAergic network seen in the EAE model and MS patients (Falco et al., 2014; Arpin et al. 2017).

Since we believe these insults have the potential to contribute to MS disability, and have demonstrated them to be driven by the inflammatory environment, it remains to be determined why currently prescribed immunomodulatory MS therapies are not effective. All currently approved MS therapies, while acting through slightly different mechanisms, aim to suppress the inflammatory response in a widespread fashion (Dargahi et al., 2017). Targeting the inflammatory response in this manner has proven more beneficial for the early phases of disease rather than later progressive stages (Torkildsen et al., 2016). It is possible that the AIS and CO insults highlighted in the present study are far more extensive in patients upon clinical presentation, and potentially beyond reversibility through anti-inflammatory treatment alone. In this case, it would be important to target

downstream of the inflammatory response. One such potential therapeutic target is calpain, the proteolytic effector of AIS disruption (Schafer et al., 2009; Del Puerto et al., 2015; Benned-Jensen et al., 2016), which may exhibit high levels of activation at the chronic stages of MS pathogenesis that is unaffected by dampening of the inflammatory response. Encouragingly, the SIN-1 *in vitro* study presented in Chapter 3 demonstrates repair of the AIS complex once calpain activity is reduced. Additionally, calpain inhibition in EAE has shown promise as mentioned above (Trager et al., 2014; Cagmat et al., 2015). Selectivity may be an issue, however, since calpain is required for certain endogenous neuronal functions (Cagmat et al., 2015).

5.5 Recommendations for Future Studies

While the present studies effectively characterize disruption of the AIS in EAE, technical challenges have prevented investigation of AIS protein clustering in postmortem tissue. As shown in Chapter 4, postmortem samples vary widely in collection time. This appears to have severe consequences on AnkG localizations since the AIS responds very rapidly to changes in neuronal activity (Evans et al., 2015) resulting in substantial AIS disruption (through AnkG localization) in the non-demented control in addition to the MS samples. In contrast, significant alterations to CO and GABAergic synaptic stability were detected in postmortem samples despite varying collection times (Chapter 4). These structures may be more resistant to the tissue processing issues seen with AnkG. Ultimately, in order to effectively investigate AIS disruption through AnkG immunolabeling in postmortem human tissue, it is important to obtain control and MS tissue that have much more consistent and reduced post-death collection times. Outside of collection

issues, differential AIS stability due to inconsistently affected CNS regions should be accounted for by pairing AIS assessments with lymphocytic and microglial markers to assess infiltration and activation, respectively. This would allow for a more effective correlation between AIS disruption and the varying degrees of inflammatory conditions with MS pathogenesis.

As described above, it would also be important to follow up the SIN-1 *in vitro* study with an investigation into the effects of exogenously applied ROS/RNS on the cisternal organelle. Correlating the CO disruption with that of the AIS is difficult in the EAE model since the first signs of insult appear concurrently at the Early 3&4 disease stage (Chapters 2 and 4). Since these structures exhibit mutual dependence for stability, understanding the order of events mechanistically is crucial for identifying therapeutic strategies. This study would involve application of SIN-1 followed by morphological assessments such as those performed in Chapter 4. Additionally, F-actin should be investigated as a potential target of ROS/RNS-induced insult since its stability is critical for CO maintenance at the AIS (Sánchez-Ponce et al., 2011). If F-actin depolymerization is targeted by oxidative stress, as hypothesized (Munnamalai and Suter, 2009; Munnamalai et al., 2014), an F-actin stabilizer such as jasplakinolide (Zhang et al., 2012) could be used to confirm F-actin's mechanistic positioning upstream of CO and AIS disruption under ROS/RNS-induced insult.

Finally, although we have demonstrated reversibility of AIS and CO disruption in EAE, it would be important to examine a more chronic disease state for more relevant therapeutic potential. Our designation of "late" disease is only nine days following achievement of peak clinical scores, a far cry from the chronic inflammatory conditions of

the human disease. It would be important to know if free radical scavenging is a viable therapeutic target for late stage disease. Additionally, as mentioned above, examining the therapeutic potential of targeting calpain, a downstream mediator of AIS complex destabilization (Schafer et al., 2009; Del Puerto et al., 2015; Benned-Jensen et al., 2016), is also critical for addressing reversibility of AIS insults following the chronic inflammatory conditions associated with MS.

5.6 Concluding Remarks

These studies identify disruption of the AIS and CO under the inflammatory environment of MS adding to the growing number of neuronal insults independent of myelin loss. Further characterization in EAE implicate microglia and the inflammatory environment of MS as drivers of AIS alterations. An *in vitro* primary neuronal system of oxidative stress allowed for elucidation of the mechanism underlying ROS/RNS-induced AIS insult revealing Ca^{2+} dysregulation to be central to these changes. Investigation of the CO, an important regulator of local Ca^{2+} levels at the AIS, in EAE and MS revealed the first described pathologically-induced alterations. CO loss was preceded by F-actin destabilization and followed by loss of GABAergic axo-axonic synaptic terminals at the AIS. Importantly both AIS and CO insults are reversible upon free radical scavenger treatment. Overall, these findings highlight the importance for the inclusion of primary neuronal insults, such as AIS and CO disruption, in future therapeutic strategies for MS.

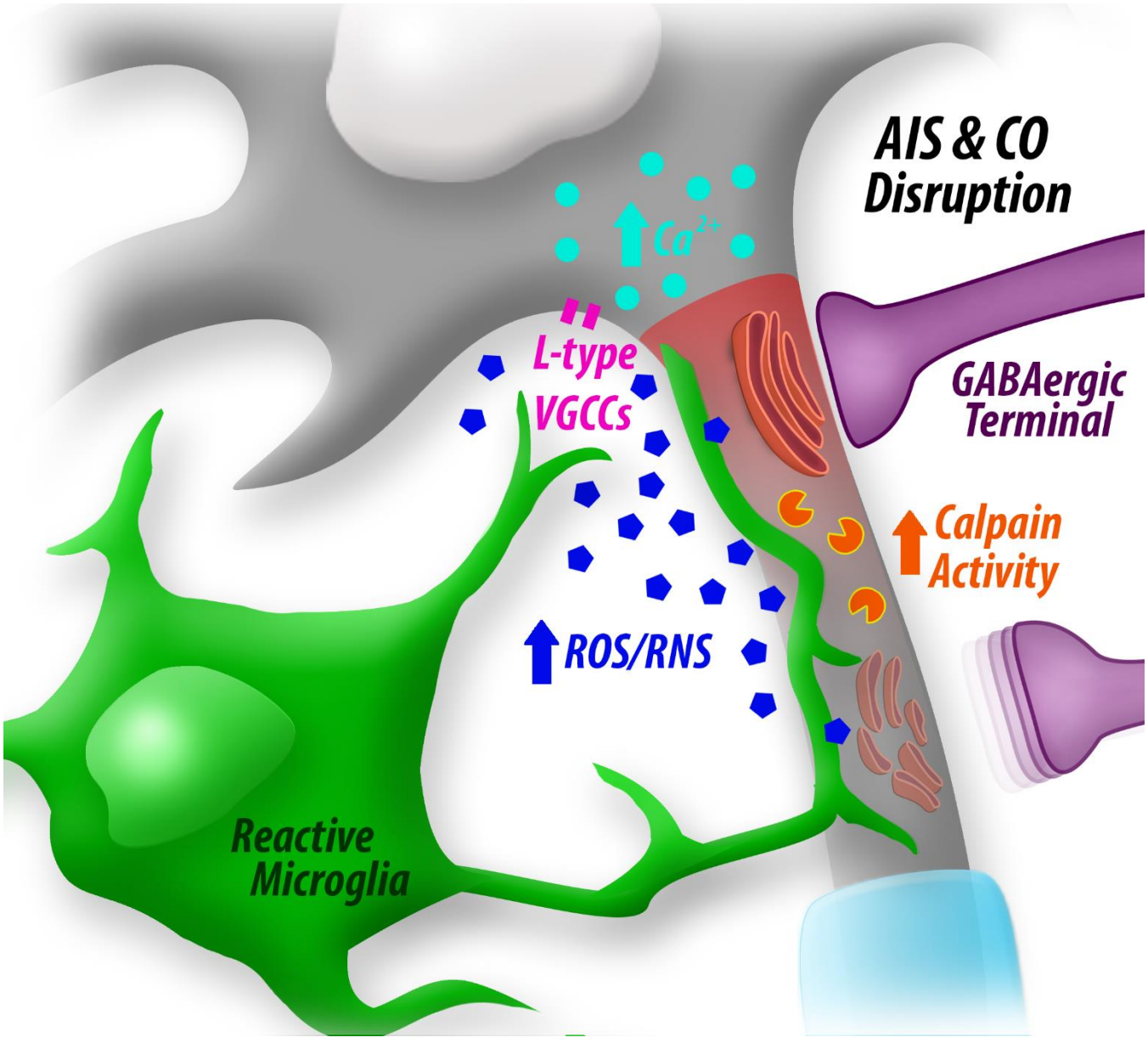
AIS & CO
Disruption
Ca2+
L-type
VGCCs
GABAergic
Terminal
Calpain
Activity
ROS/RNS
Reactive
Microglia

Figure 5.1. Proposed mechanism of inflammatory-induced AIS and CO disruption. Reactive microglia make increased associations with the AIS in EAE. These cells release ROS/RNS in close approximation to the neuron. L-type VGCCs and IP_3 receptors are both involved in ROS/RNS-induced AIS disruption. We hypothesize that the IP_3 receptors involved in this mechanism are located at the CO. The CO is also a target of ROS/RNS resulting in Ca^{2+} dysregulation locally at the AIS. This can lead to calpain activation and proteolysis of critical AIS complex protein such as AnkG. CO destabilization also results in loss of GABAergic axo-axonic synapses at the AIS. These presumed changes in activity level may also contribute to structural modification of the AIS complex.

LIST OF REFERENCES

Anonymous. TNF neutralization in MS: Results of a randomized, placebo-controlled multicenter study. the lenercept multiple sclerosis study group and the university of british columbia MS/MRI analysis group. 1999. Neurology 53(3):457-65.

Adachi R, Yamada R, Kuba H. 2014. Plasticity of the axonal trigger zone. Neuroscientist.

Adams DJ and Berecki G. 2013. Mechanisms of conotoxin inhibition of N-type (ca(v)2.2) calcium channels. Biochim Biophys Acta 1828(7):1619-28.

Aharoni R. 2014. Immunomodulation neuroprotection and remyelination - the fundamental therapeutic effects of glatiramer acetate: A critical review. J Autoimmun 54:81-92.

Alcina A, Abad-Grau Mdel M, Fedetz M, Izquierdo G, Lucas M, Fernandez O, Ndagire D, Catala-Rabasa A, Ruiz A, Gayan J, et al. 2012. Multiple sclerosis risk variant HLA-DRB1*1501 associates with high expression of DRB1 gene in different human populations. PLoS One 7(1):e29819.

Allen JE and Sutherland TE. 2014. Host protective roles of type 2 immunity: Parasite killing and tissue repair, flip sides of the same coin. Semin Immunol 26(4):329-40.

Almanza A, Navarrete F, Vega R, Soto E. 2007. Modulation of voltage-gated Ca2+ current in vestibular hair cells by nitric oxide. J Neurophysiol 97(2):1188-95.

Almolda B, Gonzalez B, Castellano B. 2011. Antigen presentation in EAE: Role of microglia, macrophages and dendritic cells. Front Biosci (Landmark Ed) 16:1157-71.

Arancibia-Carcamo IL and Attwell D. 2014. The node of ranvier in CNS pathology. Acta Neuropathol 128(2):161-75.

Arpin DJ, Gehringer JE, Wilson TW, Kurz MJ. 2017. A reduced somatosensory gating response in individuals with multiple sclerosis is related to walking impairment. J Neurophysiol :jn.00260.2017.

Ascherio A and Munger KL. 2007. Environmental risk factors for multiple sclerosis. part I: The role of infection. Ann Neurol 61(4):288-99.

Baalman K, Marin MA, Ho TS, Godoy M, Cherian L, Robertson C, Rasband MN. 2015. Axon initial segment-associated microglia. J Neurosci 35(5):2283-92.

Baalman KL, Cotton RJ, Rasband SN, Rasband MN. 2013. Blast wave exposure impairs memory and decreases axon initial segment length. J Neurotrauma 30(9):741-51.

Babbe H, Roers A, Waisman A, Lassmann H, Goebels N, Hohlfeld R, Friese M, Schroder R, Deckert M, Schmidt S, et al. 2000. Clonal expansions of CD8(+) T cells dominate the T cell infiltrate in active multiple sclerosis lesions as shown by micromanipulation and single cell polymerase chain reaction. J Exp Med 192(3):393-404.

Badawi AH and Siahaan TJ. 2013. Suppression of MOG- and PLP-induced experimental autoimmune encephalomyelitis using a novel multivalent bifunctional peptide inhibitor. J Neuroimmunol 263(1-2):20-7.

Bailey SR, Nelson MH, Himes RA, Li Z, Mehrotra S, Paulos CM. 2014. Th17 cells in cancer: The ultimate identity crisis. Front Immunol 5:276.

Baker D and Amor S. 2015. Mouse models of multiple sclerosis: Lost in translation? Curr Pharm Des 21(18):2440-52.

Bamburg JR and Bernstein BW. 2016. Actin dynamics and cofilin-actin rods in alzheimer disease. Cytoskeleton (Hoboken) 73(9):477-97.

Bankoti J, Apeltsin L, Hauser SL, Allen S, Albertolle ME, Witkowska HE, von Budingen HC. 2014. In multiple sclerosis, oligoclonal bands connect to peripheral B-cell responses. Ann Neurol 75(2):266-76.

Barateiro A, Brites D, Fernandes A. 2016. Oligodendrocyte development and myelination in neurodevelopment: Molecular mechanisms in health and disease. Curr Pharm Des 22(6):656-79.

Bas Orth C, Schultz C, Muller CM, Frotscher M, Deller T. 2007. Loss of the cisternal organelle in the axon initial segment of cortical neurons in synaptopodin-deficient mice. J Comp Neurol 504(5):441-9.

Baudry M and Bi X. 2016. Calpain-1 and calpain-2: The yin and yang of synaptic plasticity and neurodegeneration. Trends Neurosci 39(4):235-45.

Beeton C, Garcia A, Chandy KG. 2007. Induction and clinical scoring of chronic-relapsing experimental autoimmune encephalomyelitis. J Vis Exp (5):224. doi(5):224.

Bekku Y, Rauch U, Ninomiya Y, Oohashi T. 2009. Brevican distinctively assembles extracellular components at the large diameter nodes of ranvier in the CNS. J Neurochem 108(5):1266-76.

Belbasis L, Bellou V, Evangelou E, Ioannidis JP, Tzoulaki I. 2015. Environmental risk factors and multiple sclerosis: An umbrella review of systematic reviews and meta-analyses. Lancet Neurol 14(3):263-73.

Benarroch EE. 2013. Microglia: Multiple roles in surveillance, circuit shaping, and response to injury. Neurology 81(12):1079-88.

Bender KJ and Trussell LO. 2012. The physiology of the axon initial segment. Annu Rev Neurosci 35:249-65.

Bender KJ, Ford CP, Trussell LO. 2010. Dopaminergic modulation of axon initial segment calcium channels regulates action potential initiation. Neuron 68(3):500-11.

Benedeczky I, Molnar E, Somogyi P. 1994. The cisternal organelle as a ca(2+)-storing compartment associated with GABAergic synapses in the axon initial segment of hippocampal pyramidal neurones. Exp Brain Res 101(2):216-30.

Benned-Jensen T, Christensen RK, Denti F, Perrier JF, Rasmussen HB, Olesen SP. 2016. Live imaging of Kv7.2/7.3 cell surface dynamics at the axon initial segment: High steady-state stability and calpain-dependent excitotoxic downregulation revealed. J Neurosci 36(7):2261-6.

Bennett V and Baines AJ. 2001. Spectrin and ankyrin-based pathways: Metazoan inventions for integrating cells into tissues. Physiol Rev 81(3):1353-92.

Ben-Nun A and Cohen IR. 1981. Vaccination against autoimmune encephalomyelitis (EAE): Attenuated autoimmune T lymphocytes confer resistance to induction of active EAE but not to EAE mediated by the intact T lymphocyte line. Eur J Immunol 11(11):949-52.

Benusa SD, George NM, Sword BA, DeVries GH, Dupree JL. 2017. Acute neuroinflammation induces AIS structural plasticity in a NOX2-dependent manner. J Neuroinflammation 14(1):116,017-0889-3.

Benveniste EN. 1997. Role of macrophages/microglia in multiple sclerosis and experimental allergic encephalomyelitis. J Mol Med (Berl) 75(3):165-73.

Berghs S, Aggujaro D, Dirkx R,Jr, Maksimova E, Stabach P, Hermel JM, Zhang JP, Philbrick W, Slepnev V, Ort T, et al. 2000. betaIV spectrin, a new spectrin localized at axon initial segments and nodes of ranvier in the central and peripheral nervous system. J Cell Biol 151(5):985-1002.

Bhat MA, Rios JC, Lu Y, Garcia-Fresco GP, Ching W, St Martin M, Li J, Einheber S, Chesler M, Rosenbluth J, et al. 2001. Axon-glia interactions and the domain

organization of myelinated axons requires neurexin IV/Caspr/Paranodin. Neuron 30(2):369-83.

Bhattacharjee A, Whitehurst RM,Jr, Zhang M, Wang L, Li M. 1997. T-type calcium channels facilitate insulin secretion by enhancing general excitability in the insulin-secreting beta-cell line, INS-1. Endocrinology 138(9):3735-40.

Bhave S, Elford H, McVoy MA. 2013. Ribonucleotide reductase inhibitors hydroxyurea, didox, and trimidox inhibit human cytomegalovirus replication in vitro and synergize with ganciclovir. Antiviral Res 100(1):151-8.

Bjartmar C, Kinkel RP, Kidd G, Rudick RA, Trapp BD. 2001. Axonal loss in normal-appearing white matter in a patient with acute MS. Neurology 57(7):1248-52.

Black JA, Newcombe J, Trapp BD, Waxman SG. 2007. Sodium channel expression within chronic multiple sclerosis plaques. J Neuropathol Exp Neurol 66(9):828-37.

Bo L. 2009. The histopathology of grey matter demyelination in multiple sclerosis. Acta Neurol Scand Suppl (189):51-7. doi(189):51-7.

Bove R and Chitnis T. 2013. Sexual disparities in the incidence and course of MS. Clin Immunol 149(2):201-10.

Breed ER, Lee ST, Hogquist KA. 2017. Directing T cell fate: How thymic antigen presenting cells coordinate thymocyte selection. Semin Cell Dev Biol .

Britt DJ, Farias GG, Guardia CM, Bonifacino JS. 2016. Mechanisms of polarized organelle distribution in neurons. Front Cell Neurosci 10:88.

Brownlee WJ and Miller DH. 2014. Clinically isolated syndromes and the relationship to multiple sclerosis. J Clin Neurosci 21(12):2065-71.

Brucklacher-Waldert V, Stuerner K, Kolster M, Wolthausen J, Tolosa E. 2009. Phenotypical and functional characterization of T helper 17 cells in multiple sclerosis. Brain 132(Pt 12):3329-41.

Brucklacher-Waldert V, Steinbach K, Lioznov M, Kolster M, Holscher C, Tolosa E. 2009. Phenotypical characterization of human Th17 cells unambiguously identified by surface IL-17A expression. J Immunol 183(9):5494-501.

Buffington SA and Rasband MN. 2013. Na+ channel-dependent recruitment of Navbeta4 to axon initial segments and nodes of ranvier. J Neurosci 33(14):6191-202.

Buffington SA and Rasband MN. 2011. The axon initial segment in nervous system disease and injury. Eur J Neurosci 34(10):1609-19.

Buhse M. 2015. The elderly person with multiple sclerosis: Clinical implications for the increasing life-span. J Neurosci Nurs 47(6):333,9; quiz E1.

Burnard S, Lechner-Scott J, Scott RJ. 2017. EBV and MS: Major cause, minor contribution or red-herring? Mult Scler Relat Disord 16:24-30.

Buschmann JP, Berger K, Awad H, Clarner T, Beyer C, Kipp M. 2012. Inflammatory response and chemokine expression in the white matter corpus callosum and gray matter cortex region during cuprizone-induced demyelination. J Mol Neurosci 48(1):66-76.

Buttermore ED, Thaxton CL, Bhat MA. 2013. Organization and maintenance of molecular domains in myelinated axons. J Neurosci Res 91(5):603-22.

Buttermore ED, Dupree JL, Cheng J, An X, Tessarollo L, Bhat MA. 2011. The cytoskeletal adaptor protein band 4.1B is required for the maintenance of paranodal axoglial septate junctions in myelinated axons. J Neurosci 31(22):8013-24.

Cagmat EB, Guingab-Cagmat JD, Vakulenko AV, Hayes RL, Anagli J. 2015. Potential use of calpain inhibitors as brain injury therapy. In: Brain neurotrauma: Molecular, neuropsychological, and rehabilitation aspects. Kobeissy FH, editor. Boca Raton (FL): by Taylor & Francis Group, LLC.

Cain SM and Snutch TP. 2013. T-type calcium channels in burst-firing, network synchrony, and epilepsy. Biochim Biophys Acta 1828(7):1572-8.

Cappa R, Theroux L, Brenton JN. 2017. Pediatric multiple sclerosis: Genes, environment, and a comprehensive therapeutic approach. Pediatr Neurol 75:17-28.

Carletti B, Passarelli C, Sparaco M, Tozzi G, Pastore A, Bertini E, Piemonte F. 2011. Effect of protein glutathionylation on neuronal cytoskeleton: A potential link to neurodegeneration. Neuroscience 192:285-94.

Caslin HL, McLeod JJA, Spence AJ, Qayum AA, Kolawole EM, Taruselli MT, Paranjape A, Elford HL, Ryan JJ. 2017. Didox (3,4-dihydroxybenzohydroxamic acid) suppresses IL-33-induced cytokine production in primary mouse mast cells. Cell Immunol 319:10-6.

Catterall WA. 2011. Voltage-gated calcium channels. Cold Spring Harb Perspect Biol 3(8):a003947.

Chang KJ and Rasband MN. 2013. Excitable domains of myelinated nerves: Axon initial segments and nodes of ranvier. Curr Top Membr 72:159-92.

Chastain EM, Duncan DS, Rodgers JM, Miller SD. 2011. The role of antigen presenting cells in multiple sclerosis. Biochim Biophys Acta 1812(2):265-74.

Choii G and Ko J. 2015. Gephyrin: A central GABAergic synapse organizer. Exp Mol Med 47:e158.

Ciccarelli O, Barkhof F, Bodini B, De Stefano N, Golay X, Nicolay K, Pelletier D, Pouwels PJ, Smith SA, Wheeler-Kingshott CA, et al. 2014. Pathogenesis of multiple sclerosis: Insights from molecular and metabolic imaging. Lancet Neurol 13(8):807-22.

Clark KC, Josephson A, Benusa SD, Hartley RK, Baer M, Thummala S, Joslyn M, Sword BA, Elford H, Oh U, et al. 2016. Compromised axon initial segment integrity in EAE is preceded by microglial reactivity and contact. Glia 64(7):1190-209.

Claycomb KI, Johnson KM, Winokur PN, Sacino AV, Crocker SJ. 2013. Astrocyte regulation of CNS inflammation and remyelination. Brain Sci 3(3):1109-27.

Clemente D, Ortega MC, Melero-Jerez C, de Castro F. 2013. The effect of glia-glia interactions on oligodendrocyte precursor cell biology during development and in demyelinating diseases. Front Cell Neurosci 7:268.

Coman I, Aigrot MS, Seilhean D, Reynolds R, Girault JA, Zalc B, Lubetzki C. 2006. Nodal, paranodal and juxtaparanodal axonal proteins during demyelination and remyelination in multiple sclerosis. Brain 129(Pt 12):3186-95.

Cree BA, Lamb S, Morgan K, Chen A, Waubant E, Genain C. 2005. An open label study of the effects of rituximab in neuromyelitis optica. Neurology 64(7):1270-2.

Criste G, Trapp B, Dutta R. 2014. Axonal loss in multiple sclerosis: Causes and mechanisms. Handb Clin Neurol 122:101-13.

Cross AK and Woodroofe MN. 1999. Chemokines induce migration and changes in actin polymerization in adult rat brain microglia and a human fetal microglial cell line in vitro. J Neurosci Res 55(1):17-23.

Croxford JL, Olson JK, Miller SD. 2002. Epitope spreading and molecular mimicry as triggers of autoimmunity in the theiler's virus-induced demyelinating disease model of multiple sclerosis. Autoimmun Rev 1(5):251-60.

Dargahi N, Katsara M, Tselios T, Androutsou ME, de Courten M, Matsoukas J, Apostolopoulos V. 2017. Multiple sclerosis: Immunopathology and treatment update. Brain Sci 7(7):10.3390/brainsci7070078.

Das A, Guyton MK, Smith A, Wallace G,4th, McDowell ML, Matzelle DD, Ray SK, Banik NL. 2013. Calpain inhibitor attenuated optic nerve damage in acute optic neuritis in rats. J Neurochem 124(1):133-46.

Davis JQ, Lambert S, Bennett V. 1996. Molecular composition of the node of ranvier: Identification of ankyrin-binding cell adhesion molecules neurofascin (mucin+/third FNIII domain-) and NrCAM at nodal axon segments. J Cell Biol 135(5):1355-67.

de Lahunta A, Glass EN, Kent M. 2016. Embryonic development of the central nervous system. Vet Clin North Am Small Anim Pract 46(2):193-216.

De Simoni S, Linard D, Hermans E, Knoops B, Goemaere J. 2013. Mitochondrial peroxiredoxin-5 as potential modulator of mitochondria-ER crosstalk in MPP+-induced cell death. J Neurochem 125(3):473-85.

De Stefano N, Matthews PM, Fu L, Narayanan S, Stanley J, Francis GS, Antel JP, Arnold DL. 1998. Axonal damage correlates with disability in patients with relapsing-remitting multiple sclerosis. results of a longitudinal magnetic resonance spectroscopy study. Brain 121 (Pt 8)(Pt 8):1469-77.

DeHaven WI, Smyth JT, Boyles RR, Bird GS, Putney JW,Jr. 2008. Complex actions of 2-aminoethyldiphenyl borate on store-operated calcium entry. J Biol Chem 283(28):19265-73.

Del Puerto A, Fronzaroli-Molinieres L, Perez-Alvarez MJ, Giraud P, Carlier E, Wandosell F, Debanne D, Garrido JJ. 2015. ATP-P2X7 receptor modulates axon initial segment composition and function in physiological conditions and brain injury. Cereb Cortex 25(8):2282-94.

Delbro D, Westerlund A, Bjorklund U, Hansson E. 2009. In inflammatory reactive astrocytes co-cultured with brain endothelial cells nicotine-evoked ca(2+) transients are attenuated due to interleukin-1beta release and rearrangement of actin filaments. Neuroscience 159(2):770-9.

DeLuca GC, Williams K, Evangelou N, Ebers GC, Esiri MM. 2006. The contribution of demyelination to axonal loss in multiple sclerosis. Brain 129(Pt 6):1507-16.

Denic A, Johnson AJ, Bieber AJ, Warrington AE, Rodriguez M, Pirko I. 2011. The relevance of animal models in multiple sclerosis research. Pathophysiology 18(1):21-9.

DePaula-Silva AB, Hanak TJ, Libbey JE, Fujinami RS. 2017. Theiler's murine encephalomyelitis virus infection of SJL/J and C57BL/6J mice: Models for multiple sclerosis and epilepsy. J Neuroimmunol 308:30-42.

Desmazieres A, Sol-Foulon N, Lubetzki C. 2012. Changes at the nodal and perinodal axonal domains: A basis for multiple sclerosis pathology? Mult Scler 18(2):133-7.

DeVries GH. 2004. Cryptic axonal antigens and axonal loss in multiple sclerosis. Neurochem Res 29(11):1999-2006.

Didonna A and Oksenberg JR. 2015. Genetic determinants of risk and progression in multiple sclerosis. Clin Chim Acta 449:16-22.

Donkor IO. 2015. An updated patent review of calpain inhibitors (2012 - 2014). Expert Opin Ther Pat 25(1):17-31.

Doring A, Sloka S, Lau L, Mishra M, van Minnen J, Zhang X, Kinniburgh D, Rivest S, Yong VW. 2015. Stimulation of monocytes, macrophages, and microglia by amphotericin B and macrophage colony-stimulating factor promotes remyelination. J Neurosci 35(3):1136-48.

Dos Passos GR, Sato DK, Becker J, Fujihara K. 2016. Th17 cells pathways in multiple sclerosis and neuromyelitis optica spectrum disorders: Pathophysiological and therapeutic implications. Mediators Inflamm 2016:5314541.

Dours-Zimmermann MT, Maurer K, Rauch U, Stoffel W, Fassler R, Zimmermann DR. 2009. Versican V2 assembles the extracellular matrix surrounding the nodes of ranvier in the CNS. J Neurosci 29(24):7731-42.

Duffy SS, Keating BA, Perera CJ, Moalem-Taylor G. 2017. The role of regulatory T cells in nervous system pathologies. J Neurosci Res .

Dupree JL, Girault JA, Popko B. 1999. Axo-glial interactions regulate the localization of axonal paranodal proteins. J Cell Biol 147(6):1145-52.

Dupree JL, Polak PE, Hensley K, Pelligrino D, Feinstein DL. 2015. Lanthionine ketimine ester provides benefit in a mouse model of multiple sclerosis. J Neurochem 134(2):302-14.

Dupree JL, Coetzee T, Blight A, Suzuki K, Popko B. 1998. Myelin galactolipids are essential for proper node of ranvier formation in the CNS. J Neurosci 18(5):1642-9.

Dupree JL, Mason JL, Marcus JR, Stull M, Levinson R, Matsushima GK, Popko B. 2004. Oligodendrocytes assist in the maintenance of sodium channel clusters independent of the myelin sheath. Neuron Glia Biol 1(3):179-92.

Dutta R and Trapp BD. 2011. Mechanisms of neuronal dysfunction and degeneration in multiple sclerosis. Prog Neurobiol 93(1):1-12.

Dutta R, Chang A, Doud MK, Kidd GJ, Ribaudo MV, Young EA, Fox RJ, Staugaitis SM, Trapp BD. 2011. Demyelination causes synaptic alterations in hippocampi from multiple sclerosis patients. Ann Neurol 69(3):445-54.

Dutta R, McDonough J, Yin X, Peterson J, Chang A, Torres T, Gudz T, Macklin WB, Lewis DA, Fox RJ, et al. 2006. Mitochondrial dysfunction as a cause of axonal degeneration in multiple sclerosis patients. Ann Neurol 59(3):478-89.

Dzhashiashvili Y, Zhang Y, Galinska J, Lam I, Grumet M, Salzer JL. 2007. Nodes of ranvier and axon initial segments are ankyrin G-dependent domains that assemble by distinct mechanisms. J Cell Biol 177(5):857-70.

Eisner D. 2014. Calcium in the heart: From physiology to disease. Exp Physiol 99(10):1273-82.

Elaib Z, Saller F, Bobe R. 2016. The calcium entry-calcium refilling coupling. Adv Exp Med Biol 898:333-52.

El-Husseini AE, Topinka JR, Lehrer-Graiwer JE, Firestein BL, Craven SE, Aoki C, Bredt DS. 2000. Ion channel clustering by membrane-associated guanylate kinases. differential regulation by N-terminal lipid and metal binding motifs. J Biol Chem 275(31):23904-10.

Eshed-Eisenbach Y and Peles E. 2013. The making of a node: A co-production of neurons and glia. Curr Opin Neurobiol 23(6):1049-56.

Evans MD, Dumitrescu AS, Kruijssen DLH, Taylor SE, Grubb MS. 2015. Rapid modulation of axon initial segment length influences repetitive spike firing. Cell Rep 13(6):1233-45.

Evans MD, Sammons RP, Lebron S, Dumitrescu AS, Watkins TB, Uebele VN, Renger JJ, Grubb MS. 2013. Calcineurin signaling mediates activity-dependent relocation of the axon initial segment. J Neurosci 33(16):6950-63.

Fairweather D, Frisancho-Kiss S, Rose NR. 2008. Sex differences in autoimmune disease from a pathological perspective. Am J Pathol 173(3):600-9.

Faivre-Sarrailh C and Devaux JJ. 2013. Neuro-glial interactions at the nodes of ranvier: Implication in health and diseases. Front Cell Neurosci 7:196.

Falco A, Pennucci R, Brambilla E, de Curtis I. 2014. Reduction in parvalbumin-positive interneurons and inhibitory input in the cortex of mice with experimental autoimmune encephalomyelitis. Exp Brain Res 232(7):2439-49.

Farrell RA, Antony D, Wall GR, Clark DA, Fisniku L, Swanton J, Khaleeli Z, Schmierer K, Miller DH, Giovannoni G. 2009. Humoral immune response to EBV in multiple sclerosis is associated with disease activity on MRI. Neurology 73(1):32-8.

Fernandes A, Miller-Fleming L, Pais TF. 2014. Microglia and inflammation: Conspiracy, controversy or control? Cell Mol Life Sci 71(20):3969-85.

Filippi M, Preziosa P, Rocca MA. 2016. Multiple sclerosis. Handb Clin Neurol 135:399-423.

Fjaer S, Bo L, Lundervold A, Myhr KM, Pavlin T, Torkildsen O, Wergeland S. 2013. Deep gray matter demyelination detected by magnetization transfer ratio in the cuprizone model. PLoS One 8(12):e84162.

Fletcher JM, Lalor SJ, Sweeney CM, Tubridy N, Mills KH. 2010. T cells in multiple sclerosis and experimental autoimmune encephalomyelitis. Clin Exp Immunol 162(1):1-11.

Forkink M, Smeitink JA, Brock R, Willems PH, Koopman WJ. 2010. Detection and manipulation of mitochondrial reactive oxygen species in mammalian cells. Biochim Biophys Acta 1797(6-7):1034-44.

Forte M, Gold BG, Marracci G, Chaudhary P, Basso E, Johnsen D, Yu X, Fowlkes J, Rahder M, Stem K, et al. 2007. Cyclophilin D inactivation protects axons in experimental autoimmune encephalomyelitis, an animal model of multiple sclerosis. Proc Natl Acad Sci U S A 104(18):7558-63.

Franco SJ and Huttenlocher A. 2005. Regulating cell migration: Calpains make the cut. J Cell Sci 118(Pt 17):3829-38.

Freeman SA, Desmazieres A, Fricker D, Lubetzki C, Sol-Foulon N. 2016. Mechanisms of sodium channel clustering and its influence on axonal impulse conduction. Cell Mol Life Sci 73(4):723-35.

Fu L, Matthews PM, De Stefano N, Worsley KJ, Narayanan S, Francis GS, Antel JP, Wolfson C, Arnold DL. 1998. Imaging axonal damage of normal-appearing white matter in multiple sclerosis. Brain 121 (Pt 1)(Pt 1):103-13.

Fu Y, Frederick TJ, Huff TB, Goings GE, Miller SD, Cheng JX. 2011. Paranodal myelin retraction in relapsing experimental autoimmune encephalomyelitis visualized by coherent anti-stokes raman scattering microscopy. J Biomed Opt 16(10):106006.

Furukawa T. 2013. Types of voltage-gated calcium channels: Molecular and electrophysiological views. Curr Hypertens Rev 9(3):170-81.

Fusi F, Trezza A, Spiga O, Sgaragli G, Bova S. 2017. Cav1.2 channel current block by the PKA inhibitor H-89 in rat tail artery myocytes via a PKA-independent mechanism: Electrophysiological, functional, and molecular docking studies. Biochem Pharmacol .

Galiano MR, Jha S, Ho TS, Zhang C, Ogawa Y, Chang KJ, Stankewich MC, Mohler PJ, Rasband MN. 2012. A distal axonal cytoskeleton forms an intra-axonal boundary that controls axon initial segment assembly. Cell 149(5):1125-39.

Gallo P, Van Wijmeersch B, ParadigMS Group. 2015. Overview of the management of relapsing-remitting multiple sclerosis and practical recommendations. Eur J Neurol 22 Suppl 2:14-21.

Gao Z and Tsirka SE. 2011. Animal models of MS reveal multiple roles of microglia in disease pathogenesis. Neurol Res Int 2011:383087.

Gazulla J and Tintore M. 2007. P/Q-type voltage-dependent calcium channels in neurological disease. Neurologia 22(8):511-6.

Gerke V, Creutz CE, Moss SE. 2005. Annexins: Linking Ca2+ signalling to membrane dynamics. Nat Rev Mol Cell Biol 6(6):449-61.

Germain RN. 2002. T-cell development and the CD4-CD8 lineage decision. Nat Rev Immunol 2(5):309-22.

Golden LC and Voskuhl R. 2017. The importance of studying sex differences in disease: The example of multiple sclerosis. J Neurosci Res 95(1-2):633-43.

Gollan L, Salomon D, Salzer JL, Peles E. 2003. Caspr regulates the processing of contactin and inhibits its binding to neurofascin. J Cell Biol 163(6):1213-8.

Greer JE, Hanell A, McGinn MJ, Povlishock JT. 2013. Mild traumatic brain injury in the mouse induces axotomy primarily within the axon initial segment. Acta Neuropathol 126(1):59-74.

Greer JM. 2013. Autoimmune T-cell reactivity to myelin proteolipids and glycolipids in multiple sclerosis. Mult Scler Int 2013:151427.

Greter M, Heppner FL, Lemos MP, Odermatt BM, Goebels N, Laufer T, Noelle RJ, Becher B. 2005. Dendritic cells permit immune invasion of the CNS in an animal model of multiple sclerosis. Nat Med 11(3):328-34.

Griggs RB, Yermakov LM, Susuki K. 2017. Formation and disruption of functional domains in myelinated CNS axons. Neurosci Res 116:77-87.

Grubb MS and Burrone J. 2010. Activity-dependent relocation of the axon initial segment fine-tunes neuronal excitability. Nature 465(7301):1070-4.

Grubb MS and Burrone J. 2010. Building and maintaining the axon initial segment. Curr Opin Neurobiol 20(4):481-8.

Gudi V, Gingele S, Skripuletz T, Stangel M. 2014. Glial response during cuprizone-induced de- and remyelination in the CNS: Lessons learned. Front Cell Neurosci 8:73.

Gueguinou M, Chantome A, Fromont G, Bougnoux P, Vandier C, Potier-Cartereau M. 2014. KCa and ca(2+) channels: The complex thought. Biochim Biophys Acta 1843(10):2322-33.

Guemez-Gamboa A, Estrada-Sanchez AM, Montiel T, Paramo B, Massieu L, Moran J. 2011. Activation of NOX2 by the stimulation of ionotropic and metabotropic glutamate receptors contributes to glutamate neurotoxicity in vivo through the production of reactive oxygen species and calpain activation. J Neuropathol Exp Neurol 70(11):1020-35.

Gutierrez-Martin Y, Martin-Romero FJ, Henao F, Gutierrez-Merino C. 2005. Alteration of cytosolic free calcium homeostasis by SIN-1: High sensitivity of L-type Ca2+ channels to extracellular oxidative/nitrosative stress in cerebellar granule cells. J Neurochem 92(4):973-89.

Gutzmann A, Ergul N, Grossmann R, Schultz C, Wahle P, Engelhardt M. 2014. A period of structural plasticity at the axon initial segment in developing visual cortex. Front Neuroanat 8:11.

Hamada MS and Kole MH. 2015. Myelin loss and axonal ion channel adaptations associated with gray matter neuronal hyperexcitability. J Neurosci 35(18):7272-86.

Harty RC, Kim TH, Thomas EA, Cardamone L, Jones NC, Petrou S, Wimmer VC. 2013. Axon initial segment structural plasticity in animal models of genetic and acquired epilepsy. Epilepsy Res 105(3):272-9.

Hauser SL, Bar-Or A, Comi G, Giovannoni G, Hartung HP, Hemmer B, Lublin F, Montalban X, Rammohan KW, Selmaj K, et al. 2017. Ocrelizumab versus interferon beta-1a in relapsing multiple sclerosis. N Engl J Med 376(3):221-34.

Hayashi A, Kaneko N, Tomihira C, Baba H. 2013. Sulfatide decrease in myelin influences formation of the paranodal axo-glial junction and conduction velocity in the sciatic nerve. Glia 61(4):466-74.

Hedstrom KL, Ogawa Y, Rasband MN. 2008. AnkyrinG is required for maintenance of the axon initial segment and neuronal polarity. J Cell Biol 183(4):635-40.

Hedstrom KL, Xu X, Ogawa Y, Frischknecht R, Seidenbecher CI, Shrager P, Rasband MN. 2007. Neurofascin assembles a specialized extracellular matrix at the axon initial segment. J Cell Biol 178(5):875-86.

Hemmer B, Kerschensteiner M, Korn T. 2015. Role of the innate and adaptive immune responses in the course of multiple sclerosis. Lancet Neurol 14(4):406-19.

Hendrickx DA, Schuurman KG, van Draanen M, Hamann J, Huitinga I. 2014. Enhanced uptake of multiple sclerosis-derived myelin by THP-1 macrophages and primary human microglia. J Neuroinflammation 11(1):64,2094-11-64.

Heppner FL, Greter M, Marino D, Falsig J, Raivich G, Hovelmeyer N, Waisman A, Rulicke T, Prinz M, Priller J, et al. 2005. Experimental autoimmune encephalomyelitis repressed by microglial paralysis. Nat Med 11(2):146-52.

Herder V, Hansmann F, Stangel M, Skripuletz T, Baumgartner W, Beineke A. 2011. Lack of cuprizone-induced demyelination in the murine spinal cord despite oligodendroglial alterations substantiates the concept of site-specific susceptibilities of the central nervous system. Neuropathol Appl Neurobiol 37(6):676-84.

Hinman JD, Rasband MN, Carmichael ST. 2013. Remodeling of the axon initial segment after focal cortical and white matter stroke. Stroke 44(1):182-9.

Hinman JD, Duce JA, Siman RA, Hollander W, Abraham CR. 2004. Activation of calpain-1 in myelin and microglia in the white matter of the aged rhesus monkey. J Neurochem 89(2):430-41.

Hiremath MM, Saito Y, Knapp GW, Ting JP, Suzuki K, Matsushima GK. 1998. Microglial/macrophage accumulation during cuprizone-induced demyelination in C57BL/6 mice. J Neuroimmunol 92(1-2):38-49.

Hoffman W, Lakkis FG, Chalasani G. 2016. B cells, antibodies, and more. Clin J Am Soc Nephrol 11(1):137-54.

Hoflich KM, Beyer C, Clarner T, Schmitz C, Nyamoya S, Kipp M, Hochstrasser T. 2016. Acute axonal damage in three different murine models of multiple sclerosis: A comparative approach. Brain Res 1650:125-33.

Hollenbach JA and Oksenberg JR. 2015. The immunogenetics of multiple sclerosis: A comprehensive review. J Autoimmun 64:13-25.

Howell OW, Rundle JL, Garg A, Komada M, Brophy PJ, Reynolds R. 2010. Activated microglia mediate axoglial disruption that contributes to axonal injury in multiple sclerosis. J Neuropathol Exp Neurol 69(10):1017-33.

Howell OW, Palser A, Polito A, Melrose S, Zonta B, Scheiermann C, Vora AJ, Brophy PJ, Reynolds R. 2006. Disruption of neurofascin localization reveals early changes preceding demyelination and remyelination in multiple sclerosis. Brain 129(Pt 12):3173-85.

Hu H, Gan J, Jonas P. 2014. Interneurons. fast-spiking, parvalbumin(+) GABAergic interneurons: From cellular design to microcircuit function. Science 345(6196):1255263.

Huizinga R, van der Star BJ, Kipp M, Jong R, Gerritsen W, Clarner T, Puentes F, Dijkstra CD, van der Valk P, Amor S. 2012. Phagocytosis of neuronal debris by microglia is associated with neuronal damage in multiple sclerosis. Glia 60(3):422-31.

Hulst HE and Geurts JJ. 2011. Gray matter imaging in multiple sclerosis: What have we learned? BMC Neurol 11:153,2377-11-153.

Hung RJ, Pak CW, Terman JR. 2011. Direct redox regulation of F-actin assembly and disassembly by mical. Science 334(6063):1710-3.

Hutson CB, Lazo CR, Mortazavi F, Giza CC, Hovda D, Chesselet MF. 2011. Traumatic brain injury in adult rats causes progressive nigrostriatal dopaminergic cell loss and enhanced vulnerability to the pesticide paraquat. J Neurotrauma 28(9):1783-801.

Inayat MS, El-Amouri IS, Bani-Ahmad M, Elford HL, Gallicchio VS, Oakley OR. 2010. Inhibition of allogeneic inflammatory responses by the ribonucleotide reductase inhibitors, didox and trimidox. J Inflamm (Lond) 7:43,9255-7-43.

Irvine KA and Blakemore WF. 2008. Remyelination protects axons from demyelination-associated axon degeneration. Brain 131(Pt 6):1464-77.

Isaev NK, Genrikhs EE, Aleksandrova OP, Zelenova EA, Stelmashook EV. 2016. Glucose deprivation stimulates cu(2+) toxicity in cultured cerebellar granule neurons and cu(2+)-dependent zinc release. Toxicol Lett 250-251:29-34.

Ishibashi T, Ikenaka K, Shimizu T, Kagawa T, Baba H. 2003. Initiation of sodium channel clustering at the node of ranvier in the mouse optic nerve. Neurochem Res 28(1):117-25.

Ishibashi T, Dupree JL, Ikenaka K, Hirahara Y, Honke K, Peles E, Popko B, Suzuki K, Nishino H, Baba H. 2002. A myelin galactolipid, sulfatide, is essential for maintenance of ion channels on myelinated axon but not essential for initial cluster formation. J Neurosci 22(15):6507-14.

Islam MT. 2017. Oxidative stress and mitochondrial dysfunction-linked neurodegenerative disorders. Neurol Res 39(1):73-82.

Jabir MS, Hopkins L, Ritchie ND, Ullah I, Bayes HK, Li D, Tourlomousis P, Lupton A, Puleston D, Simon AK, et al. 2015. Mitochondrial damage contributes to pseudomonas aeruginosa activation of the inflammasome and is downregulated by autophagy. Autophagy 11(1):166-82.

Jahn O, Tenzer S, Werner HB. 2009. Myelin proteomics: Molecular anatomy of an insulating sheath. Mol Neurobiol 40(1):55-72.

Jamann N, Jordan M, Engelhardt M. 2017. Activity-dependent axonal plasticity in sensory systems. Neuroscience .

Jedlicka P, Schwarzacher SW, Winkels R, Kienzler F, Frotscher M, Bramham CR, Schultz C, Bas Orth C, Deller T. 2009. Impairment of in vivo theta-burst long-term potentiation and network excitability in the dentate gyrus of synaptopodin-deficient mice lacking the spine apparatus and the cisternal organelle. Hippocampus 19(2):130-40.

Jenkins SM and Bennett V. 2001. Ankyrin-G coordinates assembly of the spectrin-based membrane skeleton, voltage-gated sodium channels, and L1 CAMs at purkinje neuron initial segments. J Cell Biol 155(5):739-46.

Jilek S, Schluep M, Harari A, Canales M, Lysandropoulos A, Zekeridou A, Pantaleo G, Du Pasquier RA. 2012. HLA-B7-restricted EBV-specific CD8+ T cells are dysregulated in multiple sclerosis. J Immunol 188(9):4671-80.

Johnstone VP and Hool LC. 2014. Glutathionylation of the L-type Ca2+ channel in oxidative stress-induced pathology of the heart. Int J Mol Sci 15(10):19203-25.

Kabba JA, Xu Y, Christian H, Ruan W, Chenai K, Xiang Y, Zhang L, Saavedra JM, Pang T. 2017. Microglia: Housekeeper of the central nervous system. Cell Mol Neurobiol .

Kamate M, Chetal V, Tonape V, Mahantshetti N, Hattiholi V. 2010. Central nervous system inflammatory demyelinating disorders of childhood. Ann Indian Acad Neurol 13(4):289-92.

Kaphzan H, Buffington SA, Jung JI, Rasband MN, Klann E. 2011. Alterations in intrinsic membrane properties and the axon initial segment in a mouse model of angelman syndrome. J Neurosci 31(48):17637-48.

Katz Sand I. 2015. Classification, diagnosis, and differential diagnosis of multiple sclerosis. Curr Opin Neurol 28(3):193-205.

Kawakami N, Bartholomaus I, Pesic M, Mues M. 2012. An autoimmunity odyssey: How autoreactive T cells infiltrate into the CNS. Immunol Rev 248(1):140-55.

Kebir H, Kreymborg K, Ifergan I, Dodelet-Devillers A, Cayrol R, Bernard M, Giuliani F, Arbour N, Becher B, Prat A. 2007. Human TH17 lymphocytes promote blood-brain barrier disruption and central nervous system inflammation. Nat Med 13(10):1173-5.

Kidd D, Barkhof F, McConnell R, Algra PR, Allen IV, Revesz T. 1999. Cortical lesions in multiple sclerosis. Brain 122 (Pt 1)(Pt 1):17-26.

Kim JV, Jiang N, Tadokoro CE, Liu L, Ransohoff RM, Lafaille JJ, Dustin ML. 2010. Two-photon laser scanning microscopy imaging of intact spinal cord and cerebral cortex reveals requirement for CXCR6 and neuroinflammation in immune cell infiltration of cortical injury sites. J Immunol Methods 352(1-2):89-100.

King AN, Manning CF, Trimmer JS. 2014. A unique ion channel clustering domain on the axon initial segment of mammalian neurons. J Comp Neurol 522(11):2594-608.

Kipp M, Nyamoya S, Hochstrasser T, Amor S. 2017. Multiple sclerosis animal models: A clinical and histopathological perspective. Brain Pathol 27(2):123-37.

Kipp M, Nyamoya S, Hochstrasser T, Amor S. 2017. Multiple sclerosis animal models: A clinical and histopathological perspective. Brain Pathol 27(2):123-37.

Kipp M, Nyamoya S, Hochstrasser T, Amor S. 2017. Multiple sclerosis animal models: A clinical and histopathological perspective. Brain Pathol 27(2):123-37.

Kole MH, Letzkus JJ, Stuart GJ. 2007. Axon initial segment Kv1 channels control axonal action potential waveform and synaptic efficacy. Neuron 55(4):633-47.

Kole MH, Ilschner SU, Kampa BM, Williams SR, Ruben PC, Stuart GJ. 2008. Action potential generation requires a high sodium channel density in the axon initial segment. Nat Neurosci 11(2):178-86.

Komada M and Soriano P. 2002. Beta]IV-spectrin regulates sodium channel clustering through ankyrin-G at axon initial segments and nodes of ranvier. J Cell Biol 156(2):337-48.

Kraft GH. 2013. Evoked potentials in multiple sclerosis. Phys Med Rehabil Clin N Am 24(4):717-20.

Kremerskothen J, Plaas C, Kindler S, Frotscher M, Barnekow A. 2005. Synaptopodin, a molecule involved in the formation of the dendritic spine apparatus, is a dual actin/alpha-actinin binding protein. J Neurochem 92(3):597-606.

Kuba H. 2012. Structural tuning and plasticity of the axon initial segment in auditory neurons. J Physiol 590(Pt 22):5571-9.

Kuba H. 2010. Plasticity at the axon initial segment. Commun Integr Biol 3(6):597-8.

Kuba H, Adachi R, Ohmori H. 2014. Activity-dependent and activity-independent development of the axon initial segment. J Neurosci 34(9):3443-53.

Kumar A, Cocco E, Atzori L, Marrosu MG, Pieroni E. 2013. Structural and dynamical insights on HLA-DR2 complexes that confer susceptibility to multiple sclerosis in sardinia: A molecular dynamics simulation study. PLoS One 8(3):e59711.

Kuo CC, Su HL, Chang TL, Chiang CY, Sheu ML, Cheng FC, Chen CJ, Sheehan J, Pan HC. 2017. Prevention of axonal degeneration by perineurium injection of mitochondria in a sciatic nerve crush injury model. Neurosurgery 80(3):475-88.

Kutzelnigg A and Lassmann H. 2014. Pathology of multiple sclerosis and related inflammatory demyelinating diseases. Handb Clin Neurol 122:15-58.

Kutzelnigg A, Lucchinetti CF, Stadelmann C, Bruck W, Rauschka H, Bergmann M, Schmidbauer M, Parisi JE, Lassmann H. 2005. Cortical demyelination and diffuse white matter injury in multiple sclerosis. Brain 128(Pt 11):2705-12.

Larochelle C, Alvarez JI, Prat A. 2011. How do immune cells overcome the blood-brain barrier in multiple sclerosis? FEBS Lett 585(23):3770-80.

Lassmann H. 1999. Mechanisms of demyelination and tissue damage in multiple sclerosis. Acta Neurol Belg 99(1):6-10.

Lassmann H, van Horssen J, Mahad D. 2012. Progressive multiple sclerosis: Pathology and pathogenesis. Nat Rev Neurol 8(11):647-56.

Laurence M and Benito-Leon J. 2017. Epstein-barr virus and multiple sclerosis: Updating pender's hypothesis. Mult Scler Relat Disord 16:8-14.

Leon-Espinosa G, DeFelipe J, Munoz A. 2012. Effects of amyloid-beta plaque proximity on the axon initial segment of pyramidal cells. J Alzheimers Dis 29(4):841-52.

Leterrier C. 2016. The axon initial segment, 50Years later: A nexus for neuronal organization and function. Curr Top Membr 77:185-233.

Levesque S, Wilson B, Gregoria V, Thorpe LB, Dallas S, Polikov VS, Hong JS, Block ML. 2010. Reactive microgliosis: Extracellular micro-calpain and microglia-mediated dopaminergic neurotoxicity. Brain 133(Pt 3):808-21.

Lewen A, Matz P, Chan PH. 2000. Free radical pathways in CNS injury. J Neurotrauma 17(10):871-90.

Lewis ND, Hill JD, Juchem KW, Stefanopoulos DE, Modis LK. 2014. RNA sequencing of microglia and monocyte-derived macrophages from mice with experimental autoimmune encephalomyelitis illustrates a changing phenotype with disease course. J Neuroimmunol 277(1-2):26-38.

Li X, Kumar Y, Zempel H, Mandelkow EM, Biernat J, Mandelkow E. 2011. Novel diffusion barrier for axonal retention of tau in neurons and its failure in neurodegeneration. Embo j 30(23):4825-37.

Liu TT, Feng L, Liu HF, Shu Y, Xiao B. 2017. Altered axon initial segment in hippocampal newborn neurons, associated with recurrence of temporal lobe epilepsy in rats. Mol Med Rep 16(3):3169-78.

Liu Y, Lu L, Hettinger CL, Dong G, Zhang D, Rezvani K, Wang X, Wang H. 2014. Ubiquilin-1 protects cells from oxidative stress and ischemic stroke caused tissue injury in mice. J Neurosci 34(8):2813-21.

Longbrake EE and Racke MK. 2009. Why did IL-12/IL-23 antibody therapy fail in multiple sclerosis? Expert Rev Neurother 9(3):319-21.

Louveau A, Smirnov I, Keyes TJ, Eccles JD, Rouhani SJ, Peske JD, Derecki NC, Castle D, Mandell JW, Lee KS, et al. 2015. Structural and functional features of central nervous system lymphatic vessels. Nature 523(7560):337-41.

Lucas RM, Byrne SN, Correale J, Ilschner S, Hart PH. 2015. Ultraviolet radiation, vitamin D and multiple sclerosis. Neurodegener Dis Manag 5(5):413-24.

Luo C, Jian C, Liao Y, Huang Q, Wu Y, Liu X, Zou D, Wu Y. 2017. The role of microglia in multiple sclerosis. Neuropsychiatr Dis Treat 13:1661-7.

Luo J, Chen R, Zeng S, Yu J, Jiang G, Wang L, Qin X. 2017. The effects of berberine on a murine model of multiple sclerosis and the SPHK1/S1P signaling pathway. Biochem Biophys Res Commun 490(3):927-32.

Lustig M, Zanazzi G, Sakurai T, Blanco C, Levinson SR, Lambert S, Grumet M, Salzer JL. 2001. Nr-CAM and neurofascin interactions regulate ankyrin G and sodium channel clustering at the node of ranvier. Curr Biol 11(23):1864-9.

Ma M. 2013. Role of calpains in the injury-induced dysfunction and degeneration of the mammalian axon. Neurobiol Dis 60:61-79.

Maggio DM, Singh A, Iorgulescu JB, Bleicher DH, Ghosh M, Lopez MM, Tuesta LM, Flora G, Dietrich WD, Pearse DD. 2017. Identifying the long-term role of inducible nitric oxide synthase after contusive spinal cord injury using a transgenic mouse model. Int J Mol Sci 18(2):10.3390/ijms18020245.

Marco P, Sola RG, Ramon y Cajal S, DeFelipe J. 1997. Loss of inhibitory synapses on the soma and axon initial segment of pyramidal cells in human epileptic peritumoural neocortex: Implications for epilepsy. Brain Res Bull 44(1):47-66.

Marcus J, Honigbaum S, Shroff S, Honke K, Rosenbluth J, Dupree JL. 2006. Sulfatide is essential for the maintenance of CNS myelin and axon structure. Glia 53(4):372-81.

Marik C, Felts PA, Bauer J, Lassmann H, Smith KJ. 2007. Lesion genesis in a subset of patients with multiple sclerosis: A role for innate immunity? Brain 130(Pt 11):2800-15.

Marin MA, Ziburkus J, Jankowsky J, Rasband MN. 2016. Amyloid-beta plaques disrupt axon initial segments. Exp Neurol 281:93-8.

Marks AR. 1997. Intracellular calcium-release channels: Regulators of cell life and death. Am J Physiol 272(2 Pt 2):H597-605.

Marrie RA. 2004. Environmental risk factors in multiple sclerosis aetiology. Lancet Neurol 3(12):709-18.

Matsebatlela TM, Anderson AL, Gallicchio VS, Elford H, Rice CD. 2015. 3,4-dihydroxy-benzohydroxamic acid (didox) suppresses pro-inflammatory profiles and oxidative stress in TLR4-activated RAW264.7 murine macrophages. Chem Biol Interact 233:95-105.

Maurel P, Einheber S, Galinska J, Thaker P, Lam I, Rubin MB, Scherer SS, Murakami Y, Gutmann DH, Salzer JL. 2007. Nectin-like proteins mediate axon schwann cell interactions along the internode and are essential for myelination. J Cell Biol 178(5):861-74.

Mayhew CN, Mampuru LJ, Chendil D, Ahmed MM, Phillips JD, Greenberg RN, Elford HL, Gallicchio VS. 2002. Suppression of retrovirus-induced immunodeficiency disease (murine AIDS) by trimidox and didox: Novel ribonucleotide reductase inhibitors with less bone marrow toxicity than hydroxyurea. Antiviral Res 56(2):167-81.

McCarthy DP, Richards MH, Miller SD. 2012. Mouse models of multiple sclerosis: Experimental autoimmune encephalomyelitis and theiler's virus-induced demyelinating disease. Methods Mol Biol 900:381-401.

McMahon EJ, Suzuki K, Matsushima GK. 2002. Peripheral macrophage recruitment in cuprizone-induced CNS demyelination despite an intact blood-brain barrier. J Neuroimmunol 130(1-2):32-45.

Mecha M, Carrillo-Salinas FJ, Mestre L, Feliu A, Guaza C. 2013. Viral models of multiple sclerosis: Neurodegeneration and demyelination in mice infected with theiler's virus. Prog Neurobiol 101-102:46-64.

Mecha M, Carrillo-Salinas FJ, Mestre L, Feliu A, Guaza C. 2013. Viral models of multiple sclerosis: Neurodegeneration and demyelination in mice infected with theiler's virus. Prog Neurobiol 101-102:46-64.

Meeks JP and Mennerick S. 2007. Action potential initiation and propagation in CA3 pyramidal axons. J Neurophysiol 97(5):3460-72.

Mehndiratta MM and Gulati NS. 2014. Central and peripheral demyelination. J Neurosci Rural Pract 5(1):84-6.

Mendez-Armenta M, Nava-Ruiz C, Juarez-Rebollar D, Rodriguez-Martinez E, Gomez PY. 2014. Oxidative stress associated with neuronal apoptosis in experimental models of epilepsy. Oxid Med Cell Longev 2014:293689.

Mikoshiba K. 2015. Role of IP3 receptor signaling in cell functions and diseases. Adv Biol Regul 57:217-27.

Milo R and Miller A. 2014. Revised diagnostic criteria of multiple sclerosis. Autoimmun Rev 13(4-5):518-24.

Miron VE, Boyd A, Zhao JW, Yuen TJ, Ruckh JM, Shadrach JL, van Wijngaarden P, Wagers AJ, Williams A, Franklin RJM, et al. 2013. M2 microglia and macrophages drive oligodendrocyte differentiation during CNS remyelination. Nat Neurosci 16(9):1211-8.

Molderings GJ, Likungu J, Gothert M. 2000. N-type calcium channels control sympathetic neurotransmission in human heart atrium. Circulation 101(4):403-7.

Mosayebi G, Soleyman MR, Khalili M, Mosleh M, Palizvan MR. 2016. Changes in synaptic transmission and long-term potentiation induction as a possible mechanism for learning disability in an animal model of multiple sclerosis. Int Neurourol J 20(1):26-32.

Mullen RJ, Buck CR, Smith AM. 1992. NeuN, a neuronal specific nuclear protein in vertebrates. Development 116(1):201-11.

Munger KL, Fitzgerald KC, Freedman MS, Hartung HP, Miller DH, Montalban X, Edan G, Barkhof F, Suarez G, Radue EW, et al. 2015. No association of multiple sclerosis activity and progression with EBV or tobacco use in BENEFIT. Neurology 85(19):1694-701.

Munnamalai V and Suter DM. 2009. Reactive oxygen species regulate F-actin dynamics in neuronal growth cones and neurite outgrowth. J Neurochem 108(3):644-61.

Munnamalai V, Weaver CJ, Weisheit CE, Venkatraman P, Agim ZS, Quinn MT, Suter DM. 2014. Bidirectional interactions between NOX2-type NADPH oxidase and the F-actin cytoskeleton in neuronal growth cones. J Neurochem 130(4):526-40.

Munoz FM, Zhang F, Islas-Robles A, Lau SS, Monks TJ. 2017. Ros-induced store-operated Ca2+ entry coupled to parp-1 hyperactivation is independent of parg activity in necrotic cell death. Toxicol Sci .

Muris AH, Smolders J, Rolf L, Thewissen M, Hupperts R, Damoiseaux J, SOLARIUM study group. 2016. Immune regulatory effects of high dose vitamin D3 supplementation in a randomized controlled trial in relapsing remitting multiple sclerosis patients receiving IFNbeta; the SOLARIUM study. J Neuroimmunol 300:47-56.

Muris AH, Smolders J, Rolf L, Klinkenberg LJ, van der Linden N, Meex S, Damoiseaux J, Hupperts R. 2016. Vitamin D status does not affect disability progression of patients with multiple sclerosis over three year follow-up. PLoS One 11(6):e0156122.

Nair A, Frederick TJ, Miller SD. 2008. Astrocytes in multiple sclerosis: A product of their environment. Cell Mol Life Sci 65(17):2702-20.

Nakada C, Ritchie K, Oba Y, Nakamura M, Hotta Y, Iino R, Kasai RS, Yamaguchi K, Fujiwara T, Kusumi A. 2003. Accumulation of anchored proteins forms membrane diffusion barriers during neuronal polarization. Nat Cell Biol 5(7):626-32.

Nelson AD and Jenkins PM. 2017. Axonal membranes and their domains: Assembly and function of the axon initial segment and node of ranvier. Front Cell Neurosci 11:136.

Nguemo F, Fleischmann BK, Gupta MK, Saric T, Malan D, Liang H, Pfannkuche K, Bloch W, Schunkert H, Hescheler J, et al. 2013. The L-type Ca2+ channels blocker nifedipine represses mesodermal fate determination in murine embryonic stem cells. PLoS One 8(1):e53407.

Nikic I, Merkler D, Sorbara C, Brinkoetter M, Kreutzfeldt M, Bareyre FM, Bruck W, Bishop D, Misgeld T, Kerschensteiner M. 2011. A reversible form of axon damage in experimental autoimmune encephalomyelitis and multiple sclerosis. Nat Med 17(4):495-9.

Nimmrich V and Gross G. 2012. P/Q-type calcium channel modulators. Br J Pharmacol 167(4):741-59.

Oberheim NA, Goldman SA, Nedergaard M. 2012. Heterogeneity of astrocytic form and function. Methods Mol Biol 814:23-45.

O'Brien K, Fitzgerald DC, Naiken K, Alugupalli KR, Rostami AM, Gran B. 2008. Role of the innate immune system in autoimmune inflammatory demyelination. Curr Med Chem 15(11):1105-15.

Ohashi M, Hirano T, Watanabe K, Katsumi K, Ohashi N, Baba H, Endo N, Kohno T. 2016. Hydrogen peroxide modulates synaptic transmission in ventral horn neurons of the rat spinal cord. J Physiol 594(1):115-34.

Ohkuma S, Katsura M, Higo A, Shirotani K, Hara A, Tarumi C, Ohgi T. 2001. Peroxynitrite affects Ca2+ influx through voltage-dependent calcium channels. J Neurochem 76(2):341-50.

Oleszak EL, Chang JR, Friedman H, Katsetos CD, Platsoucas CD. 2004. Theiler's virus infection: A model for multiple sclerosis. Clin Microbiol Rev 17(1):174-207.

Olson JK. 2014. Effect of the innate immune response on development of theiler's murine encephalomyelitis virus-induced demyelinating disease. J Neurovirol 20(5):427-36.

Ontaneda D and Fox RJ. 2015. Progressive multiple sclerosis. Curr Opin Neurol 28(3):237-43.

Oreja-Guevara C, Ramos-Cejudo J, Aroeira LS, Chamorro B, Diez-Tejedor E. 2012. TH1/TH2 cytokine profile in relapsing-remitting multiple sclerosis patients treated with glatiramer acetate or natalizumab. BMC Neurol 12:95,2377-12-95.

Orellana JA, Martinez AD, Retamal MA. 2013. Gap junction channels and hemichannels in the CNS: Regulation by signaling molecules. Neuropharmacology 75:567-82.

Pan BX, Zhao GL, Huang XL, Zhao KS. 2004. Calcium mobilization is required for peroxynitrite-mediated enhancement of spontaneous transient outward currents in arteriolar smooth muscle cells. Free Radic Biol Med 37(6):823-38.

Pan Z, Kao T, Horvath Z, Lemos J, Sul JY, Cranstoun SD, Bennett V, Scherer SS, Cooper EC. 2006. A common ankyrin-G-based mechanism retains KCNQ and NaV channels at electrically active domains of the axon. J Neurosci 26(10):2599-613.

Panitch HS, Hirsch RL, Haley AS, Johnson KP. 1987. Exacerbations of multiple sclerosis in patients treated with gamma interferon. Lancet 1(8538):893-5.

Park J, Liu B, Chen T, Li H, Hu X, Gao J, Zhu Y, Zhu Q, Qiang B, Yuan J, et al. 2008. Disruption of nectin-like 1 cell adhesion molecule leads to delayed axonal myelination in the CNS. J Neurosci 28(48):12815-9.

Paul S, Shilpi, Lal G. 2015. Role of gamma-delta (gammadelta) T cells in autoimmunity. J Leukoc Biol 97(2):259-71.

Peterson JW, Bo L, Mork S, Chang A, Trapp BD. 2001. Transected neurites, apoptotic neurons, and reduced inflammation in cortical multiple sclerosis lesions. Ann Neurol 50(3):389-400.

Peterson LK and Fujinami RS. 2007. Inflammation, demyelination, neurodegeneration and neuroprotection in the pathogenesis of multiple sclerosis. J Neuroimmunol 184(1-2):37-44.

Pierson E, Simmons SB, Castelli L, Goverman JM. 2012. Mechanisms regulating regional localization of inflammation during CNS autoimmunity. Immunol Rev 248(1):205-15.

Pillai AM, Thaxton C, Pribisko AL, Cheng JG, Dupree JL, Bhat MA. 2009. Spatiotemporal ablation of myelinating glia-specific neurofascin (nfasc NF155) in mice reveals gradual loss of paranodal axoglial junctions and concomitant disorganization of axonal domains. J Neurosci Res 87(8):1773-93.

Poliak S, Salomon D, Elhanany H, Sabanay H, Kiernan B, Pevny L, Stewart CL, Xu X, Chiu SY, Shrager P, et al. 2003. Juxtaparanodal clustering of shaker-like K+ channels in myelinated axons depends on Caspr2 and TAG-1. J Cell Biol 162(6):1149-60.

Pollock JD, Williams DA, Gifford MA, Li LL, Du X, Fisherman J, Orkin SH, Doerschuk CM, Dinauer MC. 1995. Mouse model of X-linked chronic granulomatous disease, an inherited defect in phagocyte superoxide production. Nat Genet 9(2):202-9.

Pomicter AD, Shroff SM, Fuss B, Sato-Bigbee C, Brophy PJ, Rasband MN, Bhat MA, Dupree JL. 2010. Novel forms of neurofascin 155 in the central nervous system: Alterations in paranodal disruption models and multiple sclerosis. Brain 133(Pt 2):389-405.

Popescu BF, Pirko I, Lucchinetti CF. 2013. Pathology of multiple sclerosis: Where do we stand? Continuum (Minneap Minn) 19(4 Multiple Sclerosis):901-21.

Pouly S and Antel JP. 1999. Multiple sclerosis and central nervous system demyelination. J Autoimmun 13(3):297-306.

Puthussery T, Venkataramani S, Gayet-Primo J, Smith RG, Taylor WR. 2013. NaV1.1 channels in axon initial segments of bipolar cells augment input to magnocellular visual pathways in the primate retina. J Neurosci 33(41):16045-59.

Qi X, Lewin AS, Sun L, Hauswirth WW, Guy J. 2007. Suppression of mitochondrial oxidative stress provides long-term neuroprotection in experimental optic neuritis. Invest Ophthalmol Vis Sci 48(2):681-91.

Raichle ME. 2010. Two views of brain function. Trends Cogn Sci 14(4):180-90.

Rangachari M and Kuchroo VK. 2013. Using EAE to better understand principles of immune function and autoimmune pathology. J Autoimmun 45:31-9.

Rao VR and Finkbeiner S. 2007. NMDA and AMPA receptors: Old channels, new tricks. Trends Neurosci 30(6):284-91.

Rasband MN. 2010. The axon initial segment and the maintenance of neuronal polarity. Nat Rev Neurosci 11(8):552-62.

Rasband MN, Peles E, Trimmer JS, Levinson SR, Lux SE, Shrager P. 1999. Dependence of nodal sodium channel clustering on paranodal axoglial contact in the developing CNS. J Neurosci 19(17):7516-28.

Rasband MN, Tayler J, Kaga Y, Yang Y, Lappe-Siefke C, Nave KA, Bansal R. 2005. CNP is required for maintenance of axon-glia interactions at nodes of ranvier in the CNS. Glia 50(1):86-90.

Rasband MN, Trimmer JS, Schwarz TL, Levinson SR, Ellisman MH, Schachner M, Shrager P. 1998. Potassium channel distribution, clustering, and function in remyelinating rat axons. J Neurosci 18(1):36-47.

Ravens U and Schopper HP. 1990. Opposite cardiac actions of the enantiomers of bay K 8644 at different membrane potentials in guinea-pig papillary muscles. Naunyn Schmiedebergs Arch Pharmacol 341(3):232-9.

Rawes JA, Calabrese VP, Khan OA, DeVries GH. 1997. Antibodies to the axolemma-enriched fraction in the cerebrospinal fluid and serum of patients with multiple sclerosis and other neurological diseases. Mult Scler 3(6):363-9.

Rawji KS and Yong VW. 2013. The benefits and detriments of macrophages/microglia in models of multiple sclerosis. Clin Dev Immunol 2013:948976.

Rawji KS and Yong VW. 2013. The benefits and detriments of macrophages/microglia in models of multiple sclerosis. Clin Dev Immunol 2013:948976.

Recks MS, Stormanns ER, Bader J, Arnhold S, Addicks K, Kuerten S. 2013. Early axonal damage and progressive myelin pathology define the kinetics of CNS histopathology in a mouse model of multiple sclerosis. Clin Immunol 149(1):32-45.

Redondo J, Hares K, Wilkins A, Scolding N, Kemp K. 2015. Reductions in kinesin expression are associated with nitric oxide-induced axonal damage. J Neurosci Res 93(6):882-92.

Reeves TM, Greer JE, Vanderveer AS, Phillips LL. 2010. Proteolysis of submembrane cytoskeletal proteins ankyrin-G and alphaII-spectrin following diffuse brain injury: A role in white matter vulnerability at nodes of ranvier. Brain Pathol 20(6):1055-68.

Rice CM, Cottrell D, Wilkins A, Scolding NJ. 2013. Primary progressive multiple sclerosis: Progress and challenges. J Neurol Neurosurg Psychiatry 84(10):1100-6.

Rocchitta G, Migheli R, Mura MP, Grella G, Esposito G, Marchetti B, Miele E, Desole MS, Miele M, Serra PA. 2005. Signaling pathways in the nitric oxide and iron-induced dopamine release in the striatum of freely moving rats: Role of extracellular Ca2+ and L-type Ca2+ channels. Brain Res 1047(1):18-29.

Rodgers JM and Miller SD. 2012. Cytokine control of inflammation and repair in the pathology of multiple sclerosis. Yale J Biol Med 85(4):447-68.

Rosenberger TA. 2014. Targeting calpain-mediated proteolysis and peptide signaling as a strategy to reduce injury in multiple sclerosis. J Neurochem 130(2):161-4.

Rosenbluth J and Bobrowski-Khoury N. 2014. Paranodal dysmyelination in peripheral nerves of trembler mice. J Neurosci Res 92(4):476-85.

Rosenbluth J, Mierzwa A, Shroff S. 2013. Molecular architecture of myelinated nerve fibers: Leaky paranodal junctions and paranodal dysmyelination. Neuroscientist 19(6):629-41.

Rosenbluth J, Petzold C, Peles E. 2012. Dependence of paranodal junctional gap width on transverse bands. J Comp Neurol 520(12):2774-84.

Rosenbluth J, Dupree JL, Popko B. 2003. Nodal sodium channel domain integrity depends on the conformation of the paranodal junction, not on the presence of transverse bands. Glia 41(3):318-25.

Rosenzweig S and Carmichael ST. 2013. Age-dependent exacerbation of white matter stroke outcomes: A role for oxidative damage and inflammatory mediators. Stroke 44(9):2579-86.

Rosjo E, Steffensen LH, Jorgensen L, Lindstrom JC, Saltyte Benth J, Michelsen AE, Aukrust P, Ueland T, Kampman MT, Torkildsen O, et al. 2015. Vitamin D supplementation and systemic inflammation in relapsing-remitting multiple sclerosis. J Neurol 262(12):2713-21.

Rossi S, Muzio L, De Chiara V, Grasselli G, Musella A, Musumeci G, Mandolesi G, De Ceglia R, Maida S, Biffi E, et al. 2011. Impaired striatal GABA transmission in experimental autoimmune encephalomyelitis. Brain Behav Immun 25(5):947-56.

Saeki M, Kamisaki Y, Maeda S. 2000. Potentiation of carbachol-induced Ca2+ release by peroxynitrite in human neuroblastoma SH-SY5Y cells. Neurochem Res 25(7):909-14.

Salou M, Nicol B, Garcia A, Laplaud DA. 2015. Involvement of CD8(+) T cells in multiple sclerosis. Front Immunol 6:604.

Salzer JL. 2003. Polarized domains of myelinated axons. Neuron 40(2):297-318.

Salzer JL. 1997. Clustering sodium channels at the node of ranvier: Close encounters of the axon-glia kind. Neuron 18(6):843-6.

Sanchez-Ponce D, DeFelipe J, Garrido JJ, Munoz A. 2011. In vitro maturation of the cisternal organelle in the hippocampal neuron's axon initial segment. Mol Cell Neurosci 48(1):104-16.

Sanchez-Ponce D, Blazquez-Llorca L, DeFelipe J, Garrido JJ, Munoz A. 2012. Colocalization of alpha-actinin and synaptopodin in the pyramidal cell axon initial segment. Cereb Cortex 22(7):1648-61.

Schafer DP, Jha S, Liu F, Akella T, McCullough LD, Rasband MN. 2009. Disruption of the axon initial segment cytoskeleton is a new mechanism for neuronal injury. J Neurosci 29(42):13242-54.

Schiess N and Calabresi PA. 2016. Multiple sclerosis. Semin Neurol 36(4):350-6.

Schluter A, Del Turco D, Deller T, Gutzmann A, Schultz C, Engelhardt M. 2017. Structural plasticity of synaptopodin in the axon initial segment during visual cortex development. Cereb Cortex 27(9):4662-75.

Schluter A, Del Turco D, Deller T, Gutzmann A, Schultz C, Engelhardt M. 2017. Structural plasticity of synaptopodin in the axon initial segment during visual cortex development. Cereb Cortex 27(9):4662-75.

Segal BM, Constantinescu CS, Raychaudhuri A, Kim L, Fidelus-Gort R, Kasper LH, Ustekinumab MS Investigators. 2008. Repeated subcutaneous injections of IL12/23 p40 neutralising antibody, ustekinumab, in patients with relapsing-remitting multiple sclerosis: A phase II, double-blind, placebo-controlled, randomised, dose-ranging study. Lancet Neurol 7(9):796-804.

Segal M, Vlachos A, Korkotian E. 2010. The spine apparatus, synaptopodin, and dendritic spine plasticity. Neuroscientist 16(2):125-31.

Sepulveda-Diaz JE, Alavi Naini SM, Huynh MB, Ouidja MO, Yanicostas C, Chantepie S, Villares J, Lamari F, Jospin E, van Kuppevelt TH, et al. 2015. HS3ST2 expression is critical for the abnormal phosphorylation of tau in alzheimer's disease-related tau pathology. Brain 138(Pt 5):1339-54.

Serafini B, Rosicarelli B, Franciotta D, Magliozzi R, Reynolds R, Cinque P, Andreoni L, Trivedi P, Salvetti M, Faggioni A, et al. 2007. Dysregulated epstein-barr virus infection in the multiple sclerosis brain. J Exp Med 204(12):2899-912.

Shah, K.N., Wilson, E.A., Malla, R., Elford, H.L., and Faridi, J.S. (2015). Targeting ribonucleotide reductase M2 and NF-kappaB activation with Didox to circumvent tamoxifen resistance in breast cancer. Mol. Cancer. Ther. 14(11), 2411-2421.

Shahijanian F, Parnell GP, McKay FC, Gatt PN, Shojoei M, O'Connor KS, Schibeci SD, Brilot F, Liddle C, Batten M, et al. 2014. The CYP27B1 variant associated with an increased risk of autoimmune disease is underexpressed in tolerizing dendritic cells. Hum Mol Genet 23(6):1425-34.

Shepherd MN, Pomicter AD, Velazco CS, Henderson SC, Dupree JL. 2012. Paranodal reorganization results in the depletion of transverse bands in the aged central nervous system. Neurobiol Aging 33(1):203.e13,203.e24.

Shibuya K, Misawa S, Arai K, Nakata M, Kanai K, Yoshiyama Y, Ito K, Isose S, Noto Y, Nasu S, et al. 2011. Markedly reduced axonal potassium channel expression in human sporadic amyotrophic lateral sclerosis: An immunohistochemical study. Exp Neurol 232(2):149-53.

Shields DC and Banik NL. 1998. Upregulation of calpain activity and expression in experimental allergic encephalomyelitis: A putative role for calpain in demyelination. Brain Res 794(1):68-74.

Shields DC, Schaecher KE, Saido TC, Banik NL. 1999. A putative mechanism of demyelination in multiple sclerosis by a proteolytic enzyme, calpain. Proc Natl Acad Sci U S A 96(20):11486-91.

Shroff SM, Pomicter AD, Chow WN, Fox MA, Colello RJ, Henderson SC, Dupree JL. 2009. Adult CST-null mice maintain an increased number of oligodendrocytes. J Neurosci Res 87(15):3403-14.

Sie C and Korn T. 2017. Dendritic cells in central nervous system autoimmunity. Semin Immunopathol 39(2):99-111.

Simms BA and Zamponi GW. 2014. Neuronal voltage-gated calcium channels: Structure, function, and dysfunction. Neuron 82(1):24-45.

Simons M and Nave KA. 2015. Oligodendrocytes: Myelination and axonal support. Cold Spring Harb Perspect Biol 8(1):a020479.

Simpson S,Jr, der Mei IV, Taylor B. 2017. The role of vitamin D in multiple sclerosis: Biology & biochemistry, epidemiology and potential roles in treatment. Med Chem .

Singh RJ, Hogg N, Joseph J, Konorev E, Kalyanaraman B. 1999. The peroxynitrite generator, SIN-1, becomes a nitric oxide donor in the presence of electron acceptors. Arch Biochem Biophys 361(2):331-9.

Sinha S, Boyden AW, Itani FR, Crawford MP, Karandikar NJ. 2015. CD8(+) T-cells as immune regulators of multiple sclerosis. Front Immunol 6:619.

Skripuletz T, Miller E, Moharregh-Khiabani D, Blank A, Pul R, Gudi V, Trebst C, Stangel M. 2010. Beneficial effects of minocycline on cuprizone induced cortical demyelination. Neurochem Res 35(9):1422-33.

Skripuletz T, Lindner M, Kotsiari A, Garde N, Fokuhl J, Linsmeier F, Trebst C, Stangel M. 2008. Cortical demyelination is prominent in the murine cuprizone model and is strain-dependent. Am J Pathol 172(4):1053-61.

Smith JA, Park S, Krause JS, Banik NL. 2013. Oxidative stress, DNA damage, and the telomeric complex as therapeutic targets in acute neurodegeneration. Neurochem Int 62(5):764-75.

Snaidero N, Mobius W, Czopka T, Hekking LH, Mathisen C, Verkleij D, Goebbels S, Edgar J, Merkler D, Lyons DA, et al. 2014. Myelin membrane wrapping of CNS axons by PI(3,4,5)P3-dependent polarized growth at the inner tongue. Cell 156(1-2):277-90.

Sotirchos ES, Bhargava P, Eckstein C, Van Haren K, Baynes M, Ntranos A, Gocke A, Steinman L, Mowry EM, Calabresi PA. 2016. Safety and immunologic effects of high- vs low-dose cholecalciferol in multiple sclerosis. Neurology 86(4):382-90.

Spiegel I, Adamsky K, Eshed Y, Milo R, Sabanay H, Sarig-Nadir O, Horresh I, Scherer SS, Rasband MN, Peles E. 2007. A central role for Necl4 (SynCAM4) in schwann cell-axon interaction and myelination. Nat Neurosci 10(7):861-9.

Sriram S and Steiner I. 2005. Experimental allergic encephalomyelitis: A misleading model of multiple sclerosis. Ann Neurol 58(6):939-45.

Stanley ER, Berg KL, Einstein DB, Lee PS, Pixley FJ, Wang Y, Yeung YG. 1997. Biology and action of colony--stimulating factor-1. Mol Reprod Dev 46(1):4-10.

Stoler O and Fleidervish IA. 2016. Functional implications of axon initial segment cytoskeletal disruption in stroke. Acta Pharmacol Sin 37(1):75-81.

Stroissnigg H, Trancikova A, Descovich L, Fuhrmann J, Kutschera W, Kostan J, Meixner A, Nothias F, Propst F. 2007. S-nitrosylation of microtubule-associated protein 1B mediates nitric-oxide-induced axon retraction. Nat Cell Biol 9(9):1035-45.

Sun X, Wu Y, Gu M, Liu Z, Ma Y, Li J, Zhang Y. 2014. Selective filtering defect at the axon initial segment in alzheimer's disease mouse models. Proc Natl Acad Sci U S A 111(39):14271-6.

Sundstrom P, Nystrom L, Jidell E, Hallmans G. 2008. EBNA-1 reactivity and HLA DRB1*1501 as statistically independent risk factors for multiple sclerosis: A case-control study. Mult Scler 14(8):1120-2.

Susuki K. 2013. Node of ranvier disruption as a cause of neurological diseases. ASN Neuro 5(3):209-19.

Susuki K and Rasband MN. 2008. Molecular mechanisms of node of ranvier formation. Curr Opin Cell Biol 20(6):616-23.

Susuki K, Chang KJ, Zollinger DR, Liu Y, Ogawa Y, Eshed-Eisenbach Y, Dours-Zimmermann MT, Oses-Prieto JA, Burlingame AL, Seidenbecher CI, et al. 2013. Three mechanisms assemble central nervous system nodes of ranvier. Neuron 78(3):469-82.

Suzuki A, Hoshi T, Ishibashi T, Hayashi A, Yamaguchi Y, Baba H. 2004. Paranodal axoglial junction is required for the maintenance of the Nav1.6-type sodium channel in the node of ranvier in the optic nerves but not in peripheral nerve fibers in the sulfatide-deficient mice. Glia 46(3):274-83.

Szekeres T, Fritzer-Szekeres M, Elford HL. 1997. The enzyme ribonucleotide reductase: Target for antitumor and anti-HIV therapy. Crit Rev Clin Lab Sci 34(6):503-28.

Tabarkiewicz J, Pogoda K, Karczmarczyk A, Pozarowski P, Giannopoulos K. 2015. The role of IL-17 and Th17 lymphocytes in autoimmune diseases. Arch Immunol Ther Exp (Warsz) 63(6):435-49.

Taetzsch T, Levesque S, McGraw C, Brookins S, Luqa R, Bonini MG, Mason RP, Oh U, Block ML. 2015. Redox regulation of NF-kappaB p50 and M1 polarization in microglia. Glia 63(3):423-40.

Tait S, Gunn-Moore F, Collinson JM, Huang J, Lubetzki C, Pedraza L, Sherman DL, Colman DR, Brophy PJ. 2000. An oligodendrocyte cell adhesion molecule at the site of assembly of the paranodal axo-glial junction. J Cell Biol 150(3):657-66.

Tang H, Viola HM, Filipovska A, Hool LC. 2011. Ca(v)1.2 calcium channel is glutathionylated during oxidative stress in guinea pig and ischemic human heart. Free Radic Biol Med 51(8):1501-11.

Tang Y and Le W. 2016. Differential roles of M1 and M2 microglia in neurodegenerative diseases. Mol Neurobiol 53(2):1181-94.

Tang Y and Le W. 2016. Differential roles of M1 and M2 microglia in neurodegenerative diseases. Mol Neurobiol 53(2):1181-94.

Tenembaum SN. 2017. Pediatric multiple sclerosis: Distinguishing clinical and MR imaging features. Neuroimaging Clin N Am 27(2):229-50.

Thaxton C and Bhat MA. 2009. Myelination and regional domain differentiation of the axon. Results Probl Cell Differ 48:1-28.

Thaxton C, Pillai AM, Pribisko AL, Dupree JL, Bhat MA. 2011. Nodes of ranvier act as barriers to restrict invasion of flanking paranodal domains in myelinated axons. Neuron 69(2):244-57.

Tiago T, Marques-da-Silva D, Samhan-Arias AK, Aureliano M, Gutierrez-Merino C. 2011. Early disruption of the actin cytoskeleton in cultured cerebellar granule neurons exposed to 3-morpholinosydnonimine-oxidative stress is linked to alterations of the cytosolic calcium concentration. Cell Calcium 49(3):174-83.

Tong L, Prieto GA, Kramar EA, Smith ED, Cribbs DH, Lynch G, Cotman CW. 2012. Brain-derived neurotrophic factor-dependent synaptic plasticity is suppressed by interleukin-1beta via p38 mitogen-activated protein kinase. J Neurosci 32(49):17714-24.

Torre-Fuentes L, Moreno-Jimenez L, Pytel V, Matias-Guiu JA, Gomez-Pinedo U, Matias-Guiu J. 2017. Experimental models of demyelination and remyelination. Neurologia .

Trackey JL, Uliasz TF, Hewett SJ. 2001. SIN-1-induced cytotoxicity in mixed cortical cell culture: Peroxynitrite-dependent and -independent induction of excitotoxic cell death. J Neurochem 79(2):445-55.

Trager N, Smith A, Wallace Iv G, Azuma M, Inoue J, Beeson C, Haque A, Banik NL. 2014. Effects of a novel orally administered calpain inhibitor SNJ-1945 on immunomodulation and neurodegeneration in a murine model of multiple sclerosis. J Neurochem .

Traka M, Goutebroze L, Denisenko N, Bessa M, Nifli A, Havaki S, Iwakura Y, Fukamauchi F, Watanabe K, Soliven B, et al. 2003. Association of TAG-1 with Caspr2 is essential for the molecular organization of juxtaparanodal regions of myelinated fibers. J Cell Biol 162(6):1161-72.

Trapp BD, Peterson J, Ransohoff RM, Rudick R, Mork S, Bo L. 1998. Axonal transection in the lesions of multiple sclerosis. N Engl J Med 338(5):278-85.

Trebst C, Sorensen TL, Kivisakk P, Cathcart MK, Hesselgesser J, Horuk R, Sellebjerg F, Lassmann H, Ransohoff RM. 2001. CCR1+/CCR5+ mononuclear phagocytes accumulate in the central nervous system of patients with multiple sclerosis. Am J Pathol 159(5):1701-10.

Turchan J, Pocernich CB, Gairola C, Chauhan A, Schifitto G, Butterfield DA, Buch S, Narayan O, Sinai A, Geiger J, et al. 2003. Oxidative stress in HIV demented patients and protection ex vivo with novel antioxidants. Neurology 60(2):307-14.

van Noort JM, van den Elsen PJ, van Horssen J, Geurts JJ, van der Valk P, Amor S. 2011. Preactive multiple sclerosis lesions offer novel clues for neuroprotective therapeutic strategies. CNS Neurol Disord Drug Targets 10(1):68-81.

Vascak M, Sun J, Baer M, Jacobs KM, Povlishock JT. 2017. Mild traumatic brain injury evokes pyramidal neuron axon initial segment plasticity and diffuse presynaptic inhibitory terminal loss. Front Cell Neurosci 11:157.

Wang Y, Zhang P, Wyskiel DR. 2016. Chandelier cells in functional and dysfunctional neural circuits. Front Neural Circuits 10:33.

Waxman SG. 2008. Axonal dysfunction in chronic multiple sclerosis: Meltdown in the membrane. Ann Neurol 63(4):411-3.

Wiest DL. 2016. Development of gammadelta T cells, the special-force soldiers of the immune system. Methods Mol Biol 1323:23-32.

Wimmer VC, Reid CA, So EY, Berkovic SF, Petrou S. 2010. Axon initial segment dysfunction in epilepsy. J Physiol 588(Pt 11):1829-40.

Wingerchuk DM. 2011. Environmental factors in multiple sclerosis: Epstein-barr virus, vitamin D, and cigarette smoking. Mt Sinai J Med 78(2):221-30.

Wootla B, Denic A, Keegan BM, Winters JL, Astapenko D, Warrington AE, Bieber AJ, Rodriguez M. 2011. Evidence for the role of B cells and immunoglobulins in the pathogenesis of multiple sclerosis. Neurol Res Int 2011:780712.

Yamada R and Kuba H. 2016. Structural and functional plasticity at the axon initial segment. Front Cell Neurosci 10:250.

Yamada T, Fedotovskaya O, Cheng AJ, Cornachione AS, Minozzo FC, Aulin C, Friden C, Turesson C, Andersson DC, Glenmark B, et al. 2015. Nitrosative modifications of the Ca2+ release complex and actin underlie arthritis-induced muscle weakness. Ann Rheum Dis 74(10):1907-14.

Yamasaki R, Lu H, Butovsky O, Ohno N, Rietsch AM, Cialic R, Wu PM, Doykan CE, Lin J, Cotleur AC, et al. 2014. Differential roles of microglia and monocytes in the inflamed central nervous system. J Exp Med 211(8):1533-49.

Yang Y, Ogawa Y, Hedstrom KL, Rasband MN. 2007. betaIV spectrin is recruited to axon initial segments and nodes of ranvier by ankyrinG. J Cell Biol 176(4):509-19.

Yoshimura T and Rasband MN. 2014. Axon initial segments: Diverse and dynamic neuronal compartments. Curr Opin Neurobiol 27C:96-102.

Yu Y, Maureira C, Liu X, McCormick D. 2010. P/Q and N channels control baseline and spike-triggered calcium levels in neocortical axons and synaptic boutons. J Neurosci 30(35):11858-69.

Zalc B. 2006. The acquisition of myelin: A success story. Novartis found Symp 276:15,21; discussion 21-5, 54-7, 275-81.

Zamvil SS and Steinman L. 1990. The T lymphocyte in experimental allergic encephalomyelitis. Annu Rev Immunol 8:579-621.

Zeis T, Kinter J, Herrero-Herranz E, Weissert R, Schaeren-Wiemers N. 2008. Gene expression analysis of normal appearing brain tissue in an animal model for multiple sclerosis revealed grey matter alterations, but only minor white matter changes. J Neuroimmunol 205(1-2):10-9.

Zempel H, Dennissen F, Kumar Y, Luedtke J, Biernat J, Mandelkow EM, Mandelkow E. 2017. Axodendritic sorting and pathological missorting of tau is isoform specific and determined by axon initial segment architecture. J Biol Chem .

Zhang X, Cui X, Cheng L, Guan X, Li H, Li X, Cheng M. 2012. Actin stabilization by jasplakinolide affects the function of bone marrow-derived late endothelial progenitor cells. PLoS One 7(11):e50899.

Zhaowei L, Yongling X, Jiajia Y, Zhuo Y. 2014. The reduction of EPSC amplitude in CA1 pyramidal neurons by the peroxynitrite donor SIN-1 requires Ca2+ influx via postsynaptic non-L-type voltage gated calcium channels. Neurochem Res 39(2):361-71.

Zhou D, Lambert S, Malen PL, Carpenter S, Boland LM, Bennett V. 1998. AnkyrinG is required for clustering of voltage-gated na channels at axon initial segments and for normal action potential firing. J Cell Biol 143(5):1295-304.

Zhu J, Yamane H, Paul WE. 2010. Differentiation of effector CD4 T cell populations (*). Annu Rev Immunol 28:445-89.

Ziehn MO, Avedisian AA, Dervin SM, O'Dell TJ, Voskuhl RR. 2012. Estriol preserves synaptic transmission in the hippocampus during autoimmune demyelinating disease. Lab Invest 92(8):1234-45.

Zonta B, Desmazieres A, Rinaldi A, Tait S, Sherman DL, Nolan MF, Brophy PJ. 2011. A critical role for neurofascin in regulating action potential initiation through maintenance of the axon initial segment. Neuron 69(5):945-56.

Zoupi L, Markoullis K, Kleopa KA, Karagogeos D. 2013. Alterations of juxtaparanodal domains in two rodent models of CNS demyelination. Glia 61(8):1236-49.

Zuchero JB and Barres BA. 2015. Glia in mammalian development and disease. Development 142(22):3805-9.

APPENDIX ONE

Primary Cortical Neuron *In Vitro* System Methodology

Media Recipes for Primary Cortical Neuron Culture

Neurobasal Media w/out B27 (500 mL)		NB w/ B27 (50 mL)	
	500 mL		**Catalog #**
Neurobasal Media	500-7.55 mL		Gibco 21103-049
Anti-Anti	5 mL		Gibco 15240-096
B-27* (50X)	-	1 mL	Gibco 17504-044
L-Glutamine (200 mM)	1250 µL		Gibco 25030-149
Glutamate (10mM)	1300 µL		Sigma G8415-100G

Will need with and without B-27 (Thaw frozen B27 at 4ºC)

NB Media + B27 **with** anti-oxidants – for initial plating (100 µL/coverslip)

NB Media + B27 **without** anti-oxidants – for long term maintenance media (600 µL/well)

Sterilize via vacuum filtration!

Store at 4º C

Poly-D-Lysine Coating

Preparing the Solution

Borate Buffer		
	1 L	**Catalog #**
Water	1 L	
Boric Acid	3.1 g	Sigma B6768-500G
Sodium Borate	4.75 g	Sigma 221732-500G

1. Prepare Borate Buffer
2. Dissolve 100 mg of Poly-D-Lysine (Sigma P0899) in 1 mL Borate Buffer and aliquot to 100 µL, store at -20ºC.
3. For each 10 mL Borate Buffer, add 100 µL of Poly-D-Lysine stock solution, filter through 0.22 µm filters.

Preparing the coverslips

Note: coverslips should be acid washed in 1 M HCl for at least 5 hours in 60ºC water bath then rinsed thoroughly with DI H2O and stored long-term in EtOH.

1. Place desired # of coverslips on Whatman paper and let dry under UV in the hood
2. Put 100 µL of diluted Poly-D-Lysine solution on each coverslip and let sit in the hood for 1 Hr
3. Transfer to 24-well plates containing DI H2O (keep coated side up)
4. Dump and replace DI H2O at least 6 times (6 washes in DI H2O) (keep coated side up)
5. Transfer washed coverslips to Whatman paper and let dry overnight under UV in the hood (keep coated side up!)
6. Once completely dry, transfer to sterile 24 well plates for cell plating (keep coated side up)

Neuronal Culture Preparation and Plating

Pre-preparation

- Make sure the incubator is set to 37^{o}C and 5% CO_2
- Prepare 500 mL Neurobasal media (w/out B-27) and keep on ice
- Put 10 mL of NB media (w/out B-27) in 6 petri dishes and keep on ice
- Prepare Neurobasal media w/ B-27 + AO and keep on ice
- Prepare Neurobasal media w/ B-27 - AO and keep in 37^{o}C water bath
- Thaw 2 mL accutase aliquot at RT and keep on ice once thawed

Removal of Embryos

1. Euthanize the mother (containing E16 pups)

2. Remove the embryonic sac

   - Apply ethanol to belly

   - pull up skin and cut open to reveal the embryonic sac

   - remove embryonic sac and place in a petri dish containing NB media (w/o B-27) to wash off excess blood

3. Remove the individual embryos, decapitate with scissors, and place heads in a separate dish w/ NB media (w/o B-27)

Dissection of Brains ****From here on out, do all steps on ice!****

4. Place one head on a gauze pad soaked in ethanol under a dissecting microscope

5. Using two very fine forceps peel off the skin - pinch in the center and pull in opposite directions to rip it away from the brain

6. Using the same method, peel off the skull (it should be soft enough)

7. Pick up the brain with the forceps (pinch underneath and lift) and place it into an empty dish containing NB media (w/o B-27) - do this for all brains

8. Place one brain in a separate dish w/ NB media (w/o B-27) under the dissecting microscope and using forceps and micro-scissors; remove and discard the cerebellum

9. Separate the two hemispheres and turn them downward (midbrain on the bottom) - do not cut, pull them apart

10. Using two forceps method, remove the meninges from both hemispheres (separately) - meninges need to be removed to prevent blood cells and other cell types from contaminating your culture

11. Turn hemisphere back over (midbrain facing up) and cut out the midbrain w/ micro-scissors or with forceps– leaving only the cortex behind

    - place all cortex tissue in a separate dish containing NB media (w/o B-27)

12. Transfer cortices (using a transfer pipette) into 2 mL of accutase in a 15 mL conical tube

13. Let sit on ice for 10 minutes

    - do not close the conical tube lid - the cells need airflow

    - mix around every 5 minutes to break up clumps

Neuronal Isolation ****From here on out use NB media WITH B-27+AO****

14. Centrifuge the accutase/neuronal conical tube for 5 min at 900 RPM

15. Aspirate and discard supernatant w/ pipette-man and add 7 mL of complete NB media (w/ B-27+AO) – should use less than 7 mL if fewer you have fewer than 5 cortices

16. Homogenize (by trituration) w/ 10 mL pipette (until it flows smoothly)

17. Homogenize (by trituration) w/ 10 mL pipette + 1000 µL sterile tip attached (until it flows smoothly)

18. Homogenize (by trituration) w/ 10 mL pipette + 200 µL sterile tip attached

    (20 times up/down or until it flows smoothly)

19. Pass homogenate through a 70 µm cell strainer in a 50 mL conical tube.

20. Pass again through a second filter on another 50 mL conical tube = single cell solution

Neuronal Counting & Plating

21. Dilute 30 µL of single cell solution into 270 µL of trypan blue in a hemocytometer and count.

22. Dilute to desired cell concentration (30,000 neurons per coverslip) in complete NB media (w/ B-27+AO) and plate (100 µL of cell solution)

    Desired plating concentration: (30,000 cells)/(100 µL)=300,000 cells/mL

23. 1 hour after plating (after cells have adhered to the coverslip): add 600 µL of NB media w/ B27 - AO with a multi-channel pipette

24. Leave the cells in the incubator without changing media. Treatments can begin at 10 days after plating (the point at which the AIS is mature *in vitro*).

Neuronal Culture Preparation and Plating

The following steps are for treating one 24-well plate – do this for each plate separately

1. Prepare necessary amount of media with B27 (–AO)

   (Depends on number of plates to be treated – need ~11 mL per plate) – do not prepare less than 50 mL since B27 (-AO) cannot be re-frozen

2. Warm media to 37^{o}C in water bath

   (do not treat cells until it has sat at least ~15 min in the water bath)

3. Weigh out 1 mg of SIN-1 into a micro-centrifuge tube on an analytical balance

4. Prepare two 15 mL centrifuge tubes – each with the appropriate amount of media ready to use immediately upon dilution of SIN-1

   - 1 tube with 6.05 mL media (Tube 1)

   - 1 tube with 3.75 mL media (Tube 2)

SIN-1 Dilution	Final Concentration
800 µM = 1 mg in 6.05 mL	
200 µM = 1.25 mL of 800 µM in 5 mL	100 µL added = 25 µM

5. Make sure all necessary pipettes are set and ready to use for treatment

6. Use ~1 mL from Tube 1 to dissolve and rinse the tube containing 1 mg SIN-1 – quickly transfer this back to Tube 1 and vortex

7. Immediately add 1.25 mL of Tube 1 to Tube 2 and vortex

8. Quickly remove plate to be treated from incubator and add 100 µL of Tube 2 to each well – dip the tip and add directly into the existing media so none of it is lost (keep using the same tip for every well to save time)

9. Place plate back into incubator to be taken at desired time point

VITA

Kareem Clark was born in Louisville, Kentucky in 1989. He was raised in North Carolina and received a Bachelor's in Science Degree with a concentration in biochemistry from North Carolina State University in 2011. After college, Kareem was accepted into the Biomedical Sciences Doctoral Portal at the Virginia Commonwealth University School of Medicine, where he completed his neuroscience graduate training under the mentorship of Jeffery Dupree, PhD. This thesis was defended on October 30th, 2017 before the PhD committee.